12-2021

Modeling and Control of Power Electronics Interfaced Load for Transmission Power Network Analysis

Shuyao Wang
University of Tennessee, Knoxville, swang67@vols.utk.edu

Recommended Citation

Wang, Shuyao, "Modeling and Control of Power Electronics Interfaced Load for Transmission Power Network Analysis. " PhD diss., University of Tennessee, 2021.
https://trace.tennessee.edu/utk_graddiss/7023

To the Graduate Council:

I am submitting herewith a dissertation written by Shuyao Wang entitled "Modeling and Control of Power Electronics Interfaced Load for Transmission Power Network Analysis." I have examined the final electronic copy of this dissertation for form and content and recommend that it be accepted in partial fulfillment of the requirements for the degree of Doctor of Philosophy, with a major in Electrical Engineering.

Leon M. Tolbert, Major Professor

We have read this dissertation and recommend its acceptance:

Leon M. Tolbert, Fei Wang, Kevin Tomsovic, Qiang He

Accepted for the Council:

Dixie L. Thompson

Vice Provost and Dean of the Graduate School

(Original signatures are on file with official student records.)

Modeling and Control of Power Electronics Interfaced Load for Transmission Power Network Analysis

A Dissertation Presented for the
Doctor of Philosophy
Degree
The University of Tennessee, Knoxville

Shuyao Wang
December 2021

This document is dedicated to my family.

Acknowledgments

There are many people who have helped me during my Ph.D. studies. My sincerest gratitude is to my advisor, Dr. Leon Tolbert, for his inspiring wisdom, expert guidance, and timely support. I have received a lot of advice and encouragement from Dr. Tolbert when I started my Ph.D. program, and it is his kind help that guided me towards becoming skillful in research.

I would like to thank Dr. Fred Wang for instructing most of my research projects. His expert support and insightful advice inspire me to solve many problems in the research.

I would like to thank Dr. Kevin Tomsovic for leading me in conducting power-system-related research with his rich knowledge.

I would like to thank Dr. Kai Sun and Dr. Kevin Bai for the kind suggestions on my research. Also, I would like to thank Dr. Daniel Costinett and Dr. Zheyu Zhang for boarding my knowledge and experimental experiences. Additionally, I would like to thank Dr. Qiang He for kindly serving as my committee member and giving great suggestions on improving my dissertation and presentation.

I would also like to thank all the CURENT colleges, including but not limited to, Dr. Jingxin Wang, Dr. Yiwei Ma, Dr. Lin Zhu, Dr. Zhiqiang Wang, Dr. Xiaojie Shi, Dr. Handong Gui, Dr. Yunting Liu, Dr. Ishita Ray, Dr. Sheng Zheng, Dr. Shiqi Ji, Dr. Shuoting Zhang, Dr. Ren Ren, Dr. Bo Liu, Dr. Wenchao Cao, Dr. Ruirui Chen, Dr. Fei Yang, Dr. Wen Zhang, Dr. Ling Jiang, Dr. Chongwen Zhao, Dr. Xin Xu, Dr. Qingxin Shi, Dr. Yan Du, Dr. kaiqi Sun, Dr. Huangqing Xiao, Dr. Hongyu Li, Dr. Siqi Wang, Dr. Yajun Wang, Dr. Hantao Cui, Dr. Wei Feng, Ms. Jingjing Sun, Mr. Xingxuan Huang, Mr. Nattapat Praisuwanna, Ms. Paychuda Kritprajun, Ms. Min Lin, Mr. Mark Nakmali, Mr. Peter Pham, Ms. Jessica Boles, Ms. Taylor Short, Ms. Jillian Ruff, Mr. Zhe Yang,

Mr. Jiahao Niu, Ms. Emma (Le) Kong, Mr. Haiguo Li, Mr. Dingrui Li, Mr.Liang Qiao, Mr. Zhou Dong, Mr. Jacob Dyer, Mr. Craig Timms, Ms. Paige Williford, Mr. Jie Li, Mr. Spencer Cochran, Mr. Ruiyang Qin, Mr. Kamal Sabi, Mr. Andrew Foote, Mr. Jared Baxter, Mr. Young (Yang) Huang, Mr. Liyan Zhu, Mr. Yu Yan, Mr. Ximu Zhang, Mr. Ziwei Liang, Mr. Zihan Gao, Ms. Niu Jia, Mr. Yue Sun, Mr. Tianwei Xia, and Mr. Yang Liu.

I also would like to express my gratitude to all the staff members, including but not limited to, Mr. Robert Martin, Dr. Chien-Fei Chen, Dr. Anne Skutnik, Mr. Ryan Smiley, Ms. Wendy Smith, Ms. Judy Evans, Mr. Erin Wills, Mr. Chris Anderson, Mr. Jay Cooley, Ms. Lisa Beard, and Ms. Dana Bryson. Their professional help has always been reliable.

Most importantly, none of this would have been possible without the love and support from my family. My parents, Xuexin Wang and Mei Li, have always been supporting me and encouraging me to go for my dreams. I would like to thank my dear husband, Dr. Daijiafan Mao, for his continuous help and support in almost every aspect of my life. I dedicate this dissertation to my family.

This dissertation was supported primarily by the Engineering Research Center Program of the National Science Foundation and Department of Energy under NSF Award Number EEC-1041877 and the CURENT Industry Partnership Program.

Abstract

The penetration level of power electronics (PE) interfaced loads has been gradually increasing in recent years. It is beneficial to equip the electric load with a PE interface since it allows for more advanced control of the load performance. Furthermore, the increasing penetration of PE interfaced loads will bring both challenges and opportunities to power network resilience and reliability.

However, the lack of modeling and control design for PE interfaced load units in the transmission-level power network analysis, especially for these high-penetrated high-power-rating load applications, limits the accuracy of evaluating the dynamic performance and stability status of the power network. Additionally, the complex configuration and high bandwidth dynamic performance of the PE interfaced load computationally prohibit the model development in transient stability (TS) simulation programs.

Therefore, the dynamic PE interfaced load model can be characterized considering the following aspects: 1) Utilize the real-time experimental platform to represent the PE load dynamic performance since the power testbed can reflect the power grid operation with more robustness. 2) Adapt the simplified PE-based model to TS simulation tools, which focus on grid electromechanical transients and oscillations between 0.1 and 3 Hz.

Research of the PE interfaced load towards its modeling and control design in different simulation environments and the flexible contribution to the grid operation has been conducted. First, the variable speed drive (VSD) based motor load is studied as a typical PE interfaced load, which can actively interact with power grid operation. The model of VSD load is introduced and applied to the power emulator for the multi-converter-based hardware testbed (HTB) in the Center of Ultra-wide-area Resilient Electric Energy Transmission Network (CURENT). Second, the aggregated performance of multiple VSD load units with grid frequency support function is characterized. Third, the fast electric vehicle (EV) charging unit is studied as a typical PE interfaced load with high power consumption. The generic model of EV charger load is developed based on the detailed switching model. The accuracy of the proposed EV charger load TS model has been verified by comparing it to simulation results of the equivalent electromagnetic (EMT) model.

Table of Contents

List of Tables

List of Figures

Chapter 1

Introduction

1.1 Background and Motivation

Power electronics (PE) interfaced loads have gradually become one of the most commonly used types of loads in the electric power network. It is beneficial to equip electric loads with a PE interface since it not only provides a flexible way to change the power supply voltage magnitude and frequency, but also allows for more advanced control of the load performance. There are a large number of PE interfaced load types over wide power rating and application range, *e.g.,* electric vehicle (EV) charging stations, variable speed drives (VSD), consumer chargers, etc. PE interfaced loads are usually classified into the following categories [1]:

- Switch-mode power supply (SMPS) load includes “consumer electronics” devices, such as personal computers (PCs), televisions (TVs), compact disc (CD), and digital video disc (DVD) players, etc. The load power stages usually consist of a front-end rectifier, a dc link, and a dc-dc converter controlled to provide regulated output.

- Energy efficient lighting load includes compact fluorescent lamps (CFLs) and light-emitting diode (LED) lights. The LED light source circuit is mainly made up by the diode bridge rectifier, while CFLs use an electronic ballast circuit with the self-oscillating inverter to control the voltage across the fluorescent tube.

- Single-phase and three-phase VSD controlled motors can be further classified based on different types of mechanical loads, which include the constant-torque load, linear-torque load, quadratic-torque load, and constant power load.
- Distributed electric storage system (DESS), of which the storage unit is connected to the grid through a PE interface, which usually includes a pulse-width modulation (PWM) boost converter and a PWM voltage source converter (VSC).
- EV battery charging unit includes multiple power-rating levels based on different electric source formats. The EV charging unit characterizes a considerable power consumption with a growing penetration in the power grid.

The increasing penetration of PE interfaced loads will bring both challenges and opportunities to power network resilience and reliability, which is explained in the following two subsections.

1.1.1 Challenge: Distinct Load Characteristics and High Power Consumption

First, the PE interfaced load influences the grid transient stability (TS) when participating into the operation of conventional ac network [2]. A PE interfaced load is characterized as a nonlinear model with more complexity compared to the conventionally adopted load format for the TS analysis. Moreover, the growing energy consumption of some high-power-rating PE interfaced load also introduces a significant influence on the grid performance, of which the typical examples are an EV charging unit, a three-phase VSD unit, etc [3, 4].

The year-by-year development of charging infrastructure requirements in San Francisco is illustrated in Fig. 1.1 as an example [5]. It can be observed that each type of charging infrastructure (*i.e.,* workplace, public Level 2, and public dc fast) needed in the San Francisco metropolitan area grows significantly from 2017 to 2025. By 2025, there are expected to be more than 6,000 additional charge points in the workplace or public Level 2 charging, and more than 700 in dc fast charging, which is a huge increase compared with the existing number of EV charging infrastructures. Additionally, this analysis for the San Francisco EV

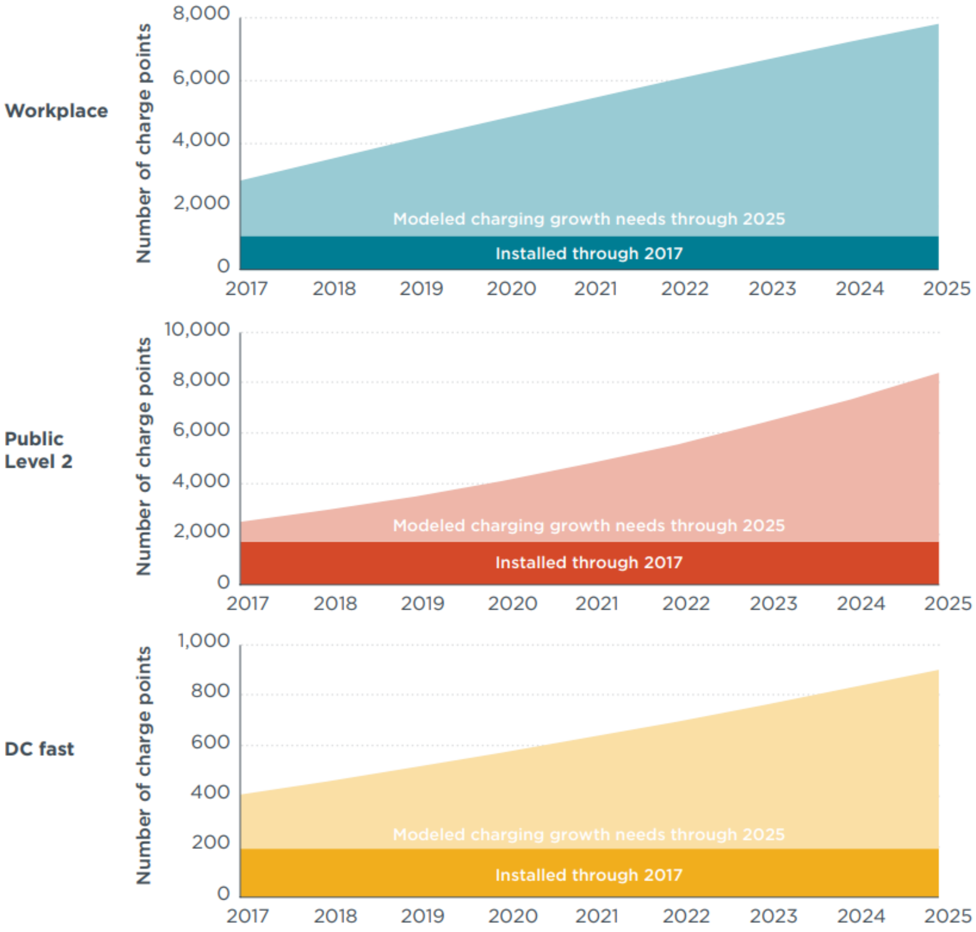

Figure 1.1: Quantifying the EV charging infrastructure gap in San Francisco metropolitan area [5].

charger expected growing trend shown in Fig. 1.1 is similar to that performed in the other 100 most populous metropolitan areas. So an EV charging unit global increasing trend will be expected in the near future.

1.1.2 Opportunity: Grid Enhancement Provided by PE Interfaced Load

Aside from influencing the power network operation due to its own characteristics, the PE interfaced load has the potential of improving the power grid stability with appropriate coordination and control.

Nowadays, renewable energy resources (RES) have been widely accepted and utilized since they play an essential role in reducing greenhouse gas emissions in the U.S. [6]. According to [7], renewable electricity generation is expected to increase to up to 38% of the total electricity generation by 2050, which is shown in Fig. 1.2. However, the increasing number of RES in the power grid introduces a severe power mismatch between the generation and demand because the RES is more intermittent and unpredictable compared with conventional generation resources. Therefore, it requires the coordination of responsive loads or energy storage units with the RES to mitigate the power mismatch issue.

The PE interfaced load is regarded as one of the best candidates for the responsive load. One of the reasons is that the PE interfaced load can respond accurately according to grid support requirements since PE interfaces can provide advanced load control. Moreover, using the PE interfaced load is cost-effective since it does not require extra investment on sensors and regulators compared with some loads inherently without PE interfaces. Therefore, the PE-based load has great potential of being used as the responsive load to promote grid performance.

1.1.3 PE Interfaced Load Model Application Current Status

However, the lack of PE interfaced load modeling and control design, especially for these high-penetrated high-power-rating load applications, limits the study of the corresponding impact on the power network dynamic performance and stability analysis. According to the survey conducted by the International Council on Large Electric Systems (CIGRE) regarding the international industry load modeling practice in 2013, the most commonly used load model for the power system analysis is the static load model as illustrated in Fig. 1.3 [8, 9].

From Fig. 1.3, the active load model and reactive load model are studied respectively as illustrated in Fig. 1.3a and Fig. 1.3b. As for the load model used in the dynamic power system analysis, 70% of the companies and institutes adopted the static model to represent the active and reactive load characteristics globally. In comparison, the application of the dynamic load is limited not only in terms of being adopted by a small portion of users, but also in terms of the limited types of dynamic load representation - typically, only the induction motor (IM) load is considered as the dynamic load and represented specifically. In contrast, other types of loads are all simplified and represented as static loads.

Meanwhile, Western Electricity Coordinating Council (WECC) has been working on improving the load representation in dynamic simulations. The WECC Composite Load Model (CLM) was tested and implemented in major industrial level simulation software by 2012, including PowerWorld Simulator, Siemens PTI PSS/E, TSAT, etc [10]. The dynamic load models provided in CLM include four types of motors. However, the dynamic performance of PE devices has not been emphasized until one of the recent updates where the PE-based RES, *e.g.,* the photovoltaic (PV) generation unit, has been classified as one of the CLM [11]. However, the model of the PE interfaced load still has not been considered yet.

One of the most important reasons for using a static load model to represent most of the electric loads, especially the PE interfaced load, is due to the fact that it is computationally prohibitive to study the large-scale transmission network with highly detailed models of any load devices. Therefore, it is not practical to represent the complex dynamic characteristics of the PE-based load, which includes the fast switching dynamics, the high-bandwidth control algorithm, and the sophisticated filtering process. However, the PE interfaced load is a typical nonlinear load. Also, some types of PE interfaced loads consume a large amount of power, *e.g.,* EV charging units, DESS, etc. Therefore, PE interfaced loads significantly affect the grid dynamic performance when being integrated into the conventional ac network [12]. Also, the PE interfaced load has the potential of improving grid stability with specific

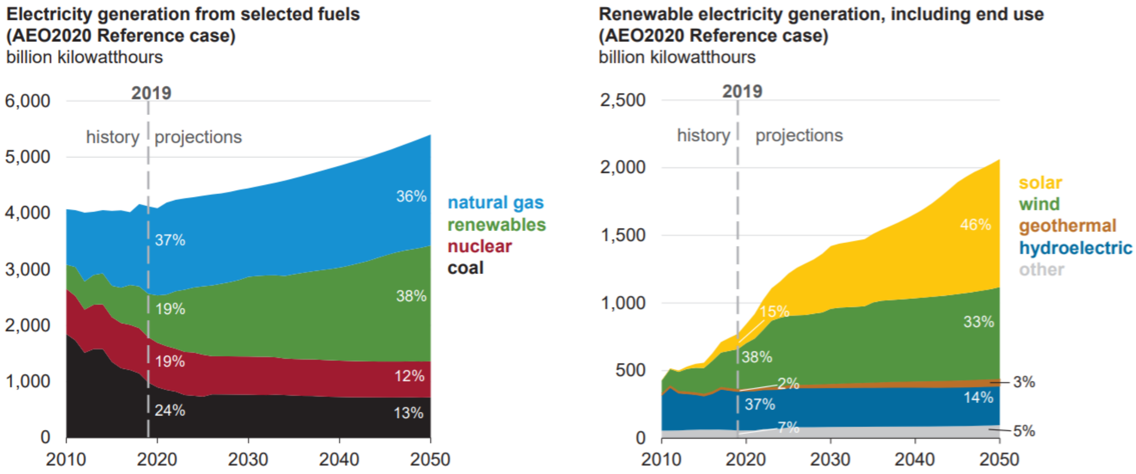

Figure 1.2: Increasing trend of renewable electricity generation [7].

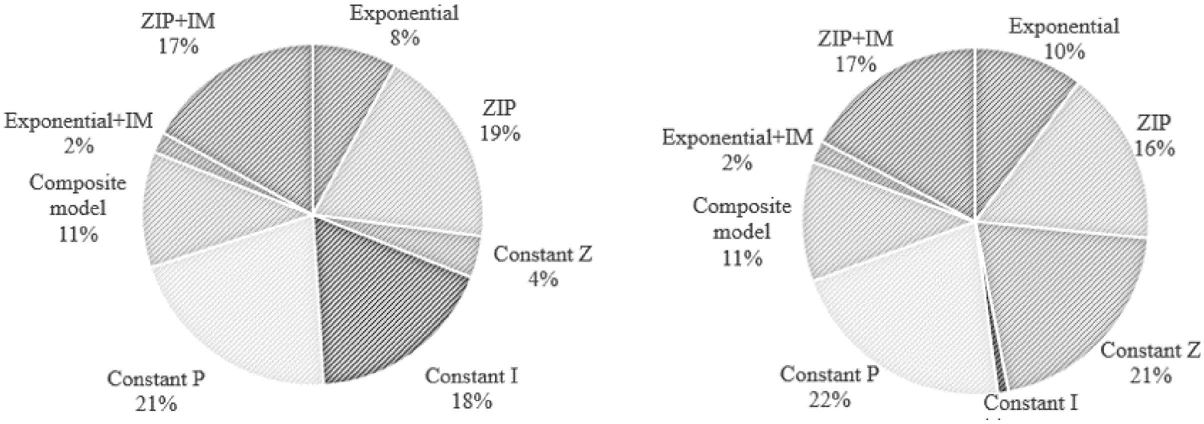

(a) Active power load model.

(b) Reactive power load model.

Figure 1.3: Load models used for dynamic power system studies [8, 9].

coordination and control, as introduced above. All of these distinct load characteristics cannot be fully reflected by the static load model. Therefore, it is of great importance to investigate how to represent the PE interfaced dynamic load performance, as well as the corresponding support functions, in the large-scale power system analysis.

1.2 Dissertation Outline

This dissertation is organized as follows in terms of exploring the modeling and control of PE interfaced load in the transmission-level power network analysis:

Chapter 2 gives a detailed literature review on the existing research progress towards utilizing industrial VSD loads with PE interfaces to perform as responsive loads to promote the power network operation, PE interfaced devices modeling method adopted by the TS simulation environment, control algorithms of fast EV charging units, and the application of the real-power electric grid emulation testbed. Meanwhile, the research topics in this dissertation are summarized in this chapter.

Chapter 3 presents detailed and simplified VSD models with open and closed-loop control schemes. The power emulator of the VSD load is developed based on the corresponding load model.

Chapter 4 presents the aggregated model of a VSD load with grid frequency support techniques. The potential of VSD loads in terms of providing an equivalent operational reserve for the grid is also discussed in this chapter.

Chapter 5 introduces the experiment exploring VSD load primary frequency support based on HTB and corresponding power emulator.

Chapter 6 introduces the simplified fast EV charging unit model, which is derived based on the detailed electromagnetic transient (EMT) model. The proposed simplified EV charger model will be used for developing the electromechanical model, which is suitable for the TS simulation environment.

Chapter 7 proposes an EV charger load model generic representation for a TS simulation environment, including the characterization of commonly used EV charger control algorithm in different operation modes. The accuracy of the proposed load model is verified by comparing the simulation results to that of the equivalent EMT benchmark model.

Chapter 8 summarizes the main conclusion of this dissertation, and introduces potential future research topics considering the PE interfaced load modeling and control.

Chapter 2

Literature Review

The increasing penetration of PE interfaced loads has introduced challenges and opportunities to the transmission power network, considering that PE loads not only perform as high-power-rating nonlinear load, but also have the potential of providing grid support flexibly. Therefore, it is no longer appropriate enough to regard the PE-based loads as static power consumption for grid analysis. Considering the compatibility of the complicated PE interfaced load model to the transmission-level power network analysis, there are two options for representing the PE-based load in the transmission power network: 1) Utilize real-time analog testing platform to represent the PE-based load dynamic performance; 2) Adapt the simplified PE-based model to TS simulation tools, which reflects the electromechanical transients and oscillations between 0.1 and 3 Hz.

In this dissertation, the investigation of the PE interfaced load mainly focuses on: 1) explore the potential of PE interfaced load on regulating the power grid frequency stability, 2) PE-based load emulator development in real-power testbed, 3) PE interfaced load dynamic model development for the transmission-level grid analysis. Reviews on the existing research about responsive loads, the PE interfaced devices modeling, and real-time power testbed are introduced in this chapter.

2.1 Responsive PE Interfaced Load Model and Controller Design

Nowadays, the vast integration of RES into the electric power grid imposes great challenges to the traditional centralized management system due to intermittence and unpredictability of RES [13, 14, 15, 16, 17]. Therefore, it is of critical importance to maintain a relative balance between the power supply and power demand instantaneously and continuously for the power grid with high-penetrated RES. Conventionally, the grid frequency stability is mainly provided by the synchronous generator (SG) primary frequency and secondary frequency control as illustrated in Fig. 2.1 [18, 19, 20].

As illustrated in Fig. 2.1, the primary frequency regulation aims to keep the balance between the generation and demand between 5-30 s following a grid disturbance, and the secondary frequency regulation restores the frequency to the nominal value in less than 15 minutes. However, due to difficulties introduced by the intermittent RES in terms of power flow balance regulation, it is more expensive and technically complex to guarantee the stability and reliability of the power grid by only using the conventional regulation scheme provided by SGs. In order to facilitate the application of RES in the future, it requires more flexible and fast response capacities to handle the generation variability. Therefore, the concept of using fast-response non-critical loads to improve grid stability has emerged in recent research.

2.1.1 Concept of Using Non-critical Load to Enhance Grid Stability

Non-critical loads can tolerate a wide variation of the supply voltage/frequency for a short time without disrupting consumers. It has been proposed in [21] that the technique of using non-critical load to achieve power flow response according to the power grid requirement is referred to as smart load (SL). Meanwhile, using non-critical loads as grid power reserve is economical since less energy storage capacity will be required accordingly [22, 23]. To simplify the notification, end-users equipped with similar techniques are all notified as "SL" in the following text, though some different names are presented in other existing studies. The general configuration of the SL is illustrated in Fig. 2.2.

The basic configuration of the SL model includes the following three parts, as illustrated in Fig. 2.2: 1) a combination of multiple identical non-critical load units, or multiple non-critical load units with similar characteristics. 2) PE interface which decouples load units from the power supply. Additionally, as for the load which originally has no PE interface configurations, it requires to install PE interface to fulfill the load responsive functions, which yields an extra investment. 3) Measurement unit and corresponding control schemes are required to be applied to the PE interface, which supports the required load response.

The basic function of SL is to flexibly adjust the power consumption following the requirement of grid support for a short duration. Therefore the modeling and control design of the SL should emphasize the flexible variation of the power flow. The SL can be classified according to the type of connected load as:

- Static smart load (SSL): the characteristics of the corresponding load can be modeled as the static load, *e.g.,* resistance load, inductance load, capacitance load, etc. Therefore, the SSL can be regarded as a controllable active and reactive power sink by appropriately adjusting the load terminal voltage magnitude V_{ES} and phase angle θ_{ES}, with actively regulating the PE interface. The basic SSL configuration is illustrated in Fig. 2.3a. The power capability of SL depends on the permissible voltage variation range of the load and PE interface, and the converter power rating limitations.

- Dynamic smart load (DSL): the dynamic load characteristics are not only related to the status of the current moment, but also related to the status of the previous moment. Therefore, the dynamic load is usually modeled by high-order differential equations, which is more complicated compared with the static load. The VSD driving non-critical rotating load, which is attributed to the high-power-rating non-critical PE interfaced load, is one of the most frequently used DSL. Existing examples utilizing VSD as DSL are mainly reviewed in this chapter considering the scope of this dissertation. The main configuration of VSD based DSL is illustrated in Fig. 2.3b.

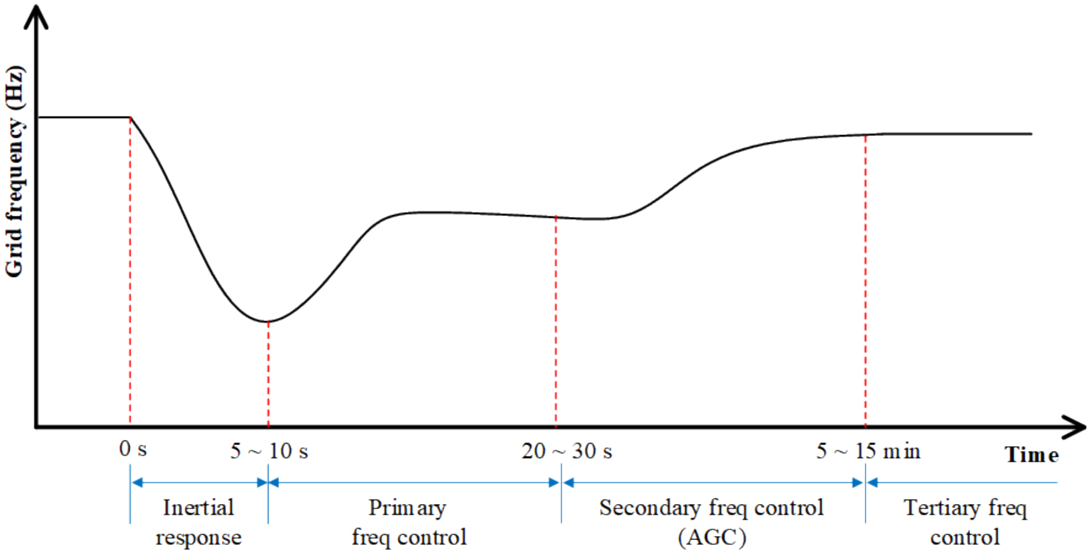

Figure 2.1: Schematic diagram of frequency control following a frequency disturbance [18, 19, 20].

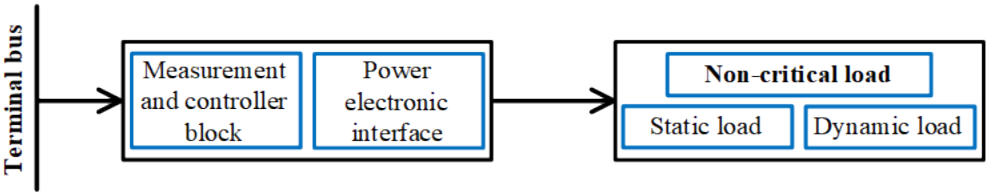

Figure 2.2: Smart load basic configuration [21].

The general circuit topologies illustrated in Fig. 2.3 are based on the assumption that the load models are represented for the transmission level. Different circuit topologies are required if representing the load for the distribution level.

2.1.2 SL Grid Support Functions

Based on the existing research, the SL main grid support functions can be classified according to the following five aspects:

- Active/reactive power control and voltage regulation [24, 22, 25, 26]. Several control schemes for regulating the SSL power consumption by adjusting the V_{ES} have been proposed in these research papers. Additionally, it has been proved that the application of SL can effectively reduce the energy storage requirements in the power network.
- Mitigation of harmonics [27], where the PE interface is utilized to improve supply voltage power quality by reducing the voltage harmonics.
- Power factor enhancement [28, 29], which is similar to the control principle of regulating the load power flow by adjusting the V_{ES}.
- Three-phase balance control [30, 31]. The load power imbalance condition is mitigated by independently regulating the PE interface in each phase.
- Grid frequency control [32, 33, 34, 35]. The supply and demand power mismatch can be mitigated by actively adjusting the SL active power consumption, thus improving the grid stability. Both the SSL and DSL have been investigated to support the grid frequency. How to provide frequency support by actively regulating DSLs is emphasized in the next subsection considering the research scope of this dissertation.

2.1.3 Grid Frequency Support Provided by VSD Load

IMs are used in a wide range of industries, such as oil, mining, marine, and other industry utilization. Meanwhile, VSDs have been widely used to control IMs because the PE-based VSD can accurately regulate the motor rotating speed according to the requirement of

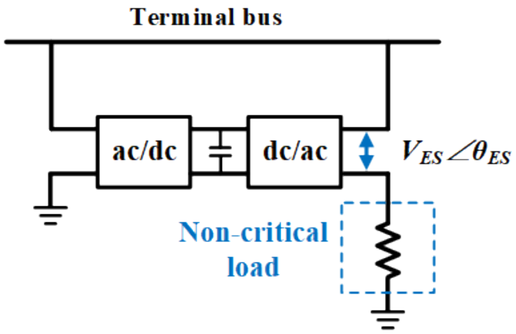

(a) SSL with series-parallel converter [22].

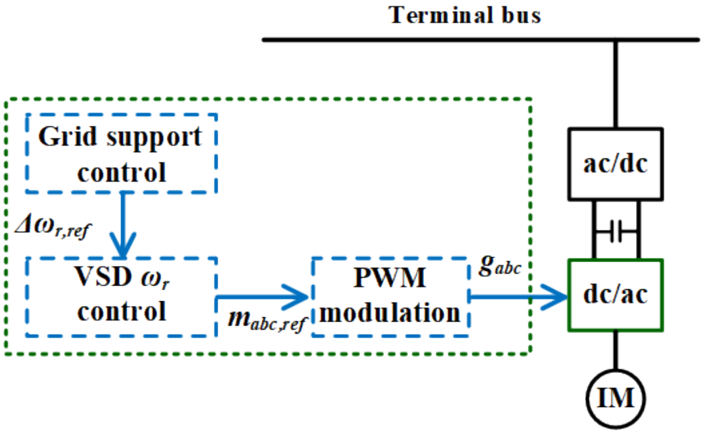

(b) VSD based DSL with series converter [21].

Figure 2.3: Main circuit topology of smart load.

customers. So the VSD has been gaining popularity in recent years, considering its benefits on performance improvement and energy savings [36]. It is estimated in [37] that energy savings from VSD systems are 787 GWh/year for fan systems and 6421 GWh/year for pump systems.

Furthermore, VSDs have the potential to improve the power grid stability, since VSD regulated motor loads can provide a variety of grid support - *e.g.,* grid frequency service - with appropriate control schemes to adjust load power. Specifically, non-critical loads, such as pumps and fans for heating, ventilation and air conditioning (HVAC), have better potential to provide grid support since a temporary adjustment of the rotating speed does not affect the load primary production process [35, 38, 36].

Compared with the SSL introduced above, a VSD load is regarded as a convenient end-user for providing grid support since the support control schemes can be directly applied to the PE-based motor drive without requiring extra investments. However, in existing research papers which discuss the VSD load frequency support, only the IM open-loop control scheme is adopted by most VSD controller designs, *e.g.,* the widely used constant volt-per-hertz control, which is also referred to as constant V/f control [36]. The basic grid frequency support scheme using VSD load is summarized below according to the existing literature[39, 40, 41]:

According to Fig. 2.4, the grid frequency deviation Δf is measured locally by the load unit, and the required VSD power consumption deviation reference ΔP_{ref} is derived based on the required droop response. Afterward, ΔP_{ref} will be transferred to rotor speed reference deviation $\Delta\omega_r$ according to the inherent motor load characteristics. Δf - ΔP_{ref} droop response will be introduced in the following subsection in detail.

Additionally, the VSD load topology mentioned in the above literature mainly includes the diode rectifier, the dc capacitor, the inverter-based motor drive with controllable switches and IM. So the motor load regenerative process should be considered as well. According to the proposed research results, the regenerative process is avoided by: 1) restricting the slew rate of the motor speed reference; 2) specifically design the VSD controller as illustrated in Fig. 2.5 [39].

As shown in Fig. 2.5, load power command P_{ref} is computed based on initial power command P_0 and ΔP_{ref} derived from the frequency deviation Δf. $\Delta\omega_{r,ref}$ is calculated using a proportional-integrator (PI) compensator with the input signal of the inverter's power deviation, which is expressed by the difference between P_{ref} and P_{inv}. This technique guarantees to avoid regeneration during the motor's speed reduction process regardless of its operating range.

Applying the open-loop constant V/f control to the VSD is cost-effective because: 1) an advanced microprocessor is not required to achieve the simple open-loop control function; 2) fewer electrical sensors are needed since no feedback information is used in the control loop. However, constant V/f control limits VSD performance accuracy, so the effectiveness of VSD frequency support function is relatively compromised. For example, an overshoot on the load power consumption is observed if the slew rate of the motor speed reference is large. Meanwhile, the critical parameters of the constant V/f controller can not be adjusted according to the real-time load performance, which is a general disadvantage of all open-loop control schemes [36].

2.1.4 P - f Droop Control

For conventional SG, if there is a sudden power mismatch between the prime motor power output and electrical power consumption, the SG is able to extract the kinetic energy from the rotating mass to slow down the rate of change of frequency (RoCoF) at the very instant of the event, and this phenomenon is regarded as inertial response. Following the inertial response, the SG will provide additional power to stabilize the deviated frequency at a new steady-state level due to the governor's droop setting [42, 43, 44]. This is a relatively slower response compared with the inertial response, which mainly depends on the governor's characteristics and prime-mover time constant.

The concept of droop control has been widely adopted by distributed generation units for power grid stability improvement. In additional to $p-f$ droop control, $v-f$ droop control is also utilized to sustain the grid voltage and active power [45, 46, 47, 48]. For PE-based generation units, the $p-f$ droop control is applied to emulate the response of the SG governor [42, 49, 50, 51, 52, 53]. The generator output active power reference deviation

ΔP_{ref} during a grid contingency is proportional to the deviation of the system frequency Δf by the predefined droop rate K_{droop} according to the droop control scheme, which is illustrated in Fig. 2.6 and expressed by (2.1).

$$\Delta P = K_{droop} \Delta f \tag{2.1}$$

As illustrated in Fig. 2.6, ΔP represents the deviation of active power contribution provided by the generation unit when grid frequency deviation occurs. Δf_{db} represents the deviation between deadband frequency f_{db} and nominal frequency f_{nom} as expressed in (2.2). f_{db} represents the threshold where the droop frequency control is activated. The definition of Δf_{max} is similar, which represents the deviation between the predefined maximum frequency f_{max} and f_{nom} as expressed in (2.3). All available power reserves are released for frequency support when grid frequency reaches f_{max}. $P_{prime,up}$ and $P_{prim,down}$ represent the maximum available power reserve in frequency increase and decrease event respectively.

$$\Delta f_{db} = f_{db} - f_{nom} \tag{2.2}$$

$$\Delta f_{max} = f_{max} - f_{nom} \tag{2.3}$$

In addition to being adopted by RES, the droop control scheme is also adopted by responsive loads for promoting grid frequency stability.

2.1.5 Research Gaps

According to the overview of the existing research, the following research gaps in terms of responsive PE interfaced load modeling and control are summarized below:

- The SSL model and control have been widely studied based on the literature review. However, investigation on DSL, of which the typical example is the VSD load, is rarely mentioned compared with that of the SSL [24, 22, 25, 26, 28, 29, 27, 30, 31].
- The aggregated representation of VSD load units has not been investigated yet according to the existing research. In [39, 40, 41], the VSD based DSL dynamic

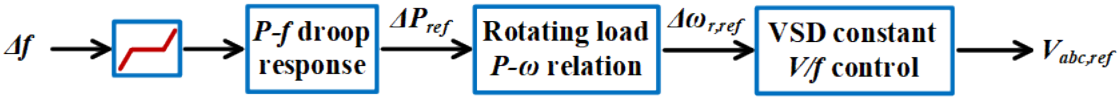

Figure 2.4: Primary frequency support control schemes adopted by VSD loads [39, 40, 41].

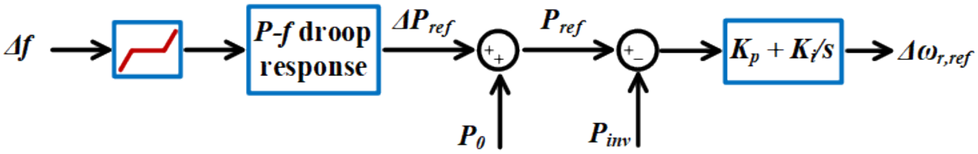

Figure 2.5: Updated primary frequency support which avoids the regenerative process [39].

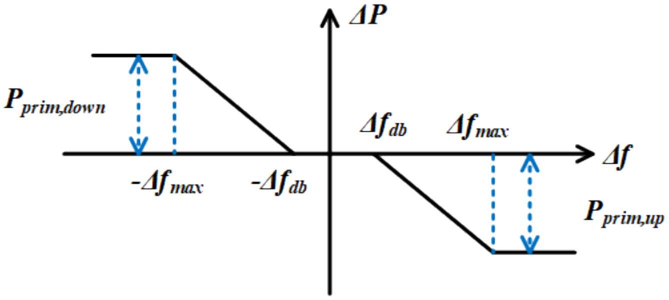

Figure 2.6: $p - f$ droop control diagram [52]

performances are modeled by one VSD load unit without justifying the accuracy of such representation method.

- The currently studied VSD load with grid frequency support functions mainly focuses on the diode front-end rectifier VSD with open-loop controllers. The active front-end rectifier VSD with sophisticated control schemes is rarely mentioned.

2.2 Multi-converter Based Hardware Testbed (HTB)

Analog experimental platforms have been widely used in power network transient studies due to their excellent performance on the accuracy, numerical robustness, and the wide time scale compared with the digital simulation [36]. The multi-converter based hardware testbed (HTB), which is developed by the Center of Ultra-wide-area Resilient Electric Energy Transmission Network (CURENT) at the University of Tennessee, is a real power testbed featuring multiple power emulator modules based on a programmable three-phase VSC [54, 55]. The CURENT HTB is advantageous to emulate the dynamic performance of large-scale power systems considering the following aspects [56]:

- Broad time scales in one system - ranging from microseconds level for PE switching dynamics, to milliseconds and seconds level for conventional power grid electromechanical transients.

- Less dependency on numerical calculation, increase the overall robustness of the whole testing system.

- Realistic power testing platform which integrates real-time communication, system protection, power grid centralized control, and visualization together.

- Capable of performing prolonged real-time experiments, meanwhile simultaneously providing power system information in detail.

2.2.1 HTB Electrical Topology

The architecture of HTB is illustrated in Fig. 2.7 [57]. A constant dc voltage source is utilized to power up the whole testbed. Modular three-phase VSCs, which can also be referred as “power emulators”, are connected to both ac and dc sides. This electrical connection allows for power circulation between ac and dc buses, so the HTB consumes almost no power except making up the power loss during circulation. According to Fig. 2.7, each power emulator is responsible for mimicking the real-time dynamic performance of one or more electrical components in the power network.

2.2.2 Power Emulator Unit Configuration

The most basic functional unit in the HTB is the VSC-based power emulator. The power emulator is capable of representing various electrical components in the power network, including the synchronous generator [57], renewable energy sources [58, 59], transmission lines [60], static and dynamic loads[61, 62], etc. The power emulators are connected according to the desired power network topology.

Power emulators are flexibly controllable and configurable, so multiple transmission-level scenarios can be performed and analyzed with specifically designed emulators [62], *e.g.,* the transmission network fault scenarios [63], the inertial response of high penetration renewable resources network [60], the fault induced delayed voltage recovery (FIDVR) [62], etc. Therefore, the creation of new HTB emulators will promote the research of the transmission-level power grid [62].

As mentioned in previous paragraphs, the regenerative architecture of HTB is developed based on voltage type emulators, current type emulators, and common dc voltage source, which is illustrated in Fig. 2.8 [64]. This regenerative configuration is highly efficient for high-power applications. The generation units, including conventional synchronous generator or RESs, are usually represented by the voltage type emulator, which provides a stable ac voltage for the emulated ac power network, while the load units are represented as the current type emulator, which actively controls the corresponding current consumption to represent the dynamic load performance.

The current controlled type emulator circuit topology and control structure in three-phase coordinates, which is also referred to as *abc* coordinates, is illustrated in Fig. 2.9 [64]. The emulator three-phase ac side is the electrical interface with the rest of the system, and the corresponding ac voltage and current - which are denoted as V_{sabc} and I_{sabc} respectively - are sampled in real-time. The sampled electric variables are used for updating the emulated power load model. Based on the previous investigation and emulator development research on HTB, almost all of the emulated electric element models are created based on *dq* coordinates since it can simplify the modeling and control design. Specifically, the ac side line-to-line voltage $V_{ll,abc}$ serves as the inputs for the phase lock loop (PLL) to determine the phase reference of *dq* coordinates, and all electrical variables in *abc* coordinates will be transferred to *dq* axis accordingly in the modeling process.

As for the modeling of the current type load emulator, V_{sdq}, which is the equivalent representation of V_{sabc} in *dq* coordinates, are usually used as the input variables for the emulated load models. As illustrated in Fig. 2.9, the emulator microprocessor generates the current reference $I_{sdq,ref}$ according to V_{sdq} following the load modeling procedure. Then the VSC gate signals g_{abc} are generated based on $I_{sdq,ref}$ through a digital current control loop and modulation process as illustrated in the solid grey box, of which the current control loop adopts PI controller in both *d* and *q*-axis [36]. In this way, the three-phase interface will mimic the emulated load characteristics by providing load current following the derived $I_{sdq,ref}$.

2.2.3 HTB Communication, Control and Visualization

As mentioned above, one of the advantages of using HTB for power system emulation is that it can mimic the practical communication of the power network, which includes the communication between the central controller and local controllers from each area, sending out commands to local electric devices, information feedback from local devices to the control layer, etc. The HTB communication system is necessary for the purpose of emulating the operation of the power network control center, and the development of communication system allows for efficiently controlling the HTB to perform multiple scenarios according to users'

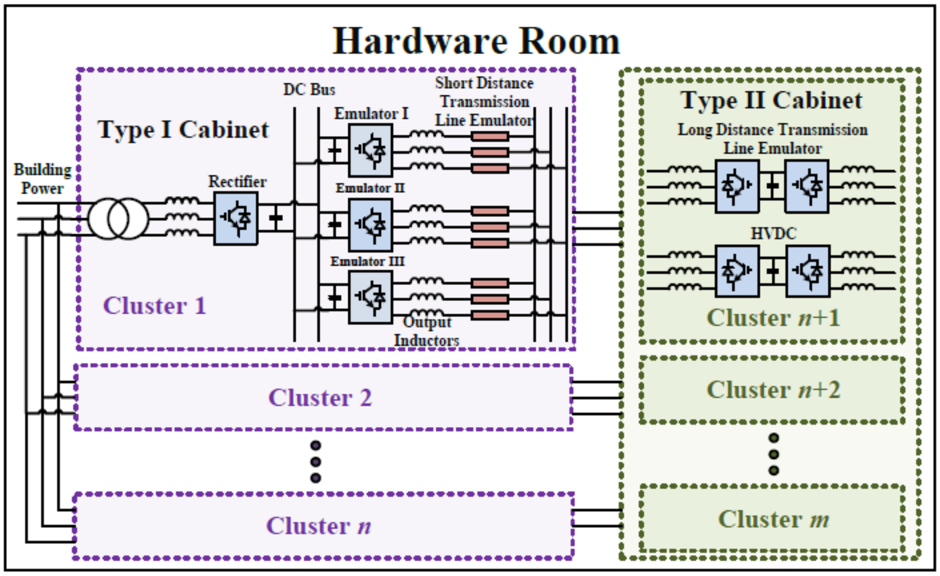

Figure 2.7: Architecture of CURENT Hardware Testbed [57].

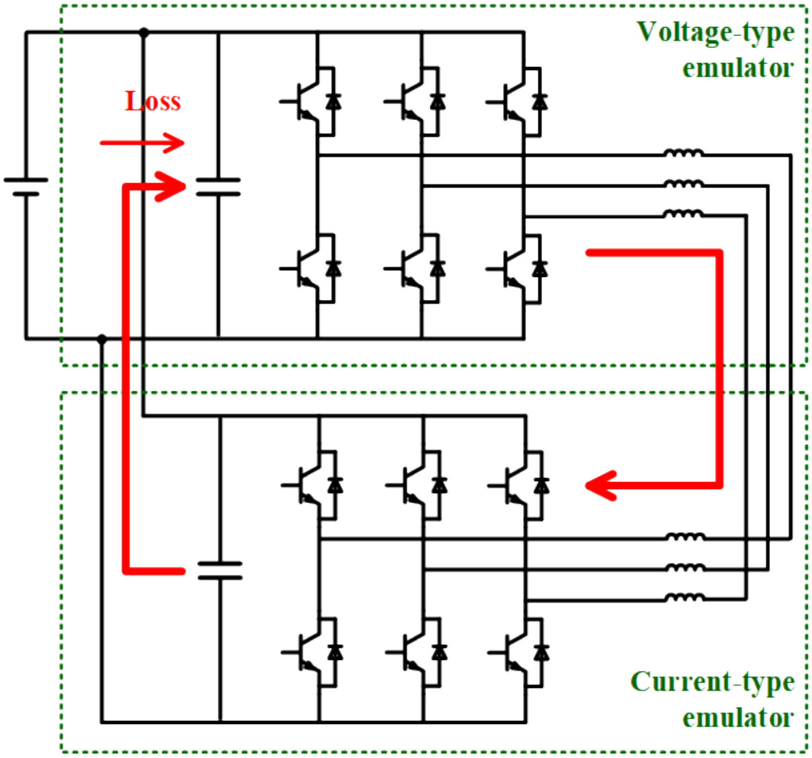

Figure 2.8: Voltage and current type power emulator circuit topology and regenerative structure [64]

requirements. For example, with the human-machine interface (HMI), users can send out control commands to low-level devices, and monitor the power system operation.

As illustrated in Fig. 2.10, the HTB consists of hardware configuration, which includes all the basic power emulators and electrical connections, and visualization/control center which is applied to monitoring the HTB operation and send out grid regulation commands [65]. So the hardware configuration represents the low-layer devices, and the control center represents the high-layer monitor and control systems. The HTB communication system plays the role of the bridge that actively connects these two parts together. The National Instruments™ (NI) LabVIEW interface is used as the HTB HMI, which is used to realize the system level communication and control implementation. Connection between the LabVIEW (users) and the HTB hardware is based on NI CompactRIO-9081.

As shown in Fig. 2.10, the bidirectional communication between the LabVIEW and the CompactRIO is realized based on Ethernet, while the bidirectional communication between the CompactRIO and power emulators is realized by CAN bus, which is developed within a Texas Instrument (TI) DSP TMS320F28335 employed by each power emulator.

Additionally, potential transformers (PTs) and current transformers (CTs) are installed to monitor the electric variables of critical buses and transmission lines. These measured signals are sent back to LabVIEW interface to mimic the real power system control center.

2.2.4 HTB Load Power Emulator Design

The electric load is one of the most important electric components in the power network, and several types of HTB load emulators have been developed in previous research. The most frequently used load type is the static load, and the "constant-impedance, constant-current, constant-power" (ZIP) load emulator has been developed in [61]. The developed ZIP load emulator is a current type emulator, and the composition can be flexibly adjusted according to the requirement of the user.

Meanwhile, the dynamic load model has also been studied. According to the previous research, load emulators related to the IM and the diode-front-end rectifier have been developed. In [66, 62], load emulators specifying the characteristics of IM load and the motor-drive-regulated air conditioner have been designed and verified on the HTB. Also, the

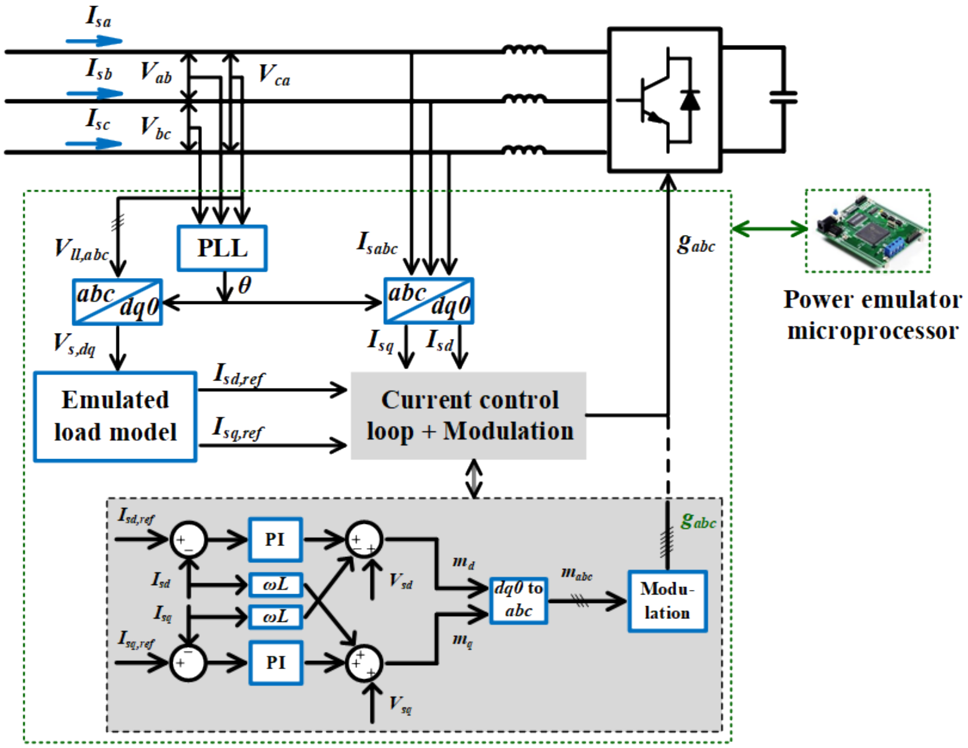

Figure 2.9: Circuit schematic and control structure of current controlled load emulator [64].

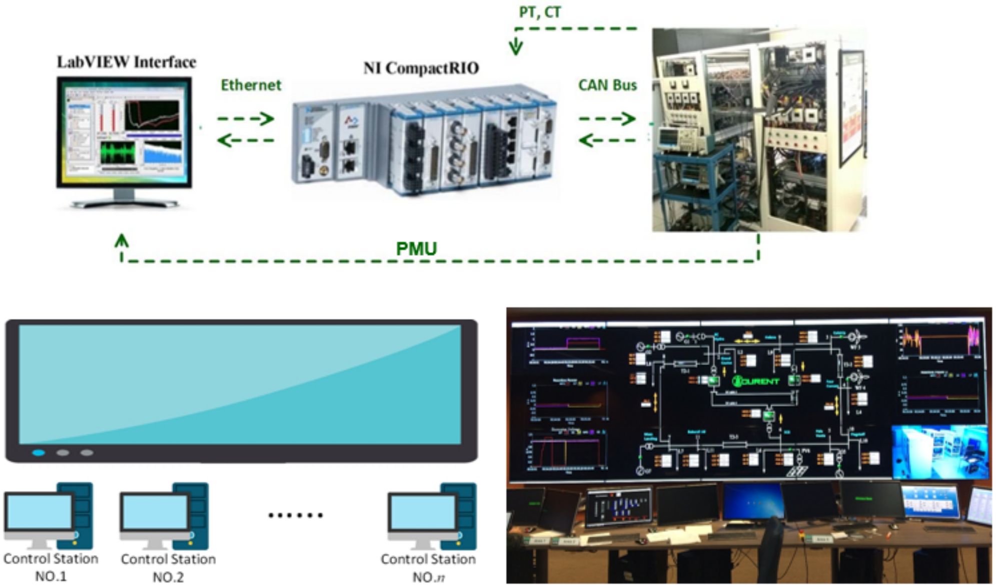

Figure 2.10: Communication architecture of CURENT HTB [65].

power emulator characterizing the three-phase diode rectifier connected with a resistor load is also introduced in [67]. However, there is still a gap between the PE interfaced dynamic load performance representation and the emulator models developed in the previous research [36].

2.2.5 Research Gaps

Although models of PE interface configuration and motor have been developed in the previous HTB emulator research, they still cannot meet all requirements of the VSD-based frequency response load performance representation:

- Characterization of the inverter-based motor drive with various control schemes has not been investigated yet. For example, the motor-drive-regulated air conditioner power emulator has been developed in [62], but only the most basic open-loop motor speed controller has been investigated, limiting the complete description of load characteristics.

- Lack of effective connection of the VSD-based load. Although the HTB emulators characterizing the VSD PE interface and the rotating load have been studied as mentioned above, these major components never operate jointly as the VSD-driven motor load. So investigation on VSD-based load should be performed based on connecting these major electric parts together as an effective load unit.

- Oversimplified load dynamic performance. The HTB power emulator characterizing the three-phase diode rectifier-based load has been proposed in [67], but the diode bridge connected load's characteristics are simplified as a resistor load, which limits the corresponding load performance representation.

2.3 Load Model Applied for Transmission-level Power Network Analysis

In this section, the commonly used PE interfaced device models adopted by the transmission-level power network study are reviewed. Furthermore, the prevailing simulation tools which allow for the PE-based device modeling are introduced. Meanwhile, the simulation tool's capability of being used for the transmission-level power grid simulation is evaluated respectively.

2.3.1 Prevailing PE-based Load Model Format

Electrical load models are classified as the static model and dynamic model in the TS analysis, which focuses on the electromechanical transients and oscillations between 0.1 and 3 Hz [68, 2]. As presented in [12], static models include: 1) ZIP model [69, 70, 71], 2) exponential model [69, 72], 3) frequency dependent model [69, 73], 4) Electric Power Research Institute (EPRI) LOADSYN model [73, 74]. In comparison, dynamic models include: 1) IM model[69, 73], 2) exponential recovery load model [75, 76], 3) Western Electricity Coordinating Council (WECC) Composite Load Model (CLM) [77, 78].

The PE interfaced load has been widely studied and modeled based on different research purposes, which can be classified into the following categories according to the existing research literature:

- Exponential model, including the standard exponential and polynomial format, is widely used in both static and dynamic analysis [79, 80, 81]. The polynomial load representation has been reported to have an excellent performance when adopted by static system evaluation, *e.g.,* the power flow analysis, the voltage stability analysis exploring the grid, etc. However, the accuracy of this type of load model will be compromised if representing the transient load performance.

- Dynamic equivalent circuit model, including both the detailed circuit model and dynamic average-value equivalent model [82, 83, 84]. The detailed model characterizes the on/off status of PE devices, thus requiring a small simulation time step. In comparison, the average model concentrates on the converter cycle-to-cycle behavior so that less computational resources are required when applied to digital simulation. However, the equivalent circuit model is widely used in the EMT rather than the TS simulation tools since it features the load circuit topology, which is too complex to be modeled in TS simulators.

- State space model/transfer function model, where the dynamics of the load electrical components and control strategies can be described based on this model format conveniently. The state space model is derived based on the system time-domain differential equations, *e.g.,* the EV fast charger model is proposed by this approach in [85]. The transfer function model is equivalent to the state space model, which represents the system frequency domain dynamics. The state space model is more suitable to be used in TS simulation environments compared with the equivalent circuit model. For example, the PE-based VSD model in TS simulation environment is proposed in [86, 87, 88, 89] using this model format. However, simplification approaches are required if considering the accessibility to the transmission-level network simulation, which is not sufficiently studied to the best of the author's knowledge.

Although it has been proved that using a dynamic load model can improve the accuracy of the power system analysis, the electric load is mostly represented by the static load model in the transmission-level system studies according to the technical report provided by CIGRE regarding the international industry load modeling practice in 2013 [8, 9]. Furthermore, from the small portion of the adopted dynamic loads, most of them are used for representing the industrial IM load. In comparison, the PE interfaced load is usually regarded as the static load assuming that it does not largely influence the power grid dynamic performance. However, this consumption is not valid if considering the distinct PE-based load characteristics and the potential contribution to grid operation.

2.3.2 Overview on Digital Simulation Tool Regarding PE-based Components

The load model format has been discussed in the last subsection. An appropriate model format should be selected based on the research purpose, as well as considering the capability of specific simulation environments. For example, PE-based devices have been extensively studied using the EMT simulation tools, but the corresponding model used for EMT environments cannot be directly used in other simulation environments. Therefore, it is of critical significance to study the capability of simulation software, and design a suitable simulation model according to specific simulation tools.

Several commercial simulation tools can be used for modeling PE-based devices according to different research purposes. Specialties and limitations of prevailing simulation tools are summarized in Table 2.1 and briefly explained below:

- Device-level simulation, prevailing commercial simulation tools under this category include PSPICE, PLECS, etc. This type of simulation tool focuses on the research and development of PE devices based circuits, and provides a simulation package with detailed information of semiconductor switches, *e.g.,* the switch turn-on resistance, the parasitic capacitance, etc. Usually, the influence of the power network connected with the studied electric device is not considered, so the ideal voltage source is adopted as the power supply. So this type of simulation tool is not used for large-scale power network simulation, though it provides the most detailed representation of PE configurations.

- Three-phase EMT simulation program includes EMTP/ATP, PSCAD/EMTDC, etc. This type of simulation program is developed considering both the dynamic performance of PE-based devices, and the corresponding interaction with the rest of the transmission-level power network. Usually, the simulation package of transmission-level components, (*e.g.,* synchronous generator model, transmission line model, etc,) and the PE-based devices, (*e.g.,* basic ac-dc converter bridge, FACTs, etc.) are provided, allowing the users to develop the power network with relatively complete details. However, such rich simulation details yield a relatively small simulation time

Table 2.1: Frequently used simulation programs including the model of PE devices.

	Device-level simulation	Three-phase EMT simulation program	Positive-sequence TS simulation program	Hybrid simulation program
Commercial software	PSPICE, PLECS, etc.	EMTP/ATP, PSCAD/EMTDC, etc.	PSS/E, PSLF, TSAT, PowerWorld, etc.	PSS/E-PSCAD Co-Simulation; TSAT-PSCAD interface; user-defined platform
Specialty	research and development of PE-device-based circuit. The power source used in circuits is usually assumed to be ideal.	Three-phase time domain simulation, capable of simulating switching dynamics of semiconductor devices. Provide specialized transmission-level simulation modules.	Single-phase phasor domain modeling approach. Suitable for three-phase balanced transmission-level power system analysis.	External power network and PE devices are simulated separately. Three-phase unbalanced conditions can be represented.
Time step	smaller than switching cycle	∼50 μs	∼4 ms	∼50 μs to ∼4 ms
Simulation time duration	N/A	Long	Short	Medium
Simulation capability	N/A	Hundreds of buses	∼100000 buses	N/A
Limitation	Not suitable for power network simulation.	Not suitable for large-scale power network studies due to limited buses and long simulation time.	Cannot fully reflect the high-frequency dynamic performance in the grid; limited capability on characterizing unbalanced grid condition; limited dynamic load models.	Communication protocol between different simulation platform; complex boundary definition.

step at ∼50 μs, which results in a great computational burden. So there are some related simulation issues that may occur, such as lack of robustness, and long simulation time length. Therefore, one of the most critical disadvantages of the three-phase EMT simulation program is the limitation on the number of simulated buses.

- Positive-sequence TS simulation program includes PSS/E, PSLF, TSAT, PowerWorld, etc. This type of simulation tool is most frequently used for the large-scale transmission-level power network analysis, of which the simulation capability can reach up to ∼100000 buses. The electrical components are all represented as single-phase phasor domain models assuming that a three-phase balanced system is studied. The simulation time step is ∼4 ms, which is suitable to represent electromechanical transient at 0.1 and 3 Hz. Disadvantages of these simulation programs include that: 1) the high-frequency dynamic performance cannot be fully reflected; 2) limitation on simulating unbalanced grid faults; 3) lack of the non-passive load model provided by the simulation package.
- The hybrid simulation is a newly emerged research topic which emphasizes the cooperation of two different simulation platforms. The concept of "hybrid simulation" includes a broad range, so the cooperation between the TS program and EMT program is emphasized. Currently, the commercial hybrid simulation tools include the PSS/E-PSCAD Co-Simulation developed by Siemens PTI, and the TSAT-PSCAD interface (TPI) developed by DSATools. The advantage of hybrid simulation is that the conventional large-scale power network and PE-based devices are simulated separately in different simulation programs with varied time steps, so it includes the advantages of both simulation environments, and conserves computational resources. However, there are not many commercial hybrid simulation tools for users to select, so the user-defined hybrid simulation environment, which combines two simulation platforms out of the users' choice, can be seen in recent research papers.

Based on the evaluation and analysis above, the TS simulation tool is more suitable for simulating transmission-level power grid compared with other simulation tools, considering the large number of buses involved, and accurate representation of power network dynamic performance. So the models of PE-based devices developed in TS simulation environments are reviewed and summarized in the following subsection according to the current research progress.

2.3.3 PE-based Device Modeled in TS Simulation Tools

Although the PE-based load in the TS program has not been extensively studied based on the author's best knowledge, there are still some research papers related to this research topic. Some of the typical research progress are reviewed below:

As proposed in [88], the performance-based VSD load model is implemented by obtaining the linearized power-voltage and power-frequency transfer functions based on the test data from the EMT model simulation. The prediction error minimization technique is utilized to optimize the VSD model transfer function. Therefore, the proposed model is represented as a controlled voltage source, of which the voltage is derived based on the load power flow. The developed model is able to capture the dynamic behaviors of a vector-controlled motor drive in linear operating range, *i.e.,* approximate to the initial operating point. So this model is suitable for being used in the small-magnitude low-frequency system oscillations condition, but not for investigating the system performance subject to large disturbances, such as voltage depressions.

A similar linearized diode front-end VSD load model has been proposed in [90, 86]. The proposed VSD model is initially expressed by PE device differential equations. Then all the load differential equations are combined and linearized at the initial operating point and expressed as a transfer function in the frequency domain. The proposed VSD load model also cannot accurately represent the dynamic performance when the power grid is subject to large disturbances.

As proposed in [89], the positive-sequence model of a diode front-end VSD load with an open-loop control scheme is proposed, which is suitable for transmission-level TS analysis. The proposed model is reasonably simplified, where the front-end rectifier is simplified as a power flow representation, the back-end inverter is represented by a constant $V-f$ control scheme, and the motor load is derived based on the equivalent transient circuit. The proposed load model is developed independently by C code.

The PE-based load model proposed in [91] has almost the same configuration and control scheme compared with that studied in [89]. The VSD load is modeled by differential equations, and the dynamic impact of the load protection scheme is considered in this research paper. The proposed VSD load is developed in Power System Toolbox (PST), which is an open-source simulation tool for both commercial and academic use.

The positive-sequence model of VSD load with active front-end and vector control is proposed in [92]. Compared with the VSD load models introduced above, the one proposed in this paper has a more complicated control scheme and electrical configuration. The main configuration of the VSD dynamic load includes the motor drive and IM, where the front-end rectifier and the back-end inverter are modeled by corresponding control schemes expressed by differential equations, and the IM is also expressed by classical differential equations in the time domain. The proposed VSD load model is represented as a controlled voltage source of which the voltage is derived based on the load current consumption. The VSD load model is developed in GE PSLF, which is a more widely used TS commercial software compared with the simulation tool selected in [91, 89]. However, the proposed VSD load dynamic model is too complex with limited simplification approaches, which may introduce too much computational burden when investigating the large-scale power network.

Moreover, the representation PE-based generation unit - also referred to as the RES units - in the TS simulation environment has been addressed and standardized. The purpose of developing such a generic generation unit model includes the following aspects [93]:

- Public availability, documentation and transparency: generic models are not subject to the non-disclosure agreement followed by the vendor-specific models. So the generic generation model provides a public, well-documented generator format for all the model specifications.

- Guarantee consistency and uniformity across the various commercial simulation software.

- The generic generation unit model is reliable for power system simulation since it has been well validated.

- Provide a relatively realistic model for evaluating the future power grid, where the parameters for the actual equipment are not yet known.

The 2^{nd} generation RES model is documented in [94]. Accordingly, the RES generic model is formed by seven generation unit modular blocks. There are three different general renewable energy electrical control models, which are denoted as *regc_a*, *reec_a/b/c* and *repc_a/b* respectively, and two wind turbine specific control models, which are denoted as *wtgp_a* and *wtgq_a* respectively. Moreover, there are two wind turbine physical configuration models, which are denoted as *wtga_a* and *wtgt_a* respectively. By appropriately connecting these modules together as shown in Table 2.2, different PE-based generation unit models can be developed. Among all the generic renewable generators, the PV generation unit/battery energy storage system are close to the configuration of the PE-based load.

Additionally, the distributed energy resource model version A (*DER_A*) is proposed in [95] for representing the aggregated dynamic behavior of the PE-based generation unit in time domain positive-sequence TS studies. The *DER_A* is supposed to be more advanced compared with the 2^{nd} generation RES model stated above, which is illustrated in Fig. 2.11. The model *DER_A* has 48 parameters and 10 states, which is roughly 1/3 of the number of parameters used in the 2^{nd} generation RES model. The proposed generation unit model is represented as a controlled voltage source of which the voltage is derived based on the generator current flow. According to Fig. 2.11, the *DER_A* model includes the following control functions: constant Q/power factor control, the terminal voltage control, the grid frequency support control, and the low voltage trip protection.

2.3.4 Fast EV Charging Unit Control Algorithm

The fast EV charging unit is a typical nonlinear load with high power consumption, which influences grid TS when participating into the power network operation [12]. Therefore, the investigation on the dynamic performance of fast EV charging load is of great importance. So the fast EV charger load is introduced below to represent the characteristics PE interfaced load units.

Table 2.2: Module combination of generic PE-based generator model [94].

RES	Model Combination
Type 3 wind turbine generation unit	*regc_a*, *reec_a*, *repc_a*, *wtgt_a*, *wtga_a*, *wtgp_a*, *wtgq_a*
Type 4 wind turbine generation unit	*regc_a*, *reec_a*, *repc_a* (optional: *wtgt_a*)
PV generation unit	*regc_a*, *reec_b/a*, *repc_a*
Battery energy storage	*regc_a*, *reec_c* (optional: *repc_a*)

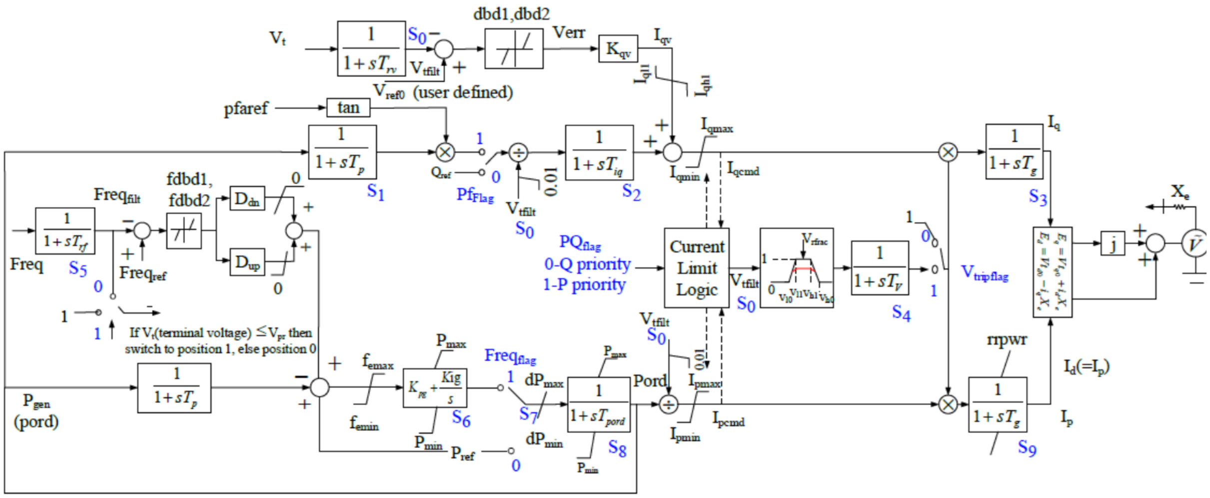

Figure 2.11: Diagram of *DER_A* model [95].

The prevalence of PE switches that can be turned on/off by gate signals, *e.g.,* insulated gate bipolar transistor (IGBT) and metal oxide semiconductor field effect transistor (MOSFET), allows for the bi-directional power regulation between the power grid and the EV batteries, which explores EV batteries potential to provide grid support functions. Therefore, aside from the conventional grid-to-vehicle (G2V) control schemes, the vehicle-to-grid (V2G) control has been gradually adopted by the EV charging unit, especially by fast dc charging units which feature a large power rating and have the potential of providing more significant support to the power grid.

2.3.4.1 EV Charger Level Classification

The EV charging infrastructure charging levels, nominal terminal voltages and connection configurations are summarized in Table 2.3 regarding the current charging technology [96, 97, 98, 99]. The EV charger load is considered as high-power-consumption units, especially for EV chargers under the category of DC level 1 - 3. For example, it is possible to charge a 25 kWh battery pack at DC Level 2 in less than 20 minutes, of which the power consumed significantly exceeds the peak power demand for an average household in the U.S. The ultra-fast charging unit features a higher power rating compared with the EV charger adopting DC charging techniques, of which the charging time can be reduced to several minutes. Therefore, the power network operation will be significantly changed with the increasing penetration of EV charger loads.

2.3.4.2 Active Front-end Rectifier Control Algorithm

According to the topology of the fast EV charging unit, the active front-end rectifier is connected between the ac network and the dc battery charger converter. The controller of the active front-end is generally designed to perform the following control schemes [100]:

- Eliminate the load current total harmonic distortion (THD) introduced by semiconductor devices.
- Provide a stable dc-link voltage for the dc battery charger converter.
- Provide unity power factor correction or reactive power compensation.

- Regulate the load active/reactive power flow separately.

In this dissertation, load current THD elimination is out of the research scope considering the relatively long time step of TS simulation programs. Considering the power flow directions, the fast EV charger control schemes can be classified as G2V and V2G operation modes for the following purposes:

1. Active Front-end Control Scheme: G2V Operation Mode

The main purpose of conventional G2V mode is to provide charging service to the EV battery according to the specific charging scheme determined by the battery status. The most common control algorithm adopted by the active front-end rectifier is to provide a stable dc voltage source for the connected power stage, which is directly used for regulating the battery charging status by adopting vector control in the dq coordinates.

According to the vector control principle, the d-axis current $I_{d,ref}$ is determined by the dc voltage control loop, of which the specific control algorithm can be illustrated in Fig 2.12:

The rectifier dc voltage is denoted as V_{dc} in the following passage in this section. One of the commonly applied V_{dc} control introduced in [101, 102, 103, 104] is illustrated in Fig. 2.12a, where ΔV_{dc} is used as the input of V_{dc} negative feedback regulation, and PI regulator is selected as compensator. The control scheme illustrated in Fig. 2.12b is similar to the one in Fig. 2.12a except that the negative feedback loop input is ${V_{dc}}^2$ [105].

Similarly, the active front-end q-axis current $I_{q,ref}$ can be determined by the reactive power reference Q_{ref}, I_q reference $I_{q,ref}$, and terminal voltage reference $V_{t,ref}$, which are illustrated in Fig 2.13 respectively:

The EV charger load reactive power regulation scheme presented in [101, 102, 106] is illustrated in Fig. 2.13a, where Q_{ref} can be decided by power factor unity control, or by higher level coordination. Also, the terminal voltage V_t is closely coupled with the reactive power flow in the transmission network, so $I_{q,ref}$ can be directly decided by $V_{t,ref}$, as illustrated in 2.13b [103, 105]. Additionally, as presented in [104], $I_{q,ref}$ can be predefined externally in cases that I_q is not required to be decided in a sophisticated manner. The simple constant I_q control is illustrated in 2.13c.

2. Active Front-end Control Scheme: V2G Operation Mode

Table 2.3: EV charging level, terminal voltage and configuration [96].

Charging Level	Terminal Voltage	Power per Vehicle	Charging Time	System Level Connection
AC Level 1	120 V 1-phase	2 kW	10∼13 h	Residential/Commercial Secondary Customer 120 V and 240 V
AC Level 2	240 V 1-phase	20 kW	1∼4 h	
AC Level 3	240 V 3-phase	43.5 kW	∼1 h	
DC Level 1	200∼450 V	36 kW	0.5∼1.44 h	Commercial Primary/Secondary Customer 480 V
DC Level 2	200∼450 V	96 kW	0.2∼0.58 h	
DC Level 3	200∼800 V	200 kW	∼10 min	
Ultra-Fast Charging (UFC)	≥800 V	500 kW	∼Gas Refueling	Sub-transmission Primary Customer 26 kV or 69 kV

Note: Ultra-Fast Charging is not yet finalized

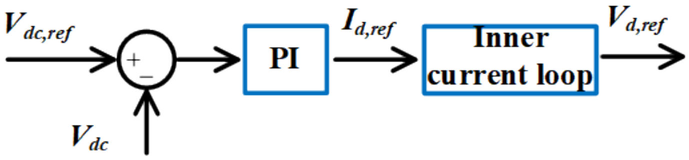

(a) V_{dc} control: V_{dc} negative feedback control.

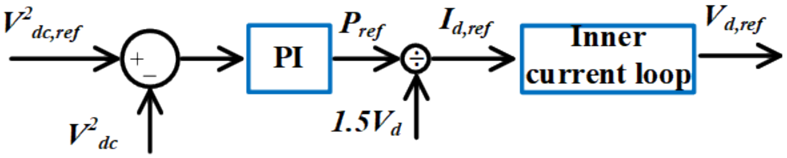

(b) V_{dc} control: $V_{dc}{}^2$ negative feedback control.

Figure 2.12: V_{dc} control commonly adopted by the EV charging unit active front-end rectifier [101, 102, 103, 104, 105].

The EV charging unit V2G application allows for the power to transfer from the EV batteries to the power network, which makes the combination of the EV charging configuration and the vehicle battery units serve as a distributed storage device. The V2G operating modes offer a variety of applications including [107]: 1) active power regulation, 2) reactive power support, 3) current harmonics filter, 4) load balancing by valley filling, 5) peak load shaving, 6) reduce utility operating cost and overall cost of service, 7) improve load factors, 8) generate revenue, 9) reduced emissions, 10) tracking of variable RES.

Among the above applications, 1) to 3) require the fast response of PE interface controller from EV charging unit. In comparison, the rest of them are attributed to long-term service, which is out of the scope of the research topic of this dissertation. The V2G reactive power regulation has been studied in many existing literature [108, 103, 109, 110], and it is almost identical to that of the G2V operation in terms of the control scheme. So here, only the active power regulation control scheme is introduced.

The active power support function which requires fast response of PE interface controller includes grid frequency support as presented in [111, 112]. The grid frequency deviation Δf is measured and sent to the rectifier controller, then a certain amount of active power P is absorbed or released according to the determined active power reference P_{ref}. The frequency support control scheme is illustrated in Fig. 2.14, which includes both the primary frequency support where the load power contribution is proportional to the Δf by K_p, and the inertial response support where the power contribution is proportional to the frequency changing rate $\frac{d\Delta f}{dt}$ by K_{in}.

2.3.5 Research Gaps

According to the overview of existing researches, the following research gaps in terms of the generic representation of PE interfaced loads are summarized below:

- Lack of accurate dynamic PE-based load model. The static load model is still widely used to represent PE-based load performance based on the existing literature [69, 73, 75, 76, 77, 78, 8, 9].

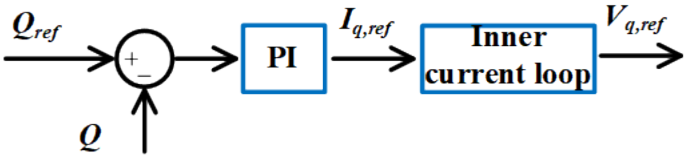

(a) Q negative feedback control.

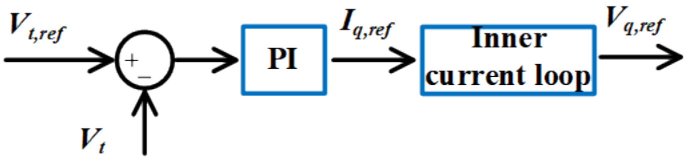

(b) V_t negative feedback control.

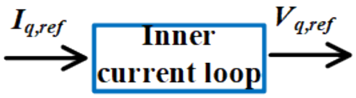

(c) I_q negative feedback control.

Figure 2.13: Q, V_t and I_q control adopted by the EV charging unit active front-end rectifier [101, 102, 103, 104, 105, 106].

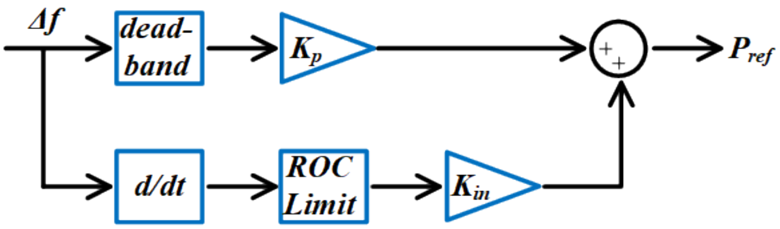

Figure 2.14: EV charging unit grid frequency support [111, 112].

- Lack of PE interfaced load generic representation in TS simulation tools. In comparison, the generic model of PE-based generation unit has been widely discussed, and it provides several advantages to grid analysis [94, 95]. There are some research papers that discuss the modeling of PE interfaced VSD load in TS simulation tools [86, 87, 88, 89, 91, 92]. However, the development of a certain type of PE-based load unit generic model, especially high-power-rating electric loads, is rarely mentioned.

2.4 Summary and Contributions

Reviews on SL model and control, HTB load emulator development, and the PE interfaced devices modeling in transmission level simulation environment have been introduced in this chapter. Considering the research focus introduced at the beginning of this chapter, the following aspects are investigated in the next chapters of this dissertation based on the research gaps discussed above:

- Three-phase VSD based motor load is studied as a typical example of the PE interfaced load, which can actively interact with the power grid operation. The model and control of VSD connected IM load with grid frequency enhancement potential is developed.

- Development of a novel HTB load power emulator, which includes a three-phase VSD detailed load with advanced controllers, and a three-phase VSD simplified model emphasizing the corresponding load active power consumption.

- Development of a VSD load aggregated model, which reflects the potential of VSD load units in terms of providing the grid frequency support to the transmission grid. The developed aggregated VSD model is applied to the HTB power emulator.

- Investigate VSD load potential of regulating grid frequency regarding varying external conditions.

- Fast EV charging unit is studied as an example of the PE interfaced load with high power consumption and high penetration level. The generic model of EV charger load, which is suitable for the TS simulation environment, is developed based on the detailed electromagnetic model.

- Development of an EV charger load generic model benchmark in TS simulation program, which includes commonly used EV charger control schemes in different operation modes.

Chapter 3

Power Emulator of Variable Speed Drive in Multi-converter Based Power Grid Emulation System

The VSD load main configuration is illustrated in Fig. 3.1. The VSD load model consists of three major parts: the front-end rectifier, the back-end inverter, and the motor with the directly connected load torque model [36].

The front-end rectifier is generally classified as: 1) passive-front-end rectifier which is composed of diodes, so the passive-front-end rectifier is also regarded as a diode-front-end rectifier; 2) active-front-end rectifier, and the active-front-end is made up of the PE switches which can be turned on/off by gate signals, *e.g.,* IGBT, MOSFET, etc. The primary function of the front-end rectifier is to provide a stabilized dc-link voltage to the next power stage.

The motor drive control scheme is embedded in the back-end inverter, so it is also referred to as the inverter-based motor drive configuration. The dynamic performance of the motor drive is mainly characterized by the specific controller applied to the back-end inverter, which will be explained in detail in the following sections.

The motor is directly connected to the inverter-based motor drive, along with the rotating load driven by it. The motor and the directly connected load will be mentioned as “motor load” together in the following sections considering the simplicity of the dissertation paper.

The motor load characterizes the motion performance of the motor and the connected load, as well as the majority of the VSD load power consumption.

In this chapter, the VSD load dynamic characteristics and modeling algorithm are introduced in detail. The modeling of the passive/active-front-end rectifier and the differences between these two types of rectifiers are introduced. Meanwhile, the modeling and control of the back-end inverter are emphasized, which includes the introduction of multiple loop motor rotor speed control schemes, and the corresponding impact on the motor load dynamic characteristics, including the load power consumption, the motor rotating speed, etc. Meanwhile, the VSD load simplified model considering different rotor speed control schemes is also proposed, which keeps a balance between model accuracy and simplicity. Additionally, the procedure of developing the VSD load power emulator is presented based on the corresponding modeling and control presented in this chapter.

3.1 VSD Front-end Rectifier Model and Control

As illustrated in Fig. 3.1, there are two commonly used VSD front-end configurations, passive-front-end and active-front-end rectifier in three-phase full-bridge configuration. The main characteristics of these two types of rectifiers are summarized below:

- The passive-front-end rectifier is cost-efficient compared with the active-front-end rectifier.
- The passive-front-end rectifier does not require a complicated gate drive system and control scheme since the switching dynamics rely on the external ac voltage source and load power consumption.
- The active-front-end rectifier allows for a bidirectional operation, which can smoothly release the regenerative power (reverse power flow) during the motor deceleration.
- The active-front-end rectifier provides a chance for the connected loads to participate in the power grid coordination because it has the potential of employing sophisticated control algorithms.

- The active-front-end rectifier is better at reducing THD than the passive-front-end rectifier.

The modeling algorithms of the above two types of VSD rectifiers are introduced in the following subsections, respectively. A comparison between these two types of VSD rectifiers in terms of the different responses towards grid disturbance is also introduced in this section.

3.1.1 Passive-front-end Topology and Modeling Algorithm

The circuit topology of the passive-front-end rectifier is illustrated in the upper yellow box on the left side of Fig. 3.1. In the VSD system, the diode rectifier converts the three-phase ac power supply to provide a stable dc voltage V_{dc} for the next power stage, along with the dc filter inductance L_{dc} and energy storage capacitance C_{dc}. Compared with the diode bridge model which has been derived in [113], the whole VSD load model in this dissertation is derived based on the load bus terminal voltage V_{sabc} according to the interface design between the load model and the HTB 2.2.2, ignoring the impact of the transmission line impedance. So the previous model algorithm, which relies on the dynamic of line impedance, is not suitable anymore. So a new diode bridge model algorithm for HTB emulator is proposed as follows [36]:

- The diode rectifier model is simplified based on the assumption that the diode switch in the rectifier is ideally disconnected when turned off, and ideally connected when turned on with forward voltage drop V_{diode} [36].
- As illustrated in Fig. 3.1, the voltage after the diode bridge, which is represented by V_{sac}, specifies the maximum line-to-line voltage of V_{sabc}. So $i_{dc,diode}$, which represents the current flowing from the diode bridge and through L_{dc}, can be expressed as [36]:

$$\frac{di_{dc,diode}}{dt} = \frac{V_{sac} - 2 \cdot V_{diode} - V_{dc}}{L_{dc}} \tag{3.1}$$

Meanwhile, V_{dc} across C_{dc} can be expressed as:

$$C_{dc}\frac{dV_{dc}}{dt} = i_{dc,diode} - i_{dc,im} \tag{3.2}$$

where $i_{dc,im}$ represents the dc current flowing directly to the inverter and bypassing C_{dc}.

- The diode bridge is under normal operating condition when $i_{dc,diode} > 0$. I_{sabc} is determined by $i_{dc,diode}$ under normal operation as expressed in (3.3) [36]:

$$I_{sk} = i_{sgnk} \cdot i_{dc,diode}, \quad (k = a, b, c) \tag{3.3}$$

where i_{sgnk} represents the direction of I_{sabc} according to V_{sac}. When i_{sgnk} = 1, the corresponding phase k current is equal to $i_{dc,diode}$, while when i_{sgnk} = -1, the phase k current is opposite to $i_{dc,diode}$. The phase k has no current flowing through when $i_{sgnk} = 0$. According to the operating principle of diode front-end rectifier, if the diode switches connect to the most positive and most negative source side ac voltage, then switches will turn on to make up a complete current flow path. So the diode switch turn-on sequence is decided by the ac voltage source V_{sac}. An example explaining how I_{sabc} is related to V_{sac} and $I_{dc,diode}$ is illustrated in Fig. 3.2. In this example, the most positive ac voltage is the phase a voltage, and the most negative ac voltage is the phase b voltage, so $V_{sac} = V_{ab}$. The current flowing path is represented by the blue line, and the current flowing through ac and dc side can be expressed as [36]:

$$I_{dc,diode} = I_{sa} = -1 \cdot I_{sb} \tag{3.4}$$

More detailed information about the relation between i_{sgnk} and V_{max} is listed in Table 3.1. However, the diode bridge is disconnected from the rest of the power network when $i_{dc,diode}$ drops to 0 since it does not allow for the regenerative power [36].

- The LC passive filter is connected in parallel to the diode front-end rectifier at the ac bus terminal to reduce the load current THD. Aside from improving the power quality, the filter capacitor is also designed to provide a considerable amount of reactive power to adjust the local power factor. The reactive power consumption of the LC passive filter usually accounts for a larger portion compared with the impact of the

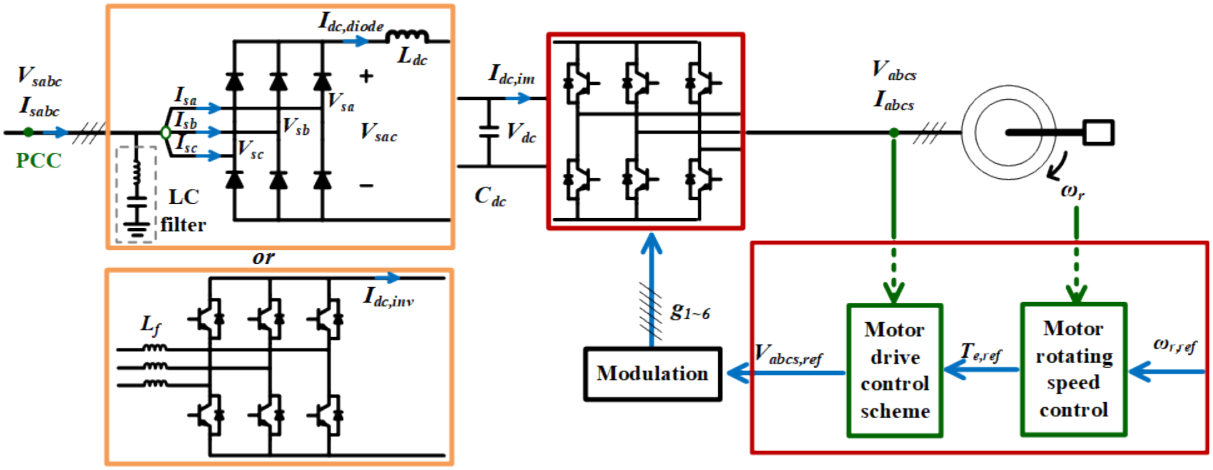

Figure 3.1: VSD load configuration [36].

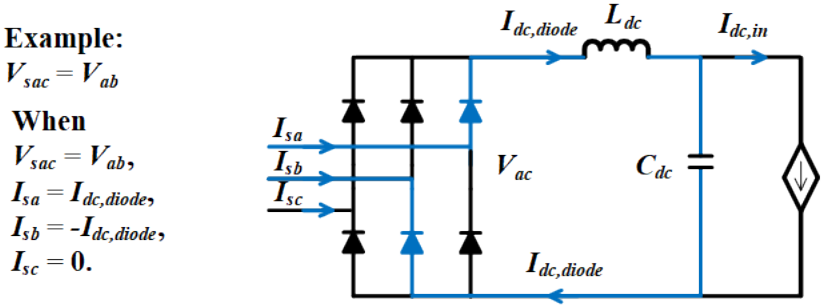

Figure 3.2: Passive-front-end model based on V_{sabc} and current direction when $i_{dc,diode} > 0$ [36].

Table 3.1: Relation between i_{sgnk} and V_{max} in normal operating conditions [36].

V_{max}	V_{ab}	V_{ac}	V_{bc}	V_{ba}	V_{ca}	V_{cb}
i_{sgna}	1	1	0	-1	-1	0
i_{sgnb}	-1	0	1	1	0	-1
i_{sgnc}	0	-1	-1	0	1	1

load current THD reduction due to Var support, so the reactive power provision is used to characterize the LC filter function in the HTB load emulator design [36]:

$$Q_{flt} = \sum V_{s,rms}^2 / Z_{flt,k} \tag{3.5}$$

where Q_{flt} represents the reactive power provided by the passive filter, $V_{s,rms}$ represents the root mean square (RMS) value of the voltage source, $Z_{flt,k}$ represents the impedance of the LC filter.

Q_{flt} characterizes the dynamic reactive power support by the passive filters according to (3.5). However, in cases where the impact of VSD reactive power consumption is not emphasized, Q_{flt} is regarded as a static value when considering the overall impact of the VSD load. For example, analysis of the grid frequency support function mainly involves the dynamic adjustment of the active power consumption of the load [36].

The VSD passive-front-end modeling procedure for the HTB power emulator is illustrated in Fig. 3.3 based on the VSD modeling principle explained above. For implementation in the DSP, the passive-front-end model expression (3.1) to (3.5) is required to be converted to discrete equations by using the backward Euler method.

In Fig. 3.3, the flow chart inside the yellow solid box illustrates the n^{th} computation cycle in the power emulator microprocessor, and the dashed lines out of the yellow solid box stand for using the computational results from the $(n-1)^{th}$ computation cycle.

As illustrated in Fig. 3.3, the input variables for each computation cycle include $I_{dc,diode}$ and V_{dc} from the last cycle, and the real-time ac side voltage V_{sabc}. The output variables include the load current I_{sabc}, or converted to the load active power consumption P_{VSD}. Then the HTB power emulator generates real power flow according to the current/power reference.

As shown in the modeling procedure, the passive-front-end model starts from the L_{dc} model expressed in (3.1) with electrical components derived from the last computation cycle, including $i_{dc,diode}$ and V_{dc}. Second, the updated $i_{dc,diode}$ is regarded as the temporary diode dc side current $i_{dc,diode,temp}$ and is sent to the comparison process: if $i_{dc,diode,temp} > 0$, then the final $i_{dc,diode} = i_{dc,diode,temp}$. Otherwise, $i_{dc,diode} = 0$ since the diode front-end rectifier does not allow for regenerative power. Third, the final $i_{dc,diode}$ is sent to the C_{dc} model expressed in (3.2) along with V_{dc} calculated in the $(n-1)^{th}$ computation cycle. Finally, the passive-front-end power flow current reference is decided by $i_{dc,diode}$ and V_{sabc} according to the modeling principle illustrated in Fig. 3.2 and Table 3.1.

3.1.2 Active-front-end Topology and Modeling Algorithm

The active-front-end rectifier is equivalent to the configuration of VSC, of which the HTB emulator design and development have been widely investigated in [58, 59, 114]. The active-front-end rectifier can participate in improving the power grid stability since it can adjust the load active/reactive power consumption respectively in a more flexible manner compared with the passive-front-end rectifier.

The circuit topology of an active-front-end rectifier is below that of a passive-front-end rectifier in Fig. 3.1. The full-bridge three-phase VSC is selected as the topology of the active-front-end rectifier in this chapter. C_{dc} is utilized for the dc energy storage, and it provides a stabilized voltage source for the next power stage, which is similar to the design of the passive-front-end rectifier. The mathematical expression of V_{dc} dynamic performance is expressed as:

$$C_{dc}\frac{dV_{dc}}{dt} = i_{dc,inv} - i_{dc,im} \tag{3.6}$$

where $i_{dc,inv}$ represents the current flowing from the active-front-end rectifier.

Equation (3.6) is similar to (3.2) except that $I_{dc,inv}$ should be modeled in a different manner from that used in a passive-front-end rectifier. In an active-front-end rectifier, L_{dc} is negligible since the current THD is small, so L_{dc} is removed from the front-end model for simplification. Therefore, $I_{dc,inv}$ cannot be modeled by the L_{dc} dynamic expression as written in (3.1). Alternatively, $I_{dc,inv}$ is expressed by using the ac-dc equal power principle expressed below:

$$I_{dc,inv} = 1.5\frac{V_{sd}I_{sd} + V_{sq}I_{sq}}{V_{dc}} \tag{3.7}$$

where V_{sd}, V_{sq}, I_{sd}, and I_{sq} represent V_{sabc} and I_{sabc} converted to dq coordinates. $I_{dc,inv}$ is derived assuming that the ac side active power flowing into the three-phase VSC bridge, and the dc side active power flowing out of the three-phase VSC bridge are always equal assumes rectifier is lossless.

Additionally, vector control based on the dq coordinates is the commonly used control scheme for the three-phase VSC. Generally, the d-axis controller is in charge of the active power related variables and functions, *e.g.,* the load active power consumption P_{rec} control, the constant dc-link voltage control, etc. Meanwhile, the q-axis controller is in charge of the reactive power related variables and functions, *e.g.,* the reactive power Q_{rec} consumption control, the power factor correction, the grid terminal voltage support, etc.

The active-front-end rectifier control scheme studied in this chapter is illustrated in Fig. 3.4. Generally, the VSC vector control is composed of the outer control loop and the inner current control loop, and the PI controller is adopted by both the outer and inner control loop. The outer control loop generates current commands $I_{sd,ref}$ and $I_{sq,ref}$, which represent the current drawn by the VSD load from the grid. According to the requirement of the VSD front-end rectifier, the constant V_{dc} control is adopted as the d-axis controller as illustrated in Fig. 3.4 to provide a stable dc power supply for the next power stage. Meanwhile, the constant Q_{rec} is adopted as the q-axis controller, and $Q_{rec,ref}$ is usually set to 0 to improve the load power factor.

According to the control scheme illustrated above, the active-front-end outer control loop in dq coordinates can be mathematically expressed as:

$$I_{sd,ref} = K_{pv}(V_{dc,ref} - V_{dc,meas}) + K_{iv}\int (V_{dc,ref} - V_{dc,meas}) \tag{3.8}$$

$$I_{sq,ref} = K_{pq}(Q_{rec,ref} - Q_{rec,meas}) + K_{iq}\int (Q_{rec,ref} - Q_{rec,meas}) \tag{3.9}$$

where K_{pv} and K_{iv}, as well as K_{pq} and K_{iq}, represent the PI controller parameters of d and q-axis controller respectively. $V_{dc,meas}$ and $Q_{rec,meas}$ represents V_{dc} and Q_{rec} measured value. $V_{dc,meas}$ can be computed by (3.6), while $Q_{rec,meas}$ can be expressed by ac side current and

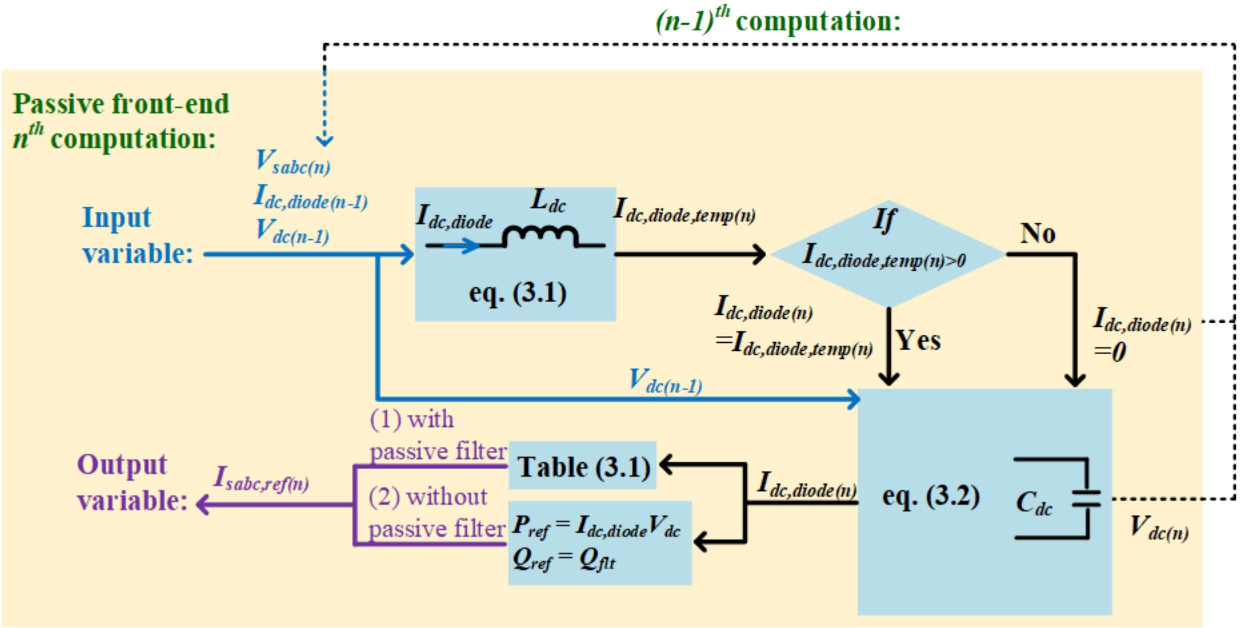

Figure 3.3: VSD passive-front-end model procedure for HTB power emulator.

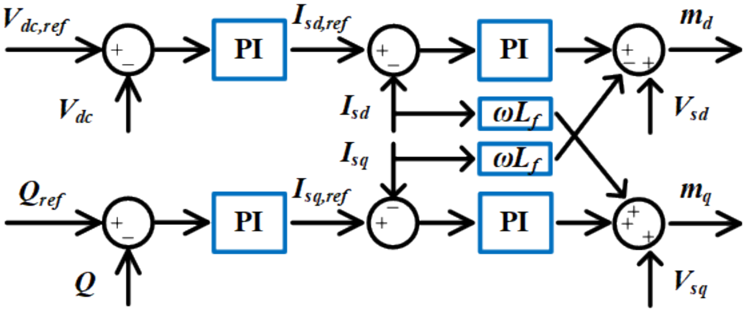

Figure 3.4: VSD active-front-end rectifier control scheme.

voltage in dq coordinates as:

$$Q_{rec,meas} = 1.5 \cdot (V_{sd} \cdot I_{sq} - V_{sq} \cdot I_{sd}) \tag{3.10}$$

Besides the expression in (3.9) which represents the classical PI controller, the feed-forward controller can also be used in Q_{rec} control which is expressed in (3.11):

$$I_{sq,ref} = \frac{Q_{rec,ref} - 1.5V_{sq}I_{sd}}{1.5V_{sd}} \tag{3.11}$$

Both (3.9) and (3.11) are regarded as frequently adopted Q_{rec} controllers. The controller using a PI regulator in (3.9) is easier to be designed to maintain the controller stability compared with the feed-forward control in (3.11), while the (3.11) is simpler. Customers can select either control scheme according to their practical requirements.

The inner current control loop is to generate appropriate modulation index m_d and m_q, providing the required line current I_{sabc} by adjusting the VSC output voltage V_{Labc}. This process is essential for regular VSC control; moreover, it is also necessary for some HTB power emulator design, *e.g.,* in [115], the VSC modulation process is required since the HTB emulator VSC configuration is used to emulate the ac-dc power stage of a battery energy storage system. However, it is not necessary for the VSD load emulator developed in this chapter to identify the m_d and m_q since only the emulator current reference is required to represent the load dynamics. So the inner current loop is ignored in the HTB load emulator design, assuming that the load current ideally follows the current reference $I_{sd,ref}$ and $I_{sq,ref}$.

The VSD active-front-end model procedure for the HTB power emulator is illustrated in Fig. 3.5 based on the modeling principle explained above. Similar to Fig. 3.3, the process inside of the solid yellow box illustrates the n^{th} computation cycle, and the dashed lines out of the green box stand for using the computational results from the last cycle, including V_{dc}, I_{sd} and I_{sq}. The dq coordinates controllers are modeled respectively based on the modeling principle introduced above. Output variables in each cycle are the command of I_{sabc}, which is the current absorbed by the rectifier on the ac side.

As shown in Fig. 3.5, the active-front-end rectifier model in d-axis starts from identifying $I_{dc,inv}$ based on the real-time V_{sabc} and I_{sdq} from the last computational cycle as expressed in

(3.7). Second, the updated $I_{dc,inv}$ is sent to V_{dc} model expressed in (3.6) along with V_{dc} from the last computational cycle. Third, the updated V_{dc} is sent to the d-axis vector controller model expressed in (3.8) for generating $I_{sd,ref}$. As explained above, I_{sd} is considered to be equal to $I_{sd,ref}$ assuming that the modulation process dynamics are ignored. Meanwhile, the active-front-end q-axis is similar to the modeling procedure comparing with that of the d-axis.

3.2 Modeling of VSD Back-end Inverter

As introduced above, the control schemes used for regulating the motor load are applied in the VSD back-end inverter, which is also regarded as the inverter-based motor drive. In this section, the different motor control algorithms are introduced, as well as how to represent them in the HTB emulator.

3.2.1 IM Voltage and Torque Expression

The IM electrical model is introduced in this section, which characterizes the electrical and mechanical dynamic performance [116]. The IM expressions in *abc* stationary frame and $dq0$ rotating frame are introduced, respectively. Meanwhile, the symbols of the machine variables, which will be frequently used in the following chapters, will be introduced in the following sections.

3.2.1.1 *abc* coordinates

The voltage equation expressed by IM variables are:

$$\mathbf{v_{abcs}} = \mathbf{r_s i_{abcs}} + \dot{\lambda}_{\mathbf{abcs}} \tag{3.12}$$

$$\mathbf{v_{abcr}} = \mathbf{r_r i_{abcr}} + \dot{\lambda}_{\mathbf{abcr}} \tag{3.13}$$

where:

$$(\mathbf{f_{abcs}})^T = \begin{bmatrix} f_{as} & f_{bs} & f_{cs} \end{bmatrix} \tag{3.14}$$

$$(\mathbf{f_{abcr}})^T = \begin{bmatrix} f_{ar} & f_{br} & f_{cr} \end{bmatrix} \tag{3.15}$$

In (3.14) and (3.15), the vector with *abc* subscript represents the variable vector composed of the three-phase electrical components. In the above equations, s and r subscript denotes the variables associated with the IM stator and rotor, respectively. So $\mathbf{v_{abcs}}$, $\mathbf{i_{abcs}}$ and $\mathbf{v_{abcr}}$, $\mathbf{i_{abcr}}$ represent the stator and rotor voltage and current vector respectively. $\mathbf{r_s}$ and $\mathbf{r_r}$ represent the diagonal matrices composed by the resistance in the stator and rotor circuit. For a magnetically linear system, the flux linkages $\lambda_{\mathbf{abcs}}$ and $\lambda_{\mathbf{abcr}}$ in (3.12) and (3.13) are expressed as:

$$\begin{bmatrix} \lambda_{\mathbf{abcs}} \\ \lambda_{\mathbf{abcr}} \end{bmatrix} = \begin{bmatrix} \mathbf{L_s} & \mathbf{L_{sr}} \\ (\mathbf{L_{sr}})^T & \mathbf{L_r} \end{bmatrix} \begin{bmatrix} \mathbf{i_{abcs}} \\ \mathbf{i_{abcr}} \end{bmatrix} \tag{3.16}$$

Neglecting the mutual leakage, the inductance matrices in (3.16) are expressed as:

$$\mathbf{L_s} = \begin{bmatrix} L_{ls}+L_{ms} & -\frac{1}{2}L_{ms} & -\frac{1}{2}L_{ms} \\ -\frac{1}{2}L_{ms} & L_{ls}+L_{ms} & -\frac{1}{2}L_{ms} \\ -\frac{1}{2}L_{ms} & -\frac{1}{2}L_{ms} & L_{ls}+L_{ms} \end{bmatrix} \tag{3.17}$$

$$\mathbf{L_r} = \begin{bmatrix} L_{lr}+L_{mr} & -\frac{1}{2}L_{mr} & -\frac{1}{2}L_{mr} \\ -\frac{1}{2}L_{mr} & L_{lr}+L_{mr} & -\frac{1}{2}L_{mr} \\ -\frac{1}{2}L_{mr} & -\frac{1}{2}L_{mr} & L_{lr}+L_{mr} \end{bmatrix} \tag{3.18}$$

$$\mathbf{L_{sr}} = L_{sr} \begin{bmatrix} cos\theta_r & cos(\theta_r+\frac{2\pi}{3}) & cos(\theta_r-\frac{2\pi}{3}) \\ cos(\theta_r-\frac{2\pi}{3}) & cos\theta_r & cos(\theta_r+\frac{2\pi}{3}) \\ cos(\theta_r+\frac{2\pi}{3}) & cos(\theta_r-\frac{2\pi}{3}) & cos\theta_r \end{bmatrix} \tag{3.19}$$

In the above inductance equations, L_{ls} and L_{ms} represent the stator windings leakage and magnetizing inductance respectively, while L_{lr} and L_{mr} are for the rotor windings. The inductance L_{sr} is the amplitude of the mutual inductances between stator and rotor windings.

After referring all rotor variables to stator windings based on stator-to-rotor turns ratios, the inductance matrices expressed in (3.19) and (3.18) are rewritten as:

$$\mathbf{L_r}' = \begin{bmatrix} L_{lr}' + L_{ms} & -\frac{1}{2}L_{ms} & -\frac{1}{2}L_{ms} \\ -\frac{1}{2}L_{ms} & L_{lr}' + L_{ms} & -\frac{1}{2}L_{ms} \\ -\frac{1}{2}L_{ms} & -\frac{1}{2}L_{ms} & L_{lr}' + L_{ms} \end{bmatrix} \tag{3.20}$$

$$\mathbf{L_{sr}}' = L_{ms} \begin{bmatrix} cos\theta_r & cos(\theta_r + \frac{2\pi}{3}) & cos(\theta_r - \frac{2\pi}{3}) \\ cos(\theta_r - \frac{2\pi}{3}) & cos\theta_r & cos(\theta_r + \frac{2\pi}{3}) \\ cos(\theta_r + \frac{2\pi}{3}) & cos(\theta_r - \frac{2\pi}{3}) & cos\theta_r \end{bmatrix} \tag{3.21}$$

The prime superscript denotes rotor variables referred to stator windings. The flux linkages are expressed by the rotor side variables after referring to the stator side in (3.22):

$$\begin{bmatrix} \lambda_{\mathbf{abcs}} \\ \lambda_{\mathbf{abcr}}' \end{bmatrix} = \begin{bmatrix} \mathbf{L_s} & \mathbf{L_{sr}}' \\ (\mathbf{L_{sr}}')^T & \mathbf{L_r}' \end{bmatrix} \begin{bmatrix} \mathbf{i_{abcs}} \\ \mathbf{i_{abcr}}' \end{bmatrix} \tag{3.22}$$

$\mathbf{v_{abcs}}$ and $\mathbf{v_{abcs}}'$ expressed by the current and IM passive component variables after referring to the stator side is written as:

$$\begin{bmatrix} \mathbf{v_{abcs}} \\ \mathbf{v_{abcr}}' \end{bmatrix} = \begin{bmatrix} \mathbf{r_s} + p\mathbf{L_s} & p\mathbf{L_{sr}}' \\ p(\mathbf{L_{sr}}')^T & \mathbf{r_r}' + p\mathbf{L_r}' \end{bmatrix} \begin{bmatrix} \mathbf{i_{abcs}} \\ \mathbf{i_{abcr}}' \end{bmatrix} \tag{3.23}$$

where $p = d/dt$.

The electromagnetic torque T_e is the derivative of field energy in terms of actual angular displacement θ_{rm}. T_e in Newton meters (Nm) expressed by electrical angular displacement θ_r is written as:

$$T_e = P(i_{abcs})^T \frac{\partial}{\partial \theta_r}[\mathbf{L_{sr}}']\mathbf{i_{abcr}}' \tag{3.24}$$

where P represents the number of pole pairs.

Furthermore, T_e and electrical rotor speed ω_r are related by:

$$T_e = \frac{J}{P}\frac{d\omega_r}{dt} + T_L \tag{3.25}$$

where J is the rotor moment of inertia, and in some cases the inertia of the connected load is also included in it. The first term on the right of equal sign is the inertial torque. In (3.25), the unit of J is kilogram·meter^2 (kg·m^2) or Joules·second^2 (J·s^2). T_L represents the load torque [116].

3.2.1.2 $dq0$ Coordinates

At the beginning of this subsection, it should be noticed that dq coordinates, which are used to express the machine variables, are different from the rotating $dq0$ coordinates mentioned in section 3.1.2. More details can be found in [116].

The three-phase variables of stator circuit elements transferring to the $dq0$ coordinates are expressed as:

$$\mathbf{f_{dq0s}} = \mathbf{K_s f_{abcs}} \tag{3.26}$$

where the transformation matrix $\mathbf{K_s}$ is expressed as:

$$\mathbf{K_s} = \frac{2}{3}\begin{bmatrix} cos\theta & cos(\theta - \frac{2\pi}{3}) & cos(\theta + \frac{2\pi}{3}) \\ sin\theta & sin(\theta - \frac{2\pi}{3}) & sin(\theta + \frac{2\pi}{3}) \\ \frac{1}{2} & \frac{1}{2} & \frac{1}{2} \end{bmatrix} \tag{3.27}$$

As expressed in (3.27), θ represents the angular position, where θ and velocity of the rotating reference frame ω are related as:

$$\frac{d\theta}{dt} = \omega \tag{3.28}$$

Similarly, rotor circuits variables in the *abc* coordinates transferring to the $dq0$ coordinates are expressed as:

$$\mathbf{f_{dq0r}}' = \mathbf{K_r}\mathbf{f_{abcr}}' \tag{3.29}$$

where the transformation matrix $\mathbf{K_r}$ is expressed as:

$$\mathbf{K_r} = \frac{2}{3}\begin{bmatrix} cos\beta & cos(\beta - \frac{2\pi}{3}) & cos(\beta + \frac{2\pi}{3}) \\ sin\beta & sin(\beta - \frac{2\pi}{3}) & sin(\beta + \frac{2\pi}{3}) \\ \frac{1}{2} & \frac{1}{2} & \frac{1}{2} \end{bmatrix} \tag{3.30}$$

$$\beta = \theta - \theta_r \tag{3.31}$$

where θ_r and ω_r are related as:

$$\frac{d\theta_r}{dt} = \omega_r \tag{3.32}$$

Substitute (3.27) and (3.30) into (3.23), voltage equations in the $dq0$ reference frame are expressed as:

$$v_{qs} = r_s i_{qs} + \omega\lambda_{ds} + p\lambda_{qs} \tag{3.33}$$

$$v_{ds} = r_s i_{ds} - \omega\lambda_{qs} + p\lambda_{ds} \tag{3.34}$$

$$v_{qr}' = r_r' i_{qr}' + (\omega - \omega_r)\lambda_{dr}' + p\lambda_{qr}' \tag{3.35}$$

$$v_{dr}' = r_r' i_{dr}' - (\omega - \omega_r)\lambda_{qr}' + p\lambda_{dr}' \tag{3.36}$$

The zero sequence is not represented here in (3.33) to (3.36) since the IM is three-phase balanced. v_{qr}' and v_{dr}' from IM are always equal to 0, so the expanded form of flux linkages expressed in (3.33) to (3.36) can be rewritten:

$$\lambda_{qs} = L_{ls} i_{qs} + L_M (i_{qs} + i_{qr}{}') \tag{3.37}$$

$$\lambda_{ds} = L_{ls} i_{ds} + L_M (i_{ds} + i_{dr}{}') \tag{3.38}$$

$$\lambda_{qr}{}' = L_{lr}{}' i_{qr}{}' + L_M (i_{qs} + i_{qr}{}') \tag{3.39}$$

$$\lambda_{dr}{}' = L_{lr}{}' i_{dr}{}' + L_M (i_{ds} + i_{dr}{}') \tag{3.40}$$

where $L_M = \frac{3}{2} L_{ms}$.

The equivalent circuits in dq coordinates based on the voltage and flux linkage equations above are illustrated in Fig. 3.6 based on the expression from (3.33) to (3.40). The IM characteristics and dynamic performances mentioned in the following chapters are based on the model introduced in this section.

Accordingly, the IM electromagnetic torque equation is expressed in terms of rotor and stator current as:

$$T_e = \frac{3}{2} P L_M (i_{qs} i_{dr}{}' - i_{qs} i_{qr}{}') \tag{3.41}$$

3.2.2 Constant Volts-per-hertz Control

To simplify the expression, the prime superscript, which denotes the rotor variables that have been referred to the stator windings, is ignored in the corresponding mathematical equations.

The constant volts-per-hertz control, which is also referred to as the constant V/f control, is a widely applied open-loop motor speed control. Applying the open-loop constant V/f control to the VSD is cost-effective because: 1) an advanced microprocessor is not required to achieve the simple open-loop control function, 2) fewer electrical sensors are needed since no feedback information is used in the control loop. The principle of using constant V/f control to regulate motor speed is based on the observation: 1) the rotor speed can be regulated by controlling the electrical frequency of stator voltage v_{abcs}, 2) the voltage magnitude should be proportional to the electrical frequency so as to maintain a constant flux linkage [36].

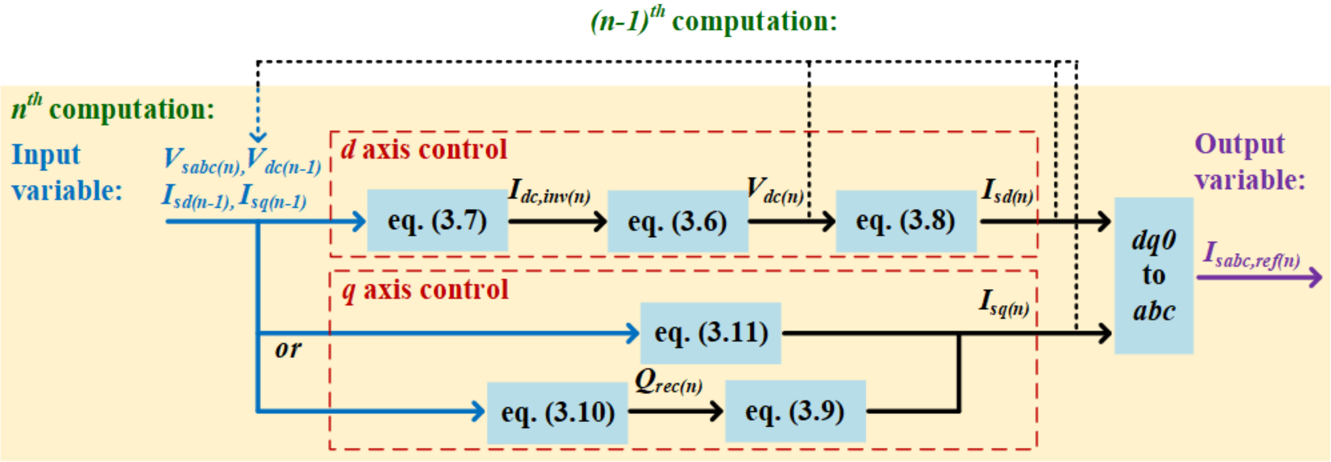

Figure 3.5: VSD active-front-end model procedure for HTB power emulator.

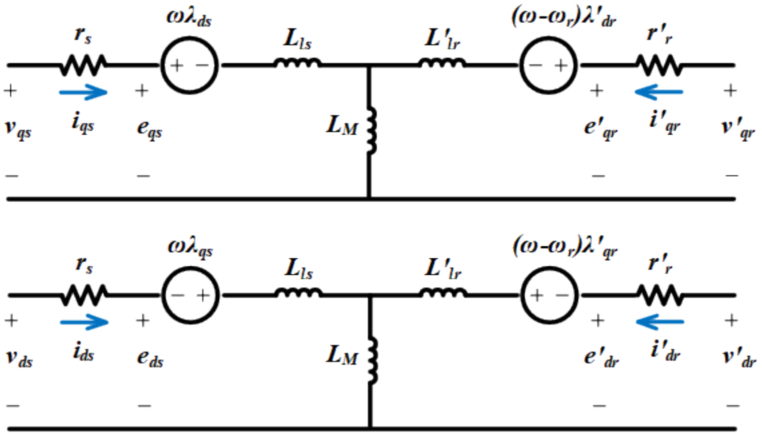

Figure 3.6: IM equivalent circuit topology in *dq* coordinates [116].

The most elementary constant V/f control is illustrated in Fig. 3.7. It can be observed that both v_{abcs} electrical frequency and voltage magnitude are determined by $\omega_{rm,ref}$. However, the rotor speed cannot reach the speed command by simply using the presented elementary constant V/f control. Furthermore, this speed controller is not accurate enough, especially when $\omega_{rm,ref}$ is much lower than its nominal speed. To improve the performance of the motor drive, some adjustments can be applied to the elementary constant V/f control. For example, ω_{rm} control accuracy can be improved by adjusting the RMS value of the terminal voltage, or by adding a stator current feedback control based on the elementary control. However, these correction methods increase the complexity of the motor drive controller, which will overshadow the advantage of adopting the constant V/f control scheme.

To maintain a balance between the accuracy of ω_r command and the motor drive control simplicity, a look-up table is inserted into the original control scheme, which demonstrates the relationship between ω_e and ω_r of IM in the static operating condition. The look-up table is derived based on the following derivations:

The electric torque at steady state in the p.u. system is expressed as:

$$T_{e,pu} = \frac{\frac{\omega_e}{\omega_b} {X_{M,pu}}^2 r_{r,pu} s |V_{as,pu}|^2}{\left[r_{s,pu} r_{r,pu} + s(\frac{\omega_e}{\omega_b})^2({X_{M,pu}}^2 - X_{ss,pu} X_{rr,pu})\right]^2 + (\frac{\omega_e}{\omega_b})^2 (r_{r,pu} X_{ss,pu} + s r_{s,pu} X_{rr,pu})^2} \tag{3.42}$$

where $X_{ss,pu}$, $X_{rr,pu}$ and $X_{M,pu}$ are expressed respectively as:

$$L_{ss} = L_{ls} + L_M \tag{3.43}$$

$$L_{rr} = L_{lr} + L_M \tag{3.44}$$

$$X_{ss,pu} = \frac{L_{ss} \cdot \omega_b}{Z_b} \tag{3.45}$$

$$X_{rr,pu} = \frac{L_{ss} \cdot \omega_b}{Z_b} \tag{3.46}$$

$$X_{M,pu} = \frac{L_M}{Z_b} \tag{3.47}$$

where L_{ss} represents the total stator inductance, L_{rr} represents the total rotor inductance, $X_{ss,pu}$, $X_{rr,pu}$ and $X_{M,pu}$ represent corresponding motor impedance in the p.u. system respectively, X_b represents the motor impedance base value. All variables in (3.42) with pu subscript stands for being represented in the p.u. system.

s in (3.42) denotes the slip of rotating speed, which is expressed as:

$$s = \frac{\omega_e - \omega_r}{\omega_e} \tag{3.48}$$

Additionally, $|V_{as,pu}|$ in (3.42) is expressed as:

$$|V_{as}| = \frac{\omega_e}{\omega_b} \tag{3.49}$$

The fan/pump type of load torque is studied as an example of typical rotating load characteristics in this section. Ignoring the mechanical loss, $T_{e,pu}$ is equivalent to the square of $\omega_{r,pu}$ in the static operating state, so (3.42) can be used to express the relation between ω_e and ω_r if replacing $T_{e,pu}$ by $\omega_{r,pu}$. Therefore, the look-up table mentioned above is derived accordingly.

Considering the look-up table compensation effect on rotor speed command, the compensated constant V/f control is illustrated in Fig. 3.8:

The elementary and compensated constant V/f controller are both developed in Simulink. The comparison of these two controllers are illustrated in Fig. 3.9. ω_r comparison is illustrated in Fig. 3.9a, where the black curve represents motor speed reference, the blue curve and red curve represent motor speed when motor drive adopts elementary and compensated constant V/f control, respectively. The elementary constant V/f control cannot regulate ω_r to be equal to the speed reference, while the compensated constant V/f control can mitigate this gap.

VSD load dynamic performance using these two different controllers are also represented by T_L, T_e and P_{VSD}, which are illustrated in Fig. 3.9b, Fig. 3.9c and Fig. 3.9d respectively. The motor electric torque and power consumption are also increased when the VSD adopts the compensated constant V/f controller, because ω_r is closer to the speed command. This compensated constant V/f model can be used to represent the condition where the elementary constant V/f controller is updated to provide a more accurate rotating speed. The advantage of this model is to maintain a good balance between the accuracy of ω_r

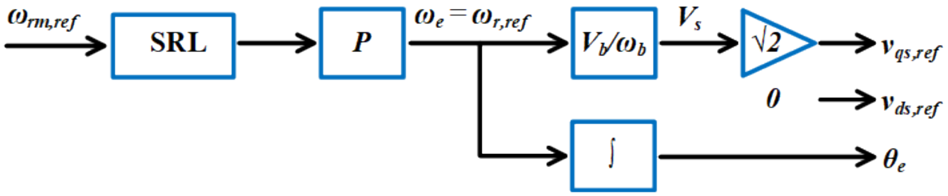

Figure 3.7: Elementary constant V/f control [116].

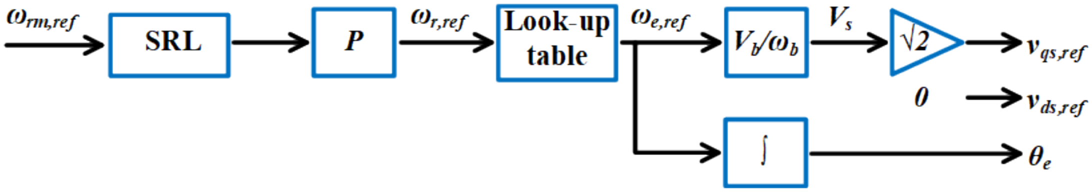

Figure 3.8: Compensated constant V/f controller with look-up table expressing the static relation between ω_e and ω_r.

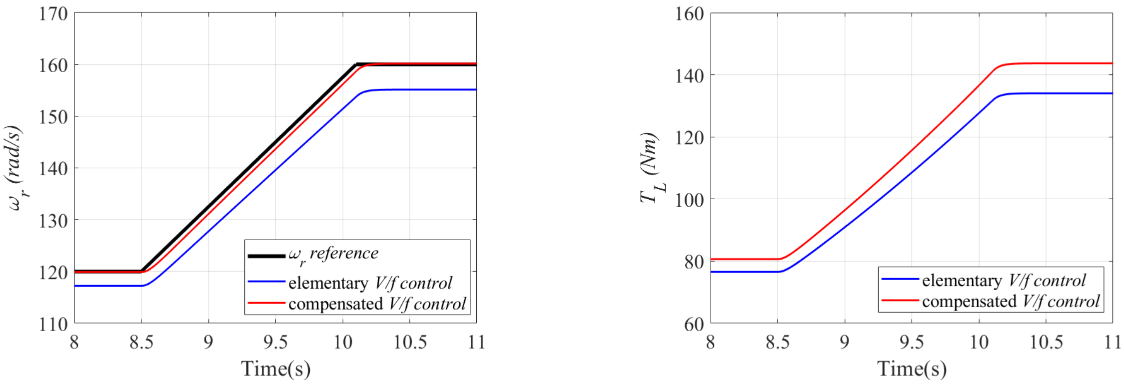

(a) IM dynamic performance: ω_r.

(b) IM dynamic performance: T_L.

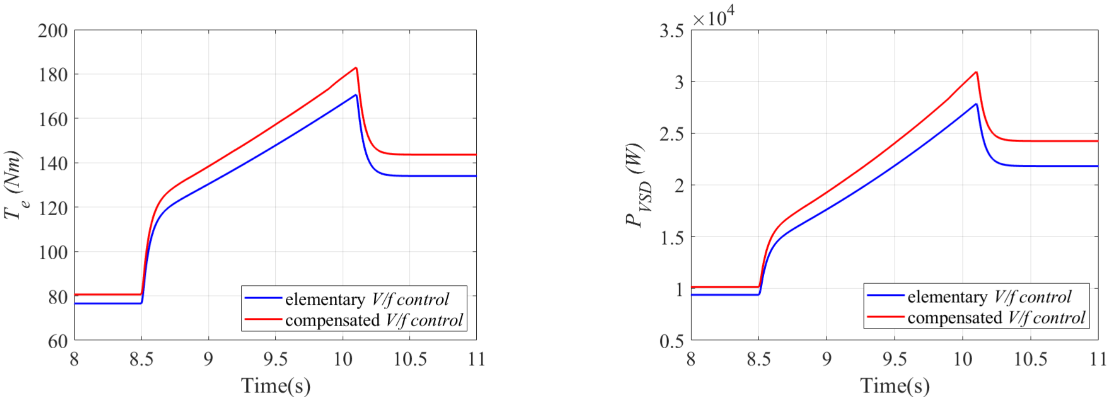

(c) IM dynamic performance: T_e.

(d) IM dynamic performance: P_{VSD}.

Figure 3.9: Dynamic performance comparison between elementary and compensated constant V/f controller based VSD load.

command and the model simplicity. The model of elementary and compensated constant V/f controller can be selected based on research purposes.

3.2.3 Field-oriented Control

It is desirable to make the motor drive perform as a torque transducer of which T_e is instantaneously approximately equal to the torque command, which is beneficial to simplify the motor speed and position control. The torque balance requirement mentioned above can be achieved by a collection of control methods, which is known as the field-oriented control (FOC) [116]. The FOC includes a number of different control permutations, which include the stator flux oriented, rotor flux oriented, and air-gap flux oriented control. In this chapter, one of the most prevalent types is introduced and modeled, which is the rotor-flux oriented control.

The operating principle of the FOC algorithm is explained below. First, T_e is expressed in (3.50) by dq coordinates rotor current and flux linkage:

$$T_e = \frac{3}{2}P(\lambda_{qr}i_{dr} - \lambda_{dr}i_{qr}) \tag{3.50}$$

Meanwhile, with a given magnitude of flux linkage, the maximum T_e is observed if the flux linkage and current vectors are perpendicular to each other [116]. Particularly, the vectors of the rotor flux linkage and rotor current are perpendicular at the motor steady state. The objective of motor drive adopting the FOC is to maintain such characteristics during transient conditions [36].

The method to achieve such perpendicular operating condition is twofold, of which the first requirement is to ensure the following two operating conditions:

$$\lambda_{qr} = 0 \tag{3.51}$$

$$i_{dr} = 0 \tag{3.52}$$

The first condition expressed in (3.51) can be satisfied by a suitable choice of reference frame. The rotor flux linkage can be referred to the d-axis totally by specifically choosing the position of the synchronous reference frame. Then the second condition expressed in (3.52) is satisfied by forcing the d-axis stator current to be constant [36].

Substitute (3.52) into (3.38) and (3.40) respectively, it is clear that:

$$\lambda_{ds} = L_{ss} i_{ds} \tag{3.53}$$

$$\lambda_{dr} = L_M i_{ds} \tag{3.54}$$

Accordingly, it can be observed that the d-axis flux is only determined by the i_{ds}. Combining (3.50) and (3.51), T_e can be rewritten as:

$$T_e = -\frac{3}{2} P \lambda_{dr} i_{qr} \tag{3.55}$$

Substitute (3.51) into (3.39), i_{qs} can be replaced by i_{qr} as expressed as:

$$i_{qr} = -\frac{L_M}{L_{rr}} i_{qs} \tag{3.56}$$

Combining (3.55) and (3.56), T_e can be expressed by i_{qs} and λ_{dr} as follows:

$$T_e = \frac{3}{2} \frac{L_M}{L_{rr}} P \lambda_{dr} i_{qs} \tag{3.57}$$

Therefore, the generic rotor flux-oriented control is depicted in Fig. 3.10 by (3.54) and (3.57).

As shown in Fig. 3.10, the q-axis stator current $I_{qs,ref}$ is formulated based on a torque command $T_{e,ref}$, and the estimated value of d-axis rotor flux $\lambda_{dr,est}$ according to (3.57). The d-axis stator current command $I_{ds,ref}$ is calculated based on (3.54).$I_{ds,ref}$ is determined by the rotor flux command, which is expressed as $\lambda_{dr,ref}$. Then the d and q-axis current is generated by the current regulation process of PE inverter-based motor drive according to corresponding $I_{ds,ref}$ and $I_{qs,ref}$.

However, $\lambda_{dr,est}$ and electrical angle θ_e are required in the FOC process as shown in Fig. 3.10. There are two different ways to represent the required values mentioned above, which are usually referred to as the direct rotor FOC and indirect rotor FOC. The direct rotor FOC is to compute the rotor flux linkage by using Hall-effect sensors which can sense the air-gap flux linkage. This method is robust with the variation of machine parameters, but it is also expensive and problematic to be applied in practice. The indirect rotor FOC estimates θ_e and $\lambda_{dr,est}$ based on the IM mathematical relation, so it is sensitive to the machine parameters variation during motor operation. The indirect rotor FOC is analyzed in this dissertation paper, though these two methods are of similar complexity in terms of modeling VSD loads. The estimated $\theta_{e,est}$ and $\lambda_{dr,est}$ are expressed in (3.59) and (3.60):

1) Using (3.56) to express i_{qr} in terms of i_{qs} and assuming $V_{qr} = 0$, $\omega_{e,est}$ and $\theta_{e,est}$ are expressed as:

$$\omega_{e,est} = \omega_r + \frac{L_M}{L_{rr}} \frac{r_r}{\lambda_{dr,est}} i_{qs} \tag{3.58}$$

$$\theta_{e,est} = \int \omega_{e,est} dt \tag{3.59}$$

2) Using (3.36) to express the relation between i_{dr} and λ_{dr} and assuming V_{dr} and $\lambda_{qr} = 0$, then, i_{dr} is replaced by λ_{dr} and i_{ds} using (3.40), and $\lambda_{dr,est}$ is expressed by the transfer function below:

$$\lambda_{dr,est} = L_M \frac{i_{ds}}{1 + (L_{rr}/R_r)s} \tag{3.60}$$

FOC is applied to the VSD inverter back-end and directly regulates the IM power supply, so the FOC model can be used to represent the inverter back-end dynamic performance in dq coordinates.

3.2.4 Direct Torque Control

The direct torque control (DTC) is another established control method for regulating T_e [116]. Two types of commonly used DTC are illustrated in Figs. 3.11 and 3.12, 1) DTC with state space vector modulation, and 2) DTC with hysteresis modulation. As illustrated in Fig. 3.12, the stator flux and T_e are firstly estimated based on stator and rotor voltage/current. Furthermore, after comparing the estimated stator flux magnitude and T_e with the corresponding reference value, a table look-up block is provided to generate the inverter switching signals. Meanwhile, sample/hold block is applied to prevent the devices from switching too fast.

The DTC with state space vector modulation is studied and modeled here. It is critical to model v_{ds} and v_{qs} in the load modeling process according to Fig. 3.11 since it determines the IM power supply. The stator flux estimation value $\lambda_{s,est}$, and $T_{e,est}$ are expressed as:

1) The stator flux in the stationary dq coordinates, λ_{qs} and λ_{ds}, are expressed as:

$$\lambda_{qs} = \int (v_{qs} - r_s i_{qs}) dt \tag{3.61}$$

$$\lambda_{ds} = \int (v_{ds} - r_s i_{ds}) dt \tag{3.62}$$

So $\lambda_{s,est}$ and $\theta_{e,est}$ are expressed respectively as:

$$\lambda_{s,est} = \sqrt{\lambda_{qs}^2 + \lambda_{ds}^2} \tag{3.63}$$

$$\theta_{e,est} = \arctan\left(-\frac{\lambda_{ds}}{\lambda_{qs}}\right) \tag{3.64}$$

2) According to (3.61) and (3.62), $T_{e,est}$ expressed by the stator flux and current is written as:

$$T_{e,est} = \frac{3}{2} P(\lambda_{ds} i_{qs} - \lambda_{qs} i_{ds}) \tag{3.65}$$

3.2.5 Constant Slip Current Control

The constant slip current control (CSCC) is similar to the FOC, where the IM is regulated by providing the stator current reference $I_{ds,ref}$ and $I_{qs,ref}$. So a current source based operation is achieved by the inverter-based motor drive in this way. As suggested by the name, the CSCC regulates stator current by adjusting the slip frequency ω_s. Meanwhile, the IM optimal operation can be realized by appropriate ω_s control, which includes both the optimal torque operation and the maximum efficiency operation.

The CSCC control algorithm is illustrated in Fig. 3.13, where T_e command value $T_{e,ref}$ serves as the input of CSCC [116]. A speed regulator can be applied as an outer loop

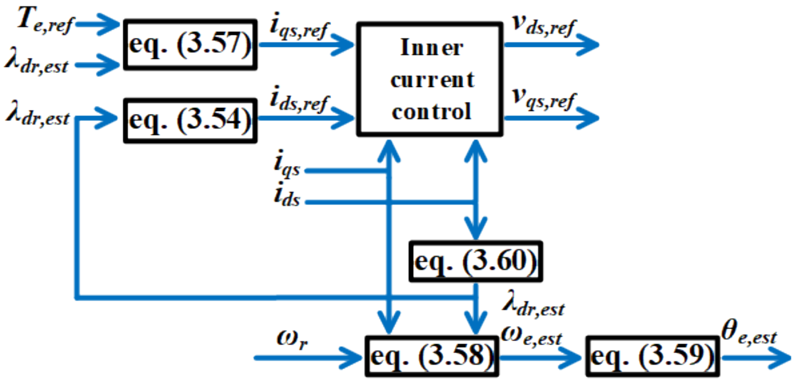

Figure 3.10: Generic rotor flux oriented control.

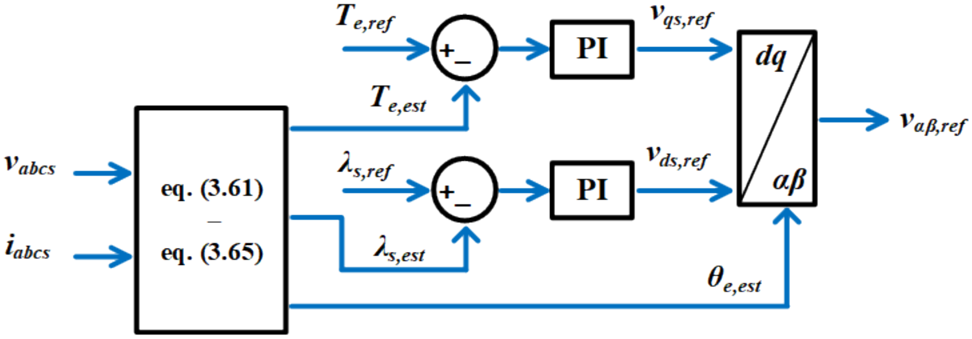

Figure 3.11: DTC with space vector modulation.

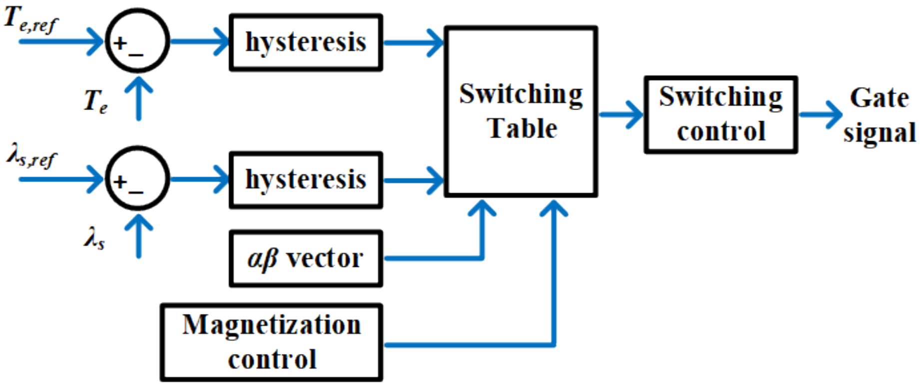

Figure 3.12: DTC with hysteresis modulation [116].

controller to decide $T_{e,ref}$, which will be introduced in the following subsection in detail. ω_s is determined based on requirements of the system optimal operation as mentioned above, and the maximum efficiency operation is selected as the optimal requirement in this section. Therefore, the predefined slip frequency $\omega_{e,set}$ is expressed as:

$$\omega_{s,set} = \frac{r_r}{L_{rr}} \frac{1}{\sqrt{\frac{{L_M}^2}{{L_{rr}}^2} \frac{r_s}{r_r} + 1}} \tag{3.66}$$

After the constant slip frequency $\omega_{e,set}$ is used, the maximum torque that can be reached at such operation mode can be computed considering the maximum rotor flux $\lambda_{r,max}$:

$$T_{e,thresh} = 3P \frac{\omega_{s,set} {\lambda_{r,max}}^2}{r_r} \tag{3.67}$$

where $T_{e,thresh}$ represents the IM threshold torque. If $T_{e,ref} \leq T_{e,thresh}$, the IM can operate at the predefined slip $\omega_{s,set}$ considering optimizing the operating efficiency.

The operation principle illustrated in Fig. 3.13 can be explained as follows: 1) when $T_{e,ref} \leq T_{e,thresh}$, and the rotor flux linkage $\lambda_r \leq \lambda_{r,max}$, ω_s is equal to $\omega_{e,set}$ and yielding the maximum efficiency; 2) when $T_{e,ref} > T_{e,thresh}$, ω_s is regulated to maintain $\lambda_{r,max}$, where now ω_s is driven by $T_{e,ref}$ instead of being a constant $\omega_{e,set}$. ω_s adopted by the motor drive when $T_{e,ref} > T_{e,thresh}$ is expressed in 3.68:

$$\omega_s = \frac{T_{e,ref} r_r}{3P {\lambda_{r,max}}^2} \tag{3.68}$$

With $T_{e,ref}$ and ω_s determined according to the control algorithm as shown in Fig. 3.13, the RMS current command $I_{s,ref}$ is expressed as:

$$I_{s,ref} = \sqrt{\frac{|T_{e,ref}|({r_r}^2 + (\omega_s L_{rr})^2)}{3P|\omega_s| {L_M}^2 r_r}} \tag{3.69}$$

Accordingly, $I_{qs,ref}$ and $I_{ds,ref}$ are expressed respectively based on the computation above:

$$I_{qs,ref} = \sqrt{2} \cdot I_{s,ref} \tag{3.70}$$

$$I_{ds,ref} = 0 \tag{3.71}$$

where $I_{qs,ref}$ equals to $\sqrt{2}I_{s,ref}$, and $I_{ds,ref}$ is regulated as 0, in order to maintain the current RMS command. And the transformation from *dq* coordinates to *abc* coordinates is expressed below:

$$\begin{bmatrix} I_{as,ref} \\ I_{bs,ref} \\ I_{cs,ref} \end{bmatrix} = \begin{bmatrix} cos\theta & -sin\theta \\ cos(\theta - \frac{2\pi}{3}) & -sin(\theta - \frac{2\pi}{3}) \\ cos(\theta + \frac{2\pi}{3}) & -sin(\theta + \frac{2\pi}{3}) \end{bmatrix} \cdot \begin{bmatrix} I_{ds,ref} \\ I_{qs,ref} \end{bmatrix} \tag{3.72}$$

3.2.6 $T_{e,ref}$ Determination Based on Speed Regulation

In Section 3.2.3, 3.2.4 and 3.2.5, the sophisticated closed-loop motor drive controllers are introduced. However, all these presented closed-loop controls provide what is essentially as electromechanical torque transducer, which is expected to effectively provide T_e according to $T_{e,ref}$. In most applications, the motor rotating speed is required to be regulated according to the speed command $\omega_{r,ref}$, instead of directly sending out $T_{e,ref}$ to the motor drive. Therefore, a closed-loop speed control scheme is adopted by all the controllers mentioned above to characterize the practical operation of the motor drive in this chapter, and the control scheme is illustrated in Fig. 3.14.

As shown in Fig. 3.14, $\omega_{r,ref}$ is provided externally, and the PI compensator is used for ω_r closed-loop regulation, which generates $T_{e,ref}$ accordingly. A low-pass filter can be selected to provide a more stabilized ω_r according to the practical requirement of the VSD system.

3.2.7 HTB VSD Emulator Design

The physical configuration and control algorithm of the inverter-based motor drive and IM load have been introduced from Section 3.2.1 to 3.2.6. The modeling and design of

VSD based load emulator are proposed in this subsection according to the VSD operation characteristics mentioned above.

The IM load emulator design is proposed in [66], of which the IM is characterized by (3.25) and from (3.33) to (3.41). Therefore, the IM emulator design will not be introduced in detail in this chapter. The model of the rotating load driven by the motor is determined by T_L characteristics, *e.g.,* the constant torque load, the torque proportional to the square of the speed, etc.

As presented in the above sections, the IM drive rotor speed regulation control is introduced, and the corresponding speed command is achieved by using either an open-loop control scheme such as constant V/f control, or closed-loop control schemes, including FOC, DTC, and CSCC. Based on the above control algorithms, the back-end inverter consisting of fully controlled PE devices is utilized to provide appropriate three-phase stator voltage v_{abcs} to the IM load. The back-end inverter is characterized by the VSC average model for brevity, of which the dynamic performance is characterized by the three-phase modulation index M_a, M_b and M_c. Since the modulation indexes fully characterize the output voltage of the inverter-based motor drive, they are equivalent to the stator voltage v_{sa}, v_{sb} and v_{sc}. Therefore, the inverter-based motor drive is mainly characterized by the corresponding control algorithm. Accordingly, the power emulator modeling procedure of the VSD back-end is illustrated in Fig. 3.15.

As presented above, the model embedded in the power emulator is in a discrete fashion, of which the emulator controller update frequency is decided by the emulator microprocessor. According to Fig. 3.15, the n^{th} computation cycle is illustrated inside of the yellow solid box, and both the inverter and the IM are modeled in the dq coordinates. At each computation cycle, the modeling starts from the VSD inverter back-end with the electrical components modeled from the last computation cycle; then the inverter back-end model provides updated IM stator voltage in dq coordinates, which is notified as v_{sd} and v_{sq}, to the IM and the connected load model [36]. The back-end inverter model includes the motor drive open-loop and closed-loop controller, which can be selected according to the research purpose. Then through the IM model, the updated electrical components, including the stator current i_{sd} and i_{sq}, and the rotor speed ω_{rm}, are stored and used for the next computation cycle.

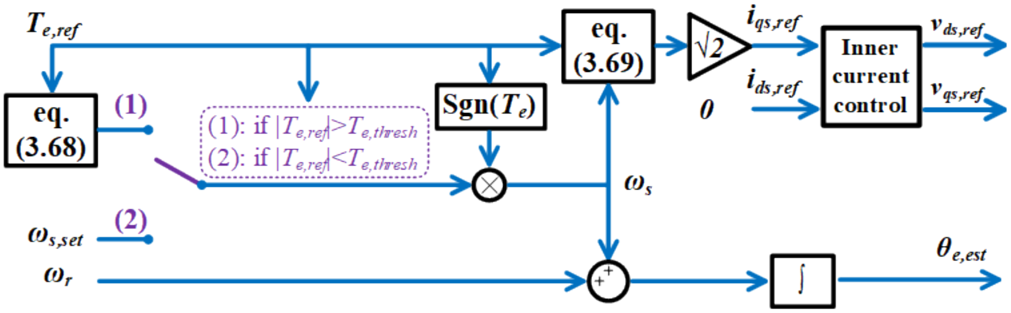

Figure 3.13: Control algorithm of the CSCC [116].

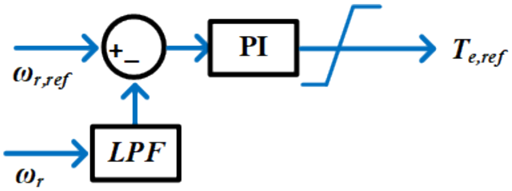

Figure 3.14: ω_r closed-loop control scheme.

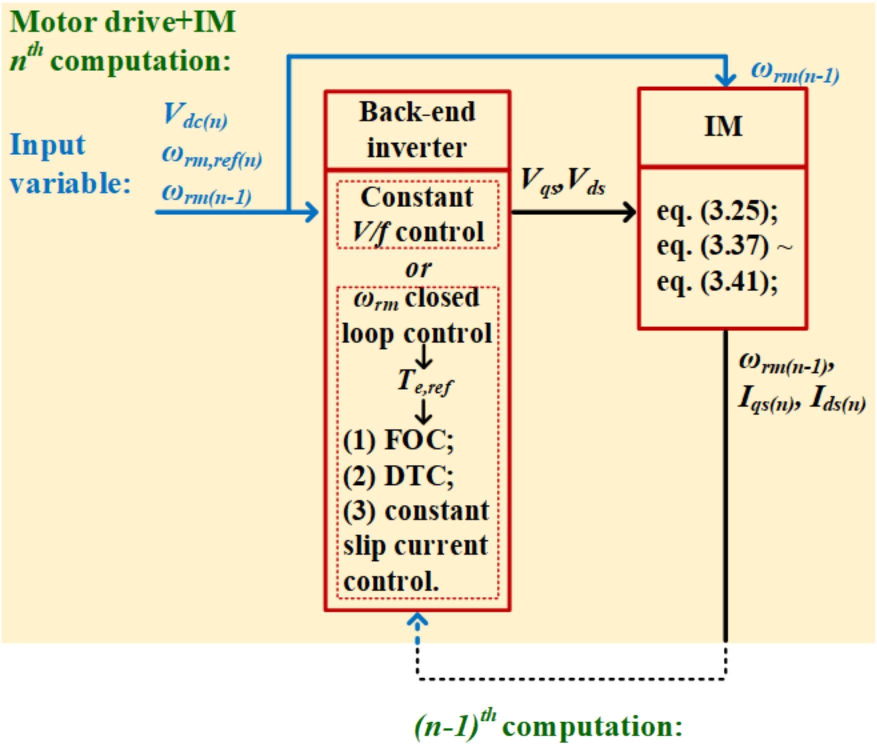

Figure 3.15: Power emulator modeling procedure of VSD back-end inverter and IM load.

The back-end inverter is classified based on the adopted motor control scheme, as shown in Fig. 3.15, since the requirement of open and closed-loop motor drive control are different. For an inverter-based motor drive utilizing closed-loop control, the corresponding n^{th} computation cycle is based on the results of the $(n-1)^{th}$ computation cycle to represent the negative feedback included in the model. In comparison, the n^{th} computational results of the motor drive with open-loop control do not rely on results from the last computation cycle since the open-loop control characterizes the real-time performance of the VSD load without considering previous performances at previous moments.

3.3 VSD Load Model Adopting Closed/Open-loop Control Schemes: Comparison and Simplification

3.3.1 Simplification Considering Passive and Active-Front-End Rectifier Performance Consistency

Detailed models of passive-front-end and active-front-end VSD loads, which can be used for HTB power emulator design, are introduced in Section 3.1.1 and Section 3.1.2, respectively. The corresponding load unit dynamic performance can be accurately reflected if designing the HTB power emulator based on the modeling principle of the detailed VSD load model. Also, the detailed model introduced above is necessary for cases when all presented model variables are required, *e.g.,* the rectifier protection design, the VSC controller design, etc.

However, it is not always practical to include all load model details considering the limited computational capability of the hardware microprocessor. For example, the dynamics of total load power consumption is more of a concern when it comes to the emulation analysis of the transmission-level power network, instead of all aspects of detailed load dynamic characteristics. Therefore, the emulator model simplification should be emphasized accordingly.

The most critical function of the VSD front-end rectifier is to convert the three-phase ac power supply into the constant V_{dc} voltage source for the back-end inverter, instead of deciding the total active power consumption P_{rec}. V_{dc} can be considered as constant considering: 1) the back-end inverter-based motor drive and C_{dc} can serve as an energy buffer, which can stabilize V_{dc}, 2) the inherent front-end rectifier response speed towards the load variation is fast, so V_{dc} is guaranteed to be relatively constant within some certain load power range. Therefore, P_{rec} is decided by the motor load for both passive and active-front-end if assuming that the power loss at the front-end rectifier is not the dominant part in the total P_{rec}.

However, the passive-front-end rectifier performs differently from the active-front-end rectifier when $P_{rec} < 0$, since it only allows for unidirectional power transportation from the power grid to the load. If P_{rec} reaches 0 in passive-front-end rectifiers when the motor is decelerating, the load power cannot be sent to the grid. Instead, the regenerative power charges C_{dc}, and this will result in an increase of V_{dc}. Additionally, the increased V_{dc} will trip the VSD overvoltage protection, which induces the disconnection between the passive-front-end rectifier and the terminal bus. However, this is not expected by the normal grid operation, so the rotor speed variation rate is usually restricted by the slew rate limiter (SRL) to prevent IM regeneration. Therefore, the dynamic performance of active-front-end and passive-front-end rectifiers can be regarded as consistent, assuming that the VSD load operation will not be interrupted by regenerative operation. Based on this consistency in the dynamic performance between the passive and active-front-end, the VSD load model with different front-end rectifiers can be further simplified considering that either rectifier can be regarded as a power transducer, assuming that: 1) the main research purpose is concentrated on evaluating the load power consumption instead of other load dynamic characteristics, 2) no significant terminal voltage variations will occur, which may activate the relay to protect the front-end rectifier. More details and numerical examples about the simplification based on performance consistency will be introduced below.

The passive and active-front-end rectifier can both be represented as a power transducer if not operating in regeneration mode. So we can specify the operation range where IM regeneration will not occur. As for the IM, the electric power P_e consumed by the load and the rotor speed ω_r are related in p.u. system as:

$$P_e = T_L \omega_r + 2H\omega_r \frac{d\omega_r}{dt} \tag{3.73}$$

where T_L represents the load torque, and H represents the IM inertia constant. T_L model is expressed according to the specific load characteristics. Here we use the fan/pump load to represent the load characteristics, which is expressed as $T_L = {\omega_r}^2$. More information about the IM mathematical expression will be introduced in the next section.

As explained above, P_e is required to be > 0 in the specified operation range, so (3.73) can be rewritten as:

$$\frac{d\omega_r}{dt} > -\frac{{\omega_r}^2}{2H} \tag{3.74}$$

So the absolute value of motor deceleration rate should be smaller than $\frac{{\omega_{r,min}}^2}{2H}$, where $\omega_{r,min}$ represents the minimum rotor speed during the operation. In conclusion, if adjusting the motor deceleration rate within this region, the dynamic performance of the passive-front-end VSD and active-front-end VSD can be regarded as a simple power transducer, which will significantly simplify the HTB emulator model.

The example below illustrates the VSD load performance with passive-front-end and active-front-end in terms of different rotor speed deceleration rates. Here in this example, rotor speed reference $\omega_{r,ref}$ decreases from 0.7 p.u. to 0.664 p.u., which is illustrated in Fig. 3.16. The inertia constant of the motor is $H = 3$ s.

As explained above, large deceleration rate makes the motor enter regenerative mode, which should be avoided considering grid support applications. According to (3.74) and the motor speed deceleration example case which is illustrated in Fig. 3.16, three different deceleration rates $\frac{d\omega_{r,ref}}{dt}$ are adopted to show the corresponding impact on the passive/active-front-end VSD load performance. Example cases are simulated in PSCAD$^{\text{TM}}$/EMTDC and illustrated in Fig. 3.17.

In Fig. 3.17a, $\omega_{r,ref}$ deceleration rate is determined by $\omega_r = 0.7$ p.u., yielding $\frac{d\omega_{r,ref}}{dt} =$ 0.0817 p.u./s according to (3.74). Since $\omega_r = 0.7$ is the motor maximum rotating speed during deceleration, the motor load will enter regenerative mode. Therefore, a significant

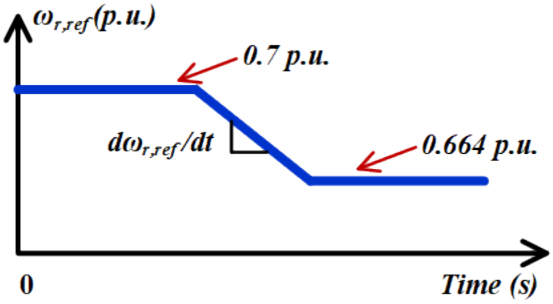

Figure 3.16: Motor rotating speed reference $\omega_{r,ref}$ variation.

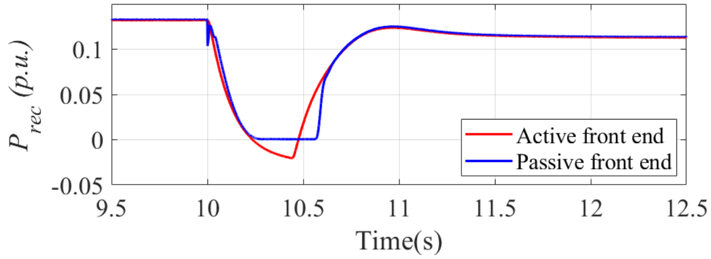

(a) $\frac{d\omega_{r,ref}}{dt} = 0.0817$ p.u./s .

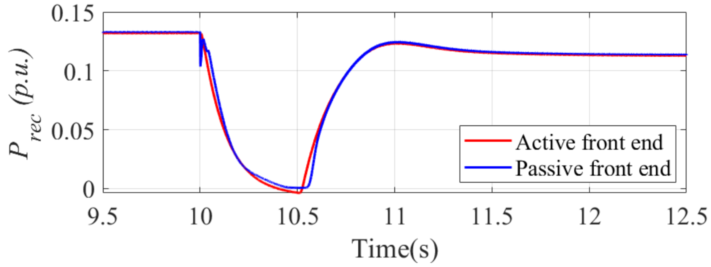

(b) $\frac{d\omega_{r,ref}}{dt} = 0.0704$ p.u./s.

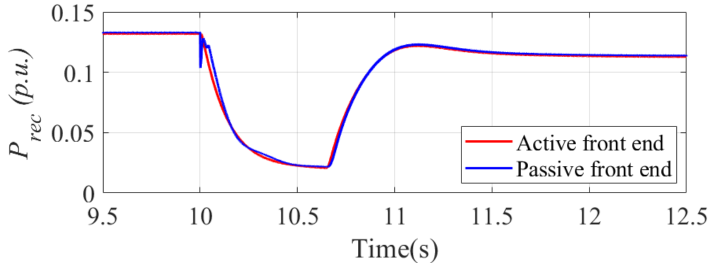

(c) $\frac{d\omega_{r,ref}}{dt} = 0.0554$ p.u./s.

Figure 3.17: Active/passive-front-end VSD load P_{rec} under different deceleration rate.

divergence in P_{rec} between active and passive-front-end VSD load is observed in Fig. 3.17a: during the regeneration process, the passive-front-end VSD load P_{rec} is 0 and the load is disconnected from the power network, while the active-front-end VSD load can transfer the regenerative power back to the grid.

In Fig. 3.17c, $\omega_{r,ref}$ deceleration rate is determined by $\omega_r = 0.57$ p.u., which is lower than the motor minimum rotating speed by about 10%. The corresponding deceleration speed is $\frac{d\omega_{r,ref}}{dt} = 0.0554$ p.u./s. P_{rec} for the active and passive-front-end VSD load are almost identical since the regeneration process is avoided when adopting the smaller deceleration rate.

In Fig. 3.17b, $\omega_{r,ref}$ deceleration rate is determined by $\omega_r = 0.65$ p.u., which is the minimum motor speed during deceleration process. So the corresponding deceleration speed is $\frac{d\omega_{r,ref}}{dt} = 0.0704$ p.u./s. Observing simulation results in Fig. 3.17b, the motor regeneration is almost avoided except the period between 10.45 s and 10.55 s. This is because the $\frac{d\omega_r}{dt}$ cannot fully follow the $\frac{d\omega_{r,ref}}{dt}$, and the absolute value of the real $\frac{d\omega_r}{dt}$ is slightly higher than the reference value, making the motor mode enter the regenerative mode temporarily.

According to the simulation results shown above, the relation between $\frac{d\omega_{r,ref}}{dt}$ and motor regeneration almost follows the (3.74), except for the speed region which is very close to the minimum ω_r. So equation (3.74) can also be used as the criteria for designing the motor drive SRL. Therefore, if the rotor deceleration rate is limited based on the criteria above, the motor regeneration will not happen, then it is of little difference between the passive and active-front-end rectifier dynamic model.

3.3.2 VSD Load Simplified Model with Closed-loop Control

As introduced in the previous sections, the back-end inverter can achieve rotating speed closed-loop control if utilizing the FOC, DTC and CSCC. Meanwhile, motor drives adopting the above closed-loop control schemes demonstrate similar dynamic characteristics if employing identical rotor speed controllers.

These three closed-loop controllers are developed based on the basic operating principle of the IM. So the similarities between these controllers are significant. For example, the DTC is regarded as the simplified version of FOC. According to Fig. 3.10 and Fig. 3.11, both the

DTC and FOC can be attributed as vector control. As for FOC, the q-axis controller is to regulate T_e which drives the IM load to accelerate and decelerate, while the d-axis is to maintain a suitable rotor flux linkage. The DTC used here is similar to FOC except that the d-axis controller regulates the stator flux linkage to avoid saturation. Additionally, the FOC provides the stator current reference, $i_{sq,ref}$ and $i_{sd,ref}$, to the inverter-based motor drive. Usually, the inverter generates the gate signals through an inner current control loop, or a hysteresis current loop. However, the DTC directly provides the stator voltage reference, skipping the process of generating $i_{qs,ref}$ and $i_{ds,ref}$. So, the inverter switching signals are generated through the space vector pulse-width modulation (SVPWM) according to the requirement of the DTC.

CSCC is similar to FOC in terms of producing $i_{qs,ref}$ and $i_{ds,ref}$ to drive the VSD back-end rectifier. Additionally, differences between these two control schemes are: 1) λ_r is regulated indirectly based on the IM electrical relation if utilizing the CSCC, while λ_r is regulated by adjusting $i_{sd,ref}$ if utilizing FOC; 2) the CSCC only determines the magnitude of the stator current RMS value, while both $i_{sq,ref}$ and $i_{sd,ref}$ are determined if using vector control.

Comparing the closed-loop controllers mentioned above, it can be concluded that T_e is achieved by regulating the electrical reference of the back-end inverter, which includes $v_{dqs,ref}$ or $i_{dqs,ref}$, and the difference is in how these references are generated. Therefore, the VSD load model adopting different motor control schemes can be simplified as an identical format based on the following considerations:

- The front-end rectifier provides a stable dc-link voltage which guarantees the normal operation of the following power stages. The extreme ac terminal voltage condition (excessive overvoltage/undervoltage) is not of consideration.

- The motor drive controller inner regulation loops, including the inner current loop in FOC and CSCC, and T_e/λ_s regulation loop, have a high control bandwidth compared with the outer speed regulation loop, so the dynamic performance of these processes can be simplified compared with the relatively slow-response process.

- The motor load reactive power consumption is decoupled by the dc-link capacitor at the front-end rectifier, so the IM reactive power consumption model can be removed from the VSD model.
- The VSD load provides a relatively constant operating efficiency η over a wide operation range. So, the total VSD power consumption is considered to be proportional to the rotating load power consumption [117, 118].

According to these conditions stated above, the process of transferring $T_{e,ref}$ to T_e can be simplified as a time delay process for the three closed-loop control algorithms studied above considering the rapid response of the inner control loop and the corresponding modulation process, while the dynamic model of the speed regulation loop is maintained in the simplified model to provide $T_{e,ref}$. Also, considering the IM dynamic equations, only the q-axis is related to reflecting the IM active power dynamic performance. Therefore, the simplified model of VSD load in p.u. system is illustrated in Fig. 3.18.

The IM and the connected load are included in this simplified model. The total VSD active power consumption $P_{VSD,pu}$ in p.u. system is not related to the front-end rectifier since we assume a normal operating condition here, as introduced in Section 3.3.1. Therefore, $P_{VSD,pu}$ is proportional to the IM consumption $P_{e,pu}$ with coefficient η_{VSD}. T_L indicates the load torque, which is determined by the dynamic characteristics of the rotating load connected to the IM.

3.3.3 VSD Load Simplified Model with Open-loop Control

The open-loop control is also referred to as constant V/f control, which is explained in detail in 3.2.2. Compared with the closed-loop motor speed control, a motor drive with an open-loop control scheme regulates the IM ω_r by adjusting the stator voltage magnitude and electrical angular frequency according to the control algorithm illustrated in Fig. 3.7 and Fig. 3.8. Without the negative feedback loop, T_e can be expressed by $\omega_{m,ref}$ according to the static operating principle in (3.42) based on the assumption that the motor drive has a much faster response compared with the dynamics of the IM rotating process.

Accordingly, the relation between T_e and $\omega_{m,ref}$ is expressed in (3.75), and the simplified VSD model with open-loop control is illustrated in Fig. 3.19.

$$T_e = \frac{{X_M}^2 r_r \frac{\omega_{e,ref}-\omega_r}{\omega_{e,ref}} \frac{\omega_{e,ref}}{\omega_b}^3}{\left[r_s r_r + \frac{\omega_{e,ref}-\omega_r}{\omega_{e,ref}} (\frac{\omega_{e,ref}}{\omega_b})^2 ({X_M}^2 - X_{ss} X_{rr})\right]^2 + (\frac{\omega_{e,ref}}{\omega_b})^2 (r_r X_{ss} + \frac{\omega_{e,ref}-\omega_r}{\omega_{e,ref}} r_s X_{rr})^2} \tag{3.75}$$

3.3.4 Simulation Studies: VSD Load Simplified Model Verification

The verification of VSD simplified model adopting closed/open-loop control scheme will be illustrated in this section. Two operation transient cases are provided to verify the load model dynamic performance, which are illustrated in Fig. 3.20. Case 1 is to reflect the VSD load dynamics when subject to T_L variation, where T_L ramps down from 200 Nm to 150 Nm during 3.5 s to 5.5 s, while $\omega_{r,ref} = 150$ rad/s. T_L variation process is illustrated in Fig. 3.20a. Case 2 reflects the VSD load dynamics when subject to $\omega_{r,ref}$ variation, where $\omega_{r,ref}$ ramps up from 120 rad/s to 160 rad/s during 3.5 to 5.5 s, while $T_L = 200$ Nm. $\omega_{r,ref}$ variation process is illustrated in Fig. 3.20b.

The closed-loop VSD load dynamic performance consistency is first verified by simulation studies in MATLAB/Simulink®. As mentioned in the sections above, motor drives adopting closed-loop control schemes, including FOC, DTC and CSCC, demonstrate similar dynamic characteristics if adopting identical rotor speed controllers. This is also the basis of developing the VSD load simplified model. So the IM rotor speed controller for VSD models is selected following the control scheme shown in Fig. 3.14 with identical control parameters.

The comparison of the VSD model with different control schemes is introduced below. The detailed VSD model with closed-loop controllers introduced above is developed in Simulink. VSD model parameters are listed in Appendix A. Comparison results of Case 1 and Case 2 mentioned above are illustrated in Fig. 3.21 and Fig. 3.22 respectively. The VSD load ω_r, T_e and P_{VSD} are recorded and compared among detailed models with different control schemes. It can be observed that the rotor speed, torque, and active power consumption dynamics are almost identical for these three VSD load models in both cases. These

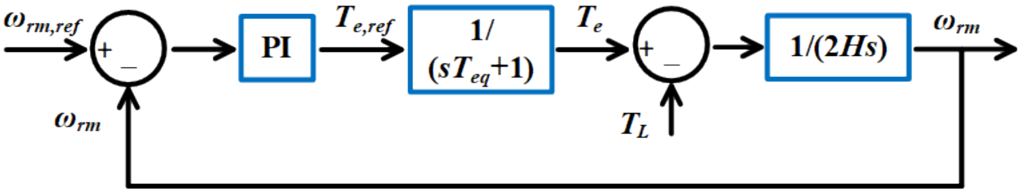

Figure 3.18: VSD simplified model utilizing closed-loop control.

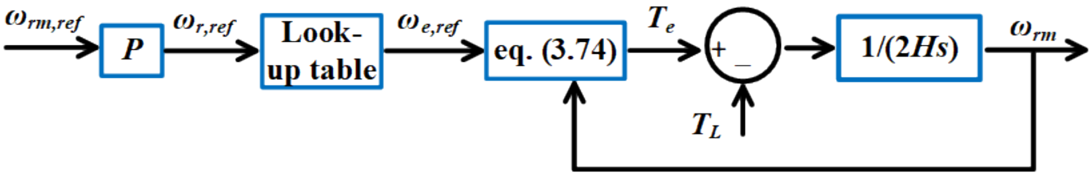

Figure 3.19: VSD simplified model utilizing open-loop control.

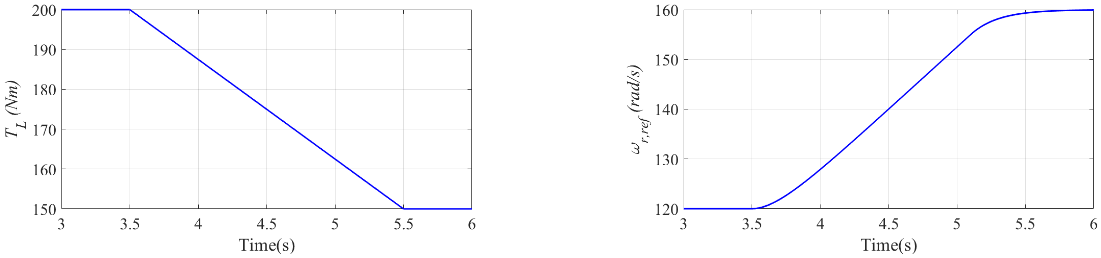

(a) Load torque T_L variation.

(b) Rotor speed reference $\omega_{r,ref}$ variation.

Figure 3.20: Two operation transient cases to verify the load model dynamic.

simulation results verify that VSD loads will demonstrate an almost identical performance when subject to external transients with different closed-loop schemes if adopting an identical ω_r controller.

The comparison between the simplified and detailed VSD load models is discussed below. The VSD load simplified models are proposed in Fig. 3.18 and Fig. 3.19, and the detailed VSD load model are introduced in Section 3.2.2 to Section 3.2.5. Simulation models of detailed and simplified VSD load are developed according to the modeling algorithm introduced above. The VSD load adopting the closed-loop controller has identical dynamic performance as discussed above, so the VSD load with FOC is selected as the benchmark model to compare with the simplified closed-loop VSD model. The comparison simulation results for Case 1 are illustrated in Fig. 3.23, where red curves represent the dynamic performance of the detailed VSD load model, and blue curves represent the simplified VSD load model.

As observed from Fig. 3.23, the simulation results of detailed and simplified model represent a good agreement with each other for the IM ω_r and T_e, which reflects the proposed closed-loop VSD simplified model can accurately reflect the motor rotating dynamic performance. The total active power P_{VSD} should have shown a mismatch between the detailed model and simplified model. This is because the detailed model P_{VSD} includes the power loss of the IM, the back-end inverter, and the front-end rectifier. In contrast, the simplified model does not contain the model of these processes. P_{VSD} only represents the IM electromagnetic power. However, the VSD efficiency η is relatively constant during a wide operation range as introduced above, so the simplified model P_{VSD} can be estimated with a predefined η to make the corresponding power consumption closer to the value computed by the detailed model. P_{VSD} illustrated in Fig. 3.23 has applied an estimated η to the original simplified model, so the power consumption values from the detailed and simplified model are very close in Fig. 3.23c. In Fig. 3.23 and Fig. 3.24, $\eta = 93.5\%$, and in Fig. 3.25 and Fig. 3.26, $\eta = 92.6\%$.

The dynamic performance comparison between the closed-loop VSD detailed model and simplified model for Case 2 is illustrated in Fig. 3.24. A close agreement between these two models can be observed in ω_r and T_e, and P_{VSD}. These phenomenons are similar to what is shown in Fig. 3.23.

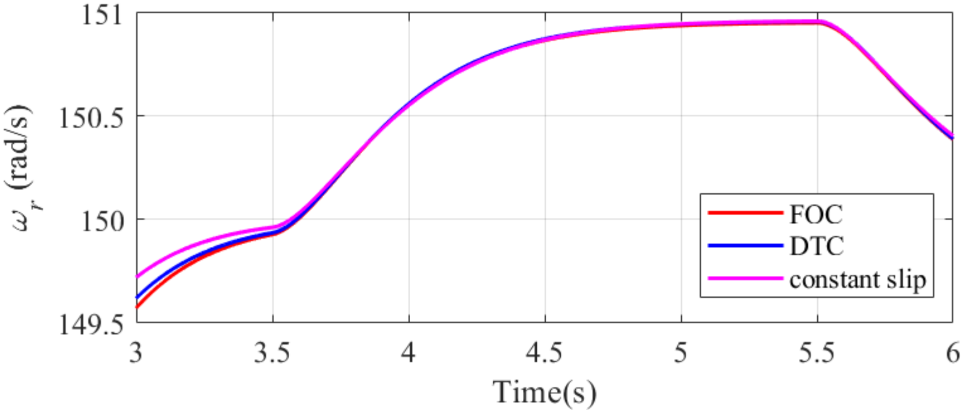

(a) ω_r in Case 1.

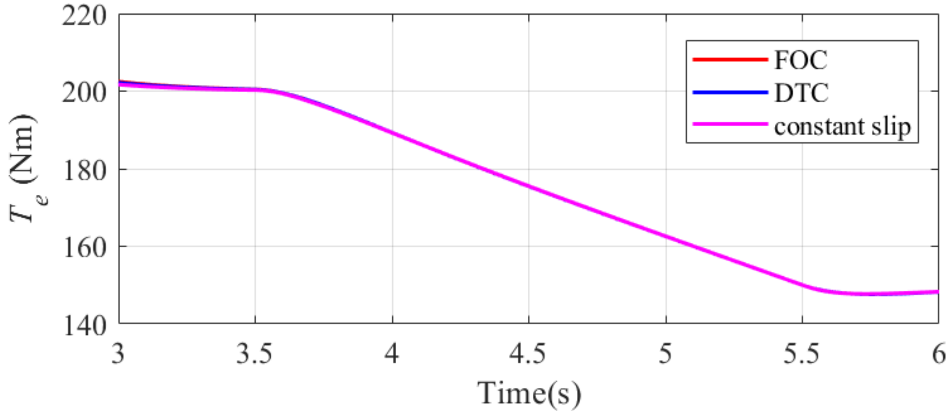

(b) T_e in Case 1.

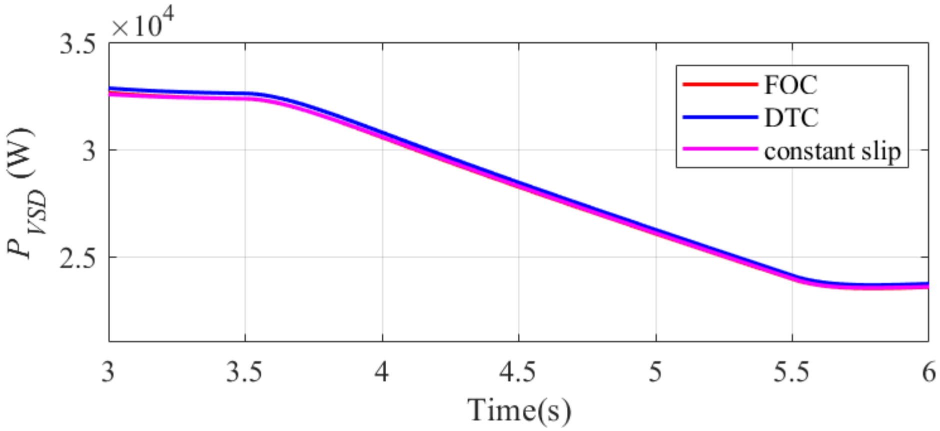

(c) P_{VSD} in Case 1.

Figure 3.21: Detailed VSD model reflecting the load dynamics in Case 1.

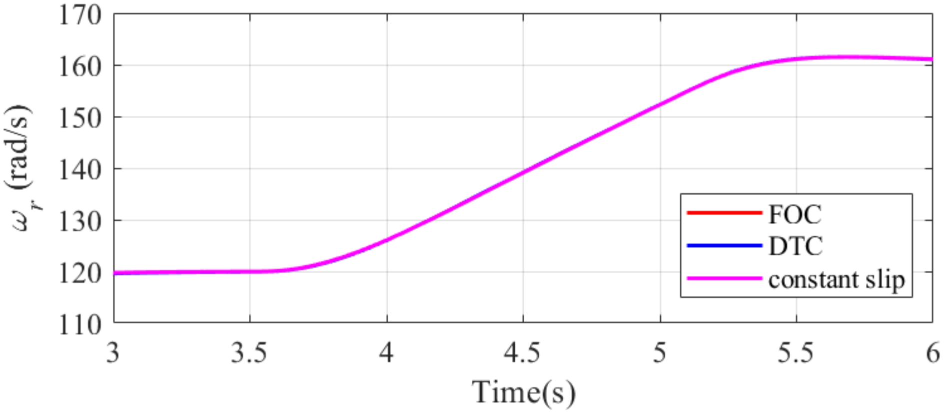

(a) ω_r in Case 2.

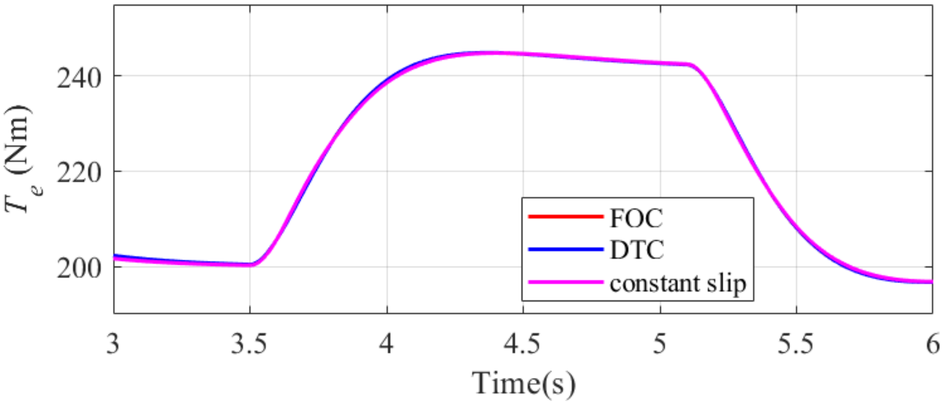

(b) T_e in Case 2.

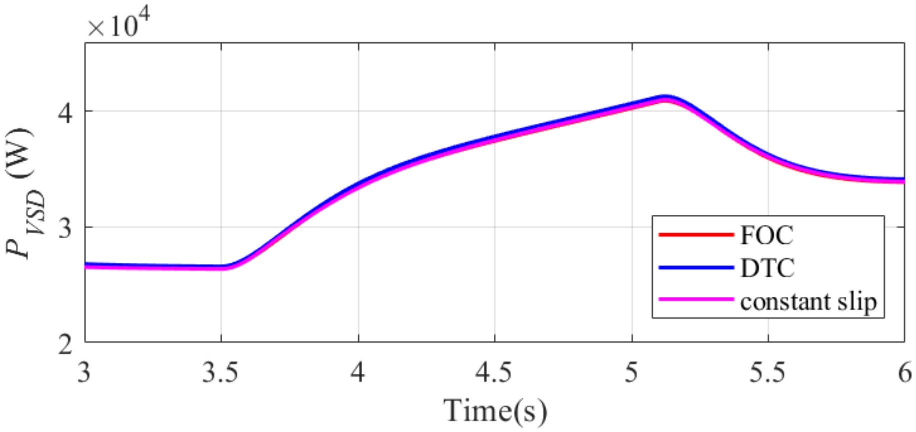

(c) P_{VSD} in Case 2.

Figure 3.22: Detailed VSD model reflecting the load dynamics in Case 2.

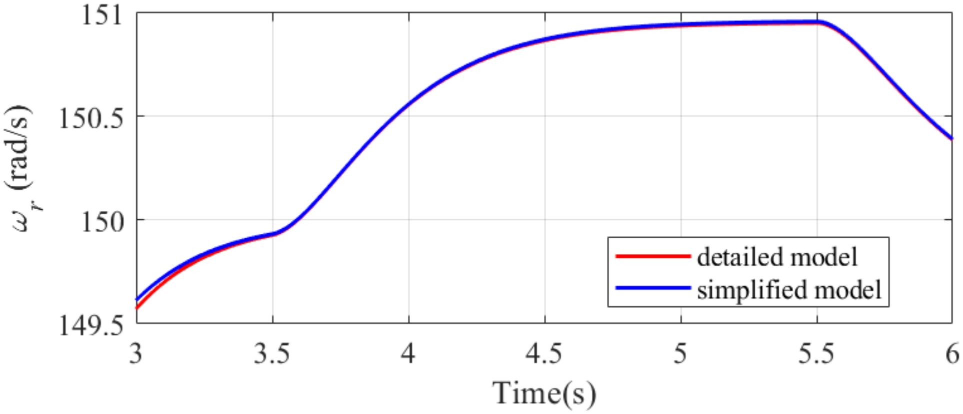

(a) ω_r in Case 1.

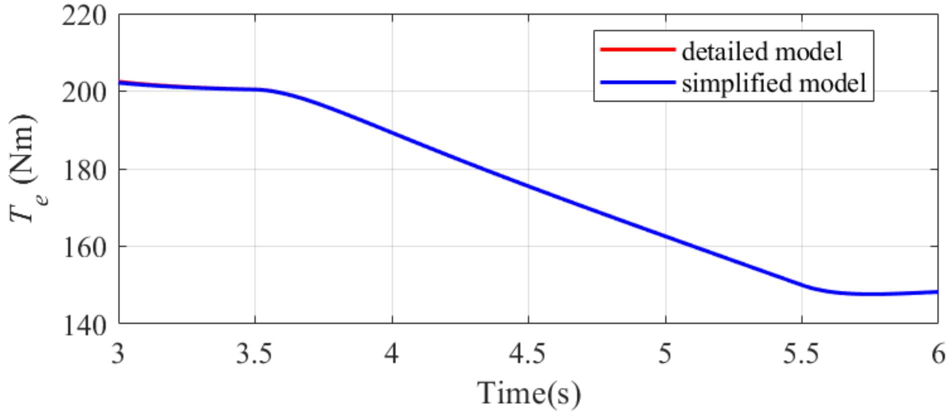

(b) T_e in Case 1.

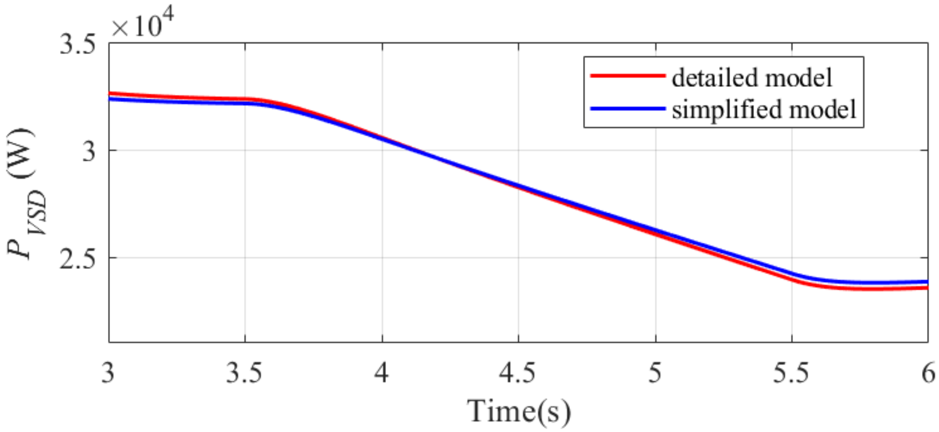

(c) P_{VSD} in Case 1.

Figure 3.23: Load dynamics in Case 1: Detailed VSD model vs. simplified VSD model with closed-loop controller.

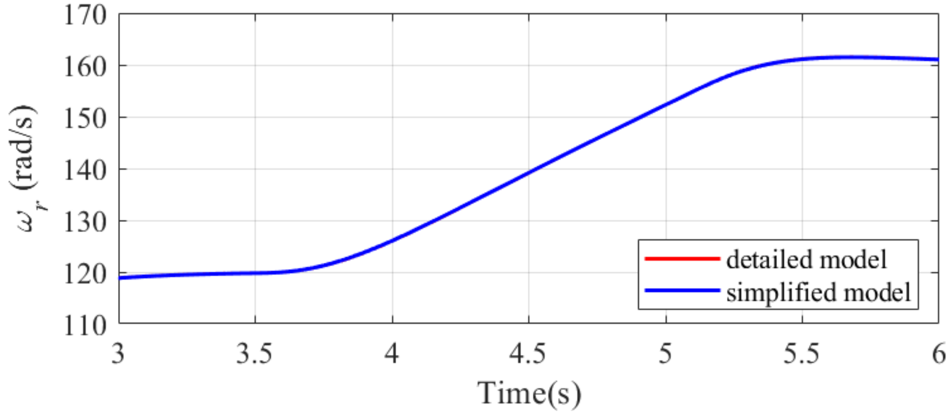

(a) ω_r in Case 2.

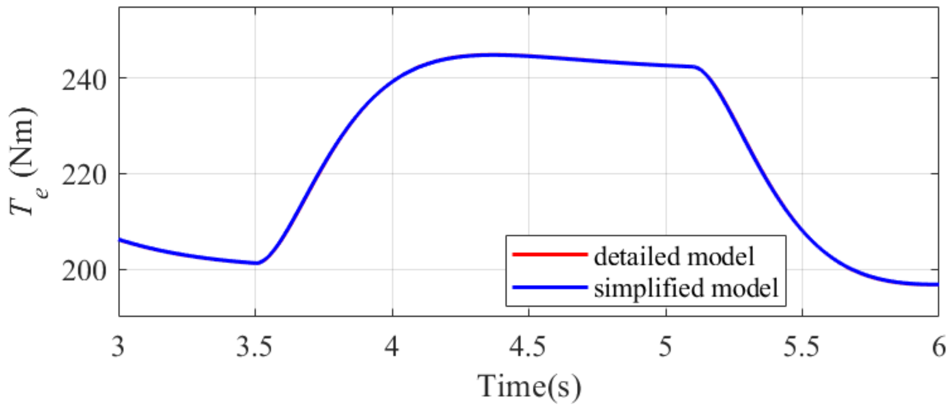

(b) T_e in Case 2.

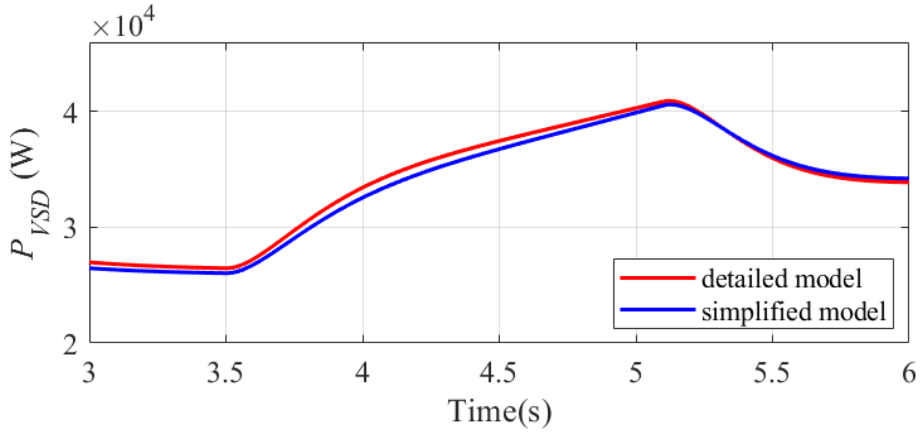

(c) P_{VSD} in Case 2.

Figure 3.24: Load dynamics in Case 2: Detailed VSD model vs. simplified VSD model with closed-loop controller.

The open-loop VSD load detailed model and simplified model are simulated and compared in Fig. 3.25 and Fig. 3.26, following the dynamic cases illustrated in Fig. 3.20. The simplified model shows a close agreement with the detailed benchmark model.

Therefore, it is verified that the simplified model is efficient and accurate in terms of representing the VSD load dynamic performance and its active power consumption according to simulation results illustrated above. Therefore, the VSD load simplified model keeps a balance between accuracy and simplicity.

3.4 VSD Load Emulator Verification Experiments

The VSD detailed model and simplified model adopting various control schemes are proposed in the previous sections. Aside from the fast switching dynamics, the VSD detailed model can reflect the load dynamic performance in several aspects, including the dynamics of the passive electrical components, the control scheme adopted by the front-end rectifier and back-end inverter, the IM electrical and mechanical dynamic performance, etc. Therefore, the HTB load emulator adopting the VSD detailed model is suitable for the emulation application where all the above load dynamics are included, *e.g.,* the VSD overload protection design, the VSD control scheme design, etc.

In comparison, the simplified VSD load model focuses on representing its active power consumption based on the motor ω_r dynamic performance. The front-end rectifier, back-end inverter and equivalent electrical representation of IM are simplified as a time delay process. So the VSD simplified model is suitable for the emulation application where only the VSD load power consumption is emphasized.

The accuracy verification results of the HTB emulator are presented in this section. The HTB power emulator is developed based on the modeling procedure illustrated in Fig. 3.15. The VSD load created by function modules provided in the Simulink library is used as the benchmark model to compare with the experimental results of the developed VSD load power emulator. Meanwhile, the consistency of the active-front-end VSD and passive-front-end VSD dynamic performance has been presented in Section 3.3.1, so only the active-front-end VSD model is adopted for model verification in this section.

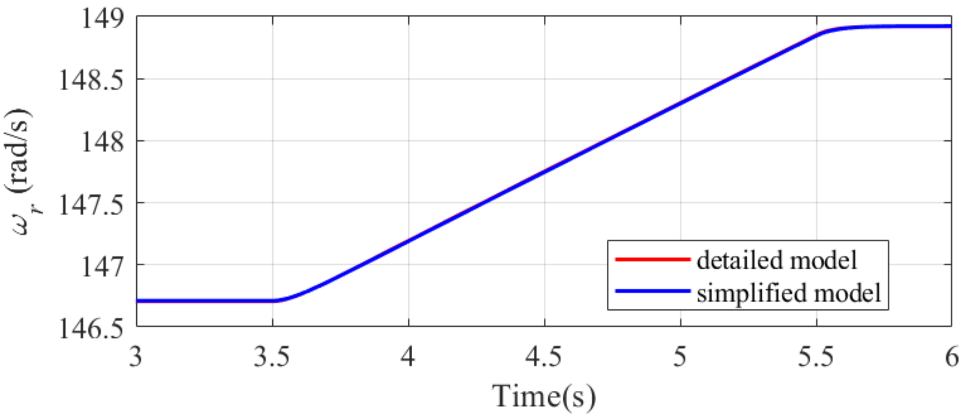

(a) ω_r in Case 1.

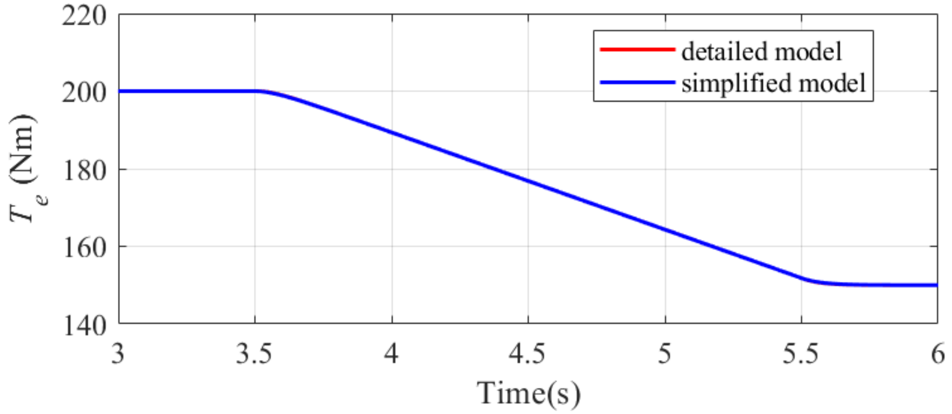

(b) T_e in Case 1.

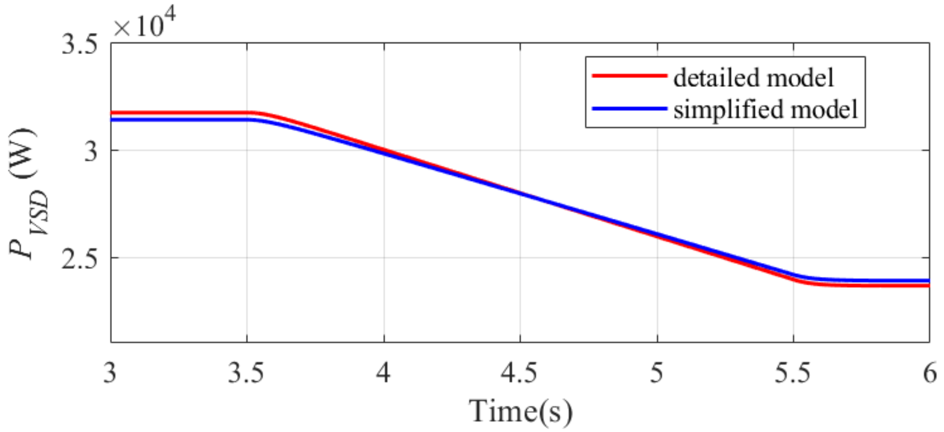

(c) P_{VSD} in Case 1.

Figure 3.25: Load dynamics in Case 1: Detailed VSD model vs. simplified VSD model with open-loop controller.

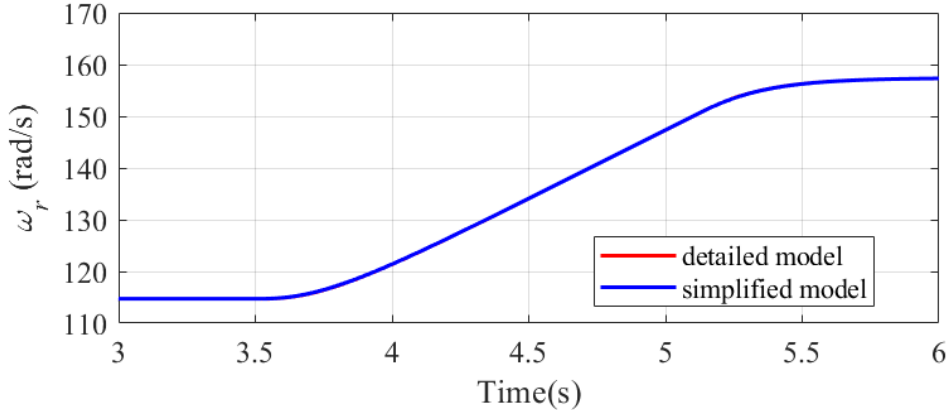

(a) ω_r in Case 2.

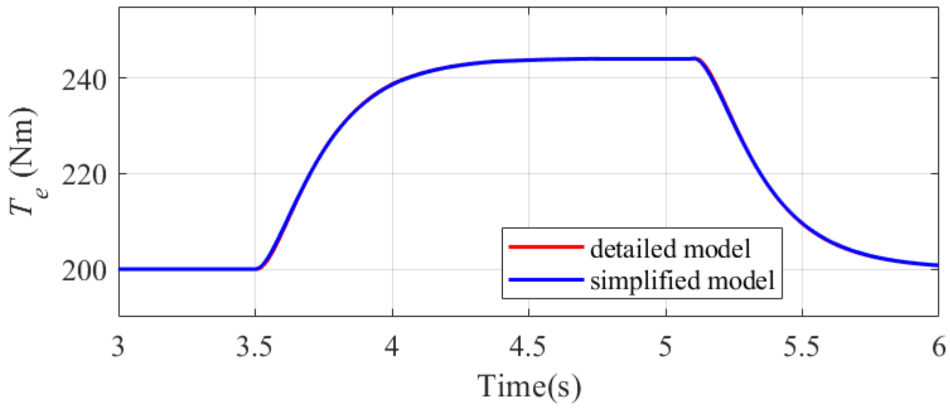

(b) T_e in Case 2.

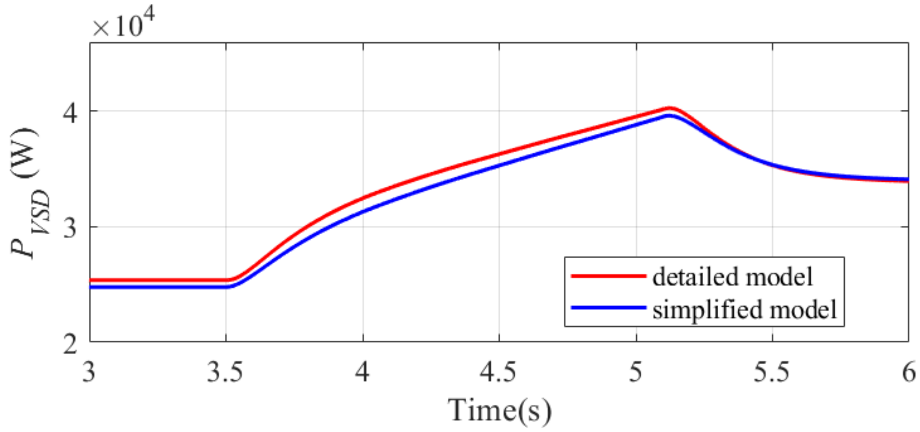

(c) P_{VSD} in Case 2.

Figure 3.26: Load dynamics in Case 2: Detailed VSD model vs. simplified VSD model with open-loop controller.

According to the introduction above, the VSD load can be classified based on the speed controllers adopted by the back-end inverter, which include: 1) VSD load with open-loop ω_r controller, 2) VSD load with closed-loop ω_r controller. In this section, the detailed and simplified VSD load model with open and closed control loops are adapted into the HTB emulator. The model verification results are illustrated and explained in detail in the following subsections.

3.4.1 Detailed Model Verification: VSD load with Open-loop controller

Two operation transient cases are provided to verify the load model dynamic performance. In Case 1, T_L ramps down from 200 Nm to 150 Nm during 3.5 s to 5.5 s, while $\omega_{r,ref}$ = 150 rad/s. In Case 2, $\omega_{r,ref}$ ramps up from 120 rad/s to 160 rad/s during 3.5 to 5.5 s, while T_L = 200 Nm.

In this subsection, the detailed VSD load model is adapted to the HTB emulator, and the elementary constant V/f controller is selected as open-loop ω_r controller, which is illustrated in Fig. 3.7. The dynamic performance of VSD load with the corresponding open-loop controller is represented by ω_r, T_e, and P_{VSD} respectively. Experimental results of Case 1 and Case 2 are shown in Fig. 3.27. The HTB experimental results are illustrated by red curves, while benchmark model simulation results are illustrated by blue curves. According to comparison results, the emulated ω_r, T_e, and P_{VSD} have a close match with the counterparts measured from the benchmark simulation, so the emulated VSD load model can accurately reflect corresponding dynamic performances.

3.4.2 Detailed Model Verification: VSD load with closed-loop controller

As introduced in the above sections, the VSD closed-loop controllers selected for modeling include FOC, DTC, and CSCC. Dynamic performances of detailed VSD load models adopting the above controllers when subjected to Case 1 and Case 2 are illustrated in Fig. 3.28, Fig. 3.29 and Fig. 3.30. According to the comparison between the simulation

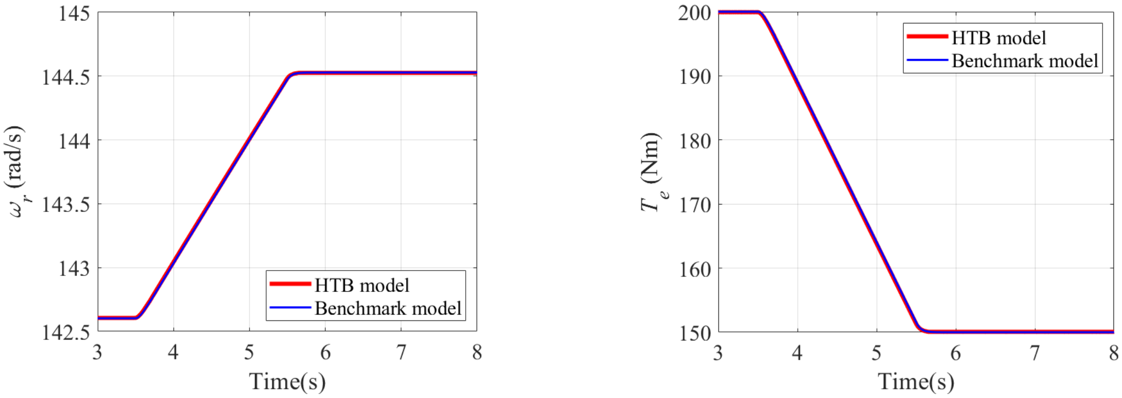

(a) ω_r in Case 1. (b) T_e in Case 1.

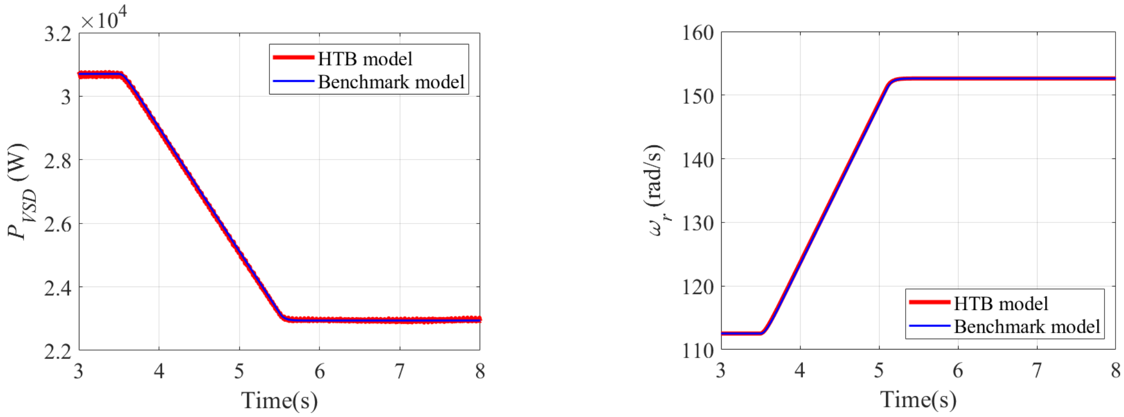

(c) P_{VSD} in Case 1. (d) ω_r in Case 2.

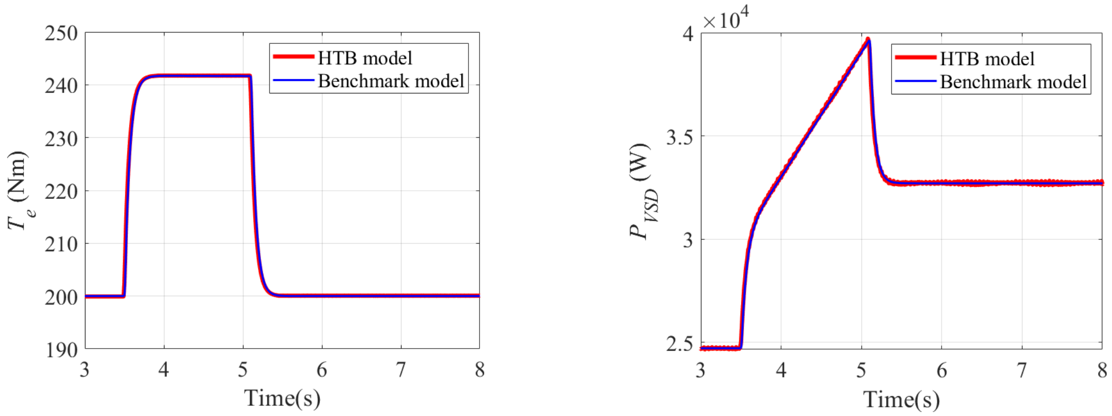

(e) T_e in Case 2. (f) P_{VSD} in Case 2.

Figure 3.27: Detailed VSD load with elementary constant V/f: HTB emulator experimental results vs. benchmark model simulation results.

and experimental results, the emulated VSD load electrical variables have a close match with those measured from the benchmark simulation. Thus the accuracy of the detailed VSD load HTB emulators is verified.

3.4.3 Simplified Model Verification

The simplified VSD load model is proposed in Section 3.3.4, including VSD load with the open and closed-loop controller. Both the above two types of simplified VSD load models are adapted to the HTB emulator, and the comparison between the power emulator experimental results and the benchmark model simulation results are presented in Fig. 3.31 and Fig. 3.32 respectively.

Similar to detailed VSD load HTB emulator verification results, the emulator adopting a simplified VSD load model can also accurately reflect the VSD dynamic performance, of which the experimental results are almost identical to that of the benchmark model simulation results. The consistency between the VSD load detailed model and simplified model has already been explained in Section 3.3.4, so the simplified VSD load power emulator is suitable for being used in the large-scale power network experiments.

3.4.4 Model Accuracy Estimation

To evaluate the accuracy of the VSD load HTB power emulator presented above, normalized root mean square error (NRMSE) is adopted to quantitatively represent how accurate the emulator models are, which is expressed as [119]:

$$NRMSE = \frac{1}{\bar{y}} \cdot \sqrt{\frac{\sum_{i=1}^{n}(y_i - \hat{y})^2}{n}} \tag{3.76}$$

where y_i is the i^{th} observation of y, $\hat{y}$ is the predicted y value given by the model, and $\bar{y}$ is the mean value of y.

Benchmark models developed in Simulink are used as the model benchmark, and power emulator experimental results are evaluated according to the benchmark model reference. The VSD load models with both the open and closed-loop control schemes in detailed and

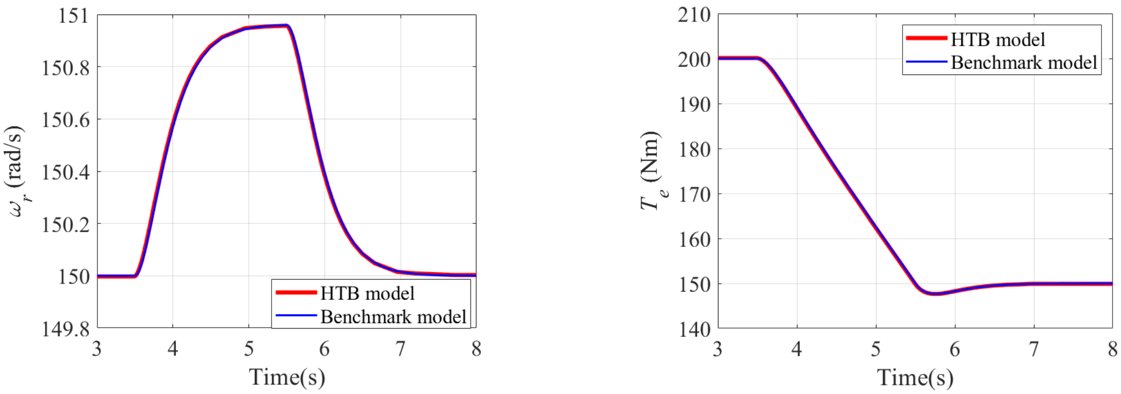

(a) ω_r in Case 1.

(b) T_e in Case 1.

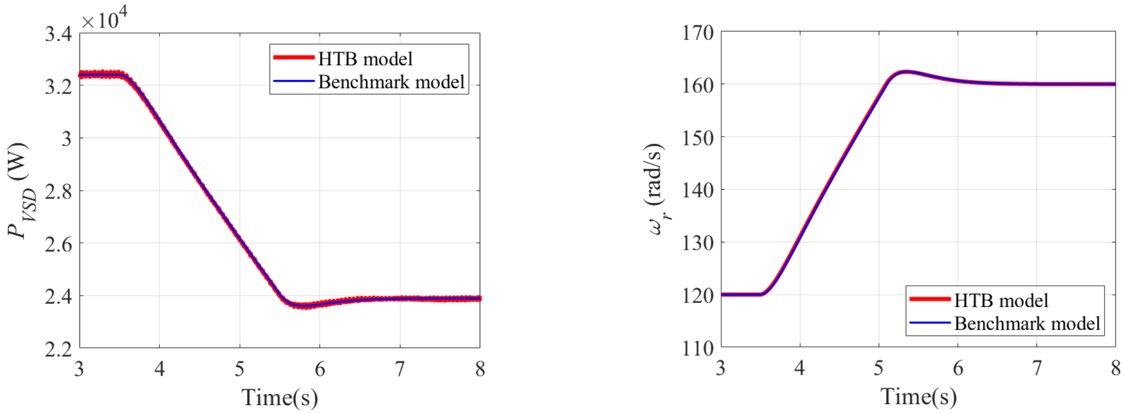

(c) P_{VSD} in Case 1.

(d) ω_r in Case 2.

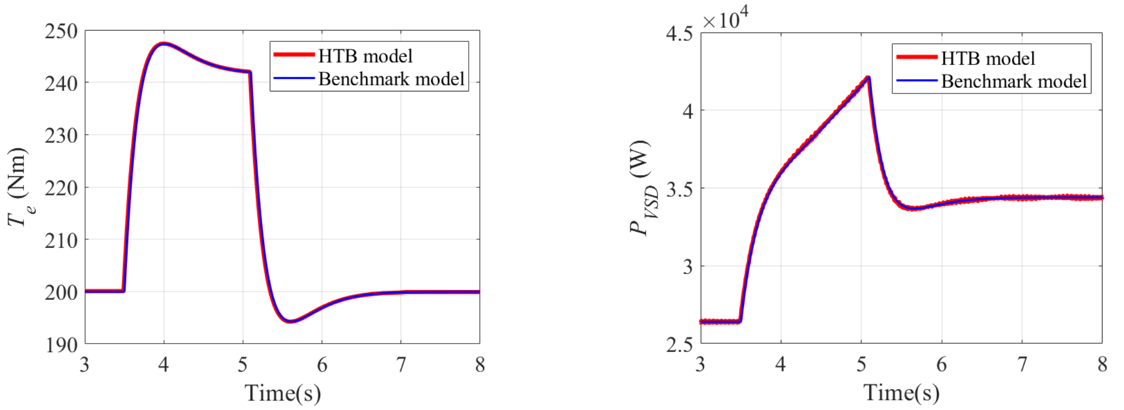

(e) T_e in Case 2.

(f) P_{VSD} in Case 2.

Figure 3.28: Detailed VSD load with FOC: HTB emulator experimental results vs. benchmark model simulation results.

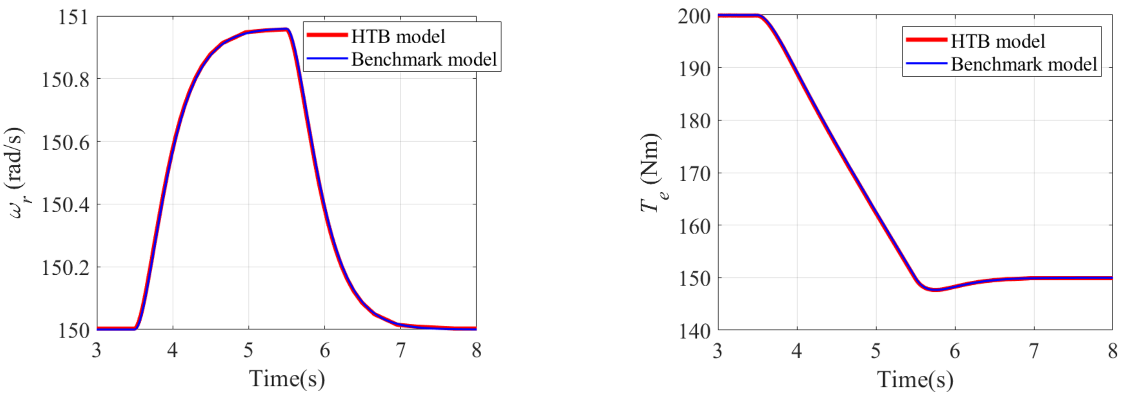

(a) ω_r in Case 1. (b) T_e in Case 1.

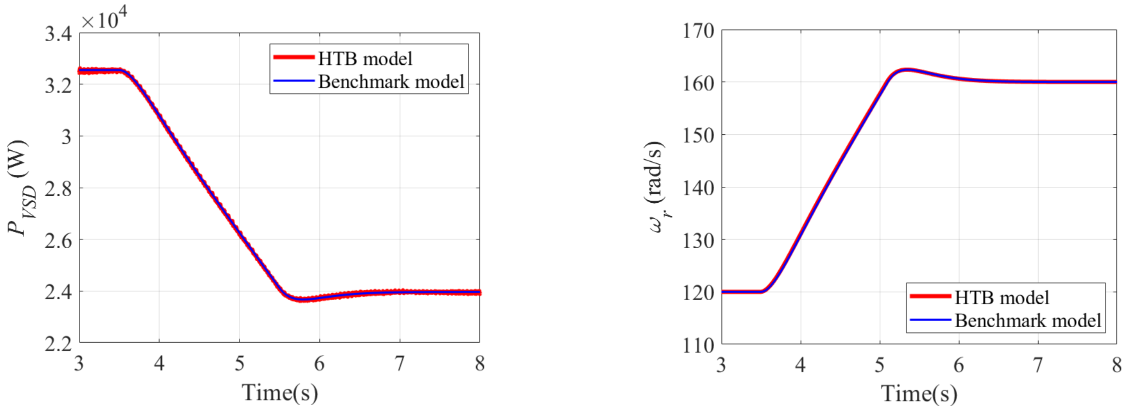

(c) P_{VSD} in Case 1. (d) ω_r in Case 2.

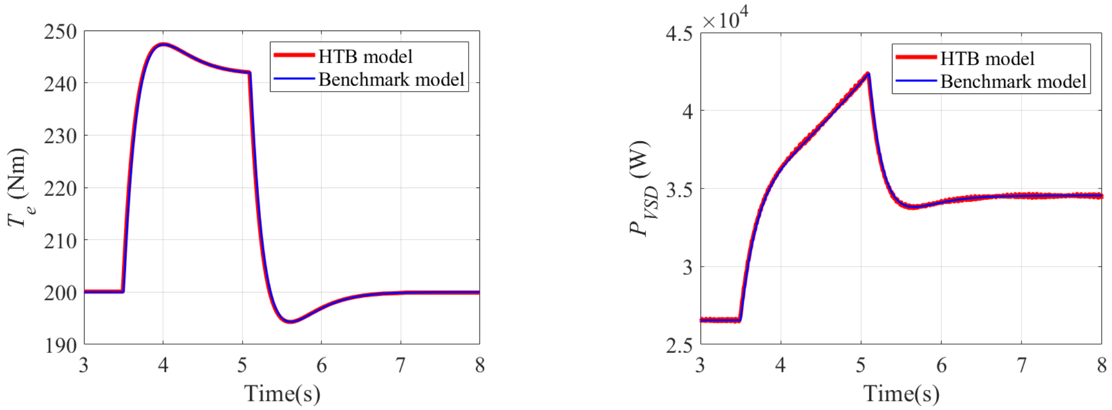

(e) T_e in Case 2. (f) P_{VSD} in Case 2.

Figure 3.29: Detailed VSD load with DTC: HTB emulator experimental results vs. benchmark model simulation results.

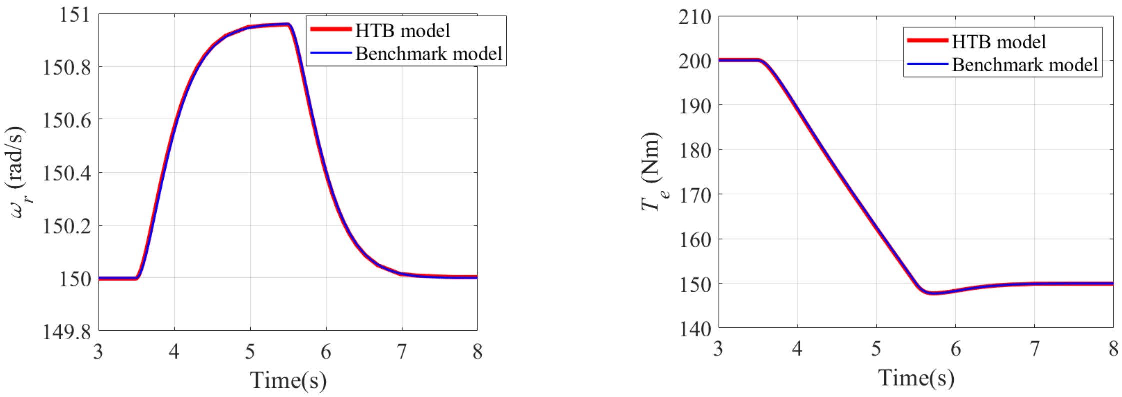

(a) ω_r in Case 1.

(b) T_e in Case 1.

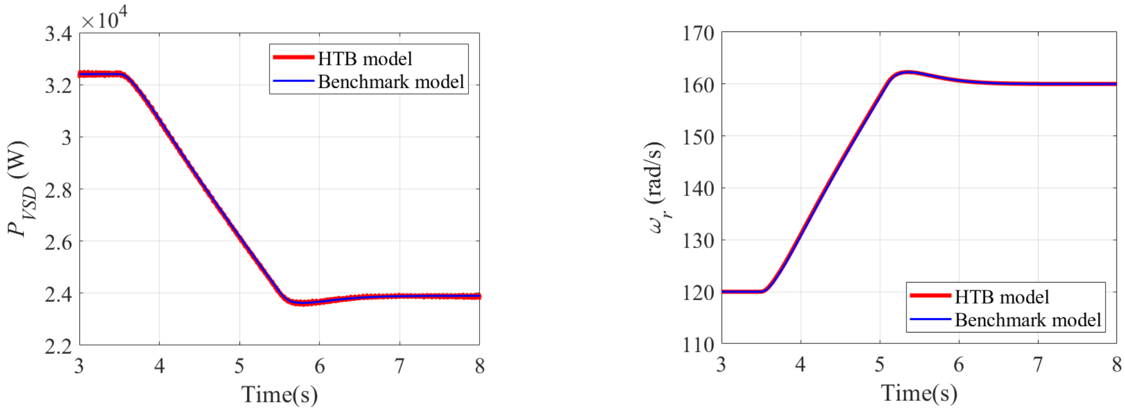

(c) P_{VSD} in Case 1.

(d) ω_r in Case 2.

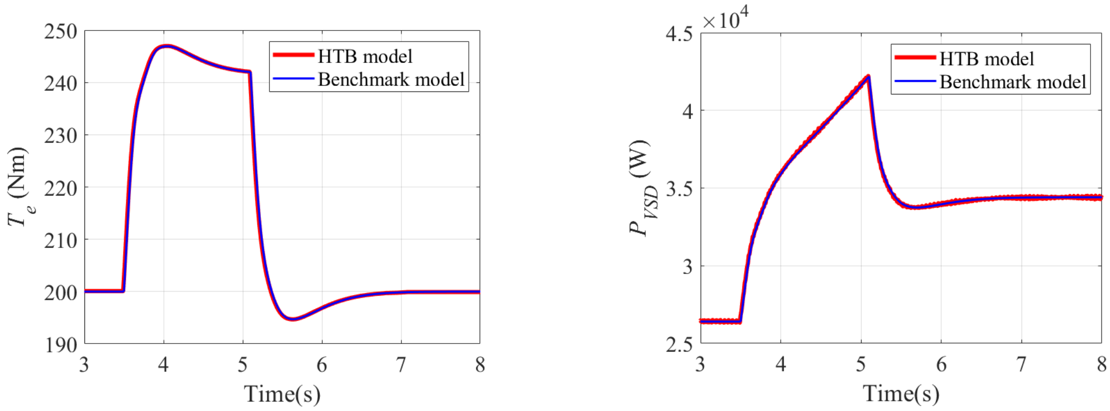

(e) T_e in Case 2.

(f) P_{VSD} in Case 2.

Figure 3.30: Detailed VSD load with CSCC: HTB emulator experimental results vs. benchmark model simulation results.

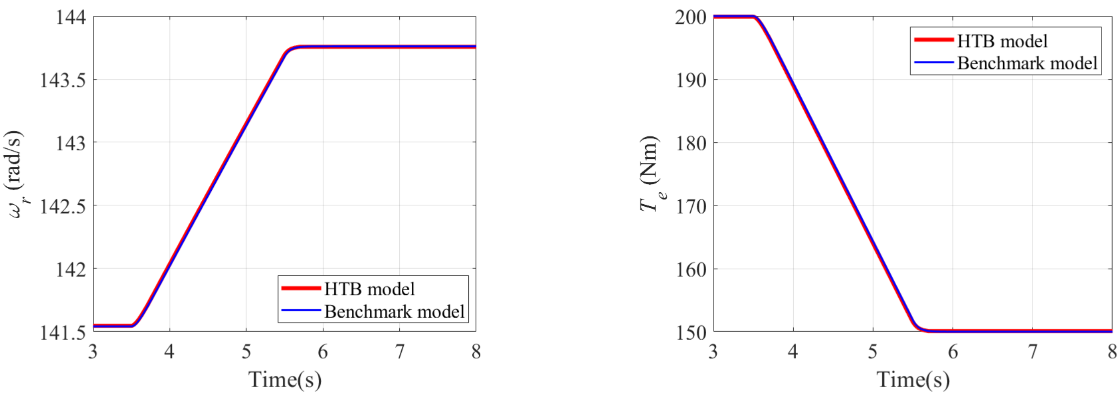

(a) ω_r in Case 1.

(b) T_e in Case 1.

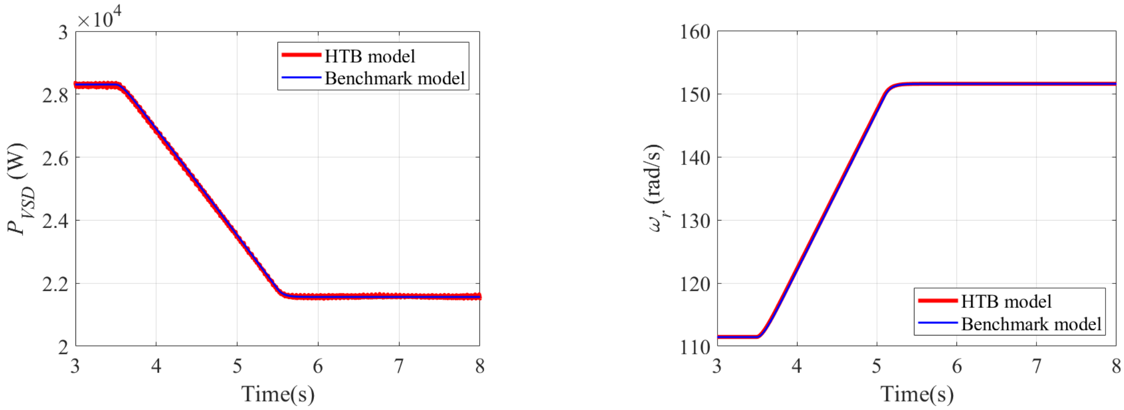

(c) P_{VSD} in Case 1.

(d) ω_r in Case 2.

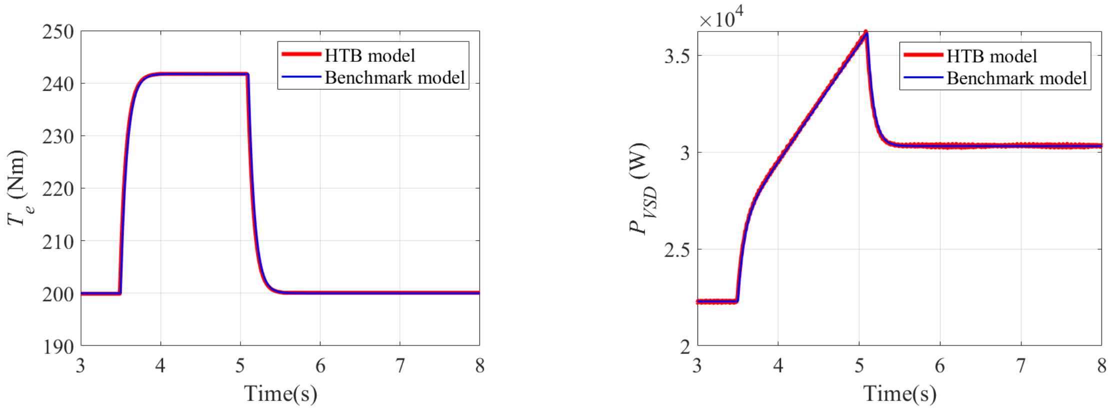

(e) T_e in Case 2.

(f) P_{VSD} in Case 2.

Figure 3.31: Simplified VSD load with elementary constant V/f: HTB emulator experimental results vs. benchmark model simulation results.

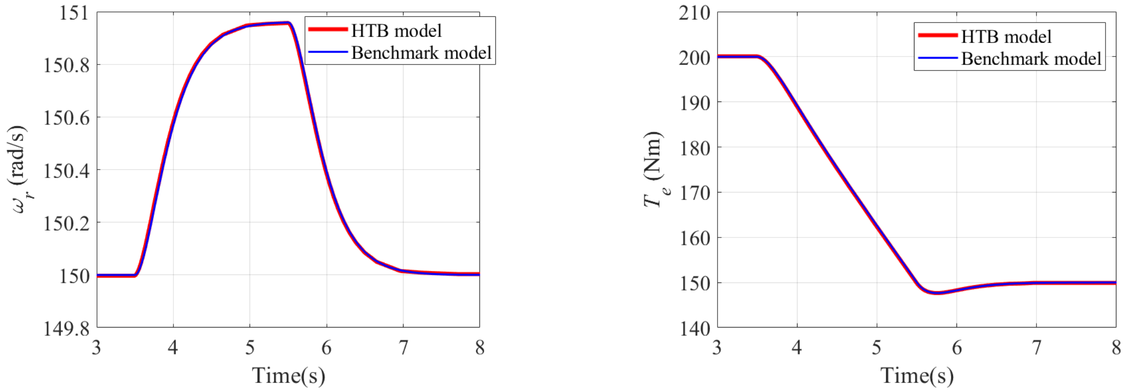

(a) ω_r in Case 1.

(b) T_e in Case 1.

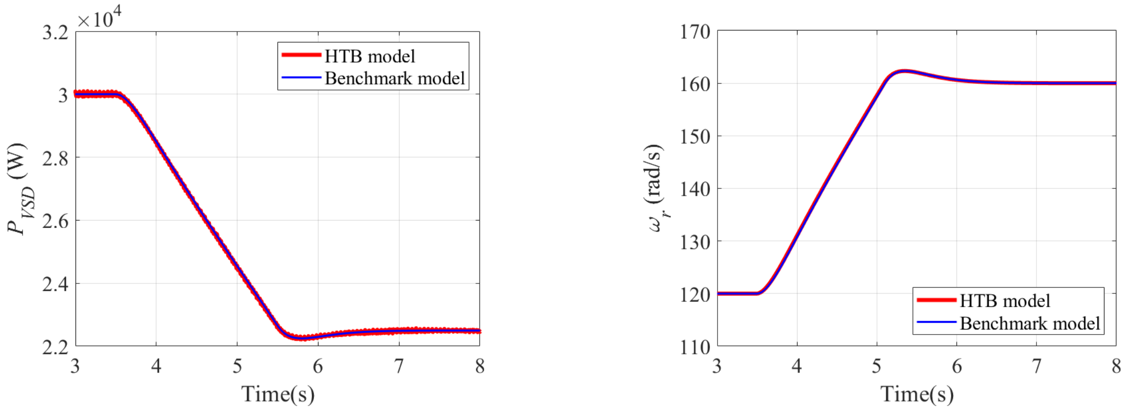

(c) P_{VSD} in Case 1.

(d) ω_r in Case 2.

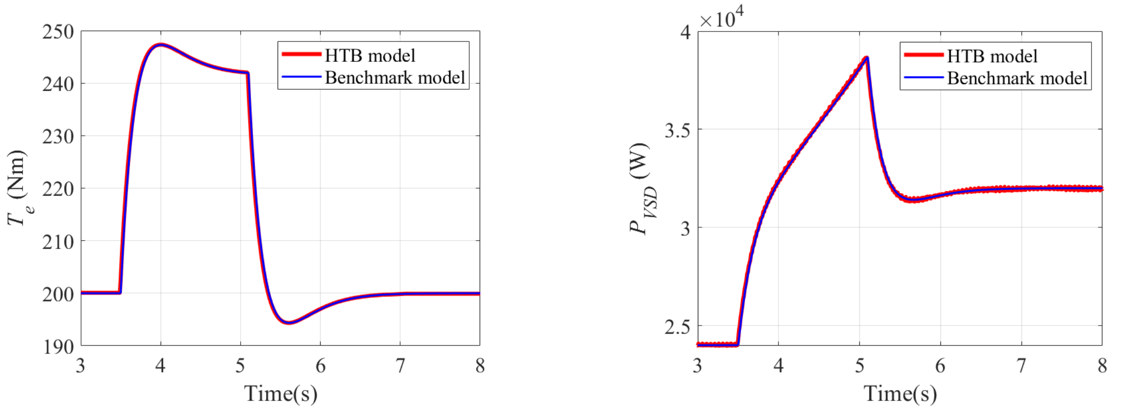

(e) T_e in Case 2.

(f) P_{VSD} in Case 2.

Figure 3.32: Simplified VSD load with closed-loop controller: HTB emulator experimental results vs. benchmark model simulation results.

simplified format are evaluated, and the accuracy rates of each model are presented in Table 3.2.

According to estimation results shown in Table 3.2, the detailed power emulator model of VSD loads is relatively more accurate compared with the simplified power emulator model, of which the NRMSE are all very close to 100%. The simplified model removed the operating loss of the load unit, and uses a constant η to represent the power mismatch between total power and rotating load power. So the model accuracy is lower than that of the detailed emulator model.

3.5 Conclusions

In this chapter, VSD load model is introduced, including the modeling algorithm of the passive-front-end rectifier, the active-front-end rectifier, and the back-end inverter with open-loop and closed-loop rotor speed control.

Moreover, the VSD load model simplification is investigated considering releasing the computational burden of corresponding simulation/emulation environments:

- The VSD operation region is specified where the passive and active-front-end rectifier have identical dynamic performance. So it is not necessary to distinguish these two types of front-end rectifiers when the VSD is within the specified operation region, which reduces the modeling complexity. The VSD load studied in the following chapters is restricted to this operation region.

- The simplified model of the VSD load which emphasizes its active power consumption is proposed. Such simplified VSD load model can accurately reflect the dynamic performance of the frequency responsive load, which will be presented in the following chapters.

Table 3.2: VSD load power emulator model accuracy estimation.

VSD control scheme	accuracy rate	VSD control scheme	accuracy rate	VSD control scheme	accuracy rate
Constant V/f	97.30%	FOC	97.81%	DTC	97.84%
CSCC	97.82%	open-loop simplified	91.65%	closed-loop simplified	92.67%

Chapter 4

Modeling and Control of VSD Based Load for Grid Primary Frequency Support

It is important to characterize aggregated load performance because using the aggregated model can reduce the complexity of the original model, which is beneficial for performing simulation in terms of saving computational resources and accelerating the simulation speed. The aggregated model plays a critical role, especially for studying the large-scale power network, since it is computationally prohibited to model a large number of end-users in the simulation or experimental testbed. In this chapter, the representation of the VSD load HTB emulator is introduced, which accurately mimics the load dynamic performance and how it can be regulated to provide primary frequency support to the power network. The VSD model frequency support control and aggregation algorithm are explained in detail in the following sections.

4.1 Frequency Responsive VSD Load

In this section, the grid frequency support control provided by the VSD load is introduced by using one VSD load unit as an example. Additionally, the simplified representation of the VSD load is also included in this section.

4.1.1 VSD Grid Frequency Control Scheme

As introduced in Chapter 2, the power consumption of non-critical electric motor loads can be regulated by accelerating and decelerating the motor rotating speed, so the grid frequency response is enhanced consequently. And the VSD provides a convenient way for regulating the motor load by adjusting the motor rotating speed according to grid frequency regulation requirements. To precisely regulate the VSD load power consumption, the VSD grid frequency control scheme is introduced in this section, which is illustrated in Fig. 4.1.

Grid frequency deviation Δf is measured at the point of common coupling (PCC) and introduced to the motor speed reference $\omega_{r,ref}$ as illustrated in Fig. 4.1. $\omega_{r,ref}$ with respect to Δf is expressed below according to the illustrated frequency support scheme [36]:

$$\Delta f = f - f_{nom} \tag{4.1}$$

$$\omega_{r,ref} = K_f \cdot \Delta f + \omega_{r,ini} \tag{4.2}$$

where f represents the measured grid frequency, f_{nom} represents the nominal grid frequency, K_f represents the coefficient of frequency control scheme, and $\omega_{r,ini}$ represents the initial rotor speed before the grid disturbance.

When f decreases below f_{nom}, $\omega_{m,ref}$ will decrease proportional to Δf following (4.2). The coefficient K_f represents the extent of load response to Δf. After the grid is stabilized, ω_r is lower than $\omega_{r,ini}$ due to Δf and K_f, thus the VSD load power consumption is lower than that before the grid disturbance, *i.e.*, when $\omega_r = \omega_{r,ini}$. Accordingly, the responsive VSD load will help mitigate the grid frequency deviation when subjected to a grid disturbance, which is similar to the effect of primary frequency control. The operating condition when f increases due to grid disturbance can be explained similarly [36].

4.1.2 VSD Load Model Simplification

The VSD load simplified model is introduced in Fig. 3.18. Considering the decoupling of the front-end and back-end PE interfaces which has been explained in Section 3.3, the VSD load dynamic performance can be expressed by the speed regulator and the IM rotor speed dynamic equations. Along with the model of frequency regulation scheme introduced in Section 4.1.1, the simplified model of VSD based pump/fan type of loads with frequency support control is expressed as Fig. 4.2.

In Fig. 4.2, the pump/fan type of load T_L is represented by ω_r following:

$$T_L = {\omega_r}^2 \tag{4.3}$$

As illustrated in Fig. 4.2, the motor drive regulation process, which includes the load voltage/current control and modulation of the PE interface configuration, is simplified as a time delay process, of which the time constant T is usually selected as the switching cycle, or twice of the switching cycle, based on the specific controller design. The switching bandwidth is much higher compared with that of the rotor speed control loop and the IM mechanical dynamic performance. The corresponding zero-pole map of the VSD load linearized model shown in Fig. 4.2 is illustrated in Fig. 4.3, assuming that the PE interface switching frequency is 10 kHz.

As shown in Fig. 4.3, the pole of the VSD transfer function representing the PE control and modulation delay is far from the rest of the zeros and poles, which are all close to $(0, 0)$, verifying that the time delay process can be ignored due to its fast dynamics. So the time delay process modeled in Fig. 4.2 can be eliminated accordingly, thus further simplifying the VSD model.

4.2 Potential of the VSD Load in Terms of Primary Frequency Support

The equivalent load operational reserve reflects the available load power reserve, which can be utilized for primary frequency response. The responsive load usually follows the droop-like control for the primary frequency as introduced in Section 2.1.4, which mimics the governor of the conventional generation unit. The VSD load can adopt a flexible controller to regulate the motor rotating speed, so it guarantees a fast and efficient frequency response which improves the power grid stability. Discussion about the VSD load frequency response

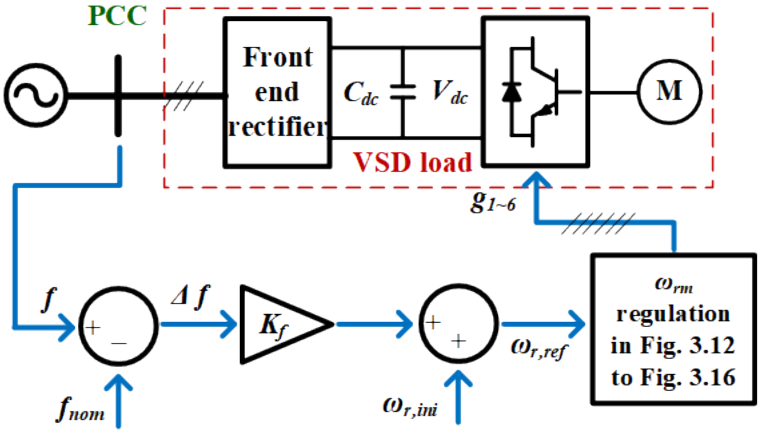

Figure 4.1: VSD frequency support control diagram [36].

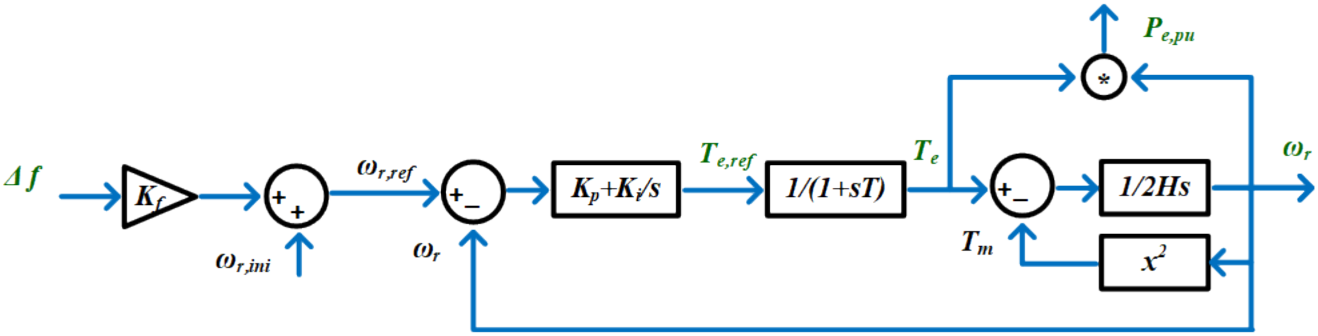

Figure 4.2: VSD driving pump/fan type of loads with frequency support control.

is presented in this section, which includes the potential of VSD load in terms of providing equivalent primary frequency response, and how to provide frequency droop control using multiple VSD load units.

4.2.1 Frequency Support Capacity of Individual VSD Load

The concept of load frequency response includes both decreasing the load power consumption when grid f is lower than f_{nom}, and increasing the power consumption when f is higher than f_{nom}. The main configuration of VSD load includes the front-end rectifier, the back-end inverter, and the motor load. Among these three major parts, the motor can tolerate the overload condition for a relatively long period of time. However, for the VSD load PE configuration, the overload capability is relatively low. As presented in [120], the VSD allows an overload of at least 60 seconds when the current lies between 100% and 150% nominal current I_{nom}. Therefore, it is not recommended to run the VSD at overcurrent status for a relatively long period of time, *i.e.,* the VSD load is not suitable to frequently provide power which is higher than I_{nom} considering the overload capability of the corresponding PE configuration.

As introduced above, the pump/fan type of load driven by VSD is selected as frequency responsive load since the rotating speed variation does not largely influence the corresponding main production process, thus allowing for a flexible adjustment of load power consumption according to the requirement of the grid frequency support scheme. Furthermore, the rotating speed of such circulation centrifugal load with VSD can be adjusted actively by the customer to achieve high operating efficiency under different operating conditions. As suggested in [121], the optimal operating speed of pump load ranges from 80% to 100% nominal rotating speed, which is denoted as $\omega_{r,nom}$. Therefore, a wide range of VSD load operating speeds provides a wide adjustment range of load power consumption without overloading the VSD. Accordingly, considering the tolerance of electric devices and the reasonable operational efficiency, the reserve power of individual VSD load unit is defined in Fig. 4.4.

As illustrated in Fig. 4.4, VSD devices operating between 79.39% and 100% $\omega_{r,nom}$ are chosen as available to be utilized as load operational reserve. Otherwise, VSD loads are

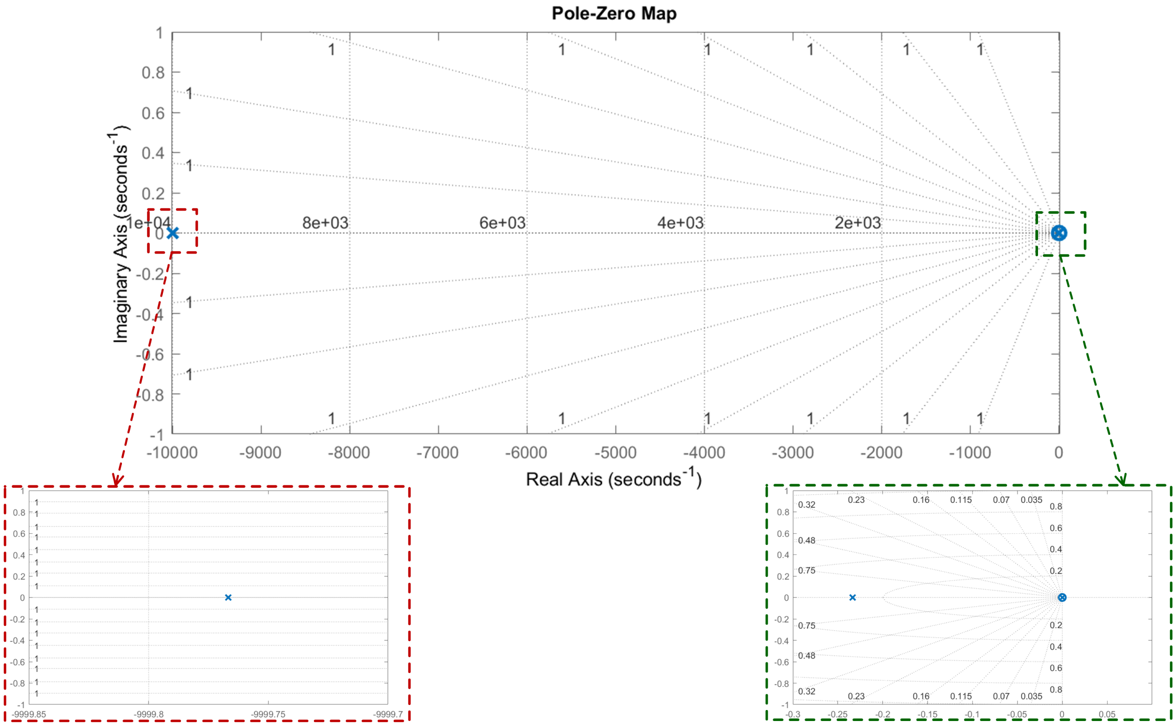

Figure 4.3: VSD linearization model zero-pole map.

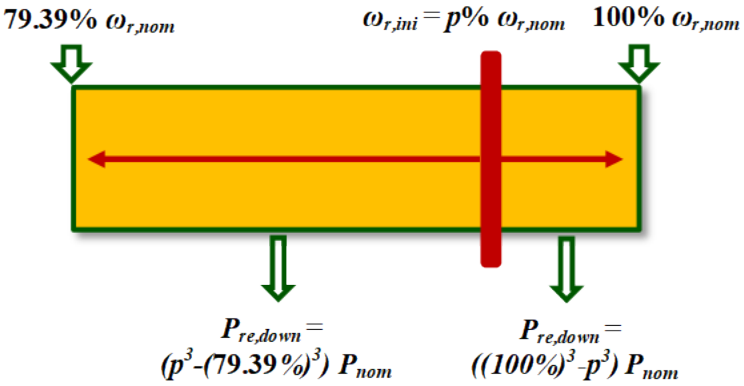

Figure 4.4: Operational reserve provided by the individual VSD load unit.

not allowed to provide frequency support. As for the pump/fan type of load, of which T_L is proportional to the square of ω_r, the predefiend initial speed can be transferred to the initial load consumed power ranging from 50% to 100% P_{nom}, where P_{nom} denotes the VSD nominal power. Assume that $\omega_{r,ini} = p\% \ \omega_{r,nom}$, then the operational reserve is classified as following two aspects:

- Individual VSD load unit downwards power reserve $P_{re,down,i}$, which represents the power reserve for supporting the condition when grid frequency decreases. $P_{re,down,i}$ is expressed as:

$$P_{re,down,i} = ((p\%)^3 - (79.39\%)^3) \cdot P_{nom} \tag{4.4}$$

- Individual VSD load unit upwards power reserve $P_{re,up,i}$, which represents the power reserve for supporting the condition when grid frequency increases. $P_{re,up,i}$ is expressed as:

$$P_{re,up,i} = ((100\%)^3 - (p\%)^3) \cdot P_{nom} \tag{4.5}$$

4.2.2 Frequency Support Capacity of Multiple VSD Load Units Following Equivalent Droop Response

The total power reserve in p.u. value provided by multiple VSD load units at different frequency events can be expressed respectively in (4.6) and (4.7) based on the individual load unit power reserve expression in (4.4) and (4.5):

$$P_{re,down} = \frac{\sum_{i=1}^{n} P_{re,down,i}}{P_{base,sys}} \tag{4.6}$$

$$P_{re,up} = \frac{\sum_{i=1}^{n} P_{re,up,i}}{P_{base,sys}} \tag{4.7}$$

where the frequency decrease and increase event are expressed in (4.6) and (4.7), respectively. Assume there are n VSD load units in the studied load center, and the grid power base in the corresponding region is $P_{base,sys}$.

According to the definition of the primary frequency droop curve which is presented in Section 2.1.4, the K_{droop} is determined by the lower and upper threshold power, which is denoted as $P_{prim,down}$ and $P_{prim,up}$ respectively. $P_{prim,down}$ and $P_{prim,up}$ should not exceed the limit of available operational reserve power $P_{re,down}$ and $P_{re,up}$, which is expressed as:

$$|P_{prim,down}| \leq |P_{re,down}| \tag{4.8}$$

$$|P_{prim,up}| \leq |P_{re,up}| \tag{4.9}$$

Therefore, not all the available power reserves P_{re} from each VSD load unit are to be utilized in the frequency event, since the power reserve threshold P_{prim} is not required to be equivalent to P_{re}. Regardless of the frequency deviation direction, assume the ratio between P_{re} and P_{prim} of the droop controller is expressed as:

$$K_{prim} = \frac{P_{prim}}{P_{re}} \tag{4.10}$$

Substitute (4.10) into (4.6) or (4.7), P_{prim} can be expressed as:

$$P_{prim} = \frac{\sum_{i=1}^{n} P_{re,i}}{P_{base,sys}} \cdot K_{prim} \tag{4.11}$$

According to the primary frequency droop control expression, the total power contributed by VSD loads in p.u. value is denoted as $\Delta P_{VSD,tot,pu}$, and is expressed as:

$$\Delta P_{VSD,tot,pu} = K_{droop} \Delta f_{pu} \tag{4.12}$$

where Δf_{pu} represents the p.u. value of grid frequency deviation. K_{droop} is expressed as:

$$K_{droop} = \frac{P_{prim}}{f_{max} - f_{db}} \tag{4.13}$$

where f_{db} represents the frequency deadband over which the VSD load should be responsive to Δf, and when f reaches f_{max} VSD load power contribution should reach P_{prim}. Equation (4.13) is in consistent with Fig. 2.6 in Section 2.1.4.

The overall VSD load contribution should follow the droop regulation as expressed in (4.12). The power contribution $\Delta P_{VSD,pu,i}$ of a single VSD unit i is modeled below.

According to the VSD frequency regulation expressed in (4.2), $P_{VSD,pu,i}$ of VSD unit i is expressed as:

$$P_{VSD,pu,i} = (\omega_{ri,ini,pu} + K_{fi} \cdot \Delta f_{pu})^3 \tag{4.14}$$

where K_{fi} represents K_f in i^{th} VSD unit.

Accordingly, $\Delta P_{VSD,pu,i}$ compared with the initial load power consumption is expressed as:

$$\Delta P_{VSD,pu,i} = 3\omega_{ri,ini,pu}^2 (K_{fi} \cdot \Delta f_{pu}) + 3\omega_{ri,ini,pu}(K_{fi} \cdot \Delta f_{pu})^2 + (K_{fi} \cdot \Delta f_{pu})^3 \tag{4.15}$$

The grid frequency deviation in p.u. value is quite small, so ignore Δf terms which are higher than first-order in (4.15), $\Delta P_{VSD,pu,i}$ is simplified as:

$$\Delta P_{VSD,pu,i} = 3\omega_{ri,ini,pu}^2 \cdot K_{fi} \cdot \Delta f_{pu} \tag{4.16}$$

Accordingly, the total VSD load power contribution expressed by the sum of individual loads is expressed as:

$$\Delta P_{VSD,tot,pu} = \frac{\sum_{i=1}^{n} 3K_{fi}\omega_{ri,ini,pu}^2 P_{base,i}}{P_{base,sys}} \cdot \Delta f_{pu} \tag{4.17}$$

Based on the expression in (4.17), the required K_{droop} is achieved by adjusting K_{fi} in i^{th} VSD load unit. Substitute (4.17) and (4.13) into (4.12), the expression of K_{fi} is shown below:

$$K_{fi} = \frac{P_{re,pu,i} K_{prim}}{3\omega_{ri,ini,pu}^2 (f_{max} - f_{db})} \tag{4.18}$$

where $P_{re,pu,i}$ represents the power reserve of i^{th} VSD unit in p.u. value.

4.2.3 Numerical Study: Using VSD Loads to Provide Frequency Droop Response

The example of VSD load potential in terms of providing $p-f$ droop control is represented below using the derivation from the last section. The performance of VSD load group is represented by 18 VSD load units with different controller parameters, $P_{base,i}$ and $\omega_{ri,ini,pu}$. The parameters used for developing VSD load in this example are listed in Appendix B.

The VSD load unit operation status $P_{base,i}$ and $\omega_{ri,ini,pu}$ are randomly generated. For simplification consideration, $P_{base,i}$ is scaled as (4.19), and $\omega_{ri,ini,pu}$ is selected between 79.39% and 100% $\omega_{r,nom}$ as explained in the last section. The initial operation status of 18 VSD load units are illustrated in Fig. 4.5a.

$$1 \leq P_{base,i} \leq 2 \tag{4.19}$$

K_{droop} is determined based on P_{prim} provided by the VSD load group following (4.8) and (4.9). So different composition of the VSD $P_{base,i}$ and $\omega_{ri,ini,pu}$ will yield different P_{prim}, thus providing different K_{droop} to the power grid. The equivalent droop curve provided by the VSD load group based on the initial operation status in Fig. 4.5a is shown in Fig. 4.5b.

The simulation results represented in Fig. 4.5b is based on the aggregated VSD model developed in Simulink, which is composed by 18 VSD load units introduced above. The blue curve represents the desired droop control, and the red dot represents the VSD load response in the simulation. As illustrated in Fig. 4.5b, $K_{droop,up}$ and $K_{droop,down}$ are decided respectively by $P_{prim,up}$ and $P_{prim,down}$. It is shown that K_{droop} applied for the frequency increase and frequency decrease events are different based on the VSD unit load status. In this example, $K_{droop,up} = 0.2667$ p.u./Hz and $K_{droop,down} = 0.2333$ p.u./Hz.

4.3 VSD Load Aggregation Principle

As explained in the previous sections, it is important to represent the electrical components by the aggregated model, especially in terms of evaluating the performance of the large-scale power network. Following this principle, it can be concluded that the design of the HTB power emulator will be more efficient and precise if the performance of multiple VSD load units can be represented by an acceptable number of aggregated VSD models.

Assume multiple VSDs employing the frequency support control are located at one load center, which is represented as connected to one load bus in the power network transmission level model. The total power consumption $P_{VSD,tot}$ will be varied according to Δf due to the VSD grid support function. $P_{VSD,tot}$ considering the frequency support can be characterized as:

$$P_{VSD,tot} = f(x, u) \tag{4.20}$$

where u represents the input variable Δf, x represents all the state variables involved in (4.20).

Practically, Δf is measured locally by the current sensor applied in each VSD load unit. Assume the input variable Δf is identical for all VSD loads at a certain load center, and all VSD loads involved follow the same model format as illustrated in Fig. 4.2, which includes both the frequency regulation scheme model and the VSD load model. Therefore, the initial estimate for the VSD aggregated model is that it also follows the same model representation as that in Fig. 4.2, *i.e.,* the aggregated representation of multiple VSD load units is equivalent to that of one VSD load unit if characterizing the performance expressed in (4.20). The aggregated model initial estimation can be further validated if appropriate model parameters can be identified to represent the aggregated performance of multiple VSD load units.

Since we assume that the aggregated VSD load model format is known, so the grey-box system identification algorithm can be used to identify the model parameters of the aggregated model. To increase the identification efficiency, the model parameters are identified based on the following two steps in this dissertation: 1) Use the black-box system identification algorithm for a linearized model to decide the initial load model parameters,

2) Use the grey-box system identification algorithm to identify load parameters based on initial values derived in step 1).

4.3.1 VSD Load Clustering Principle

The linearized model of a single VSD is illustrated in Fig. 4.6 based on the nonlinear model shown in Fig. 4.2. According to Fig. 4.6, the parameters for the VSD linearization model includes the frequency regulation coefficient K_f, the PI controller parameters K_p and K_i, the IM inertia constant H, the initial rotating speed $\omega_{r,ini}$ and the initial electric torque $T_{e,ini}$. ω_r is regulated by a closed-loop speed controller with PI regulator. The VSD power consumption deviation $\Delta P_{e,pu}$ linearization expression is proportional to the electric torque deviation ΔT_e and the rotor speed deviation $\Delta\omega_r$, which is expressed as:

$$\Delta P_{e,pu} = \Delta T_e \cdot \omega_{r,ini} + T_{e,ini} \cdot \Delta\omega_r \tag{4.21}$$

The transfer function of the VSD linearized model can be derived according to Fig. 4.6. The frequency response of the VSD load varies in the time domain when adopting different bandwidths for the main controllers. This can also be observed by observing the time-domain load active power response, or evaluating the VSD ω_r controller open-loop gain. An example of two VSD load units with different control bandwidths is illustrated in Fig. 4.7.

The blue curve illustrates the VSD ω_r control bandwidth of 10 rad/s, while the orange curve illustrates that of 100 rad/s in Fig. 4.7. The VSD load response characteristics with diverse ω_r control bandwidths in both time and frequency domain are observed. Considering the discrepancy of the load response stated above, it is not accurate to combine the VSD load with significantly different control bandwidth together to derive the aggregated model. So the accuracy of the equivalent aggregated VSD model will be increased if multiple VSD loads can be classified based on controller bandwidth before developing the aggregated model. VSD load units with close control bandwidth can be clustered together and aggregated separately, and here in this section, VSD loads with 10 times of control bandwidth difference are supposed to be clustered separately. Example cases to verify this clustering principle will be illustrated in the following sections.

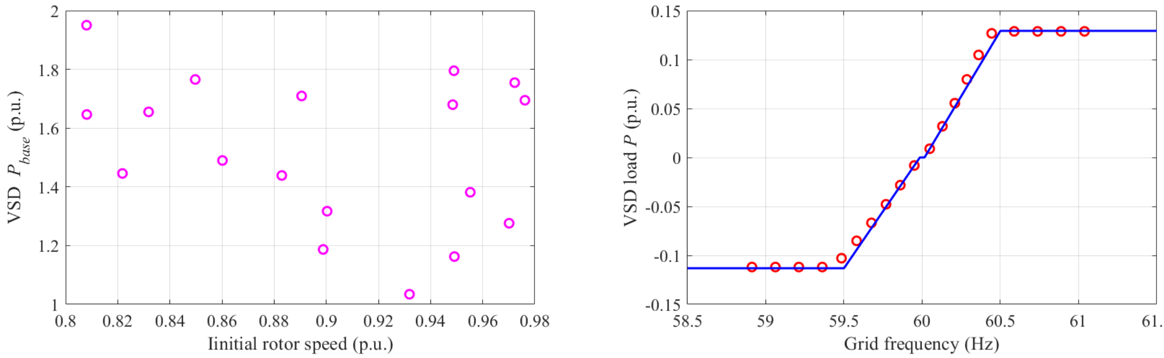

(a) VSD load unit initial operation status: $\omega_{ri,ini,pu}$ vs.$P_{base,i}$.

(b) VSD aggregated load frequency response following the required K_{droop}.

Figure 4.5: Numerical study example: primary frequency response provided by VSD loads.

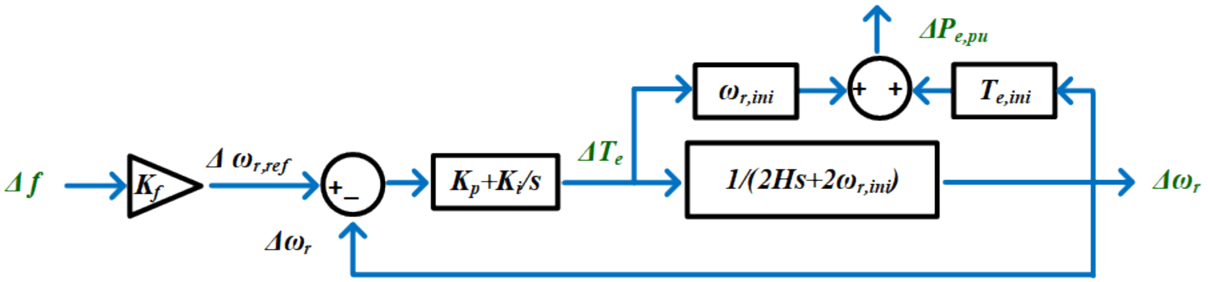

Figure 4.6: Linearized model for the single VSD load unit.

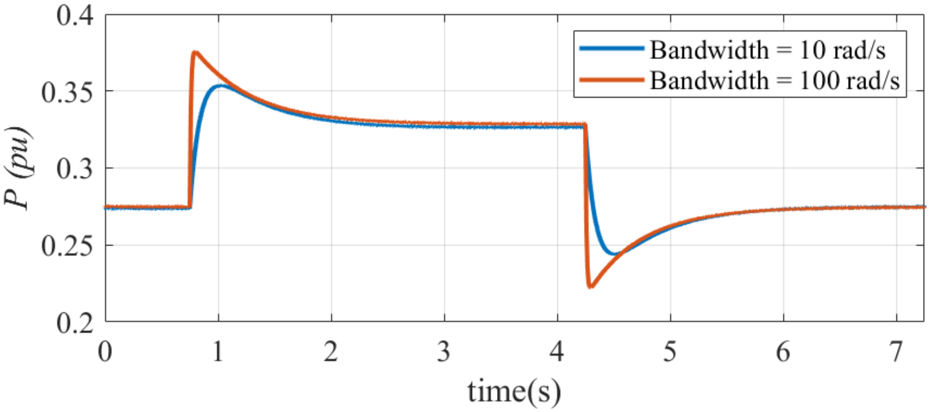

(a) Load active power consumption comparison.

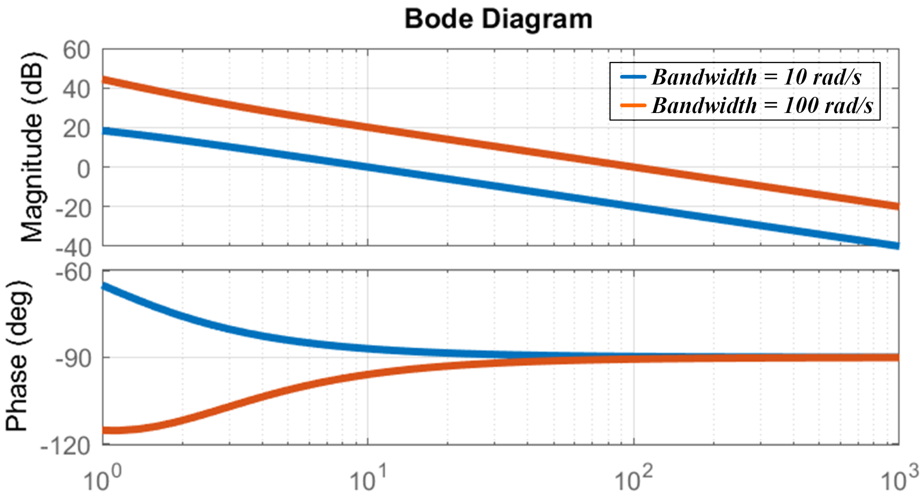

(b) VSD open-loop gain comparison.

Figure 4.7: VSD load comparison between different ω_r control bandwidth: time and frequency domain.

4.3.2 Black-box System Identification for Linearized Model

The first step of the aggregated model parameter identification process, which focuses on identifying the initial model parameters by the black-box system identification algorithm, is explained in this subsection. The aggregated VSD load linearized model has been introduced in Fig. 4.6. Accordingly, the VSD load model transfer function can be expressed as (4.22):

$$\frac{\Delta P_{e,pu}}{\Delta f} = \frac{a_2 s^2 + a_1 s + a_0}{b_2 s^2 + b_1 s + b_0} \tag{4.22}$$

where in (4.22), the input variable is Δf, and the output variable is $\Delta P_{e,pu}$.

The system identification algorithm for black-box model is adopted in order to identify coefficients in the transfer function (4.22), *i.e.,* a_2, a_1, a_0, b_2, b_1 and b_0. The above coefficients are expressed respectively as:

$$b_2 = 2H_{eq} \tag{4.23}$$

$$b_1 = 2\omega_{r,ini,eq} + K_{p,eq} \tag{4.24}$$

$$b_0 = K_{i,eq} \tag{4.25}$$

$$a_2 = 2H_{eq}K_{f,eq}K_{p,eq}\omega_{r,ini,eq} \tag{4.26}$$

$$a_1 = K_{f,eq}(2H_{eq}K_{i,eq}\omega_{r,ini,eq} + 2{\omega_{r,ini,eq}}^2 K_{p,eq} + T_{e,ini,eq}K_{p,eq}) \tag{4.27}$$

$$a_0 = K_{f,eq}K_{i,eq}(2{\omega_{r,ini,eq}}^2 + T_{e,ini.eq}) \tag{4.28}$$

According to Fig. 4.6, there are 6 model parameters that are required to be identified to develop the VSD aggregated model, which are the equivalent IM inertia constant H_{eq}, the equivalent initial rotor speed $\omega_{r,ini,eq}$, the equivalent initial electromagnetic torque $T_{e,ini,eq}$, the equivalent ω_r controller coefficients $K_{i,eq}$ and $K_{p,eq}$, and the equivalent frequency controller coefficient $K_{f,eq}$. However, these 6 model parameters stated above cannot be directly computed by a_2 to b_0 based on (4.23) and (4.28). Since b_2 is used as the divisor of nominator terms, it is usually scaled to 1 in the final identification results. So the following parameter optimization algorithm is used to select the optimal model parameters, which is illustrated in Fig. 4.8.

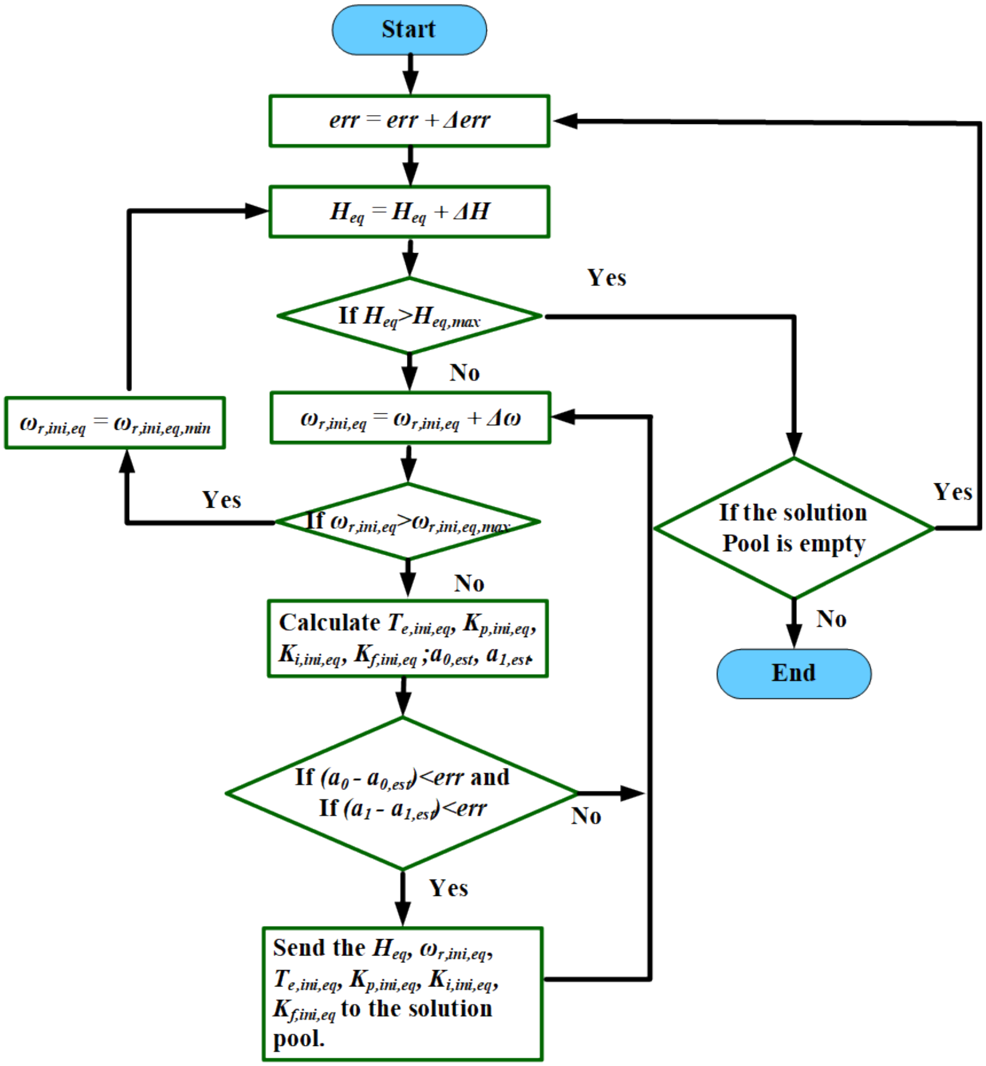

Figure 4.8: Optimization algorithm for selecting the optimal model parameters.

The proposed optimization algorithm is based on the exhaustive method. First, an err is defined at the beginning of the optimization algorithm, which represents the upper limit of the mismatch between the estimated coefficient from the optimization algorithm and the real coefficient from the VSD linearized model derived by the black-box parameter identification algorithm.

The next step is to define the initial value of H_{eq}, $\omega_{r,ini,eq}$. Along with (4.23) and (4.26), the estimated value of $T_{e,ini,eq}$, $K_{p,ini,eq}$, $K_{i,ini,eq}$ and $K_{f,ini,eq}$ can be computed. Then the estimated value of a_0 and a_1, which are denoted as $a_{0,est}$ and $a_{1,est}$, can be computed with the four estimated coefficients stated above.

The last step is to compare the coefficient a_0 and a_1 which are provided by the black-box system identification algorithm, with the estimated coefficient $a_{0,est}$ and $a_{1,est}$ which are provided by the proposed optimization scheme. If the mismatch between the real value and the estimated value is smaller than the predefined err for both a_0 and a_1, then the final estimated model parameter sets, which includes H_{eq}, $\omega_{r,ini,eq}$, $T_{e,ini,eq}$, $K_{p,ini,eq}$, $K_{i,ini,eq}$ and $K_{f,ini,eq}$, will be sent to the solution pool. Otherwise, the estimated coefficients will be discarded.

The above estimation process will be repeated with the predefined err, and when each computation iteration starts, the H_{eq} and $\omega_{r,ini,eq}$ initial value will increase by predefined ΔH and $\Delta\omega$. All H_{eq} and $\omega_{r,ini,eq}$ selected for optimization are within a predefined range, which are expressed respectively as:

$$H_{eq,min} \leq H_{eq} \leq H_{eq,max} \tag{4.29}$$

$$\omega_{r,ini,eq,min} \leq \omega_{r,ini,eq} \leq \omega_{r,ini,eq,max} \tag{4.30}$$

After scanning all H_{eq} and $\omega_{r,ini,eq}$ within the predefined range, the solution pool will be checked. If there are no estimated model parameter sets sent to the solution pool, it means that the err, which is used to evaluate the accuracy of $a_{0,est}$ and $a_{1,est}$, is too strict to draw a solution. So err will be increased and repeat the above optimization process again until the solution pool is no longer empty.

4.3.3 Grey-box System Identification for Nonlinear Model

The linearized VSD model cannot accurately reflect the dynamic load performance, especially when the transient operating conditions diverge significantly from the initial operating point. The grey-box system identification algorithm for the nonlinear model is used to further improve the accuracy of the equivalent VSD load aggregated model. The system identification results for the black-box model introduced in Section 4.3.2 are used as the initial guess of the model parameters for identifying the equivalent nonlinear VSD load model.

As stated above, the model format of the equivalent aggregated VSD model is identical to that of the single VSD load unit model, so the required parameters for the equivalent aggregated VSD load model are the same as that illustrated in Fig. 4.2, including the equivalent inertia constant H_{eq}, the equivalent rotating speed reference $\omega_{r,ref,eq}$, the equivalent frequency regulation coefficient $K_{f,eq}$, the equivalent ω_r, regulation PI controller parameter $K_{i,eq}$ and $K_{p,eq}$. The VSD grey-box model is expressed by state variables in p.u. value as follows:

$$\frac{d\Delta f}{dt} = u \tag{4.31}$$

$$\frac{dT_{e,eq}}{dt} = K_{p,eq}K_{f,eq}u - K_{p,eq}\frac{T_{e,eq} - {\omega_{r,eq}}^2}{2H_{eq}} + K_{i,eq}(K_{f,eq}f + \omega_{r,ref,eq} - \omega_{r,eq}) \tag{4.32}$$

$$\frac{d\omega_{r,eq}}{dt} = \frac{T_{e,eq} - {\omega_{r,eq}}^2}{2H_{eq}} \tag{4.33}$$

$$y = T_{e,eq} \cdot \omega_{r,eq} \tag{4.34}$$

where the state variables include Δf, equivalent electric torque $T_{e,eq}$ and equivalent motor rotating speed $\omega_{r,eq}$. Additionally, u represents the input variable which is the differential of Δf, y represents the output variable which is the aggregated VSD load active power consumption of $P_{VSD,tot}$.

The solution derived from the VSD linearized black-box model is used as the initial estimate of the state variables and VSD model parameters, which can be concluded as:

- The initial value of VSD model state variables Δf_0, $T_{e,eq,0}$ and $\omega_{r,eq,0}$ is defined as:

$$\begin{bmatrix} \Delta f_0 \\ T_{e,eq,0} \\ \omega_{r,eq,0} \end{bmatrix} = \begin{bmatrix} 0 \\ T_{e,ini,eq} \\ \omega_{r,ini,eq} \end{bmatrix} \tag{4.35}$$

  where the coefficient $T_{e,ini,eq}$ and $\omega_{r,ini,eq}$ are derived and explained in Section 4.3.2.

- The initial value of VSD model parameters, which include H_{eq}, $\omega_{m,ref,eq}$, $K_{f,eq}$, $K_{p,eq}$ and $K_{i,eq}$, employ model parameters solution derived from the VSD linearized black-box model. $\omega_{m,ref,eq}$ is regarded as equivalent to $\omega_{r,ini,eq}$ which is derived in Section 4.3.2. $P_{VSD,tot}$ can be represented by $\omega_{m,eq}$ in p.u. value as follows, assuming the mechanical power loss is negligible.

$$P_{VSD,tot} = {\omega_{r,eq}}^3 \tag{4.36}$$

  Therefore, $\omega_{r,eq,0}$ and $\omega_{m,ref,eq}$ can be identified by the initial load power consumption $P_{VSD,tot}$. The only restriction for the remaining parameters is ≥ 0.

The combination of linearized model identification and nonlinear model identification can significantly reduce the complexity of the system identification process, making it easier to get a converged solution.

4.3.4 VSD Aggregated Model Identification Example

The MATLAB® system identification toolbox is used to identify the equivalent aggregated VSD load model. As stated above, the VSD clustering based on ω_r control bandwidth will promote the accuracy of the aggregated model. So in the following part of Section 4.3.4, the model aggregation and parameter identification of VSD loads with different control bandwidth is introduced, and then the positive impact of load cluster is presented.

4.3.4.1 Aggregated Model Parameter Identification: with Close Control Bandwidth

Two groups of VSD load models are used as examples of performing the aggregated model parameter identification. One consists of individual VSD devices with control bandwidth = 10 rad/s, and the other consists of VSD devices with control bandwidth = 100 rad/s. The model parameters of each VSD load unit are listed in Table 4.1 and Table 4.2 respectively.

As shown in (4.20), the VSD model is expressed as a single-input single-output system. According to (4.22) and (4.31), the input variable of the aggregated VSD load model expression is Δf, and the output variable is the total active power consumption $P_{VSD,tot}$, which is subject to the variation of Δf. Based on the VSD information listed in Table 4.1 and Table 4.2, simulation tests are performed to collect the input and output data as shown in Fig. 4.9 and Fig. 4.10, which are required by the model parameter identification. The input/output data shown above are used for the VSD aggregated model identification studies introduced below.

As shown in Fig. 4.10, the power consumption of each VSD load unit with respect to Δf variation are illustrated in Fig. 4.10a and Fig. 4.10b. The black curves in Fig. 4.10a and Fig. 4.10b represent the average total power consumption $P_{VSD,agg}$ of 9 VSD load units in p.u. system, which is expressed as:

$$P_{VSD,agg} = \frac{\sum_{n=1}^{9}(P_{VSD,n} \cdot P_{base,n})}{\sum_{n=1}^{9} P_{base,n}} \tag{4.37}$$

where $P_{VSD,n}$ and $P_{base,n}$ represent the power consumption and power base value of each VSD load unit. $P_{VSD,agg}$ is used as output values for aggregated VSD model parameter identification.

The model identification results are listed in Table 4.3, which includes the estimated aggregated model parameters of VSD load with different control bandwidth, where VSD load units with control bandwidth = 10 rad/s is referred to as VSD group No. 1, and the VSD load units with control bandwidth = 100 rad/s are referred to as VSD group No. 2. The comparison of load power response between the estimated model and measured response data in each group are illustrated in Fig. 4.11a and Fig. 4.11b respectively. It can be observed

Table 4.1: VSD model parameters with control bandwidth = 10 rad/s.

VSD No.	H (s)	K_p	K_i	$\omega_{m,ref}$ (p.u.)	K_f
1	1	20.039	3.5076	0.65	4
2	1	20.046	3.5084	0.7	4
3	1	20.046	3.5084	0.75	4
4	1.5	30.024	5.2547	0.65	4
5	1.5	30.028	5.2554	0.7	4
6	1.5	30.028	5.2554	0.75	4
7	2	40.018	7.0039	0.65	4
8	2	40.018	7.0039	0.7	4
9	2	40.018	7.0039	0.75	4

Table 4.2: VSD model parameters with control bandwidth = 100 rad/s.

VSD No.	H (s)	K_p	K_i	$\omega_{m,ref}$ (p.u.)	K_f
1	1	199.97	349.99	0.65	4
2	1	199.97	349.99	0.7	4
3	1	199.97	349.99	0.75	4
4	1.5	299.96	524.95	0.65	4
5	1.5	299.96	524.95	0.7	4
6	1.5	299.96	524.95	0.75	4
7	2	399.94	699.97	0.65	4
8	2	399.94	699.97	0.7	4
9	2	399.94	699.97	0.75	4

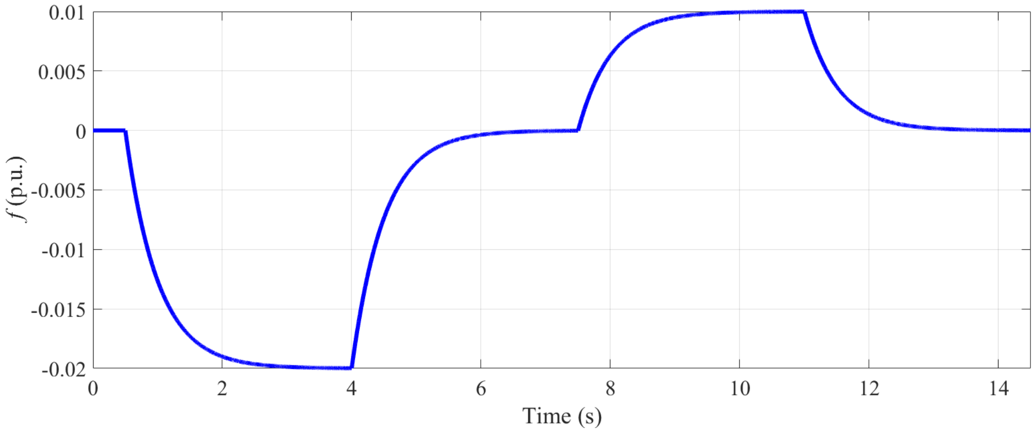

Figure 4.9: The aggregated VSD load model identification input variable: Δf in p.u. value.

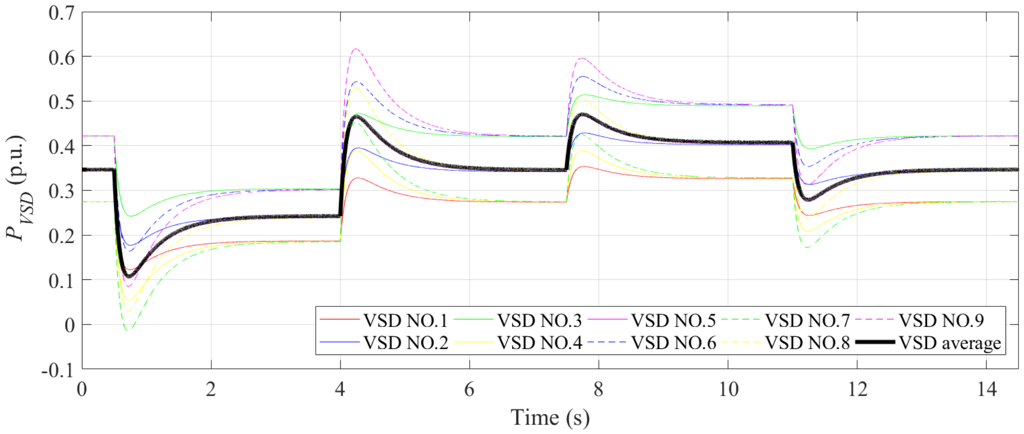

(a) Power consumption of VSD load with 10 rad/s rotor speed control bandwidth.

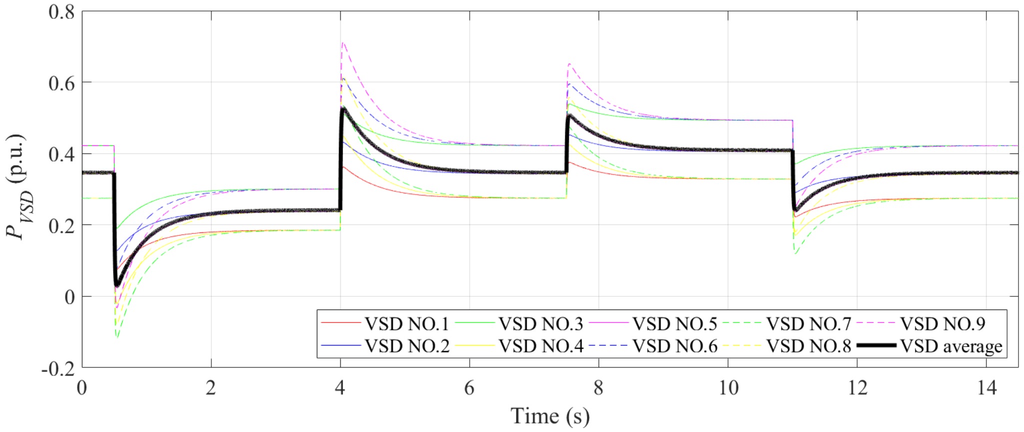

(b) Power consumption of VSD load with 100 rad/s rotor speed control bandwidth.

Figure 4.10: The aggregated VSD load model identification output variable: power consumption in p.u. value.

that both estimated aggregated models achieve a close match compared with the original measured power output of multiple VSD devices, where the accuracy rate of group No. 1 is 99.81%, and the accuracy rate of group No. 2 is 99.41%.

4.3.4.2 Aggregated Model Parameter Identification: with Diverse Control Bandwidth

As mentioned in Section 4.3.1, the step responses of VSD devices with different control bandwidth are not consistent when observed in both the time domain and frequency domain. So the aggregated model accuracy will be compromised without clustering the load units before deriving the aggregated model.

To further justify the proposed clustering principle, the VSD aggregation model identification is carried out for a group of multiple VSD load models with significantly different control bandwidths. The measured model input and output variables illustrated in Fig. 4.9 and Fig. 4.10 are used here for the parameter identification. To demonstrate the diverse control bandwidth of each load unit, VSD devices with control bandwidth = 10 rad/s and 100 rad/s are combined together in this study, where each accounts for 50% of the total power consumption.

The model identification results are listed below, which includes the estimated model parameters in Table 4.4 and the response comparison in Fig. 4.12. Comparing with the example in Section 4.3.4.1, the accuracy rate shown in Table 4.4 is not as good as the identification results where VSD aggregated models are clustered and estimated separately. Also, the estimated parameter $K_{i,est} = 0$, and this is due to the preset constraint $K_{i,est} \geq 0$. A $K_{i,est}$ which is smaller than 0 will be provided if this constraint is removed, and the identification results are not shown here for simplicity consideration. The mismatch on $K_{i,est}$ means that the aggregated model for this case no longer follows the predefined VSD model format since the equivalent PI controller does not maintain its practical function anymore. Meanwhile, the accuracy rate of this parameter identification case is 94.48%, which is significantly lower than the last two cases where the clustering process is involved.

Table 4.3: VSD aggregated model estimated parameters and accuracy rate.

VSD group No.	H_{est}	$K_{p,est}$	$K_{i,est}$	$\omega_{m,ref,est}$	$K_{f,est}$	accuracy
1	1.4995	30.16556	3.8448	0.7049	4.002	99.81%
2	1.5176	325.6324	49.1555	0.7049	3.9877	99.41%

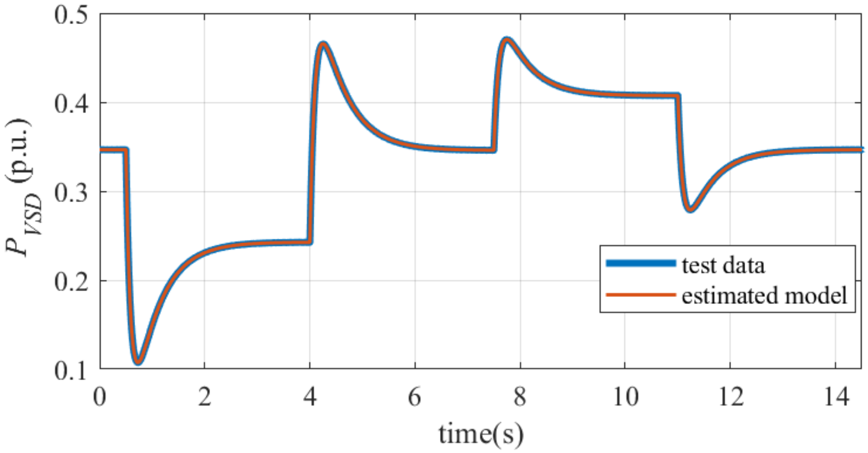

(a) Response comparison of VSD group 1.

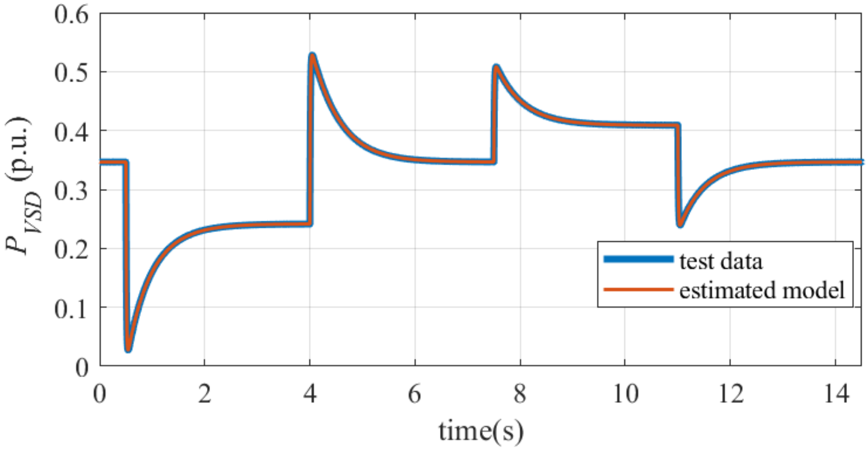

(b) Response comparison of VSD group 2.

Figure 4.11: Comparison of load power response between the estimated model and measured response data.

Table 4.4: VSD aggregated model estimated parameters without clustering.

H_{est}	$K_{p,est}$	$K_{i,est}$	$\omega_{m,ref,est}$	$K_{f,est}$	accuracy
1.429	76.0365	0	0.7049	4.0527	94.48%

Therefore, the predefined VSD model format is not suitable for the VSD aggregated model if multiple diverse different control bandwidths are included in the VSD load unit group.

4.4 Responsive VSD Load Impact on Grid Frequency

4.4.1 VSD Load Control Architecture

For the large-scale power network with multiple load units, an effective controller structure is critical for appropriately utilizing responsive load's potential. The existing responsive load control structures which are commonly used for providing grid frequency support mainly consist of the following three types: decentralized controller[122, 123, 124], centralized controller[125, 126], and hierarchical hybrid controller[127, 128, 129].

The main characteristic of the decentralized control method, which is illustrated in Fig. 4.13a, is that the control signal of each device is generated locally and independently by the individual controller. The advantage of such a control scheme is it has a simple communication network without sending signals to the control center/system operator. However, the decentralized control structure lacks the capability to coordinate between different load units. And the local controller cannot perform self-adjustment according to the available load power reserve in the grid. Therefore, the aggregated performance of the responsive load is less effective to follow the required droop response.

The main characteristic of the decentralized control method, which is illustrated in Fig. 4.13b, is that control signals of all devices are generated by the control center. The advantage of the centralized controller is that it can largely utilize the potential of responsive loads by coordinating each load device's operation, because the control center can process the information of all responsive loads. However, the centralized control system compromises the communication speed. Meanwhile, the control capability of the centralized control is limited, considering that the number of load devices processed by the one single control center is relatively small.

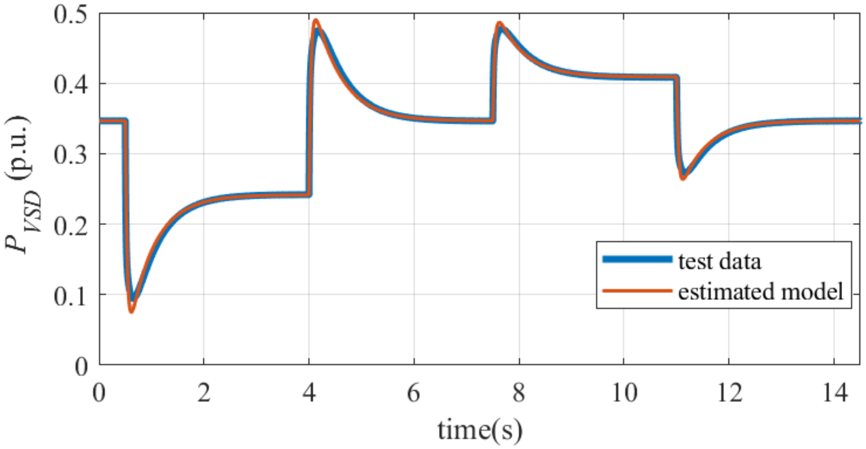

Figure 4.12: Comparison of load power response between the measured response data and the estimated model without clustering VSD units according to controller bandwidth.

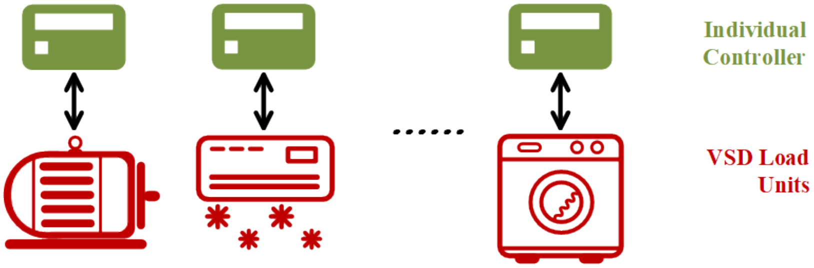

(a) Decentralized control.

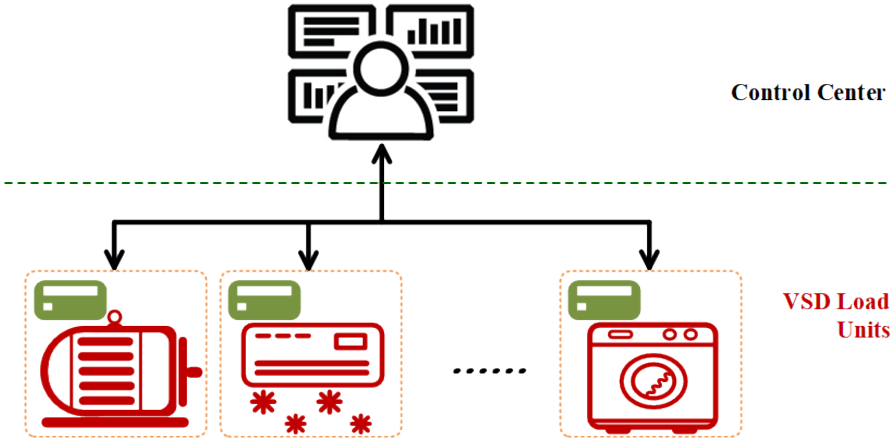

(b) Centralized control.

Figure 4.13: Frequently used controller structure for responsive load [128].

The hybrid hierarchical control architecture is regarded as a mix of the centralized controller and the decentralized controller. Different from the centralized controller, the control center of the hybrid control architecture is regarded as the top-layer controller, which is only responsible for processing some critical parameters which are related to the overall regulation of the power network operation. Below the top layer controller, the load aggregator plays the role of the bridge between individual load units and the control center – the load aggregator generates control commands for load units according to the control signals provided by the top layer controller. The load units will respond to the grid frequency event respectively with the command provided by the load aggregator.

The multiple VSD loads operation is regulated by a hybrid controller in this dissertation, considering the advantages stated above. The adopted hybrid control architecture is shown in Fig. 4.14.

The control center is at the top layer, which is responsible for deciding K_{droop} based on the grid power reserve P_{prim}, and these commands are updated every several hours. The load aggregator is at the middle layer, which coordinates available VSD load units, so each load unit sends its corresponding operation status to the load aggregator, *e.g.,* $\omega_{r,ini,i}$, $P_{base,i}$ and $P_{re,i}$. Meanwhile, the load aggregator sends K_{droop} command to each load by transferring it to K_{prim}, frequency threshold and selection command. The bi-directional communication between load aggregator and load units can be around once every 2 minutes or longer, considering reducing the communication cost.

VSD load units are at the local layer, and these devices are assumed to be able to measure the grid frequency locally. So load units can respond to the frequency event rapidly according to the control command sent by the load aggregator.

4.4.2 System Implementation for Frequency Responsive Load

Industrial end-use loads, such as ventilation fans or water circulation cooling pumps, can be actively controlled to provide grid frequency service. The following implementations are required to realize the hybrid hierarchical control introduced above: 1) Local measurement units and effective load controllers should be implemented for the load unit level. 2) A load aggregator is necessary which serves as an intermediate provider, and it is helpful for letting more individual load units participate in power grid dispatch. 3) The central control is provided by the grid utility company for a particular region. The frequency support commands are decided by the control center by evaluating the overall operation status of the whole grid.

Besides, bidirectional communication channels should be provided between each layer in the hierarchical control architecture, as illustrated in Fig. 4.14.

4.4.3 VSD Load Primary Frequency Support Efficiency Considering Communication Delay

As introduced in Section 4.4, centralized control architecture can flexibly coordinate the load units during the grid frequency event, since the control center directly provides performance command to the load units. However, the load cannot respond rapidly considering the relatively long communication delay, which is due to the long communication path from load to the top control layer [130]. In comparison, the load can respond to the frequency deviation instantaneously if adopting the decentralized control architecture, but it is complicated to realize the coordination between multiple load units. The hybrid architecture has the advantage of both centralized and decentralized control architecture, which features overall coordination within the load units group with rapid frequency response. However, this rapid response is based on the predefined load coordination provided by the load aggregator, which is updated frequently (around every two minutes or longer). It is still necessary to consider the communication delay if applying real-time coordination algorithm to the hybrid control architecture.

The frequency support efficiency of the hybrid control architecture presented above is introduced in this subsection, including the load coordination scheme and communication delay model. Meanwhile, the frequency responsive load with centralized control architecture is also modeled and studied compared to the introduced hybrid control architecture-based responsive load.

4.4.3.1 Simplified Power System Model

The VSD load frequency support function is simulated and examined in Simulink, where a simplified power grid model is adopted, as illustrated in Fig. 4.15. Critical model parameters used to build the power system are listed in Table 4.5.

As shown in Fig. 4.15, the function block named "VSD load model" represents the VSD load and corresponding control system model illustrated in Fig. 4.14. If changing the power ΔP_{in} sent to the governor, a power mismatch between generation and demand is created, thus introducing power grid frequency events. So power system frequency contingency is created accordingly to evaluate the VSD load frequency support in the following part of this section. Additionally, to emphasize the responsive load primary frequency support function, the generator secondary frequency support control is disabled in this simplified system model.

4.4.3.2 Coordination Algorithm on Hybrid VSD Control Architecture

As introduced above, the hybrid control architecture features advantages of both decentralized and centralized control architecture, which largely decrease the communication delay. However, the real-time coordination between load units depends on communication between load aggregators and end users. So in this section, the frequency responsive VSD load with real-time coordination is simulated and compared with other control schemes and architectures. The operation principle of adopted coordination method is summarized as:

- The number of VSD load units N_{VSD} involved in frequency support is decided based on Δf as expressed in (4.39):

  $$N_{VSD} = \frac{\Delta f}{f_{max} - f_{db}} \cdot N_{VSD,tot} \tag{4.38}$$

  where $N_{VSD,tot}$ represents the number of total available VSD load units. Load aggregator will keep N_{VSD} at the maximum value during the frequency event to avoid the frequent switch on/off of load units.

  Meanwhile, frequency control coefficient K_{fi} for each load unit, which is expressed in (4.18), is required to be adjusted according to N_{VSD} following (4.39) to maintain the

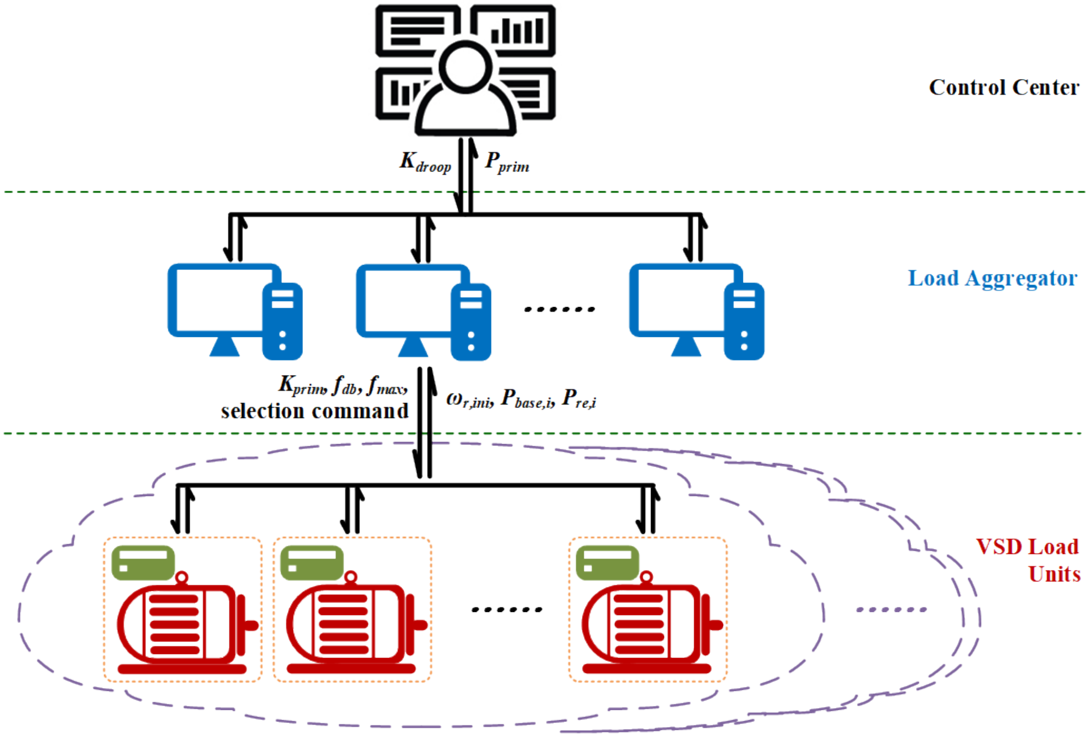

Figure 4.14: Frequency responsive VSD load hybrid control architecture.

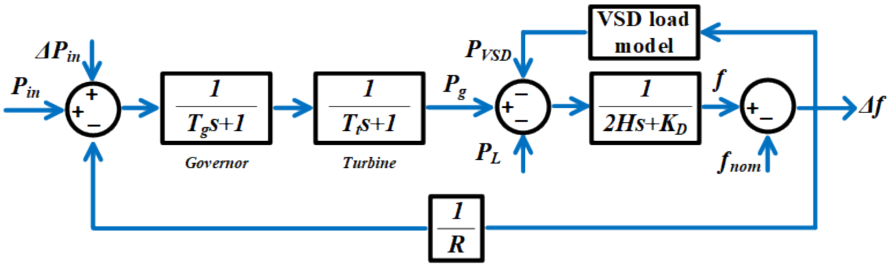

Figure 4.15: Simplified power system model.

Table 4.5: Simplified power system model parameters.

Parameter	T_g	T_t	H (s)	K_D	R
Value	0.4	0.1	3	0.02	0.05

required K_{droop}.

$$K'_{fi} = \frac{N_{VSD,tot}}{N_{VSD}} \cdot K_{fi} \tag{4.39}$$

where K'_{fi} represents K_{fi} after adjustment.

- Load aggregators randomly dispatch the participation of VSD load units periodically (*e.g.,* every 15 minutes), which helps balance the usage of each load unit.

4.4.3.3 Numerical Studies: VSD Load Grid Support Function

Frequency support comparison between different control architectures focusing on impact of communication delay is introduced in this subsection. Model of VSD load with different control architectures in power system illustrated as Fig. 4.15 is developed in Simulink. The frequency increase and decrease events with different generation-demand power mismatch are evaluated and illustrated in Fig. 4.16 and Fig. 4.17.

In the frequency decrease event shown in Fig. 4.16 and Fig. 4.17, VSD load regulated by hybrid control architecture without real-time coordination is equivalent to communication delay = 0. This is because coordination commands are sent to VSD loads before the frequency event happens, so each load unit will respond to Δf spontaneously. In comparison, VSD load regulated by hybrid control architecture with real-time coordination is represented as with relatively short communication delay, and model with communication delay = 0.3 s and 0.4 s are both regarded as equivalent to this control architecture as shown in Fig. 4.16. This is because that in the hybrid architecture, coordination commands will be sent from the aggregator to load units after the frequency event occurs, which requires a relatively short communication path. Additionally, the communication delay is longer when adopting a centralized controller since each load unit cannot measure and respond to Δf spontaneously, so communication delay = 1 s is used to represent the centralized control architecture.

As shown by simulation results comparison in frequency increase and decrease event, VSD load regulated by hybrid control architecture without coordination has the best frequency support function due to the negligible communication delay. In comparison, when communication delay = 0.3 s and 0.4 s, the frequency support efficiency is slightly worse than

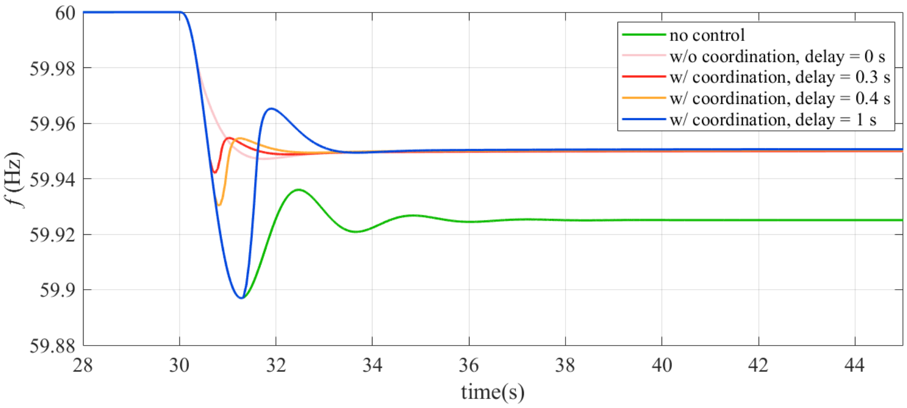

(a) ΔP_{in} = -0.025 p.u.

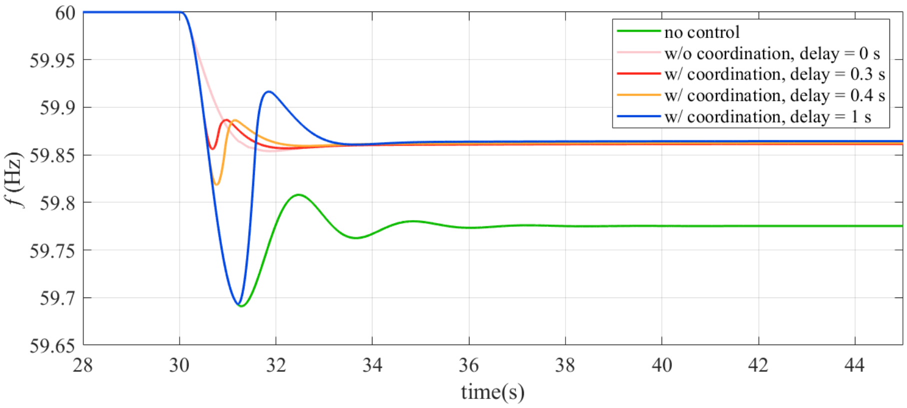

(b) ΔP_{in} = -0.075 p.u.

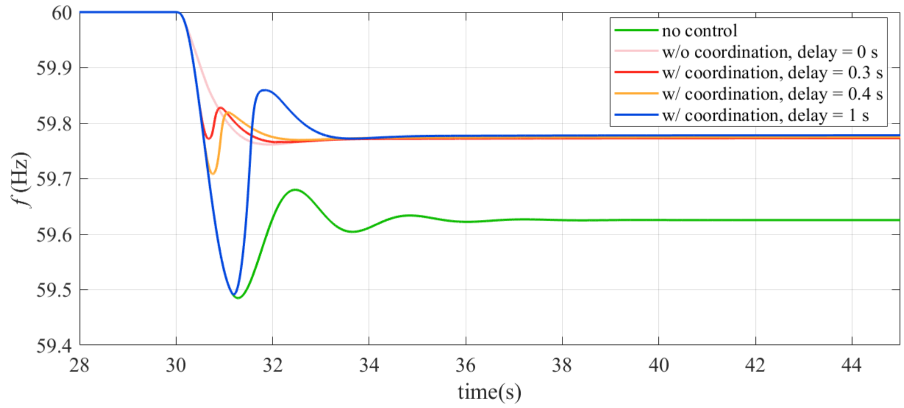

(c) ΔP_{in} = -0.125 p.u.

Figure 4.16: Frequency decrease event: evaluation of communication delay impact on frequency responsive VSD load grid support efficiency.

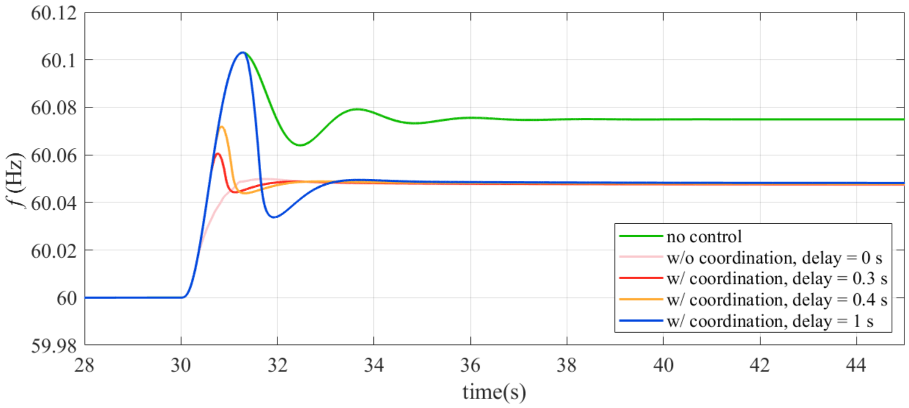

(a) $\Delta P_{in} = 0.025$ p.u.

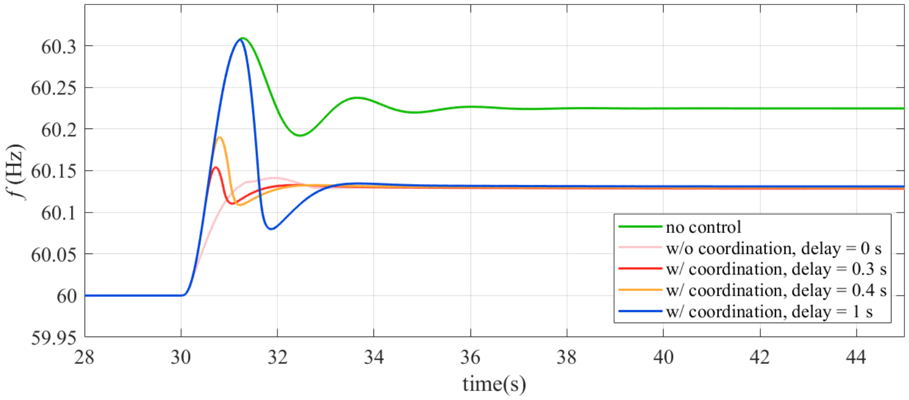

(b) $\Delta P_{in} = 0.075$ p.u.

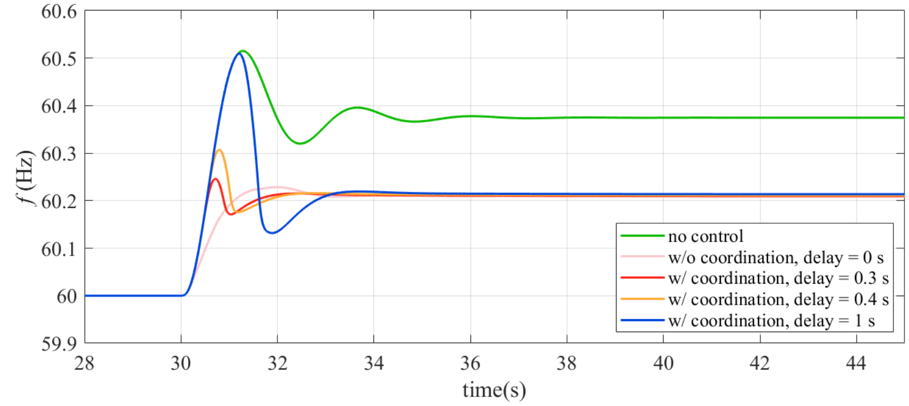

(c) $\Delta P_{in} = 0.125$ p.u.

Figure 4.17: Frequency increase event: evaluation of communication delay impact on frequency responsive VSD load grid support efficiency.

in the last case. Additionally, in Fig. 4.16b and Fig. 4.16c, the frequency support efficiency are almost identical between communication delay $= 0$ s and $= 0.3$ s, which is because higher Δf introduces higher active power support. So VSD load regulated by hybrid control architecture with coordination can also effectively support the grid frequency with short communication delay. In comparison, the centralized control architecture simulated in this section cannot effectively mitigate the grid frequency nadir, as shown by the blue curves. This is because the grid model inertia constant is low, considering high renewable generation penetration. So according to the simulation results, the responsive load with the centralized controller cannot be fully activated before grid frequency reaches a nadir, resulting in a frequency nadir almost as much as that without any responsive load involved.

Meanwhile, all control architecture can be designed to follow the predefined K_{droop} regardless of ΔP_{in} as shown in Fig. 4.16c.

Accordingly, hybrid control architecture with and without coordination can provide effective frequency support in both transients and stabilized operating conditions. The hybrid control architecture without coordination can simplify the control and communication design, while the hybrid control architecture with coordination can decrease the number of load units required to participate in the grid support function.

4.5 Conclusions

In this chapter, the aggregated performance of providing frequency support by multiple VSD load units is characterized based on the simplified model which is presented in the last chapter. The VSD load aggregated model is specifically designed for the pump/fan load of which T_L is proportional to the square of ω_r. Additionally, the VSD aggregated model parameter identification method is proposed.

The potential of VSD loads in terms of providing primary frequency support has also been discussed in this chapter. The equivalent operational reserve provided by each VSD load unit is identified, which makes up the total power reserve for primary frequency support provided by VSD load units in the studied region. The mathematical expression of matching the required droop rate by adjusting frequency support coefficient K_{fi} in each VSD load unit is also elaborated.

Additionally, the hybrid control architecture is adopted to control multiple responsive VSD loads' performance. The responsive load frequency support performance with different control architecture and coordination schemes are simulated and compared by Simulink models. The hybrid control architecture is shown to regulate the frequency performance more effectively, compared with centralized control architecture.

Chapter 5

VSD Load Grid Frequency Support: Experimental Verification and Discussion

5.1 VSD Grid Frequency Support Experimental Analysis Performed on HTB

The evaluation of VSD load primary frequency support is conducted on the HTB, which is illustrated in Fig. 5.1. The secondary frequency support is disabled to emphasize the primary frequency support efficiency. The responsive load experimental results are shown and explained in this section.

As mentioned in previous sections, VSD based pump/fan loads are appropriate candidates for frequency responsive loads. According to the current load profile, only a small portion of this type of motor load is driven by the VSD, resulting in limited responsive load power reserve. However, the end-user electrification will greatly promote the conversion of motor loads to electric drives in the near future as expected in [131]. Therefore, it is reasonable to predict that a considerable number of motor loads will evolve to VSD loads. The VSD frequency responsive load experiments introduced in this section are based on this assumption, that a relatively high penetration level of VSD based motor load will appear in the future power grid, and exert considerable impact on the grid operation.

Western Electricity Coordinating Council (WECC) system is emulated in the HTB, and VSD load experiments introduced in this chapter are performed based on it. The responsive VSD load model is integrated into the southeastern area of the simplified WECC system to evaluate the frequency support functions. The simplified WECC diagram is illustrated in Fig. 5.2. The VSC-based power emulators in HTB mimic Bus 1 to 10, of which red circles represent generation buses, green circles represent load buses, and blue circles represent generation and load combined buses.

There are two possible solutions to represent the aggregated VSD load dynamic performance in HTB experiments: 1) Use multiple VSC based power emulators, and each emulator adopts one VSD load unit model, which is illustrated in Fig. 5.3a; 2) Use one VSC based power emulator which characterizes multiple VSD load unit models. The second option, which is illustrated in Fig. 5.3, is adopted since it is beneficial to simplify the HTB power network configuration and decrease the number of power emulators. Meanwhile, considering the computational processing capability of the power emulator DSP, 6 to 8 VSD load units with diverse model parameters are applied to one power emulator unit.

5.2 VSD Load Frequency Support Experimental Verification

The responsive VSD load penetration level changes based on different weather and time of the day, so the overall impact of frequency support function will vary significantly. 8 cases are tested to fully represent frequency support function at different operating points: 1) normal summer at 4 am, 2) normal summer at 10 am, 3) normal summer at 4 pm, 4) normal summer at 10 pm, 5) hot summer at 4 am, 6) hot summer at 10 am, 7) hot summer at 4 pm, 8) hot summer at 10 pm. The responsive VSD load is evenly applied to each load bus. The load profile of each load bus is presented in Table 5.1.

Figure 5.1: HTB Experimental platform.

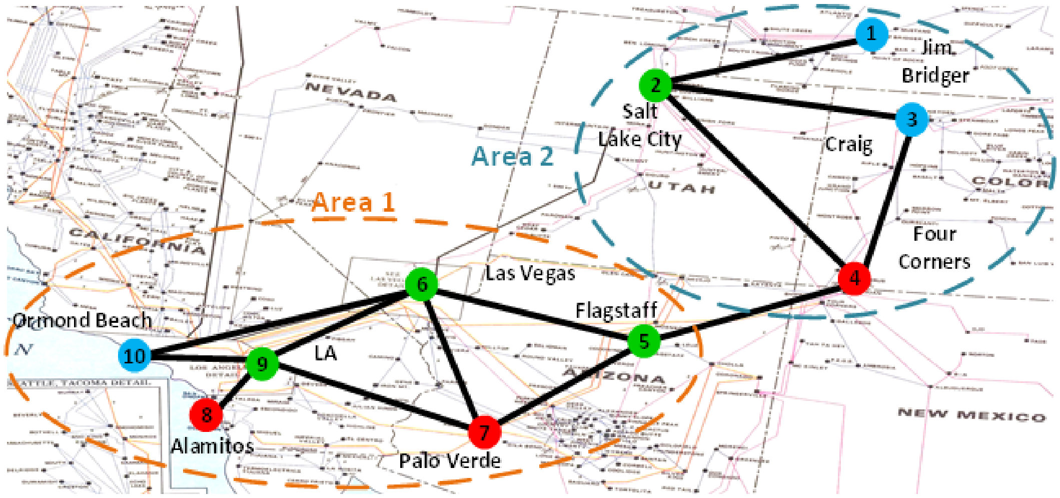

Figure 5.2: Simplified WECC power system.

Table 5.1: Test power network load profile.

Bus	P (p.u.)	Bus	P (p.u.)	Bus	P (p.u.)	Bus	P (p.u.)
1	0.1	2	0.1	3	0.1	5	0.1
6	0.2	9	0.35	10	0.04		

5.2.1 Frequency Event with Unequal K_{droop}

First, the VSD load grid frequency support function with unequal K_{droop} is performed and analyzed. In this scenario, the generation unit emulator model parameters are listed in Table 5.2. Also, 8 different operating points with various VSD load penetration levels are listed in Table 5.3. K_{droop} for each load unit is decided according to (4.13), so K_{droop} is different considering different P_{re} as listed in Table 5.3. The grid frequency increase event is performed by shedding 0.08 p.u. of the total load at Bus 5, and the grid frequency decrease event is performed by tripping 0.08 p.u. of the total generation at Bus 7. G7 and G4, which represent generators at Bus 7 and 4, are used to demonstrate the grid frequency at area 1 and 2, respectively. The load at Bus 2 and 5, which are represented as L2 and L5, are selected to represent the VSD load response when subject to frequency variation.

Grid frequency increase event for Case 1 to 8 is illustrated in Fig. 5.4. All represented cases demonstrate different grid support potential under the same power mismatch condition. Grid frequency deviation is more significant in cases with less amount of VSD load, and less significant with more VSD load. For example, Δf is the smallest in Case 1, and the largest in Case 7, corresponding to different load penetration levels in each case. Meanwhile, more load active power support is provided in cases with higher VSD load percentage by observing L2 and L5 experimental results.

As shown in Fig. 5.5, similar frequency support performance is observed in the grid frequency decrease event: in cases which have higher VSD load penetration level, more active power supports are provided by loads to mitigate the generation and load power mismatch, thus yielding less grid Δf. Fig. 5.5 only includes the experimental results from Case 1 to 4 for simplification since the trend is similar for the other 4 cases.

5.2.2 Frequency Event with Equal K_{droop}

Next, the VSD load grid frequency support function with equal K_{droop} is also investigated. Although equal K_{droop} is applied, the grid support performance may vary due to unequal VSD load penetration level. To emphasize the impact of responsive load account, a relatively low VSD load penetration level is adopted in this experiment compared with the last scenario,

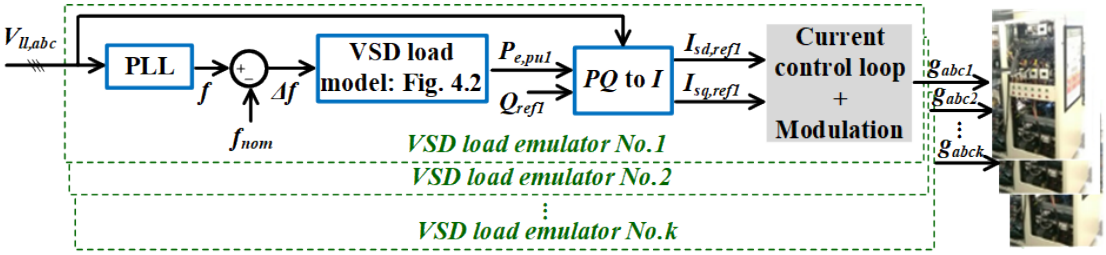

(a) Option No. 1: Multiple VSC based power emulators, each emulator adopts one responsive VSD load model.

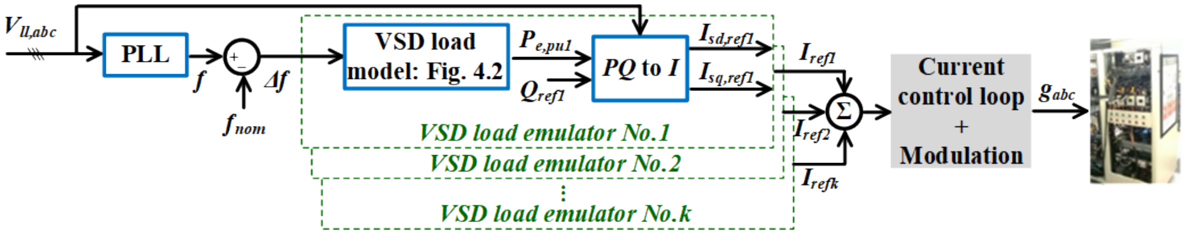

(b) Option No. 2: One VSC based power emulator, which adopts multiple responsive VSD load models.

Figure 5.3: Aggregated responsive VSD load representation in the HTB.

Table 5.2: HTB generation unit model parameters.

Generator No.	T_g	T_t	H (s)	K_D	R
G1	0.2	0.0	13	0.0	0.1
G2	0.2	0.0	6	0.0	0.1
G3	0.2	0.0	13	0.0	0.1
G7	0.2	0.0	13	0.0	0.1
G8	0.2	0.0	13	0.0	0.1
G10	0.2	0.0	6	0.0	0.1

Table 5.3: VSD load penetration level: for unequal K_{droop} scenarios.

Weather	4 am	10 am	4 pm	10 pm
Normal summer	26.26%	17.62%	15.0%	19.74%
Hot summer	16.92%	10.48%	8.34%	11.16%

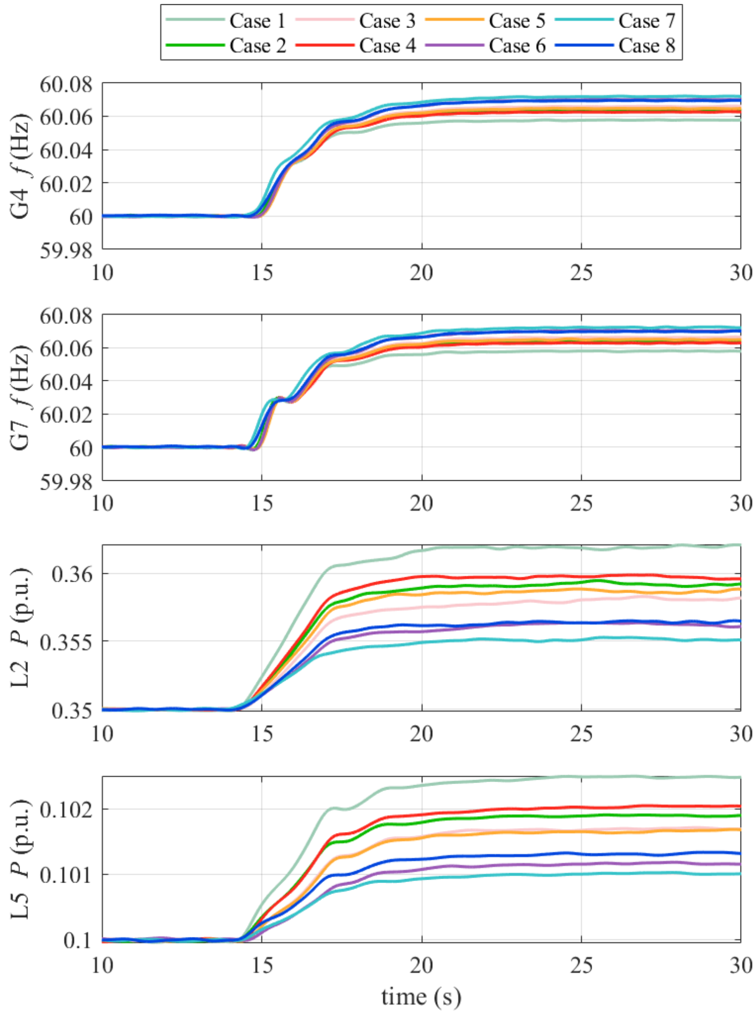

Figure 5.4: VSD load providing grid frequency support in the frequency increase event with unequal K_{droop}.

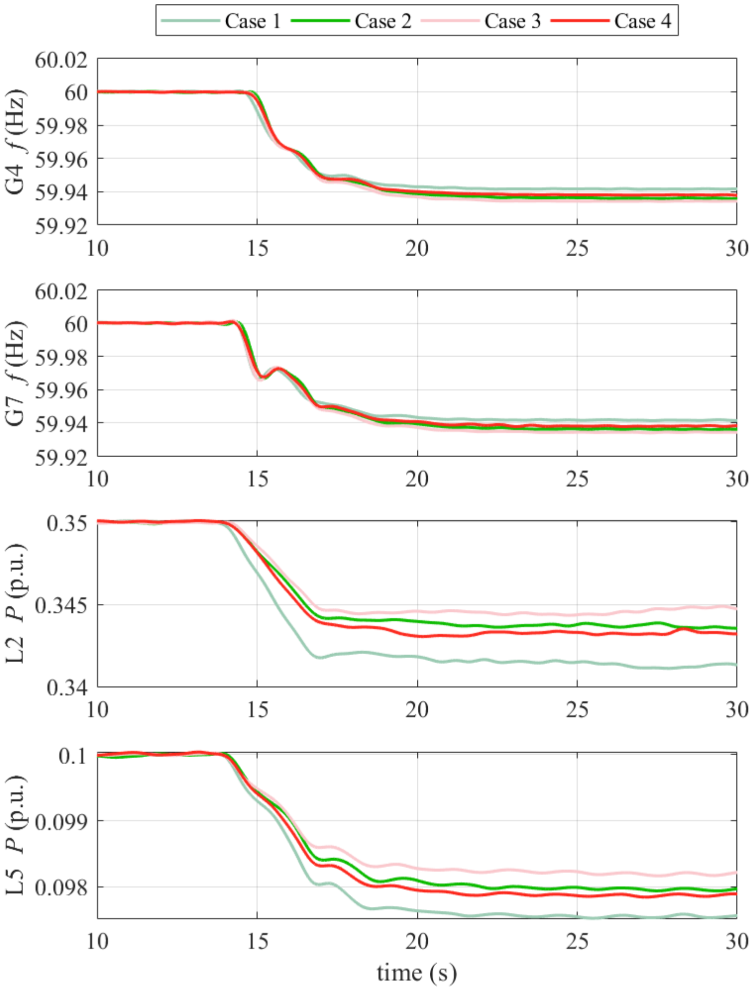

Figure 5.5: VSD load providing grid frequency support in the frequency decrease event with unequal K_{droop}.

which is listed in Table 5.4. Experimental results comparison for frequency increase event between Case 4 and 8 is illustrated in Fig. 5.6 and Fig. 5.7. When $K_{droop} = 20$ p.u./Hz, the grid frequency response of each load is very similar since the required active power contribution can be provided in each case, so different cases show similar grid frequency performance in Fig. 5.6.

In comparison, if increasing K_{droop} to 40 p.u./Hz, the required active power support cannot be fully provided by Case 8 considering the limited VSD load power reserve. So a significant grid frequency and power difference are observed between Case 4 and 8 in Fig. 5.7. In conclusion, the VSD load power reserve limit varies considering different operating points, leading to different impacts to the grid even with identical K_{droop} command. Therefore, the frequency support decision should be effectively made considering the impact of responsive load amount, *i.e.,* a large K_{droop} can be satisfied when load power reserve is sufficient, and K_{droop} should be decreased appropriately when the load reserve is limited.

5.3 Communication Delay Impact on Frequency Support Efficiency

As introduced in Section 4.4.3, the responsive load communication delay is almost negligible if adopting hybrid control architecture, since the load units are required to measure Δf and respond to it locally. Meanwhile, responsive loads will be periodically updated with coordination signals, which are sent from the top control layer before frequency events occur. In comparison, loads adopting centralized control architecture cannot respond rapidly considering the long communication path from load to the top control layer. Experiments in terms of mimicking the communication delay for different control architectures are performed on HTB and represented in this section. The communication delay impact on frequency support performance is investigated and discussed.

Table 5.4: VSD load penetration level: for equal K_{droop} scenarios.

Weather	4 am	10 am	4 pm	10 pm
Normal summer	13.13%	8.81%	7.50%	9.87%
Hot summer	8.46%	5.24%	4.17%	5.58%

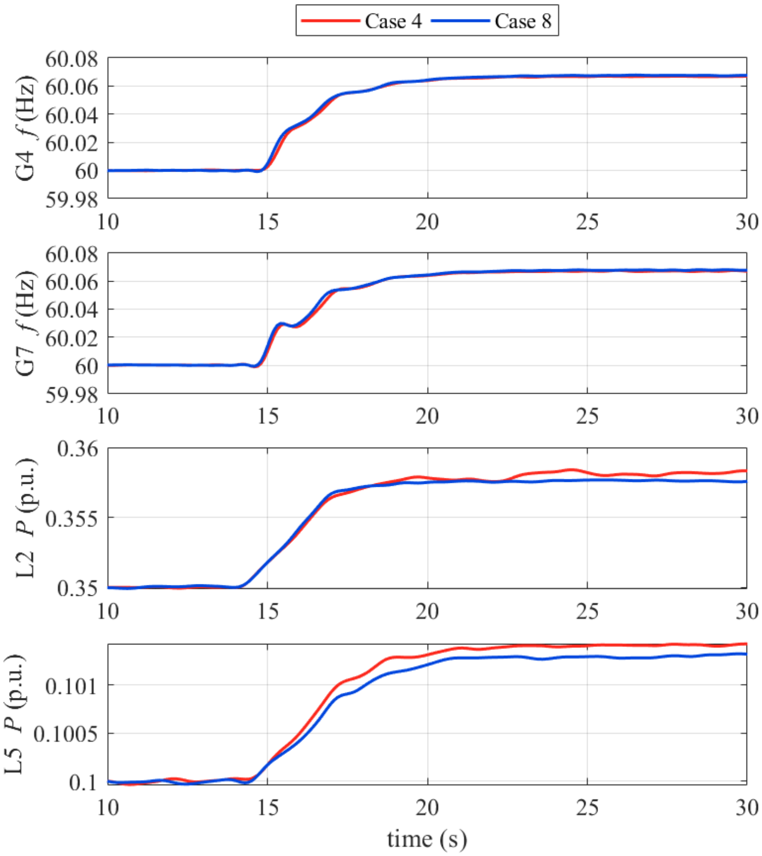

Figure 5.6: VSD load providing grid frequency support in the frequency increase event with equal K_{droop}: $K_{droop} = 20$ p.u./Hz.

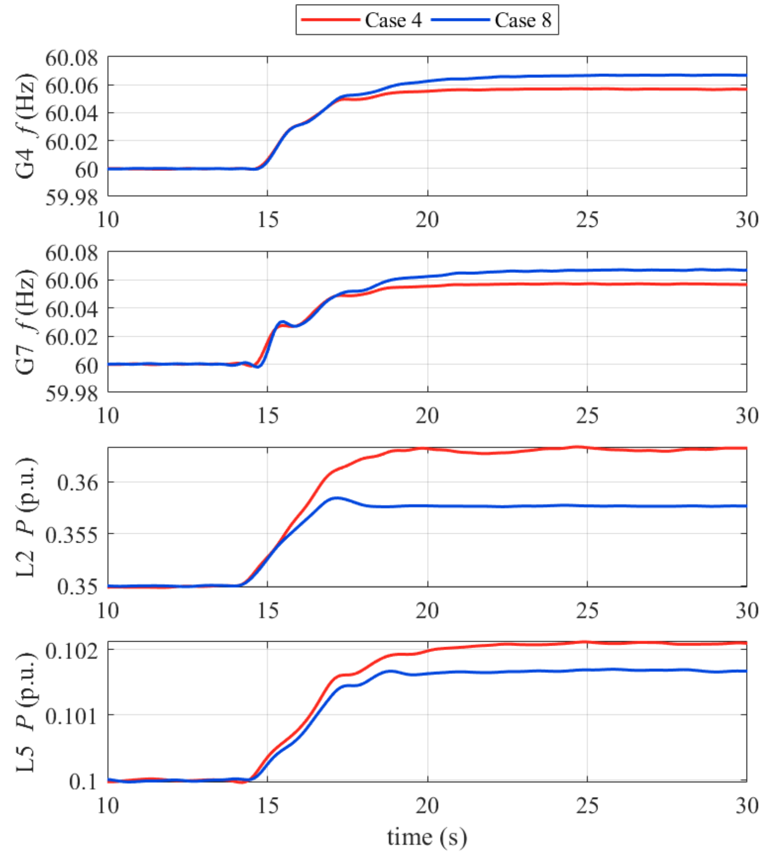

Figure 5.7: VSD load providing grid frequency support in the frequency increase event with equal K_{droop}: $K_{droop} = 40$ p.u./Hz.

5.3.1 Power Network Configuration and Generation Unit Design

As shown by simulation results in Section 4.4.3.3, communication delay influences the grid frequency transient performance right after the contingency occurs. So in this scenario, relatively low inertia constant values are applied to generation unit power emulators considering 1) emphasize the grid frequency transient response after the frequency event, 2) represent the power grid low inertia status when RES penetration level is high. Critical model parameters for HTB generation emulators are listed in Table 5.5. The responsive VSD load penetration level follows Table 5.3.

5.3.2 Frequency Increase/Decrease Event with Different Communication Delay Amounts

In this scenario, the following delay amount T_d are considered in experiments: 0.4 s, 0.8 s, and 1.2 s. In comparison, the following cases are also included: no VSD load support, and VSD load with $T_d = 0$. Communication delay amount reflects control architectures adopted by responsive loads: $T_d = 0$ is equivalent to adopting hybrid control architecture, while $T_d \neq 0$ is equivalent to centralized control architecture. For the equivalent hybrid control model, the signal transfer process is ignored assuming that the coordination commands have already been sent to each VSD load.

The frequency increase event is created by the load shed at Bus 5. Different T_d and load shed amounts are applied to responsive loads and the power grid, of which the corresponding experimental results are illustrated in Fig. 5.8. In Fig. 5.8a where load shed = 0.05 p.u., responsive VSD loads contribute to mitigating Δf by providing active power support during frequency events. Meanwhile, f stabilizes at the same value regardless of T_d in cases where responsive loads are applied. As shown in Fig. 5.8a, the frequency support is most effective when there is no communication delay. Meanwhile, f transient response when $T_d = 0.4$ s is similar to that when $T_d = 0$ s. However, longer T_d introduces larger frequency nadir. This is because PE-based responsive load can respond to Δf command rapidly, so it can contribute to mitigating frequency nadir right after frequency disturbance occurs if T_d is short. Furthermore, load shed = 0.08 p.u. is also tested and illustrated in Fig. 5.8b. The above phenomena can be similarly reflected when applying different load shed amounts. Additionally, the communication delay experimental results are consistent with simulation results shown in Section 4.4.3.3.

Meanwhile, the frequency decrease event is created by generation trip at Bus 7, which is illustrated in Fig. 5.9. Similar to the frequency increase events explained above, faster VSD load response results in smaller frequency nadir, which is beneficial to improving the power network stability.

In conclusion, VSD loads with hierarchical control architecture can effectively promote frequency support efficiency considering the rapid load response.

5.4 Conclusion

- The impact of different load operating points is investigated regarding frequency support capability. Experimental results show that the VSD load can effectively mitigate the grid frequency deviation if operating within the total load power reserve. Meanwhile, droop control coefficient K_{droop} is decided according to the power grid operating point, which is significantly influenced by the time of the day and the weather.

- According to experimental results, VSD load power reserve limit varies with the time and weather, leading to varied frequency support performance even with identical K_{droop} command.

- The impact of control architecture on the frequency support efficiency is investigated. Responsive load performance regulated with different control architectures can be represented with different communication delays. Experimental results show that the hybrid control architecture without real-time coordination can rapidly respond to grid frequency deviation without any communication delays, while the hybrid control with real-time coordination has to go through a communication delay before effectively activated. The frequency support performance of the hybrid control is much better than the centralized control since the communication delay between load units and load aggregator is much shorter.

Table 5.5: HTB generation unit model parameters.

Generator No.	T_g	T_t	H (s)	K_D	R
G1	0.2	0.0	5	0.0	0.1
G2	0.2	0.0	6	0.0	0.1
G3	0.2	0.0	5	0.0	0.1
G7	0.2	0.0	5	0.0	0.1
G8	0.2	0.0	5	0.0	0.1
G10	0.2	0.0	6	0.0	0.1

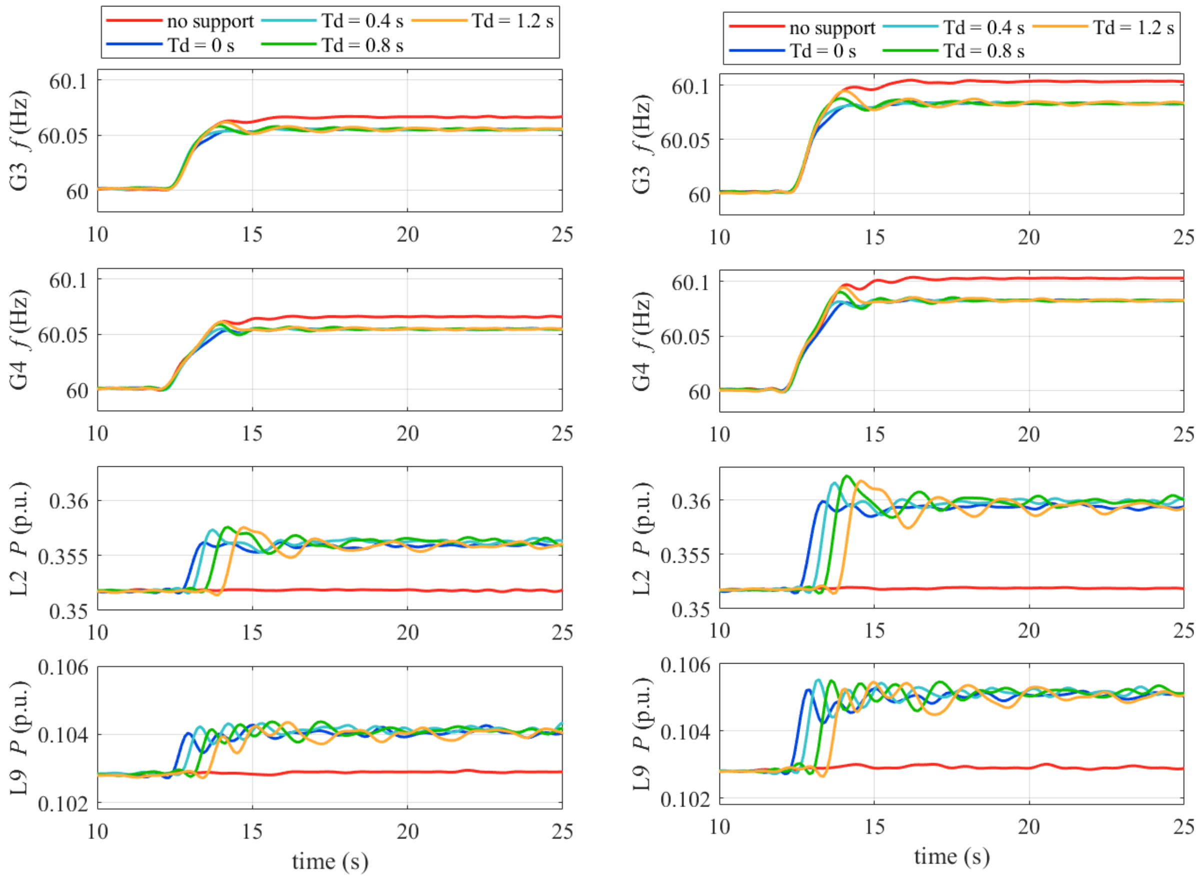

(a) 0.05 p.u. load shed at Bus 7.

(b) 0.08 p.u. load shed at Bus 7.

Figure 5.8: VSD load providing grid frequency support in the frequency increase event.

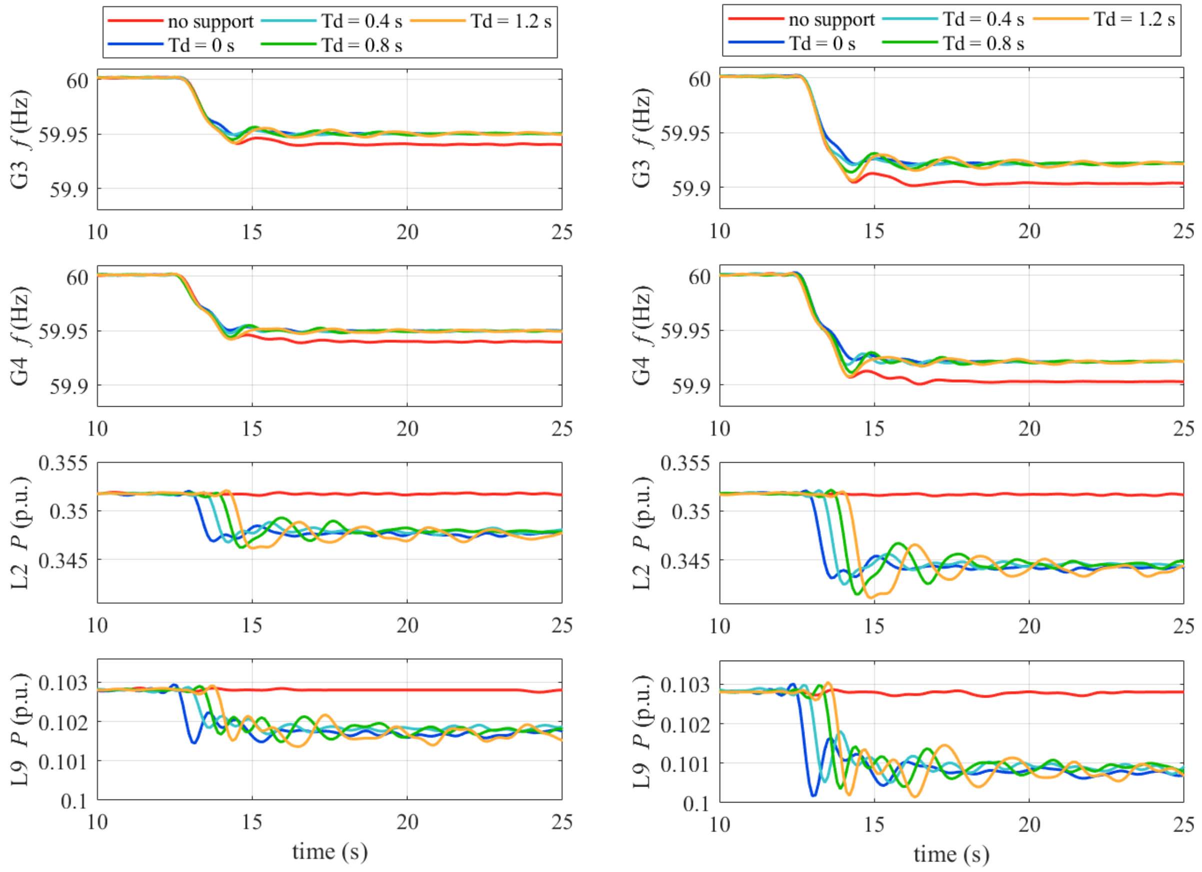

(a) 0.05 p.u. generation trip at Bus 6.

(b) 0.08 p.u. generation trip at Bus 6.

Figure 5.9: VSD load providing grid frequency support in the frequency decrease event.

Chapter 6

Modeling and Simplification of Fast Electric Vehicle Charging Unit for Transient Stability Simulation Environments

As presented in Section 2.3.2, the PE interface dynamic performance cannot be fully reflected in TS simulation programs because the TS simulation mainly focuses on the electromechanical transients in the power grid. Thus TS simulation tools cannot process the high-bandwidth dynamic performance of electric devices. Therefore, the PE interfaced load should adapt to the TS simulation environment based on reasonable simplification. The fast EV charging unit is regarded as a typical example of a PE interfaced load, and the corresponding simplified model, which is suitable for utilization in the TS simulation program is introduced in this chapter.

6.1 Three-Phase EV Charging Unit: Topology and Control Algorithm

The most common topology of the fast EV charging unit is the three-phase full-bridge active-front-end rectifier connected with the buck converter, and corresponding control schemes are implemented into each power stage, respectively. In this chapter, the model and control scheme of the EV charging unit is discussed. Additionally, reasonable model simplification is introduced, which benefits the adoption of EV charger model into the TS simulation environment.

6.1.1 Topology and Application of Different Power Stages

The circuit topology of the fast EV charging unit studied in this dissertation is illustrated in Fig. 6.1, which includes the terminal ac bus V_t, the main charging circuit, and the battery load. Generally speaking, the charging circuit consists of two power stages: one of which is the three-phase active-front-end rectifier transferring the ac voltage supply to a stable dc voltage, and the other is a dc-dc converter regulating the battery charging mode [2]. As illustrated in Fig. 6.1, Z_L represents the adjacent transmission line impedance, L_f represents the active-front-end filter inductance, C_{dc} represents the rectifier dc-link capacitance, L_b represents the battery charger filter inductance, C_b represents the battery charger capacitance.

Therefore, there are four parts that are under consideration in the EV charger load modeling based on the EV charging unit illustrated above, which are: 1) terminal voltage V_t and transmission line impedance, 2) EV charger active-front-end, 3) dc-dc converter for battery regulator, and (4) EV battery load. V_t and transmission line impedance represent the interconnection between the power grid and the load, the active-front-end rectifier and the dc-dc converter mainly represent how the EV charger load performs according to the control scheme, and the EV battery load model represents the charging and discharging dynamic performance.

6.1.2 EV Charging Unit: Control Scheme Specification

Conventionally, uni-directional EV charging units are commonly applied, which can only be used for charging the EV battery. The prevalence of the three-phase rectifier made up of full-controlled switching devices allows for the development of bi-directional EV charging units, which have the potential to provide power grid support. Multiple G2V and V2G control algorithms have been introduced in Section 2.3.4.2. Except for the control and planning scheme focusing on the relatively long time scale, the following typical control algorithms which represent the most prevalent EV charger control functions are selected for load model studies:

1) G2V mode:

- Constant V_{dc} control: One of the most commonly used d-axis control schemes, which is used to provide a stable dc voltage for the next power stage. The constant V_{dc} control algorithm studied in this chapter is illustrated in Fig. 6.2.
- $I_{q,ref}$ determination: There are multiple methods to regulate $I_{q,ref}$ as introduced in Section 2.3.4.2. Here the constant reactive power Q control is modeled in this chapter, as illustrated in Fig. 6.3.

2) V2G mode:

- Primary frequency support: The EV charger load can be utilized to absorb or release active power according to the specific change of grid frequency deviation Δf, which will promote the overall power network stability. The EV charger load primary frequency regulation scheme is illustrated in Fig. 6.4.

  The constant Q control introduced from the G2V mode control scheme is very similar to the V2G reactive power regulation, so the constant Q control can also be adapted and attributed to the V2G control scheme. Therefore, the V2G reactive power regulation is not introduced and modeled in this chapter.

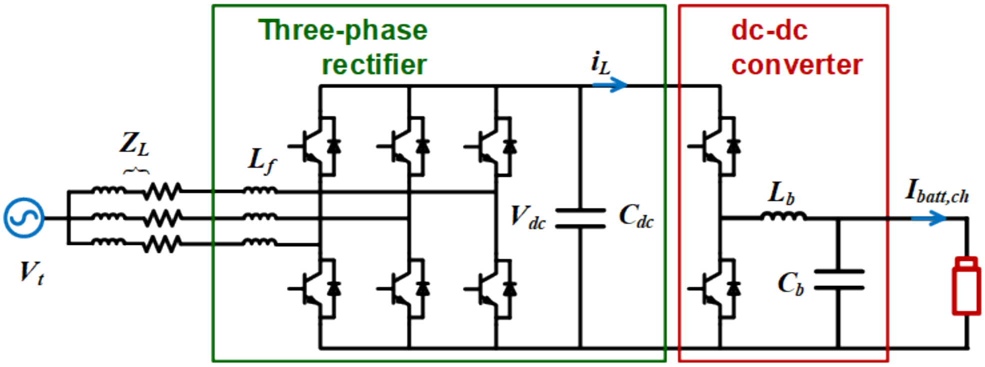

Figure 6.1: EV fast charging unit circuit topology.

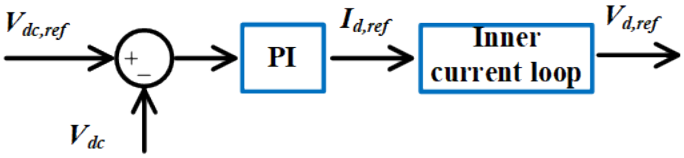

Figure 6.2: Typical G2V mode controller: constant V_{dc} control.

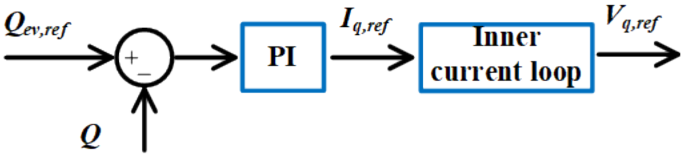

Figure 6.3: Typical G2V mode controller: constant Q control.

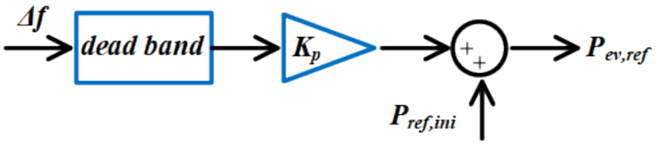

Figure 6.4: Typical V2G mode controller: primary frequency support control.

6.2 EV Charger Unit Model Simplification

As explained in Section 2.3.2, the detailed PE interfaced load model cannot be directly used for the transmission-level power network analysis considering the limitation of computational resources, so reasonable simplification is required when developing load models for TS simulation tools. The EV charger load simplification mainly lies in the following two aspects: 1) simplification of active-front-end rectifier, 2) simplification of the dc-dc battery charger.

6.2.1 Active-front-end Rectifier Simplification

TS simulators only focus on the electromechanical transients and oscillations between 0.1 and 3 Hz. So it is not necessary to reflect the detailed PE device model which characterizes the on/off switching status. The commonly used PE interface average-value model in *dq* coordinates is adopted, which concentrates on the converter cycle-to-cycle behavior so that fewer computational resources are required.

EV charging unit average model is illustrated in Fig. 6.5, the EV charger front-end rectifier side ac voltage is equally characterized by modulation indices m_d and m_q respectively. Moreover, these modulation indices are characterized by the rectifier control scheme, which is illustrated in Fig. 6.6. The active-front-end rectifier control schemes introduced in the last section are applied to d and q coordinates to provide $I_{d,ref}$ and $I_{q,ref}$ respectively.

The bandwidth of inner current control loop is so high that it is not appropriate to be characterized by TS simulators. So the EV charger unit ac current consumption is assumed to ideally follow the current command, with the inner current loop performing as a time delay.

Fig. 6.5 emphasizes the EV charging unit rectifier, so the dc-dc converter is simplified as a current source. The modeling and simplification of the fast EV charger second power stage are elaborated in the following section.

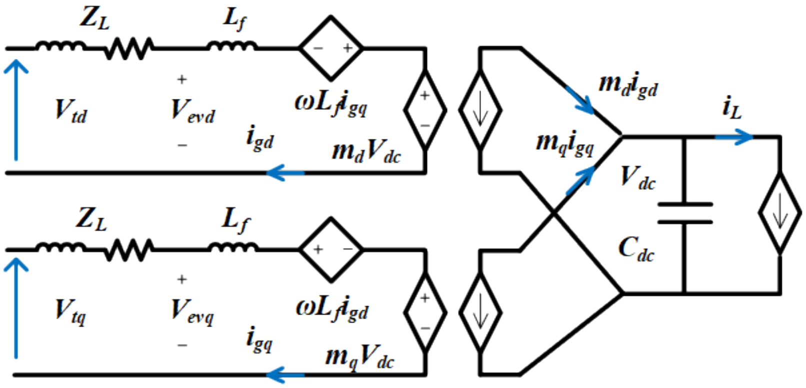

Figure 6.5: EV charging unit three-phase active-front-end average model.

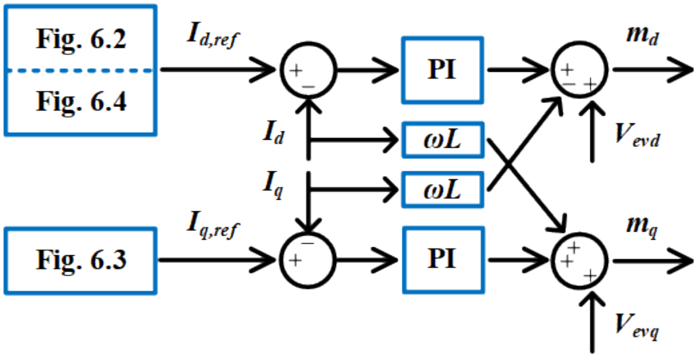

Figure 6.6: Control scheme of EV charging unit three-phase active-front-end.

6.2.2 DC-DC Converter and Battery Load Model

The dc-dc converter is powered by V_{dc} which is provided by the EV charger three-phase rectifier. As illustrated in Fig. 6.1, it is directly connected to the EV battery. The IGBT is used in the dc-dc buck converter in order to allow for the V2G application. Similar to that of the three-phase rectifier, the dc-dc converter also operates based on the fast switching of PE-based devices. So the corresponding average model is adopted to represent the simplified dynamic performance of a battery charger, which is illustrated in Fig. 6.7.

The three-phase rectifier output V_{dc} is simplified as a dc voltage source in the second power stage average model for simplification. As shown in Fig. 6.7, the corresponding dynamic performance is characterized by modulation index D_b. The average model can be mathematically expressed as:

$$V'_{dc} = D_b \cdot V_{dc} \tag{6.1}$$

$$I'_L = \frac{I_L}{D_b} \tag{6.2}$$

Two basic charging modes are adopted by the dc-dc converter, the constant current (CC) and constant voltage (CV) mode [84]. Which charging mode to use is determined based on the battery state of charge (SoC). The CC and CV mode control, which are selected to evaluate the battery charger model in this chapter, are illustrated in Fig. 6.8.

The CC mode control scheme is basically an i_{batt} feedback control loop with the PI regulator, which provides the buck converter modulation index reference $D_{b,ref}$. The CV mode control scheme is also designed based on regulating i_{batt}. As illustrated in Fig. 6.8, the voltage across the battery at the moment when the CV mode is activated, is used as the battery reference voltage $V_{batt,ref}$. Then $V_{batt,ref}$ is used for generating $I_{batt,ref}$ along with the SoC based on the analytical expression $f(SoC, I_{batt}, V_{batt,ref})$, which will be introduced in the following text.

The lithium-ion battery is selected as the battery load in this chapter, and the Shepherd model is used to characterize the battery performance [132]. For a single battery cell, the equivalent model can be illustrated as Fig. 6.9, where $E_{batt,sng}$ represents the internal battery voltage, $i_{batt,sng}$ represents the battery current flow ($i_{batt,sng} > 0$ when discharging the battery, and $i_{batt,sng} < 0$ when discharging the battery), R_0 represents the series resistance, and $V_{batt,sng}$ represents the battery output voltage, which is equivalent to V_{batt} in Fig. 6.7.

$E_{batt,sng}$ expression in Fig. 6.9 is:

$$E_{batt,sng} = E_{ocv} - K\frac{J}{J - \int i_{batt,sng}dt} \cdot \int i_{batt,sng}dt - K\frac{J}{\int i_{batt,sng}dt - 0.1J} \cdot i_{batt,sng} + Ae^{-B\int i_{batt,sng}dt} \tag{6.3}$$

where E_{ocv} represents the nominal open circuit voltage in V, J represents the battery cell capacity in Ah, K represents polarization constant in Ω, A represents exponential zone amplitude in V, and B represents inverse exponential zone time constant in Ah^{-1}.

Therefore, $V_{batt,sng}$ based on the battery charging and discharging process model in (6.3) is expressed as:

$$V_{batt,sng} = E_{batt,sng} - R_0 \cdot I_{batt,sng} \tag{6.4}$$

The SoC which reflects the charging status can be expressed as:

$$SoC = \frac{J - \int i_{batt,sng}dt}{J} \tag{6.5}$$

Based on (6.3), (6.4) and (6.5), $f(SoC, I_{batt}, V_{batt,ref})$ can be mathematically expressed and used for deciding current reference in the CV mode as introduced above. Equations (6.3) to (6.5) are only valid between $SoC = 20\%$ to 100%.

6.2.3 DC-DC Converter and Battery Load Simplification

The EV battery model can be simplified reasonably according to the Shepherd model expressed in (6.3). As illustrated in Fig. 6.10, the EV battery package comprises $b_{series} \cdot b_{para}$ battery cells connected together, *i.e.,* b_{series} battery cells are connected in series, and b_{para} of battery series strings are connected in parallel. The battery package voltage V_{batt} and battery charging current $I_{batt,ch}$, of which the positive direction is flowing into the battery package, are expressed in (6.6) and (6.7).

$$V_{batt} = b_{series} \cdot V_{batt,sng} \tag{6.6}$$

$$I_{batt,ch} = -b_{para} \cdot I_{batt,sng} \tag{6.7}$$

According to the SoC expression in (6.5), $\int i_{batt,sng} dt$ can be replaced by SoC, which is expressed as:

$$int = J(1 - SoC) \tag{6.8}$$

where int is used to represent $\int i_{batt,sng} dt$.

Substitute (6.6), (6.7) and (6.8) into (6.3), the relation between the output voltage V_{batt} and $I_{batt,ch}$ is expressed as:

$$V_{batt} = b_{series} \cdot (E_{cov} + C_1 \frac{I_{batt,ch}}{b_{para}} + C_2) \tag{6.9}$$

where C_1 and C_2 in (6.9) are expressed respectively as:

$$C_1 = R_0 + K \frac{J}{int - 0.1J} \tag{6.10}$$

$$C_2 = Ae^{-Bint} - K \frac{J}{J - int} int \tag{6.11}$$

Cell SoC does not change drastically for a short period of time, so the SoC and int can be regarded as a constant value considering the time scale of concern in this chapter. Therefore, V_{batt} is linear to $i_{batt,ch}$ according to (6.9) since the EV charger load dynamic performance is almost negligible within a short period of time. Example EV battery package parameters are listed in Table. 6.1, V_{batt} is expressed by $I_{batt,ch}$ in (6.12) based on the corresponding model parameters:

$$V_{batt} = 100 \cdot (3.366 + 0.0012 \cdot I_{batt,ch} - 0.0117) \tag{6.12}$$

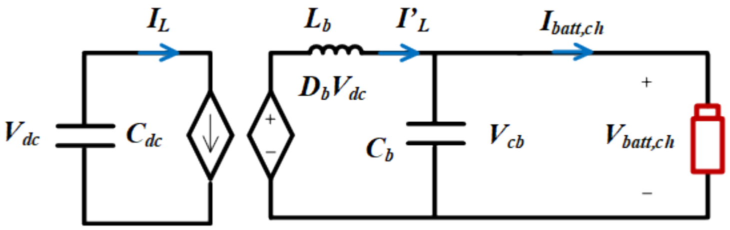

Figure 6.7: EV charging unit dc-dc converter average model.

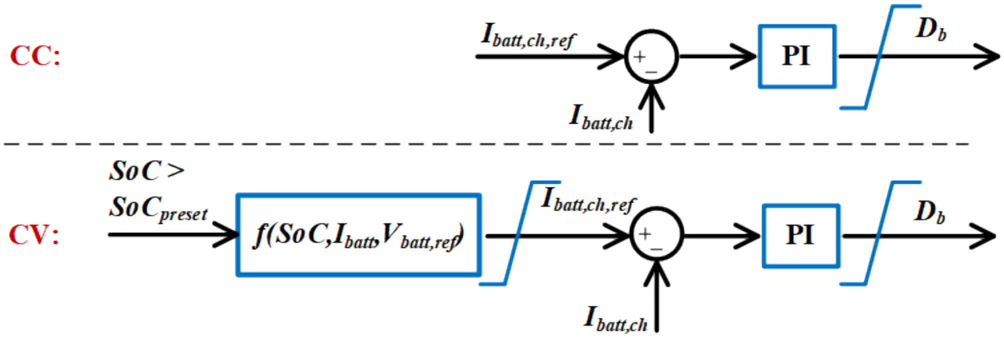

Figure 6.8: Control scheme of EV battery charger: CC and CV mode.

Table 6.1: Example EV battery package parameters.

Parameter	Value	Parameter	Value	Parameter	Value
J	2.3 Ah	SoC	60%	E_{cov}	3.366 V
R_0	0.01 Ω	K	0.0076 Ω	A	0.2642 V
B	26.5487 Ah^{-1}	b_{series}	100	b_{para}	30

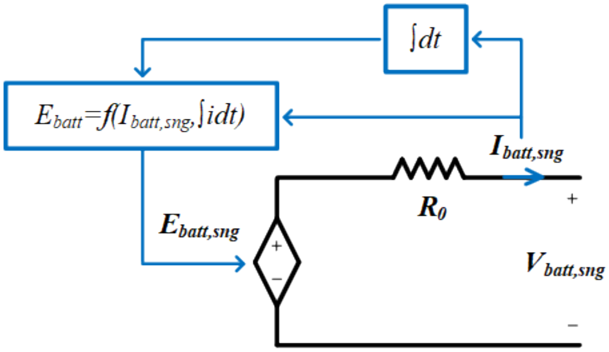

Figure 6.9: Single battery cell Shepherd model.

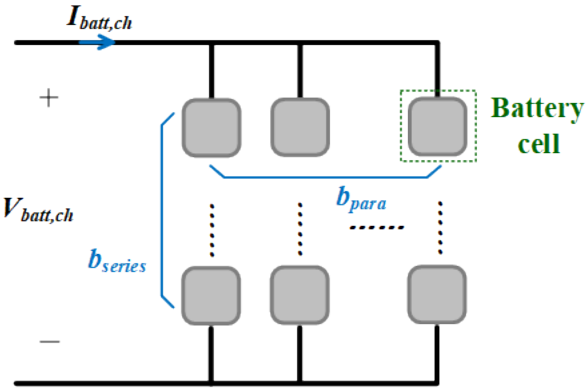

Figure 6.10: EV battery package model: consists of $b_{series} \cdot b_{para}$ battery cells.

According to (6.12), $I_{batt,ch}$ variation only accounts for 0.035% of V_{batt} variation, so V_{batt} is also considered as a constant value when studying the EV charger load dynamic performance during a short time scale. Therefore, the EV battery is simplified as a constant voltage source of which the terminal output voltage mainly relies on the SoC.

Generally, the battery charger buck converter constant current controller has a higher bandwidth compared with that of the rectifier controller. For example, the dynamic performance of $I_{batt,ch}$ from EV charging unit simulation model developed in Simulink is illustrated in Fig. 6.11. $I_{batt,ch}$ transient due to the ac terminal bus voltage is illustrated in Fig. 6.11a, where the ac grid side voltage V_t decreases to 80% of its initial value at t = 0.6 s, and recovers to its original value at t = 0.8 s. As shown in Fig. 6.11a, there is a negligible oscillation occurring on $I_{batt,ch}$ compared with its initial value before the grid contingency. I_{batt} almost maintains constant according to I_{batt} reference value, which is denoted as $I_{batt,ch,ref}$, during the illustrated time duration. Moreover, the process of I_{batt} following the variation of $I_{batt,ch,ref}$ is illustrated in Fig. 6.11b. $I_{batt,ch,ref}$ decreases from 12.5 A to 0 A at t = 0.6 s, and ramps back to 12.5 A at t = 0.8 s, while V_t maintains constant during this process. Meanwhile, I_{batt} almost follows the variation of $I_{batt,ch,ref}$ ideally.

Therefore, a further simplification of the buck converter is performed accordingly: if the control bandwidth of V_{dc} is much slower than that of $I_{batt,ch}$, then the dynamic performance of $I_{batt,ch}$ can be ignored regarding to that of V_{dc}. According to rectifier and buck converter control schemes which are illustrated in Fig. 6.2 and Fig. 6.8 respectively, the open-loop gain of V_{dc} and $I_{batt,ch}$ are shown in Fig. 6.12a and Fig. 6.12b.

The controller open-loop gain in Fig. 6.12 includes both the controller model and the electrical component model of the EV charging unit with reasonable simplifications. As illustrated in Fig. 6.12a, the relation between I_d and I_{dc} in the p.u. value is expressed in (6.13) according to the power equivalent principle. The contribution of q-axis components, $V_{q,pu}$ and $I_{q,pu}$, are ignored for simplification since the value of which are negligible compared with the corresponding d-axis components. The time constant T_{eq} is usually defined to be equal to the corresponding VSC switching period, which refers to the time delay of

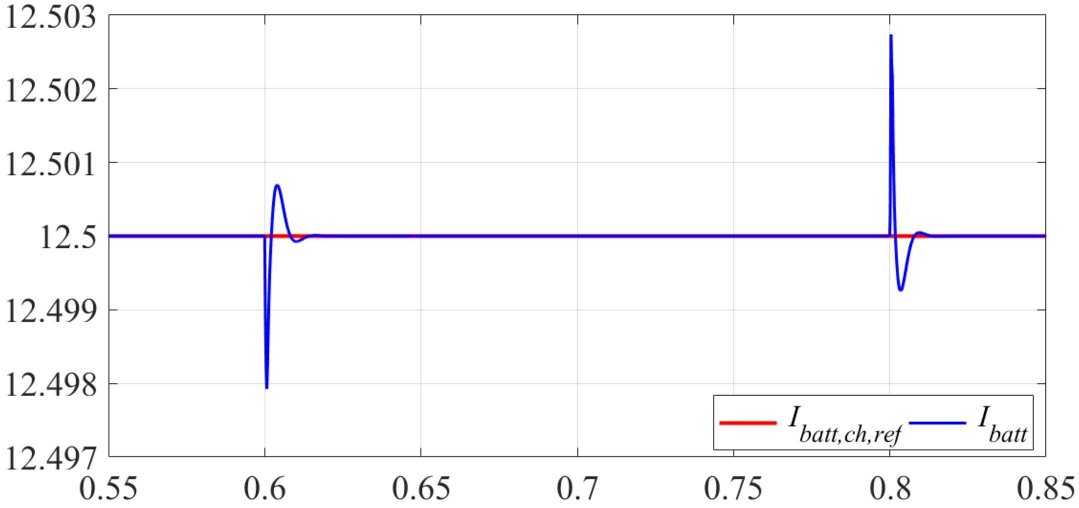

(a) $I_{batt,ch}$ vs. $I_{batt,ch,ref}$ when subject to V_t variation.

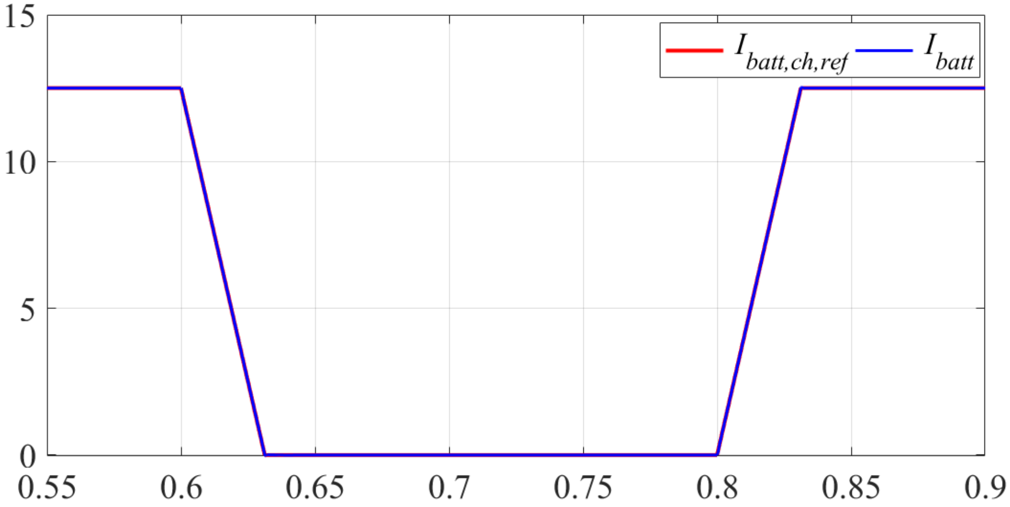

(b) $I_{batt,ch}$ vs. $I_{batt,ch,ref}$ when subject to $I_{batt,ch,ref}$ variation.

Figure 6.11: Dynamic performance of $I_{batt,ch}$ subject to external disturbance.

transferring the current reference value to the real current.

$$I_{dc,pu} = \frac{I_{d,pu} \cdot V_{d,pu}}{V_{dc,pu}} \tag{6.13}$$

As illustrated in Fig. 6.12b, V_{dc} is regarded as a constant value, which is denoted as $V_{dc,in}$, in the corresponding transfer function. So the dc voltage after the buck converter V'_{dc} can be expressed as:

$$V'_{dc} = D_b \cdot V_{dc,in} \tag{6.14}$$

So V_{dc} and $I_{batt,ch}$ open-loop gain are expressed respectively in (6.15) and (6.16), where $K_{p,dc}$, $K_{i,dc}$ and $K_{p,I}$, $K_{i,I}$ are PI regulators control parameters in the constant V_{dc} controller and the CC/CV mode controller, $I_{ac,base}$ and $V_{dc,base}$ are the base value used for transferring the electric components between the p.u. value and the real value. The parameters used in (6.15) and (6.16) are listed in Table 6.2.

$$G_{vdc} = \frac{V_{d,pu} I_{dc,base}}{V_{dc,pu} V_{dc,base}} \cdot \frac{K_{i,dc} + K_{p,dc} S}{C_{dc} S^2 (1 + S T_{eq})} \tag{6.15}$$

$$G_{Ibatt} = \frac{V'_{dc}(K_{i,I} + K_{p,I} S)}{L_b S^2} \tag{6.16}$$

The open-loop gain bode plot of V_{dc} and $I_{batt,ch}$ are illustrated in Fig. 6.13, where the V_{dc} loop gain is represented by the red curve, and $I_{batt,ch}$ loop gain is represented by the blue curve. According to Fig. 6.13, the bandwidth of G_{vdc} and G_{Ibatt} are equal to 1195 rad/s and 8375 rad/s respectively. Therefore, it can be concluded that the dynamic response process of $I_{batt,ch}$ controller can be regarded as $I_{batt,ch}$ following $I_{batt,ch,ref}$ in real time due to its high control bandwidth compared with that of V_{dc} controller in the active-front-end rectifier. Therefore, the EV charger second power stage can be further simplified as a controlled current source following $I_{batt,ch,ref}$.

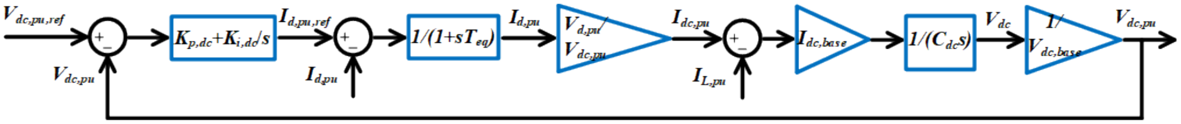

(a) EV charging unit rectifier V_{dc} open-loop gain.

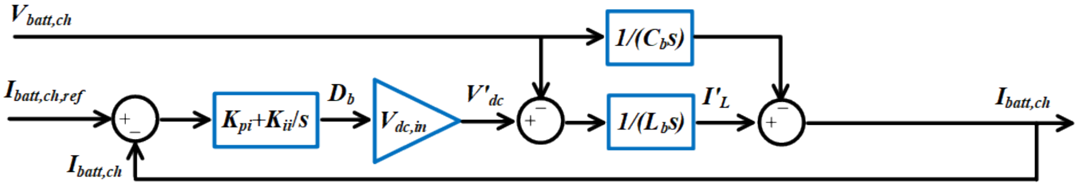

(b) EV charging unit dc-dc converter $I_{batt,ch}$ open-loop gain.

Figure 6.12: EV charging unit: three-phase rectifier and dc-dc converter controller open-loop gain.

Table 6.2: EV charging unit model parameters in (6.15) and (6.16).

Parameter	Value	Parameter	Value	Parameter	Value
$K_{p,dc}$	153	$K_{i,dc}$	4022	T_{eq}	0.0001s
$V_{d,pu}$	1	$V_{dc,pu}$	1	$I_{dc,base}$	6.25 A
$V_{dc,base}$	800 V	C_{dc}	0.0014 F	$K_{p,I}$	0.034
$K_{i,I}$	123.25	V_{dc}	800 V	L_b	5 mH
C_b	30 μF				

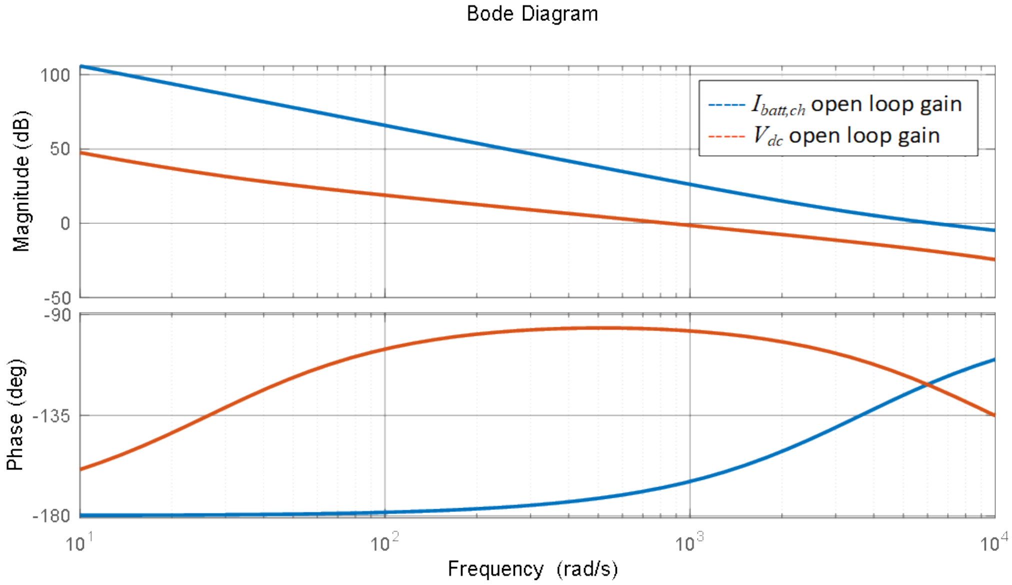

Figure 6.13: open-loop gain bandwidth comparing V_{dc} and $I_{batt,ch}$.

6.3 Conclusions

In this chapter, the EV charging unit simplified model is presented. The following simplification approaches are adopted by the simplified EV charger model:

- The VSC dynamic average-value model is adopted to represent the EV charger electric circuit, including the three-phase VSC from the first power stage, and the dc-dc converter from the second power stage.

- The battery charging current $I_{batt,ch}$ closely follows $I_{batt,ch,ref}$ since the buck converter has a higher control bandwidth compared with the V_{dc} control in the active-front-end. So the EV battery and the buck converter are jointly regarded as a current source following $I_{batt,ch,ref}$.

- The dynamic performance of the active-front-end rectifier inner current control loop is simplified as a first-order system considering that the corresponding control bandwidth is higher than that of the outer control loop.

Chapter 7

Model Benchmark of Fast Electric Vehicle Charging Unit for Transient Stability Simulation Environments

As presented in previous chapters, the wide adoption of EV and fast EV charging stations is leading to a gradually increasing requirement of electromechanical model of the fast EV charging unit, considering the accurate analysis of transmission-level power network operation status involving EV charger stations as the major load consumption. Based on the simplified model of the fast EV charger load unit introduced in the last chapter, the specific response of EV charger load in terms of the grid contingency is introduced and included in the load model. At last, the generic EV charger model suitable for the TS simulation environment is developed and verified compared with the equivalent EMT benchmark model developed in the PSCAD$^{\text{TM}}$/EMTDC.

7.1 EV Charger Model under Terminal Voltage Contingency

As introduced in the above chapters, the integration of EV charger loads into the conventional ac network affects the system transient stability. Hence it is important to investigate the EV charger load dynamic performance, and among which the load characteristics during the grid contingency is of great significance[12, 133, 134]. The dynamic modeling characterizing the fast EV charging unit performance when subject to voltage sag and momentary power outage is introduced in this section.

7.1.1 Active Power Cut-off and PCC Voltage Support

There are a few literatures discussing the low voltage ride-through (LVRT) control scheme of fast EV charging units based on author's knowledge. For example, the LVRT scheme introduced in [135], which is adopted by EV charging units to enhance the grid stability, is performed by cutting off the load active power and adjusting the load reactive power. The wind farm and HVDC LVRT standard is presented in (7.1) [136, 137, 138, 139, 140]:

$$\begin{cases} P_{EV} = P_{EVs}, Q_{EV} = Q_{req} \quad when \quad V_{mag} > 0.8p.u. \\ P_{EV} = 0, Q_{EV} = Q_{req} \quad when \quad 0.5p.u. \leq V_{mag} \leq 0.8p.u. \\ P_{EV} = 0, Q_{EV} = 0, \quad when \quad V_{mag} < 0.5p.u. \end{cases} \tag{7.1}$$

where P_{EV} and Q_{EV} represent the active and reactive power consumption of the EV charging load unit. P_{EVs} is the total charging power of the connected EV battery, and as presented in [135], the EV charger load is under normal operating condition when $V_{mag} > 0.8p.u.$, so $P_{EV} = P_{EVs}$ stands for the normal charging operation without grid contingency interference. P_{EV} and P_{EVs} will not be distinguished in the following paragraphs for simplicity. Q_{req} represents the required reactive power consumption which is used to maintain the EV terminal bus voltage at the permissible range. V_{mag} represents the EV charger terminal voltage magnitude in p.u. value.

As expressed in (7.1), P_{EV} decreases to 0 when $V_{mag} \leq 0.8p.u.$, and Q_{EV} is utilized to maintain V_{mag} within the appropriate operating range. When V_{mag} is too low, the charging unit will disconnect from the grid. This proposed LVRT scheme is beneficial to avoid grid voltage instability.

7.1.2 EV Charging Unit LVRT Design Requirement

As presented in [141], the EV charger load trip during voltage sag may introduce a significant overvoltage phenomenon after the grid voltage is recovered, which is harmful to the grid stability. This is because the EV charger load dropping off results in a high power mismatch between the power supply and demand after the grid fault is cleared. Moreover, the response of EV charging unit to power-quality events is suggested in SAE J2894 as below [142]:

- Voltage sag: EV chargers must remain energized if the supply voltage drops to 80% of the nominal value for up to 2 s.
- Momentary outage: EV chargers must ride through a complete loss of voltage for up to 12 cycles.

Accordingly, EV charger loads are required to keep energized during the conditions mentioned above. Otherwise, EV charger loads are allowed to be tripped from the power network. Although the situation, where voltage sags below 80% but remains nonzero, is not explicitly covered by the standard, usually the customers can design the EV charger loads to withstand the voltage sag for a predefined period of time, and then trip the load if the terminal voltage does not recover prior to the predefined time period.

Therefore, the EV charger load dynamic performance should be modeled considering the design of the corresponding LVRT scheme during grid events to improve the proposed load model accuracy. However, the LVRT scheme is not clearly specified according to authors' best knowledge. So an LVRT control is designed and adopted by the fast EV charger studied in this chapter to present a more practical load response [2]. The LVRT algorithm characterizing the EV charger load response when subject to the voltage sag and momentary outage mentioned above is illustrated in Fig. 7.1 and expressed in (7.2):

$$I_{batt,ref} = \begin{cases} I_{batt,ref,nom}, \quad when \quad V_{mag} > V_{th1} \\ (-V_{th2} + V_{mag})/(V_{th1} - V_{th2}), \quad when \quad V_{th2} \leq V_{mag} \leq V_{th1} \\ 0, \quad when \quad V_{mag} < V_{th2} \end{cases} \tag{7.2}$$

where $I_{batt,ref}$ represents the battery current control command, $I_{batt,ref,nom}$ represents the nominal current command, V_{mag} represents the V_t magnitude, and V_{th1}, V_{th2} both represent the control threshold for V_{mag} .

The LVRT scheme presented in Fig. 7.1 and in (7.2) represent a gradual decrease process of $I_{batt,ch,ref}$. This ride-through design aims to partially keep the EV charger function, but remove the potential instability introduced by the constant power load, which is equivalent to the load model characterizing the normal operating condition of the EV charging unit. According to the presented LVRT scheme, the power consumption of the EV charging unit is supposed to decrease so that the EV charging load can ride through the severe voltage sag and keep energized from the grid, without inducing a grid instability or disconnection from the power network.

The determination of threshold voltage V_{th1} and V_{th2}, which characterize how to regulate the power consumption during the voltage sag event, is based on the following aspects: 1) The LVRT regulation is presented by [142], but the specific criterion for the ride-through scheme is not defined by the above standard, or suggested by any other references to the best of the author's knowledge; 2) the power rating of the converter configuration of the EV charger units, of which the power converter usually follows the design that the converter should be capable of riding through twice of the nominal current for 12 cycles; 3) the power flow capability of the load connected feeder network subject to varied terminal voltage, which is commonly represented by the grid $P - V$ curve. The author selected V_{th1} and V_{th2} in the following sections considering the specific requirement of the grid. However, the design guideline of the EV charging unit LVRT control scheme is out of the scope of this chapter.

7.1.3 EV Charging Unit Restart after Grid Event

The EV charging load unit is not allowed to remain energized if the terminal voltage sag or power outage is over the designed tolerance range. So the load is tripped from the connected power network due to protecting the load device from the power-quality event. After the grid fault is cleared, the EV charger load is required to reconnect to the power grid. As suggested by [142], a gradual restart of battery chargers after a specified time delay is desirable to help mitigate issues brought by "cold load pickup", which usually includes the protective relays initiating de-energization of an unfaulted circuit due to the excessive pickup current [143]. The load restart scheme after grid events adopted in this chapter is illustrated in Fig. 7.2 [142].

According to Fig. 7.2, after longer or deeper than the specified voltage sag/momentary outage or a complete loss of the utility ac power, the restart of EV supply equipment (EVSE) should be delayed for a minimum of 2 minutes, plus an additional pseudo-randomized timer by EVSE. This period will begin each time power has been restored. Meanwhile, to prevent voltage sags due to rapid increase in charger input current, and to avoid excessive trips of protective equipment during cold load pickup, the EV charger load reference charging current shall ramp back at the rate no faster than 40 A/s.

7.2 EV Charger Realization in TS Simulator

According to existing studies of modeling power converter based facilities, such as HVDC [144, 145, 146, 147, 148, 149], the positive-sequence model of PE interfaced devices in the TS simulator is usually divided into the following three parts [2]:

- The ac side dynamic model, which includes the PCC, the decoupling inductance, and the equivalent PE interfaced device ac side model, where the ac side model is usually specified as an ac voltage source.
- The dc side dynamic model specifies the dynamic performance of the dc-link capacitor, which serves as the dc energy storage component.
- The dynamic controller model, which characterizes the dynamic performance of the ac and dc side models.

According to the EV charging unit average model illustrated in Fig. 6.5, the equivalent physical model of the fast EV charger in the TS simulator is illustrated in Fig. 7.3, which characterizes a combination of the ac and dc side models. The controllers specifying the dynamic performance are not shown in Fig. 7.3 [2].

As shown in Fig. 7.3, the equivalent electromechanical model of the fast EV charging unit mainly comprises ac side and dc side equivalent models, which follows the basic configuration

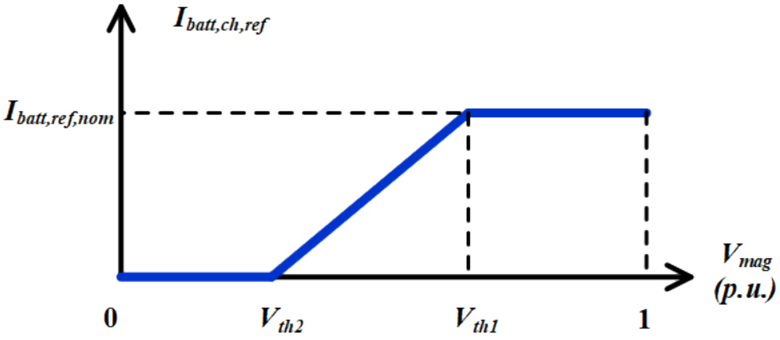

Figure 7.1: EV fast charging unit LVRT control scheme [2].

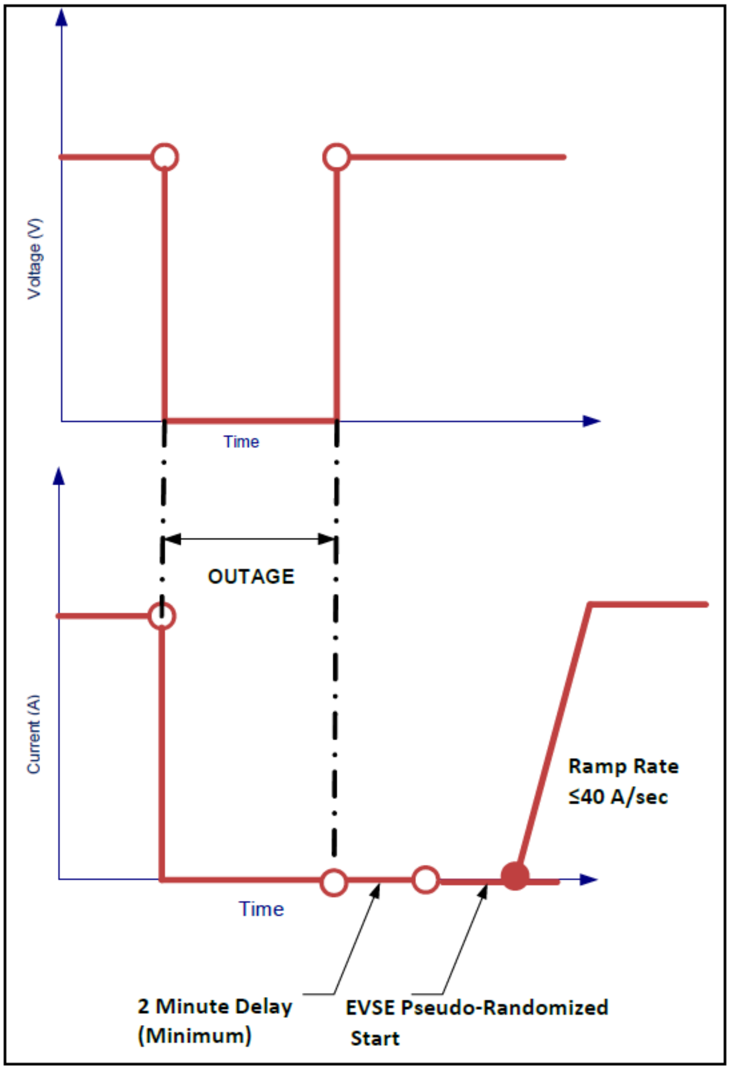

Figure 7.2: Cold load pick-up and load rate relationship [142].

of PE-based devices positive-sequence model as mentioned above. At ac side, an equivalent ac voltage source is employed, where critical model parameters are listed below: I represents the load current at ac side, X_L represents the line impedance between the EV charger and the PCC, and V_{ev} represents the equivalent ac voltage source which characterizes the EV charger load. On dc side, the power transmitted from the ac terminal is converted to a dc current source, of which i_{dc} represents the current injection from the equivalent dc current source, i_L represents the current consumption from the second power stage of the EV charging unit, and C_{dc} represents the dc-link capacitance. The parameter notification is consistent with that illustrated in Fig. 6.1. The ac and dc sides are connected by the power balance principle, which is expressed in (7.3):

$$1.5(V_d \cdot I_d + V_q \cdot I_q) = V_{dc} \cdot I_{dc} \tag{7.3}$$

7.2.1 Electrical Variables Transformation between TS and EMT Model Expression

The ac equivalent model of the EV fast-charging unit should be represented in the phasor domain if adapted into the TS simulation environment. Therefore, the transformation between the dq coordinates and the phasor domain is necessary. The phasor domain coordinates, denoted as RI coordinates in the following passage, is illustrated in Fig. 7.4 by solid black lines, where the real and imaginary axis are used to represent the phase angle and the amplitude of the electrical variables [150]. The corresponding phasor variables remain constant at the steady state operating point in the RI coordinates. The dq coordinates, which are illustrated by the black dash lines in Fig. 7.4, rotate at the fundamental frequency of the connected ac grid. V and I notation in Fig. 7.4 show an example of the voltage and current in RI coordinates, and θ_1 and θ_2 represent V and I phase angle respectively. Accordingly, I lags behind V by $(\theta_1 - \theta_2)$, and V is selected to identify the position of d-axis. So the transformation from the dq coordinates to the phasor domain is expressed as follows [2]:

$$\begin{aligned} I_R &= \sqrt{i_d^2 + i_q^2} \cdot \cos(\theta_2) \\ I_I &= \sqrt{i_d^2 + i_q^2} \cdot \sin(\theta_2) \end{aligned} \tag{7.4}$$

$$\begin{aligned} \theta_d = \theta_2 - \theta_1 &= \arctan(i_q/i_d) \\ \theta_2 &= \arctan(V_I/V_R) + \theta_d \end{aligned} \tag{7.5}$$

where i_d and i_q represent the current I in the dq coordinates; V_R and V_I represent the voltage V in the RI coordinates; I_R and I_I represent I in the RI coordinates; θ_d represents the angle difference between θ_1 and θ_2 [2].

In this chapter, the PCC voltage V_t is aligned with the d-axis, so the corresponding voltage and current variables used to represent the EV charger load dynamic performance in TS simulation environment should be transferred to RI coordinates following (7.4) and (7.5) respectively [2].

7.2.2 EV Charging Unit AC Terminal Specification

A comparison between the EV charging unit load model in the EMT simulator and TS simulator is illustrated in Fig. 7.5. Combining with the dc side model and corresponding controllers, the framework of the positive-sequence EV charger model proposed in this paper is illustrated in Fig. 7.5a. The constant V_{dc} and constant Q controller are selected to illustrate the modeling structure in the TS simulation environment as an example. Basically, the equivalent PE load TS model is derived based on the equivalent EMT model which is illustrated in Fig. 7.5b [2].

The difference between the EMT model and TS model proposed in this chapter is that the proposed model includes reasonable simplification considering that the TS simulation tools concentrate on the transients and oscillations between 0.1 and 3 Hz, so the switching dynamics and the fast controller transients are eliminated from the proposed TS model, which has been discussed in the last chapter in detail.

As shown in Fig. 7.5a, the VSC vector control is employed to generate the reference current in dq coordinates, $I_{d,ref}$ and $I_{q,ref}$. The process of driving the PE interface to generate real line current I_d and I_q is represented by a first-order system due to model simplification. With I_d and I_q derived by the controller model, V_{ev} in phasor domain is expressed as [2]:

$$\dot{V_{ev}} = \dot{V_t} - (R_L + jX_L)\dot{I_{ref}} \tag{7.6}$$

where $\dot{I_{ref}}$ represents the PE interface grid side current command, of which the phasor expression is derived by (7.4) and (7.5). V_{ev} in phasor domain is used to represents the load characteristics of the developed EV charging unit model.

7.2.3 EV Charging Unit Model Appropriate Operation Scope

As introduced in Chapter 6, the EV charger load model is developed based on the dynamic average-value modeling approach. So the semiconductor device switching performances, which are characterized in the EMT simulator, will not be included. Therefore, the limitation of the developed model is that the corresponding PE interface switching harmonics related phenomena are not able to be characterized. This is reasonable for the TS simulator load unit model, considering the potential computational burden introduced by multiple buses included in the power network. Instead, the developed EV charger model can represent the following performance which does not significantly influenced by switching harmonics, including:

- Load active/reactive power consumption variation. The developed PE-based load can represent the corresponding power consumption dynamic performance due to the variation of load operating condition.

- Response to power grid contingency and disturbance following the control schemes adopted by PE interfaces. When the load is subject to the power grid events, which induce terminal voltage magnitude and frequency variation, the load can provide self-protection response and grid support response accordingly.

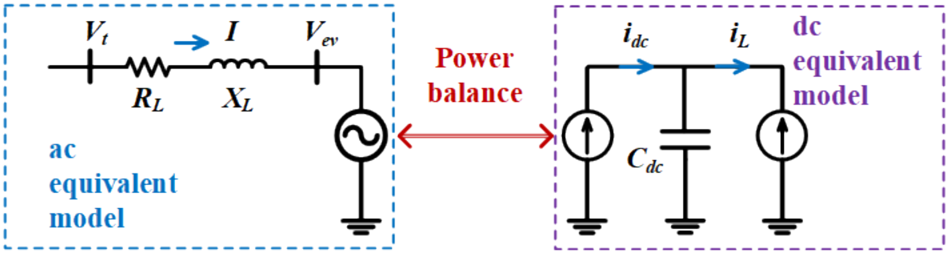

Figure 7.3: Equivalent physical model of fast EV charger in TS simulator [2].

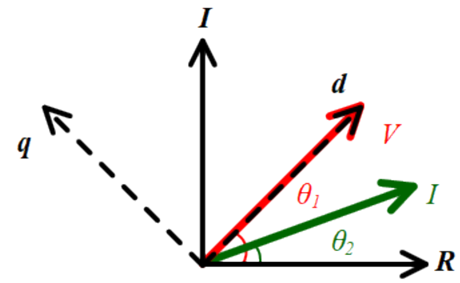

Figure 7.4: Reference frame transformation: between *dq* coordinates and *RI* coordinates [2].

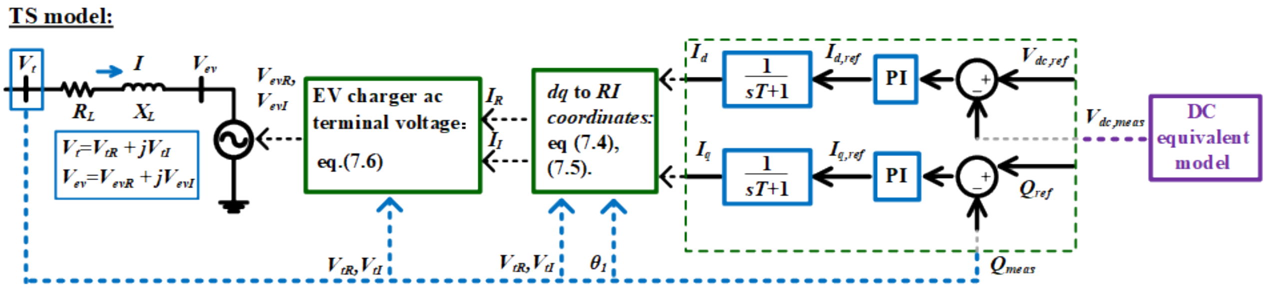

(a) Framework of the positive-sequence EV charger model in the TS simulator [2].

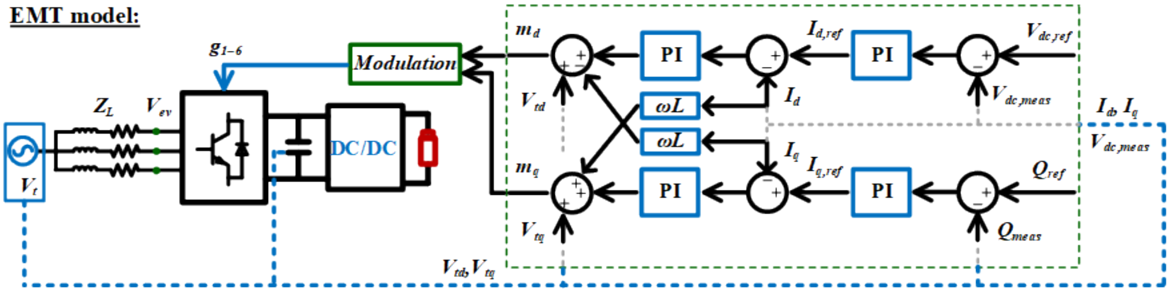

(b) Framework of the EV charger model in the EMT simulator.

Figure 7.5: Comparison between EV charging unit load model in EMT simulator and TS simulator.

Therefore, the EV charger unit model developed in this chapter is appropriate to be used in transient studies which meet with the operation scope introduced above.

7.3 Fast EV Charging Unit Model Benchmark

The TS model of the fast EV charging unit is developed in DSATools$^{\text{TM}}$/TSAT based on the modeling process presented in Section 7.2, and the accuracy of the proposed electromechanical model is verified. As illustrated in Fig. 7.6, the EV charger model is connected to the IEEE 3-machine 9-bus transmission network at Bus 5, and all the other loads in the power grid are constant impedance loads [2]. The overall load profile is listed in Table 7.1.

The detailed EMT model of the network above has been developed in the PSCAD$^{\text{TM}}$/EMTDC as the benchmark model to evaluate the accuracy of the TS model. The controller reference step response, the transmission line disconnection, three-phase ground fault remote/close to the EV charger load bus, and grid frequency support are simulated and analyzed respectively in the following subsections. Meanwhile, the different dynamic performance between the proposed load model and the static model is also specified [2]. The electrical model and controller parameters are listed in Appendix C.

7.3.1 Controller Reference Step Response

The TS model is built based on a combination of the average PE power stage model and the corresponding controllers in DSATools$^{\text{TM}}$/TSAT, which follows the model structure illustrated in Fig. 7.5a. The selected EV charger control functions, which are illustrated in Figs. 6.2, 6.3 and 6.4, are modeled following the proposed PE load modeling structure respectively. All these introduced EV charger load models will be simulated and verified in the following paragraphs.

The step response is performed on the EV charger TS simulation model to evaluate the dynamic response when it is subject to the grid small disturbance, where a step change of the controller reference is characterized. The TS model of EV charging unit adopting constant V_{dc} and constant Q control schemes are analyzed first.

$V_{dc,ref}$ increase/decrease events are illustrated in Fig. 7.7 and Fig. 7.8 respectively. $V_{dc,ref}$ increased from 1 p.u. to 1.05 p.u. in $V_{dc,ref}$ increase simulation case, while $V_{dc,ref}$ decreased from 1.05 p.u. to 1 p.u. in $V_{dc,ref}$ decrease simulation case. Both V_{dc} and the EV charging unit active power consumption P_{EV} are measured to evaluate the load dynamic performance, where the red curves illustrate the simulation results of the corresponding power network and load unit benchmark model developed in PSCAD$^{\text{TM}}$/EMTDC, while the blue curves illustrate simulation results of the electromechanical model developed in TSAT.

Similarly, Q_{ref} increase/decrease events are illustrated in Fig. 7.9 and Fig. 7.10 respectively. Q_{ref} increased from 0 p.u. to 0.1 p.u. in Q_{ref} increase simulation case, while Q_{ref} decreased from 0.1 p.u. to 0 p.u. in Q_{ref} decrease simulation case. Both the EV charging unit reactive power consumption Q_{EV} and the load connected bus voltage V_5 are measured to evaluate the load dynamic performance.

According to the simulation results illustrated in Fig. 7.7 to Fig. 7.10, the electromechanical model developed in TSAT can effectively follow the controller reference deviation, and the electromechanical model simulation results matches well with the EMT model when subject to the reference value step response. Therefore, it is shown that the EV charging unit TS simulation model can accurately mimic the dynamic performance of the equivalent EMT load model.

7.3.2 Transmission Line Disconnection

As illustrated in Fig. 7.6, one of the transmission lines between Bus 7 and Bus 8 is tripped to evaluate the load model performance during small grid disturbance. The transmission line is tripped at t = 2.5 s and lasts for 0.2 s. P_{EV} and V_5 are measured to represent the dynamic performance of the EV charger load. Simulation results are illustrated in Fig. 7.11, where red curves illustrate the EMT model performance, and blue curves illustrate the proposed TS model performance. It can be observed from simulation results that the dynamic performance of the TS EV charging load model presents a good match with that of the equivalent EMT benchmark model [2].

In the comparison case performed in TSAT, the proposed EV charger model is replaced by the equivalent constant impedance load at Bus 5, and the corresponding static load

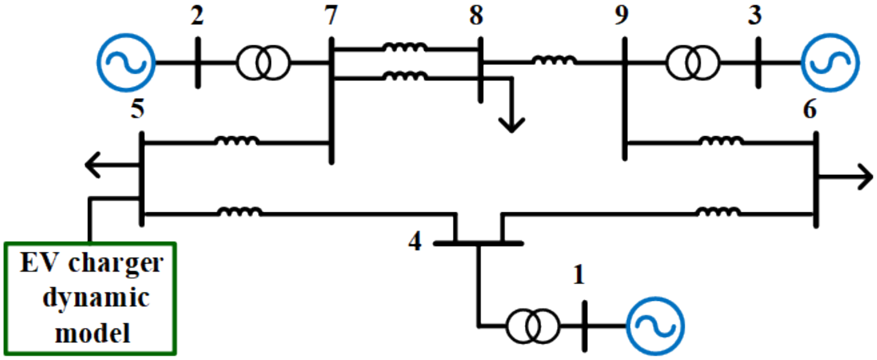

Figure 7.6: Fast EV charger integrated into the 3-machine 9-bus system [2].

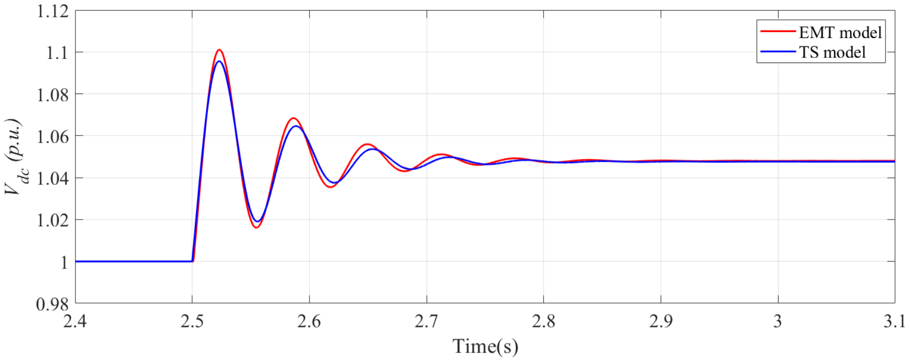

(a) V_{dc} response to $V_{dc,ref}$ step change.

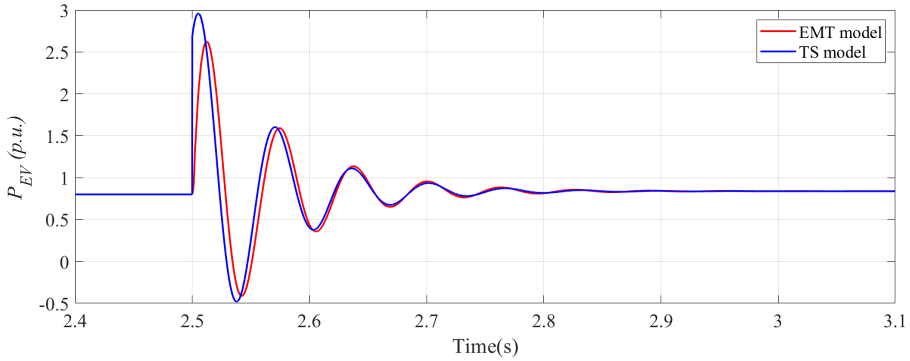

(b) P_{EV} response to $V_{dc,ref}$ step change.

Figure 7.7: EV charging unit dynamic response to $V_{dc,ref}$ step change: $V_{dc,ref}$ increase from 1 p.u. to 1.05 p.u..

Table 7.1: Load profile at Bus 5,6 and 8 [2].

Bus	Load type	Active Power (MW)	Reactive Power (MVA)
5	dynamic EV charger	80	0
5	constant impedance	45	50
6	constant impedance	90	30
8	constant impedance	100	35

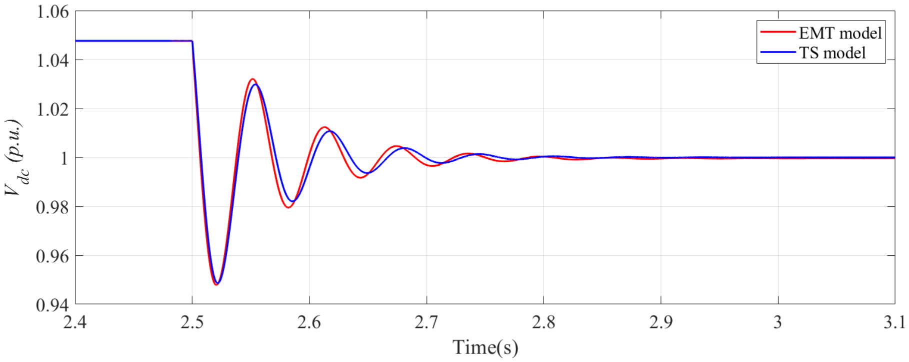

(a) V_{dc} response to $V_{dc,ref}$ step change.

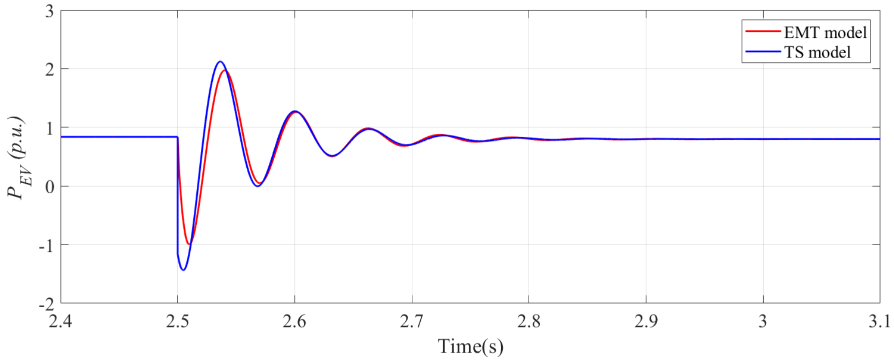

(b) P_{EV} response to $V_{dc,ref}$ step change.

Figure 7.8: EV charging unit dynamic response to $V_{dc,ref}$ step change: $V_{dc,ref}$ decrease from 1.05 p.u. to 1 p.u..

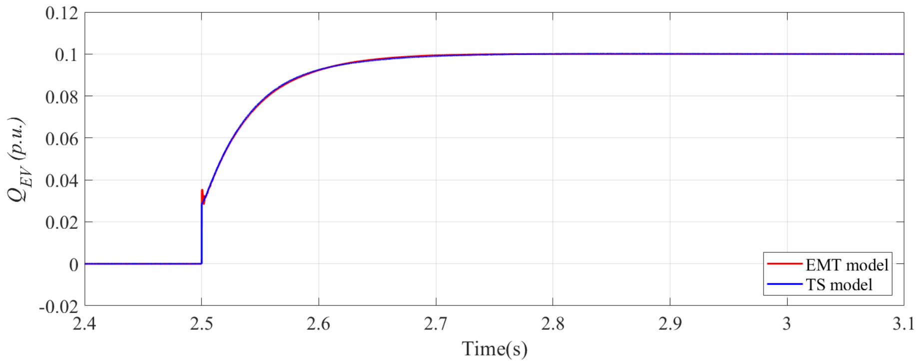

(a) Q_{EV} response to Q_{ref} step change.

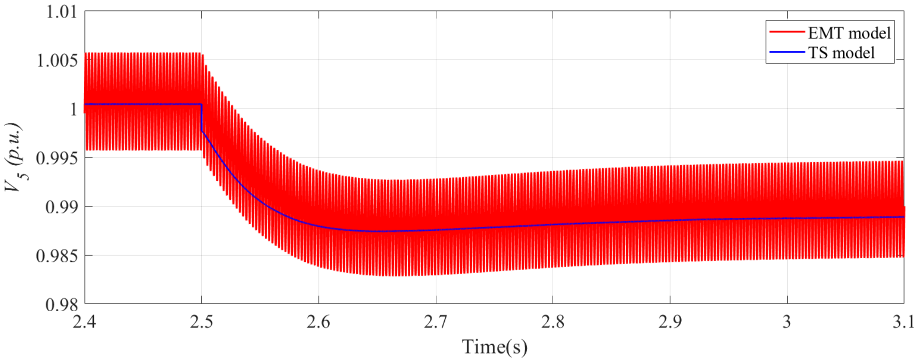

(b) V_5 response to Q_{ref} step change.

Figure 7.9: EV charging unit dynamic response to Q_{ref} step change: Q_{ref} increase from 0 p.u. to 0.1 p.u..

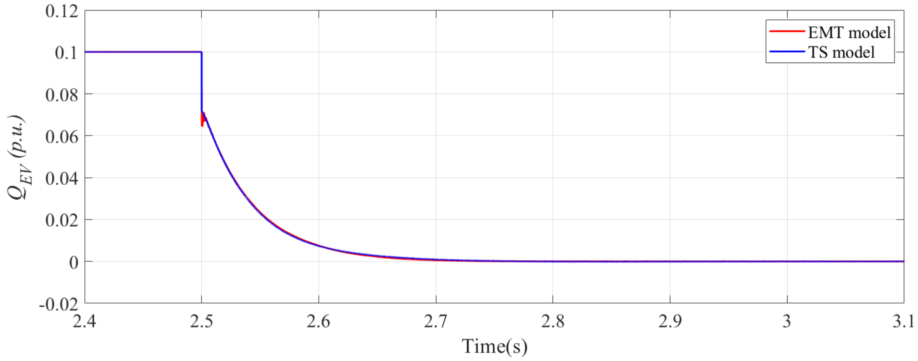

(a) Q_{EV} response to Q_{ref} step change.

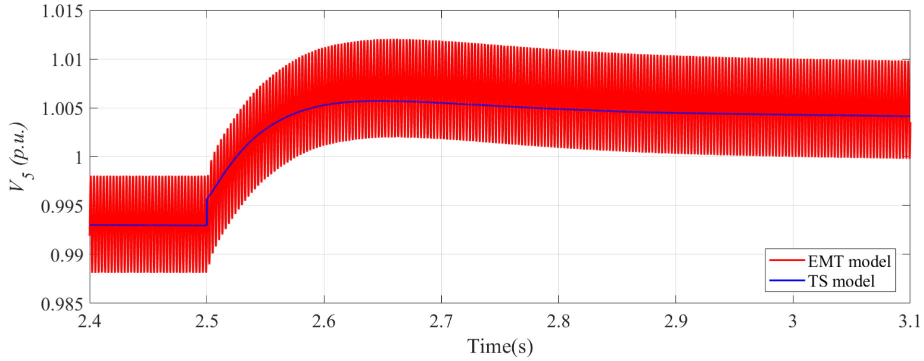

(b) V_5 response to Q_{ref} step change..

Figure 7.10: EV charging unit dynamic response to Q_{ref} step change: Q_{ref} decrease from 0.1 p.u. to 0 p.u..

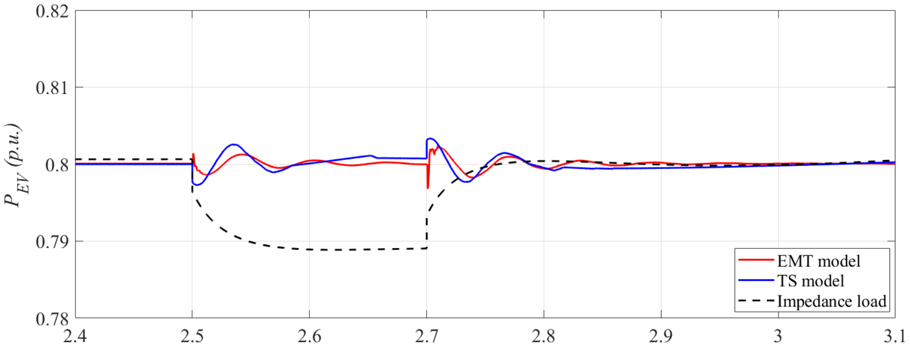

(a) P_{EV} response to transmission line disconnection.

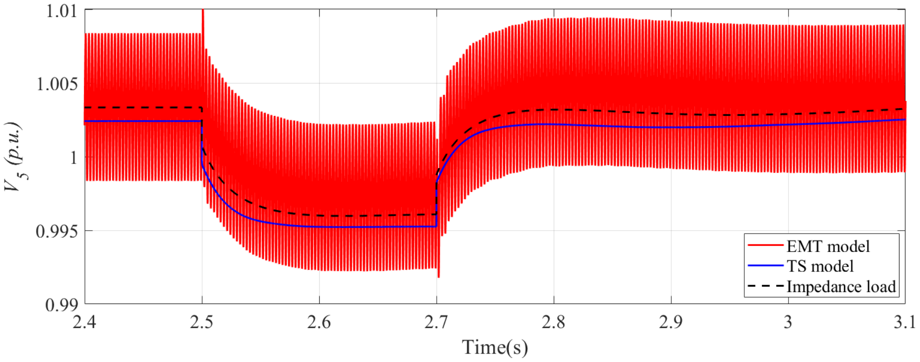

(b) V_5 response to transmission line disconnection.

Figure 7.11: Transmission line disconnection between Bus 7 and 8 [2].

performance is illustrated by black dash curves in Fig. 7.11. And according to the simulation results comparison, the static load cannot represent the P_{EV} dynamic performance compared with the proposed dynamic load model. So it also shows that the power system simulation and analysis accuracy will be compromised if using the static load to represent the dynamic load, especially during the grid contingency [2].

7.3.3 Ground Fault Remote from EV Charging Unit Terminal

A three-phase ground fault at Bus 8 is applied to evaluate the load model performance during a grid contingency. The LVRT control is applied to the EV charger to withstand the low terminal voltage, of which the threshold voltage is qualitatively defined as $V_{th1} = 0.6$ p.u. and $V_{th2} = 0.3$ p.u. in the simulation. Bus 8 is grounded with impedance at t = 2.5 s and lasts for 0.2 s. The dynamic performance of the EV charger ac and dc side model are both evaluated, where the following variables are recorded respectively: P_{EV}, V_5 and V_{dc}. Simulation results of the above variables are illustrated in Fig. 7.12. Both the ac side and dc side performance of the TS model achieve a good match with that of the EMT model. The simulation results in TSAT with equivalent constant impedance load and constant power load at Bus 5 are also illustrated in Fig. 7.12 to compare with the proposed EV charger load model. According to Fig. 7.12a, remote ground fault induces a small terminal voltage variation, which results to EV charger load active power consumption oscillation at t = 2.5 s and t = 2.7 s [2]. In comparison, the equivalent constant impedance load power consumption drops with terminal voltage sag, and the constant power load will keep the previous power consumption during the grid contingency. The terminal voltage variation comparison between dynamic EV load, constant impedance load and constant power load is illustrated in Fig. 7.12b. The different impact on V_5 between different load models is not significant since the difference for load power consumption during contingency is not large.

7.3.4 Ground Fault Close to EV Charging Unit Terminal

In this case, a three-phase ground fault is applied at Bus 5 to which the EV charger load is directly connected, so the ground fault influences the EV charger load more severely

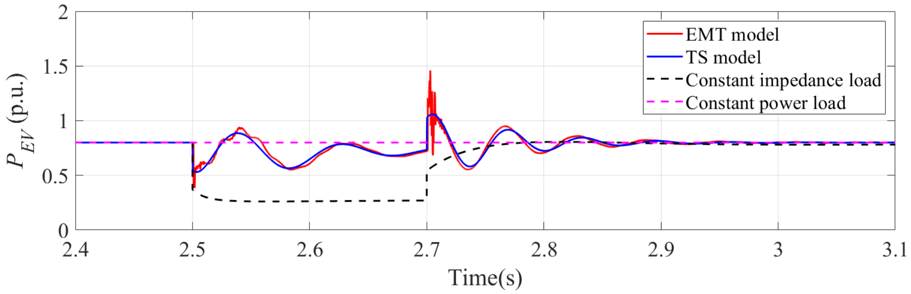

(a) P_{EV} response to ground fault.

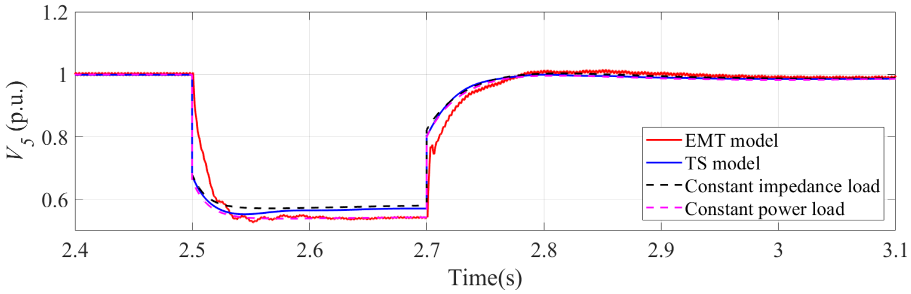

(b) V_5 response to ground fault.

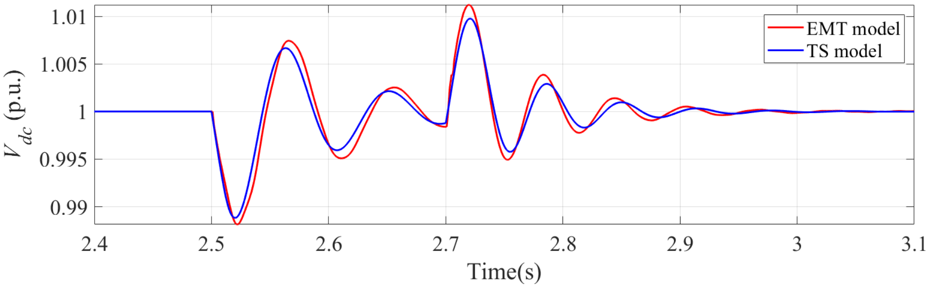

(c) V_{dc} response to ground fault.

Figure 7.12: EV charger model: Response to remote ground fault at Bus 8 [2].

compared with the last case. The simulation results are illustrated in Fig. 7.13, and compared with those of PSCAD$^{\text{TM}}$/EMTDC models. It is observed from the simulation results that the performance of the proposed EV charging model achieves a relatively good match with that of the EMT model [2]. Similar to the last case, simulation results with the equivalent constant impedance load and constant power load are also illustrated. As shown in Fig. 7.13a, the EV charger load LVRT is activated to respond against the drastic terminal voltage sag. In comparison, the constant power load is converted as impedance load when subject to the extremely low voltage. When the fault is cleared, the load active power consumption of the three different load models are significantly different. The EV charger load oscillation will introduce impact to the rotor angle stability, which cannot be reflected by static load model. In conclusion, the proposed dynamic TS model for PE-based load reflects the corresponding load performance more accurately comparing with equivalent static loads.

7.3.5 V2G Mode: Primary Frequency Support

The primary frequency support provided by the EV charging units in the V2G model has been presented in Fig. 6.4. The second power stage is simplified as a constant dc voltage source in the V2G mode. So the dynamic model of EV charging load in the V2G model can be developed based on the G2V mode model according to Fig. 7.5a and Fig. 6.6 respectively, which represents the control structure and model principle, respectively.

The grid frequency increase event is created by a load shedding at Bus 6 when t = 3 s, of which 50% of the active power loads are disconnected from the power network. The EV charger load response at this frequency event is measured in both TS and EMT simulation environment, which is illustrated in Fig. 7.15. The frequency controller parameter K_p is selected as 50, and the frequency deadband is ± 0.015 Hz. When the EV charging unit detects a grid frequency deviation Δf, an extra power consumption reference to $P_{EV,ref}$ will be generated by the frequency support control and then be added to $P_{EV,ref}$. Both the generator rotor speed and P_{EV} in p.u. value are measured to evaluate the proposed TS load performance.

Simulation results in Fig. 7.15 show that the EV charger load power consumption increases to contribute to the primary frequency support with the grid frequency increasing.

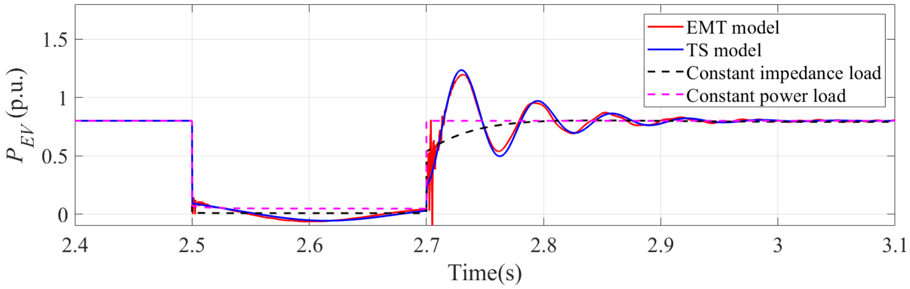

(a) P_{EV} response to ground fault.

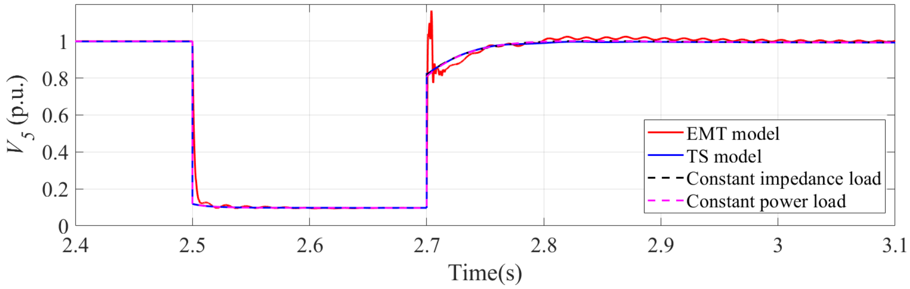

(b) V_5 response to ground fault.

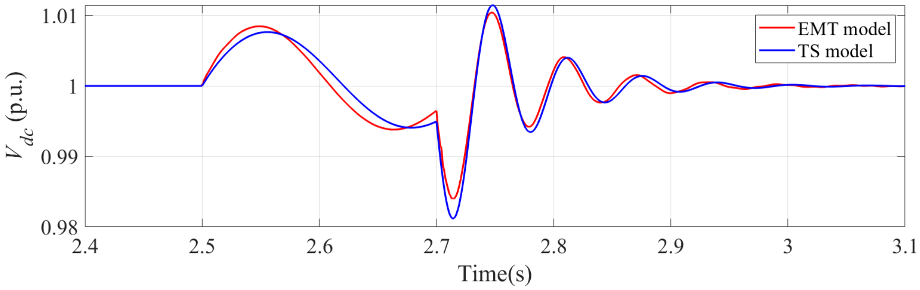

(c) V_{dc} response to ground fault.

Figure 7.13: EV charger model: Response to close ground fault at Bus 5 [2].

And simulation results from the developed TSAT model show a close match with that of the EMT model. Meanwhile, load restoration is also performed to evaluate the process that $P_{EV,ref}$ gradually decreases. As illustrated in Fig. 7.16, the load at But 6 is restored when t = 15 s. $P_{EV,ref}$ gradually decreases to the original value with the recovery of the grid frequency. Similarly, the TS simulation results closely matched with the corresponding EMT benchmark model simulation results, which verifies the accuracy of the developed EV charger model in the TS simulation environment.

7.4 Discussion: PE-Based Load Impact on Power Grid Stability

In this Chapter, the fast EV charging unit is studied as the typical PE interfaced load in the TS simulation environment. The PE-based load has the potential to contribute to the power network stability, since the PE interface can adopt control functions which is beneficial to improving the grid operation. In this way, the PE-based electric load can actively respond to the grid contingency and disturbance, other than the conventionally used static load, which can only perform as a power sink. The positive impact of PE load on grid stability can be summarized below according to the analysis and evaluation in this Chapter:

- PE-based load can actively respond to low bus voltage. Grid voltage collapse will occur if the electric load consumption is not appropriately managed. As introduced in Section 7.1, the LVRT technique is adopted in the PE interface to adjust the load power consumption following the terminal voltage magnitude. When bus voltage is low, the load will perform as constant impedance load with an appropriate regulation scheme, which significantly improves the voltage stability margin. In comparison, the accuracy of grid voltage stability analysis will be compromised if using a static load model to represent PE interfaced load units.

- PE interfaces can provide grid support functions, which facilitate the grid operation and improve the stability. This is similar to PE-based renewable generation units, of which the PE interfaces are required to equip with grid operation control functions, *e.g.,* grid frequency support, grid voltage support, and other ancillary services. The PE-based load can also employ such control functions to improve the power grid operation.

- PE interface can serve as an energy buffer to the electric load units. The PE interface front-end VSC and C_{dc}, as illustrated in the previous chapters, can serve as the energy buffer for the following power stage. Therefore, the grid disturbance can be temporarily decoupled from the electric load connected to the PE interface. Compared with the grid-connected load units, the PE interfaced load can sustain the normal grid operation by mitigating the electric loads' drastic response. For example, the PE interface can mitigate the prolonged power network voltage sag by preventing the air conditioner motor from stalling.

7.5 Conclusions

In this chapter, the LVRT technique of the fast EV charger load is introduced and included in the EV charger load model design. Additionally, the fast EV charging unit model, which is suitable for the TS simulation environment, is developed. A detailed explanation of how to realize the proposed model in the TS simulation program has been introduced.

The proposed TS model of EV charging unit is developed in the TSAT, and several grid disturbance and contingency cases regarding both the EV charger G2V mode and V2G mode are performed in TSAT with the proposed load model, including controller reference step response, transmission line disconnection, EV charger load subject to three-phase remote and close ground fault, and grid frequency support. The simulation results are compared to that measured from the equivalent EMT benchmark model developed in PSCAD$^{\text{TM}}$/EMTDC. TS simulation results and EMT simulation results show good consistency with each other, which demonstrates the accuracy of the proposed EV charger load model for the TS simulation environment.

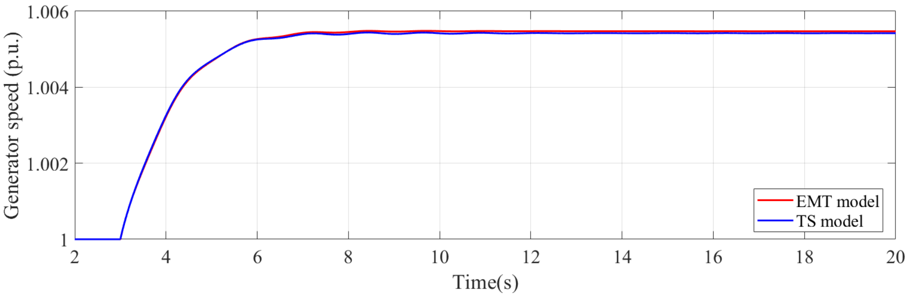

(a) Grid frequency response to load shed at Bus 6.

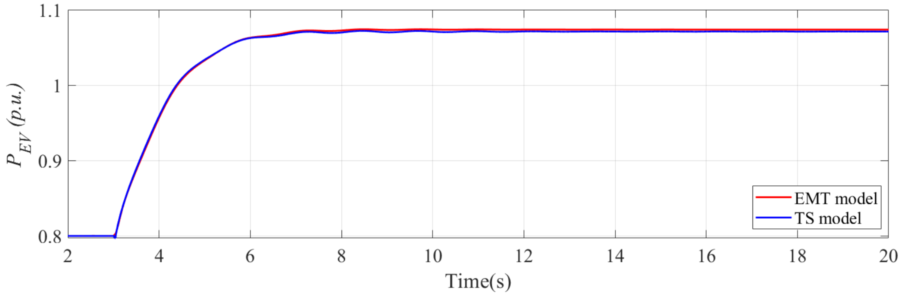

(b) Active power support provided by the EV charger load.

Figure 7.14: EV charger V2G mode: Response to load shed at Bus 6.

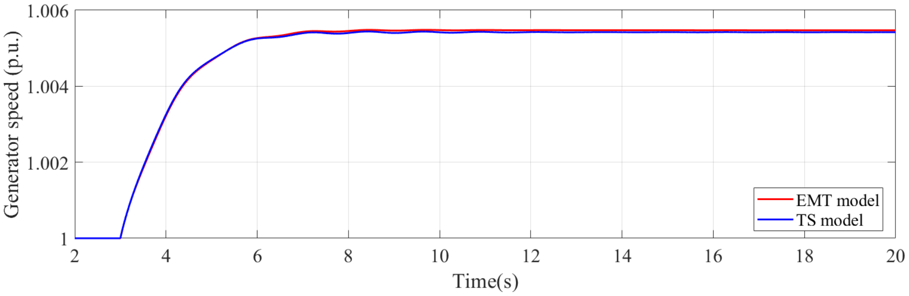

(a) Grid frequency response to load shed at Bus 6.

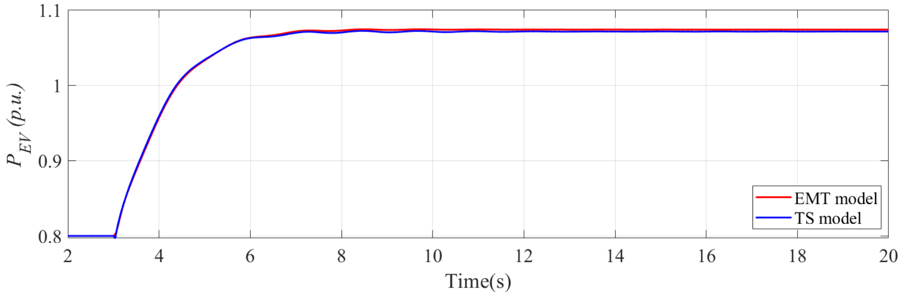

(b) Active power support provided by the EV charger load.

Figure 7.15: EV charger V2G mode: Response to load shed at Bus 6.

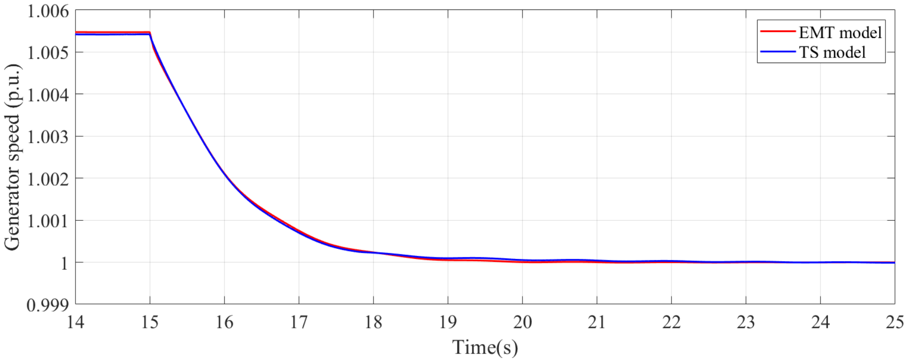

(a) Grid frequency response to load shed at Bus 6.

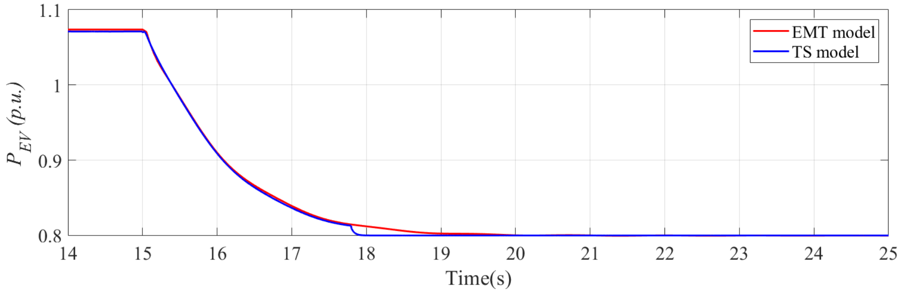

(b) Active power support provided by the EV charger load.

Figure 7.16: EV charger V2G mode: response to load restoration at Bus 6.

Chapter 8

Conclusion and Future Work

8.1 Summary

In previous chapters, the typical PE interfaced loads are studied in terms of model development and the flexible interaction with the power grid operation. In Chapter 3 and Chapter 4, the VSD load dynamic performance is characterized by the detailed model and simplified aggregated model, respectively. The VSD detailed, simplified, and aggregated models have been developed and applied to the HTB power emulators, which can accurately mimic the dynamic performance of the corresponding VSD load. Additionally, the potential of VSD load units to provide equivalent primary frequency support has been investigated. The hybrid control architecture is adopted to regulate and coordinate multiple responsive VSD loads' performance. The responsive load frequency support performance with different control architecture and coordination schemes are simulated and compared based on Simulink models. The hybrid control architecture is shown to regulate the frequency performance more effectively, compared with other control architectures. In conclusion, the grid frequency support function applied to the VSD controller makes the VSD load unit perform as a responsive load which can support the power grid frequency, thus improving the power network stability.

In Chapter 5, evaluation of VSD load primary frequency support is conducted on the HTB. The simplified aggregated VSD load-based power emulator, which is developed and introduced in Chapter 3 and Chapter 4, is used to represent the aggregated responsive VSD loads' performance, promoting a good balance between accuracy and model efficiency. The impact of power reserve and control architecture on responsive load performance is evaluated and discussed: 1) Experimental results show that the VSD load can effectively mitigate the grid frequency deviation if operating within the total load power reserve. Meanwhile, droop control coefficient K_{droop} is decided according to the power grid operating point, which is significantly influenced by time of the day and weather. Additionally, experimental results show that the VSD load power reserve limit varies with the time and weather, leading to varied frequency support performance even with identical K_{droop} command. 2) Comparing the impact of different control architectures, the hybrid control architecture with and without real-time coordination can both achieve a much better frequency support performance compared with that of the centralized controller since the former can provide a relatively short communication delay.

In Chapter 6 and Chapter 7, the generic model of the fast EV charging load has been developed for the TS simulation program. The EV charger load model is first simplified based on the detailed switching model: 1) VSD average model is adopted to replace the PE device switching dynamics, 2) real battery charging current closely follow the battery charging current command considering the high control bandwidth of the buck converter, 3) inner current control loop of the rectifier is simplified as a first-order system. The proposed simplified EV charging unit TS model is developed in TSAT. Several grid disturbances and contingencies are performed on the developed load model, including controller reference step response, transmission line disconnection, EV charger load subject to three-phase remote and close ground fault, and grid frequency support. The accuracy of the proposed TS model has been verified by comparing it to the simulation results of the equivalent EMT model.

8.2 Contributions

In this dissertation, the following research contributions are made, in terms of PE interfaced load modeling and control in multiple simulation/experimental platforms, and grid support potential investigation:

- Development of a novel HTB load power emulator, which includes: 1) the three-phase VSD detailed load with advanced controllers, 2) the three-phase VSD simplified model emphasizing the corresponding load active power consumption.
- Development of a VSD load aggregated model, which reflects the VSD load potential in terms of providing the grid frequency support in the transmission power network. The developed aggregated VSD load model is also applied to the HTB power emulator.
- Investigate VSD load potential of regulating grid frequency regarding varying external and internal requirements.
- Development of the generic model of EV charger load based on the detailed EMT model, which is suitable for the TS simulation environment.
- Development of an EV charger load generic model benchmark in TS simulation program, which includes commonly used EV charger control schemes in different operation modes.

8.3 Future Work

8.3.1 VSD Load Model with Multiple Operation Modes

The responsive VSD load dynamic performance is modeled in this dissertation, which focuses on the capability of providing power grid frequency support functions. Accordingly, the simplified and aggregated model of the VSD load unit is developed based on the VSC d coordinate and motor q coordinate since it only focuses on the active power consumption dynamics of the load. The proposed simplified model is valid based on the assumption that only grid disturbance is considered, which requires motor speed command varies within a predefined range. And this model design and the corresponding assumption are sufficiently accurate according to the research scope of this dissertation. However, a more well-rounded VSD load model is necessary to be investigated in future research, which focuses on the following aspects:

- Aside from the frequency support model investigated in this dissertation, VSD load units with multiple operation modes should be modeled and integrated as VSD load generic model. For example, VSD load should actively respond to grid contingency, such as terminal voltage variation, voltage supply outage, etc. So generic VSD load unit should include voltage sag mode, power outage mode, frequency contribution mode, normal operation mode, etc. In each mode, both the load supportive response and the grid and self-protection scheme should be modeled.
- VSD load unit generic model should effectively identify the operation mode according to external and internal conditions. Meanwhile, a smooth mode transition should be designed accordingly.

Active interactions between PE-based load and the power grid will improve the power grid operation stability, which is especially critical considering the increasing application of RES. In future research, the updated VSD load unit supporting the power grid performance in more operation status will be investigated in depth. The model format developed for the VSD load unit can also be promoted to other types of PE interfaced load units, which can provide more electric service to power networks.

8.3.2 PE-Based Load Impact on Transmission-Level Power Grid

The impact of PE-based load units on transmission-level power operation is to be further explored. Conventionally, the electric loads are modeled as static load units, which has a limited impact on the grid stability analysis. As introduced in the above chapters, the PE-based load can more actively participate in the operation of the power grid, so the following aspects related to the power grid stability are recommended to be evaluated for future research:

- Power system small-disturbance rotor angle stability analysis. The generic PE-based load small-signal model should be developed for performing the corresponding stability analysis. Specifically, how to design the PE-based load to improve the system damping should be emphasized.

- Power system TS analysis. Similarly, the PE-based load impact on mitigating the first swing instability to maintain power system synchronism should be explored.
- Power system voltage stability analysis. The PE-based load can support grid voltage to maintain at the nominal range by adopting specific control schemes, *e.g.,* reactive power control scheme, and LVRT scheme. The research on coordinating multiple PE-based loads in the power grid to improve voltage stability is recommended to be performed.

Bibliography

[1] Jovica V Milanovic, Julija Matevosiyan, A Borghetti, SZ Djokic, and ZY Dong. Modelling and aggregation of loads in flexible power networks. *JM CIGRE WG C*, 4:605, 2014. 1

[2] Shuyao Wang, Haiguo Li, Yiwei Ma, Wang Fred, and Leon Tolbert. Electromechanical transient modeling of fast electric vehicle charging unit. In *IEEE Power Energy Society General Meeting*, pages 1845–1850, 2020. 2, 26, 148, 165, 167, 168, 169, 170, 171, 172, 173, 174, 175, 176, 179, 180, 181, 182, 183

[3] Daijiafan Mao, Jiankang Wang, Jun Tan, Guangyi Liu, Yiran Xu, and Jie Li. Location planning of fast charging station considering its impact on the power grid assets. In *IEEE Transportation Electrification Conference and Expo*, pages 1–5, 2019. 2

[4] Daijiafan Mao, Jun Tan, and Jiankang Wang. Location planning of PEV fast charging station: an integrated approach under traffic and power grid requirements. *IEEE Trans. Intell. Transp. Syst.*, 22(1):483–492, 2020. 2

[5] Michael Nicholas, Dale Hall, and Nic Lutsey. Quantifying the electric vehicle charging infrastructure gap across us markets. *International Council on Clean Transportation*, 2019. 2, 3

[6] Energy Information Administration. Renewable energy explained. `https://www.eia.gov/energyexplained/renewable-sources/`, June 2020. 4

[7] Energy Information Administration. Annual energy outlook 2020. `https://www.eia.gov/outlooks/aeo/`, Jan 2020. 4, 6

[8] K Yamashita, S Martinaz Villanueva, and JV Milanovic. Initial results of international survey on industrial practice on power system load modelling conducted by CIGRE WG C4. 605. In *Proc. CIGRE Symp.*, volume 4, 2011. 5, 6, 27, 38

[9] Jovica V Milanovic, Koji Yamashita, Sergio Martínez Villanueva, Sasa Ž Djokic, and Lidija M Korunović. International industry practice on power system load modeling. *IEEE Trans. Power Syst.*, 28(3):3038–3046, 2012. 5, 6, 27, 38

[10] Dmitry Kosterev, Jun Wen, Richard J Bravo, Steve Yang, John Undrill, William Price, John D Kueck, Bernard C Lesieutre, and Joseph H Eto. Development and implementation of composite load model in WECC. In *CIGRE 2015 Grid of the Future Symposium*, pages 1–7, 2015. 5

[11] Qiuhua Huang, Renke Huang, Bruce J Palmer, Yuan Liu, Shuangshuang Jin, Ruisheng Diao, Yousu Chen, and Yu Zhang. A generic modeling and development approach for WECC composite load model. *Electric Power Systems Research*, 172:1–10, 2019. 5

[12] Anmar Arif, Zhaoyu Wang, Jianhui Wang, Barry Mather, Hugo Bashualdo, and Dongbo Zhao. Load modeling—a review. *IEEE Trans. Smart Grid*, 9(6):5986–5999, 2017. 5, 26, 33, 164

[13] Frede Blaabjerg, Remus Teodorescu, Marco Liserre, and Adrian V Timbus. Overview of control and grid synchronization for distributed power generation systems. *IEEE Trans. Ind. Electron.*, 53(5):1398–1409, 2006. 10

[14] Juan Manuel Carrasco, Leopoldo Garcia Franquelo, Jan T Bialasiewicz, Eduardo Galván, Ramón Carlos PortilloGuisado, MA Martin Prats, José Ignacio León, and Narciso Moreno-Alfonso. Power-electronic systems for the grid integration of renewable energy sources: A survey. *IEEE Trans. Ind. Electron.*, 53(4):1002–1016, 2006. 10

[15] John P Barton and David G Infield. Energy storage and its use with intermittent renewable energy. *IEEE Trans. Energy Convers.*, 19(2):441–448, 2004. 10

[16] Wencong Su, Jianhui Wang, and Jaehyung Roh. Stochastic energy scheduling in microgrids with intermittent renewable energy resources. *IEEE Trans. Smart Grid*, 5(4):1876–1883, 2013. 10

[17] Sercan Teleke, Mesut E Baran, Subhashish Bhattacharya, and Alex Q Huang. Rule-based control of battery energy storage for dispatching intermittent renewable sources. *IEEE Trans. Sustain. Energy*, 1(3):117–124, 2010. 10

[18] M Crosa di Vergagni and F Conte. Frequency support by distributed demand side management of building cooling systems. In *International Youth Conference on Energy (IYCE)*, pages 1–5, 2015. 10, 12

[19] Wenzhong Gao, Ziping Wu, Jianhui Wang, and Shusheng Gu. A review of inertia and frequency control technologies for variable speed wind turbines. In *Chinese Control and Decision Conference*, pages 2527–2533. IEEE, 2013. 10, 12

[20] Kevin P Schneider, Nikitha Radhakrishnan, Yingying Tang, Francis K Tuffner, Chen-Ching Liu, Jing Xie, and Dan Ton. Improving primary frequency response to support networked microgrid operations. *IEEE Trans. Power Syst.*, 34(1):659–667, 2018. 10, 12

[21] Tong Chen, Yu Zheng, Balarko Chaudhuri, and Shu Yuen Ron Hui. Distributed electric spring based smart thermal loads for overvoltage prevention in LV distributed network using dynamic consensus approach. *IEEE Transactions on Sustainable Energy*, 11(4):2098–2108, 2019. 10, 12, 14

[22] Chi Kwan Lee and Shu Yuen Hui. Reduction of energy storage requirements in future smart grid using electric springs. *IEEE Trans. Smart Grid*, 4(3):1282–1288, 2013. 10, 13, 14, 17

[23] Daijiafan Mao, Hussam J Khasawneh, Mahesh S Illindala, Benjamin L Schenkman, and Daniel R Borneo. Economic evaluation of energy storage options in a microgrid with flexible distribution of energy and storage resources. In *Industrial & Commercial Power Systems Technical Conference*, pages 1–7, 2015. 10

[24] Siew-Chong Tan, Chi Kwan Lee, and SY Hui. General steady-state analysis and control principle of electric springs with active and reactive power compensations. *IEEE Trans. Power Electron.*, 28(8):3958–3969, 2012. 13, 17

[25] Xiao Luo, Zohaib Akhtar, Chi Kwan Lee, Balarko Chaudhuri, Siew-Chong Tan, and Shu Yuen Ron Hui. Distributed voltage control with electric springs: Comparison with STATCOM. *IEEE Trans. Smart Grid*, 6(1):209–219, 2014. 13, 17

[26] Kwan-Tat Mok, Siew-Chong Tan, and SY Ron Hui. Decoupled power angle and voltage control of electric springs. *IEEE Trans. Power Electron.*, 31(2):1216–1229, 2015. 13, 17

[27] Parag Kanjiya and Vinod Khadkikar. Enhancing power quality and stability of future smart grid with intermittent renewable energy sources using electric springs. In *IEEE International Conference on Renewable Energy Research and Applications*, pages 918–922, 2013. 13, 17

[28] Yan Shuo, Siew-Chong Tan, CK Lee, and SY Ron Hui. Electric spring for power quality improvement. In *IEEE Applied Power Electronics Conference and Exposition*, pages 2140–2147, 2014. 13, 17

[29] S Yan, SC Tan, CK Lee, and RSY Hui. Electric spring for power quality improvement. *IEEE Trans. Smart Grid*, 1(3):320–331, 2010. 13, 17

[30] Shuo Yan, Siew-Chong Tan, Chi-Kwan Lee, and SY Ron Hui. Reducing three-phase power imbalance with electric springs. In *IEEE International Symposium on Power Electronics for Distributed Generation Systems*, pages 1–7. IEEE, 2014. 13, 17

[31] Shuo Yan, Siew-Chong Tan, Chi-Kwan Lee, Balarko Chaudhuri, and SY Ron Hui. Electric springs for reducing power imbalance in three-phase power systems. *IEEE Trans. Power Electron.*, 30(7):3601–3609, 2014. 13, 17

[32] Xia Chen, Yunhe Hou, Siew-Chong Tan, Chi-Kwan Lee, and Shu Yuen Ron Hui. Mitigating voltage and frequency fluctuation in microgrids using electric springs. *IEEE Trans. Smart Grid*, 6(2):508–515, 2014. 13

[33] Zohaib Akhtar, Balarko Chaudhuri, and Shu Yuen Ron Hui. Primary frequency control contribution from smart loads using reactive compensation. *IEEE Trans. Smart Grid*, 6(5):2356–2365, 2015. 13

[34] Xiao Luo, Chi Kwan Lee, Wai Man Ng, Shuo Yan, Balarko Chaudhuri, and Shu Yuen Ron Hui. Use of adaptive thermal storage system as smart load for voltage control and demand response. *IEEE Trans. Smart Grid*, 8(3):1231–1241, 2016. 13

[35] Diptargha Chakravorty, Balarko Chaudhuri, and Shu Yuen Ron Hui. Rapid frequency response from smart loads in Great Britain power system. *IEEE Trans. Smart Grid*, 8(5):2160–2169, 2016. 13, 15

[36] Shuyao Wang, Yiwei Ma, Taylor Short, Leon M Tolbert, and Fred Wang. Power emulator of variable speed drive with grid frequency support in multi-converter based power grid emulation system. In *IEEE Energy Conversion Congress and Exposition*, pages 1694–1701, 2020. 15, 16, 19, 21, 25, 42, 44, 45, 46, 47, 57, 62, 63, 69, 99, 101

[37] U.S. Department of Energy. United States industrial electric motor systems market opportunities assessment. Technical report, U.S. Department of Energy, 2002. 15

[38] Yuan Liu, Pavel V Etingov, Soumya Kundu, Zhangshuan Hou, Qiuhua Huang, Huifen Zhou, Malini Ghosal, Daniel P James, Jian Zhang, YuLong Xie, et al. Open-source high-fidelity aggregate composite load models of emerging load behaviors for large-sale analysis. Technical report, Pacific Northwest National Lab.(PNNL), Richland, WA (United States), 2020. 15

[39] Mostafa Malekpour, Rasoul Azizipanah-Abarghooee, Fei Teng, Goran Strbac, and Vladimir Terzija. Fast frequency response from smart induction motor variable speed drives. *IEEE Trans. Power Syst.*, 35(2):997–1008, 2019. 15, 17, 18

[40] Rasoul Azizipanah-Abarghooee and Mostafa Malekpour. Smart induction motor variable frequency drives for primary frequency regulation. *IEEE Trans. Energy Convers.*, 35(1):1–10, 2019. 15, 17, 18

[41] Jesús Carmona-Sánchez, Mike Barnes, and Judith M Apsley. Virtual energy storage: Converting an AC drive to a smart load. *IEEE Trans. Energy Convers.*, 33(3):1342–1353, 2018. 15, 17, 18

[42] Hongzhi Liu and Zhe Chen. Contribution of VSC-HVDC to frequency regulation of power systems with offshore wind generation. *IEEE Trans. Energy Convers.*, 30(3):918–926, 2015. 16

[43] Yujun Li, Zeren Zhang, Yong Yang, Yingyi Li, Hairong Chen, and Zheng Xu. Coordinated control of wind farm and VSC–HVDC system using capacitor energy and kinetic energy to improve inertia level of power systems. *International Journal of Electrical Power & Energy Systems*, 59:79–92, 2014. 16

[44] F Gonzalez-Longatt. Frequency control and inertial response schemes for the future power networks. In *Large Scale Renewable Power Generation*, pages 193–231. Springer, 2014. 16

[45] B Silva, CL Moreira, L Seca, Y Phulpin, and JA Pecas Lopes. Provision of inertial and primary frequency control services using offshore multiterminal HVDC networks. *IEEE Trans. Sustain. Energy*, 3(4):800–808, 2012. 16

[46] Mengran Yu, Adam Dyśko, Campbell D Booth, Andrew J Roscoe, and Jiebei Zhu. A review of control methods for providing frequency response in VSC-HVDC transmission systems. In *International Universities Power Engineering Conference*, pages 1–6, 2014. 16

[47] Oluwole D Adeuyi, Marc Cheah-Mane, Jun Liang, Nick Jenkins, Yanan Wu, Chang Li, and Xueguang Wu. Frequency support from modular multilevel converter based multi-terminal HVDC schemes. In *IEEE Power & Energy Society General Meeting*, pages 1–5, 2015. 16

[48] Shuyao Wang, Shuoting Zhang, Yiwei Ma, Fred Wang, and Leon M Tolbert. Analysis of MTDC inertia emulation impact on connected ac systems. In *IEEE Energy Conversion Congress and Exposition*, pages 3705–3712. IEEE, 2018. 16

[49] Adri Junyent-Ferr, Yousef Pipelzadeh, and Tim C Green. Blending HVDC-link energy storage and offshore wind turbine inertia for fast frequency response. *IEEE Trans. Sustain. Energy*, 6(3):1059–1066, 2014. 16

[50] Oluwole Daniel Adeuyi, Marc Cheah-Mane, Jun Liang, and Nick Jenkins. Fast frequency response from offshore multiterminal VSC–HVDC schemes. *IEEE Trans. Power Del.*, 32(6):2442–2452, 2016. 16

[51] Johan Morren, Sjoerd WH De Haan, Wil L Kling, and JA Ferreira. Wind turbines emulating inertia and supporting primary frequency control. *IEEE Trans. Power Syst.*, 21(1):433–434, 2006. 16

[52] Ioannis D Margaris, Stavros A Papathanassiou, Nikos D Hatziargyriou, Anca D Hansen, and Poul Sorensen. Frequency control in autonomous power systems with high wind power penetration. *IEEE Trans. Sustain. Energy*, 3(2):189–199, 2012. 16, 18

[53] Jia Liu, Yushi Miura, and Toshifumi Ise. Comparison of dynamic characteristics between virtual synchronous generator and droop control in inverter-based distributed generators. *IEEE Trans. Power Electron.*, 31(5):3600–3611, 2015. 16

[54] Liu Yang, Yiwei Ma, Jingxin Wang, Jing Wang, Xiaohu Zhang, Leon M Tolbert, Fred Wang, and Kevin Tomsovic. Development of converter based reconfigurable power grid emulator. In *IEEE Energy Conversion Congress and Exposition*, pages 3990–3997, 2014. 19

[55] Shuoting Zhang, Yiwei Ma, Liu Yang, Fred Wang, and Leon M Tolbert. Development of a hybrid emulation platform based on RTDS and reconfigurable power converter-based testbed. In *IEEE Applied Power Electronics Conference and Exposition*, pages 3121–3127, 2016. 19

[56] CURENT. CURENT research: Hardware test-bed. `https://curent.utk.edu/files/8414/8709/3719/Tolbert_Fact_Sheet_Web.pdf`, 2015. 19

[57] Liu Yang, Jing Wang, Yiwei Ma, Jingxin Wang, Xiaohu Zhang, Leon M Tolbert, Fei Fred Wang, and Kevin Tomsovic. Three-phase power converter-based real-time synchronous generator emulation. *IEEE Trans. Power Electron.*, 32(2):1651–1665, 2016. 20, 22

[58] Wenchao Cao, Yiwei Ma, Jingxin Wang, Liu Yang, Jing Wang, Fred Wang, and Leon M Tolbert. Two-stage PV inverter system emulator in converter based power

grid emulation system. In *IEEE Energy Conversion Congress and Exposition*, pages 4518–4525, 2013. 20, 48

[59] Yiwei Ma, Liu Yang, Fred Wang, and Leon M Tolbert. Voltage closed-loop virtual synchronous generator control of full converter wind turbine for grid-connected and stand-alone operation. In *IEEE Applied Power Electronics Conference and Exposition*, pages 1261–1266, 2016. 20, 48

[60] Shuoting Zhang, Bo Liu, Sheng Zheng, Yiwei Ma, Fei Wang, and Leon M Tolbert. Development of a converter-based transmission line emulator with three-phase short-circuit fault emulation capability. *IEEE Trans. Power Electron.*, 33(12):10215–10228, 2018. 20

[61] Jing Wang, Liu Yang, Yiwei Ma, Jingxin Wang, Leon M Tolbert, Fei Fred Wang, and Kevin Tomsovic. Static and dynamic power system load emulation in a converter-based reconfigurable power grid emulator. *IEEE Trans. Power Electron.*, 31(4):3239–3251, 2015. 20, 23

[62] Shuyao Wang, Haiguo Li, Jingxin Wang, Li, Yiwei Ma, Leon Tolbert, and Fred Wang. A power converter based real-time air-conditioner motor emulator. In *IEEE Applied Power Electronics Conference and Exposition*, pages 70–76, 2020. 20, 23, 25

[63] Yiwei Ma, Liu Yang, Fred Wang, and Leon M Tolbert. Short circuit fault emulation by shunt connected voltage source converter. In *IEEE Energy Conversion Congress and Exposition*, pages 2622–2628, 2015. 20

[64] Jing Wang. *Versatile three-phase power electronics converter based real-time load emulators*. PhD dissertation, The University of Tennessee, 2015. 20, 21, 22, 24

[65] Liu Yang. *Three-phase power converter based real-time synchronous generator emulation*. PhD dissertation, The University of Tennessee, 2015. 23, 24

[66] Jing Wang, Yiwei Ma, Liu Yang, Leon M Tolbert, and Fred Wang. Power converter-based three-phase induction motor load emulator. In *IEEE Applied Power Electronics Conference and Exposition*, pages 3270–3274, 2013. 23, 69

[67] Metin Kesler, Engin Ozdemir, Mithat C Kisacikoglu, and Leon M Tolbert. Power converter-based three-phase nonlinear load emulator for a hardware testbed system. *IEEE Trans. Power Electron.*, 29(11):5806–5812, 2014. 25

[68] Siqi Wang, Evangelos Farantatos, and Kevin Tomsovic. Wind turbine generator modeling considerations for stability studies of weak systems. In *IEEE North American Power Symposium (NAPS)*, pages 1–6, 2017. 26

[69] Prabha Kundur, Neal J Balu, and Mark G Lauby. *Power system stability and control*, volume 7. McGraw-Hill New York, 1994. 26, 38

[70] Soo-Hyoung Lee, Seo-Eun Son, Sung-Moo Lee, Jong-Man Cho, Kyung-Bin Song, and Jung-Wook Park. Kalman-filter based static load modeling of real power system using K-EMS data. *Journal of Electrical Engineering and Technology*, 7(3):304–311, 2012. 26

[71] He Renmu, Ma Jin, and David J Hill. Composite load modeling via measurement approach. *IEEE Trans. Power Syst.*, 21(2):663–672, 2006. 26

[72] P Regulski, DS Vilchis-Rodriguez, S Djurović, and V Terzija. Estimation of composite load model parameters using an improved particle swarm optimization method. *IEEE Trans. Power Del.*, 30(2):553–560, 2014. 26

[73] WW Price, HD Chiang, HK Clark, C Concordia, DC Lee, JC Hsu, S Ihara, CA King, CJ Lin, Y Mansour, K Srinivasan, C W Taylor, and E Vaahedi. Load representation for dynamic performance analysis. *IEEE Trans. Power Syst.*, 8(2), 1993. 26, 38

[74] WW Price, CW Taylor, and GJ Rogers. Standard load models for power flow and dynamic performance simulation. *IEEE Trans. Power Syst.*, 10(CONF-940702-), 1995. 26

[75] David J Hill. Nonlinear dynamic load models with recovery for voltage stability studies. *IEEE Trans. Power Syst.*, 8(1):166–176, 1993. 26, 38

[76] Daniel Karlsson and David J Hill. Modelling and identification of nonlinear dynamic loads in power systems. *IEEE Trans. Power Syst.*, 9(1):157–166, 1994. 26, 38

[77] Dmitry Kosterev, Anatoliy Meklin, John Undrill, Bernard Lesieutre, William Price, David Chassin, Richard Bravo, and Steve Yang. Load modeling in power system studies: WECC progress update. In *IEEE Power and Energy Society General Meeting-Conversion and Delivery of Electrical Energy in the 21st Century*, pages 1–8, 2008. 26, 38

[78] Anish Gaikwad, Penn Markham, and Pouyan Pourbeik. Implementation of the WECC composite load model for utilities using the component-based modeling approach. In *IEEE/PES Transmission and Distribution Conference and Exposition (T&D)*, pages 1–5, 2016. 26, 38

[79] Adam John Collin. *Advanced load modelling for power system studies.* PhD dissertation, The University of Edinburgh, Edinburgh, Nov 2013. 26

[80] CH Dharmakeerthi, N Mithulananthan, and TK Saha. Impact of electric vehicle fast charging on power system voltage stability. *International Journal of Electrical Power & Energy Systems*, 57:241–249, 2014. 26

[81] Ahmed MA Haidar and Kashem M Muttaqi. Behavioral characterization of electric vehicle charging loads in a distribution power grid through modeling of battery chargers. *IEEE Trans. Ind Appl.*, 52(1):483–492, 2015. 26

[82] Pourya Shamsi and Babak Fahimi. Dynamic behavior of multiport power electronic interface under source/load disturbances. *IEEE Trans. Ind. Electron.*, 60(10):4500–4511, 2012. 26

[83] Wei Jiang and Babak Fahimi. Multiport power electronic interface—concept, modeling, and design. *IEEE Trans. Power Electron.*, 26(7):1890–1900, 2010. 26

[84] Mauricio Restrepo, Jordan Morris, Mehrdad Kazerani, and Claudio A Canizares. Modeling and testing of a bidirectional smart charger for distribution system EV integration. *IEEE Trans. Smart Grid*, 9(1):152–162, 2016. 26, 153

[85] Daijiafan Mao, Karun Potty, and Jiankang Wang. The impact of power-electronics-based load dynamics on large-disturbance voltage stability. In *IEEE Power & Energy Society General Meeting (PESGM)*, pages 1–5, 2018. 27

[86] Xiaodong Liang. Linearization approach for modeling power electronics devices in power systems. *IEEE Trans. Emerg. Sel. Topics Power Electron.*, 2(4):1003–1012, 2014. 27, 31, 40

[87] Xiaodong Liang and Jinwei He. Load model for medium voltage cascaded H-bridge multi-level inverter drive systems. *IEEE Power Energy Technol. Syst. J.*, 3(1):13–23, 2016. 27, 40

[88] Yuan Liu, Vijay Vittal, and John Undrill. Performance-based linearization approach for modeling induction motor drive loads in dynamic simulation. *IEEE Trans. Power Syst.*, 32(6):4636–4643, 2017. 27, 31, 40

[89] Deepak Ramasubramanian and Vijay Vittal. Positive sequence induction motor speed control drive model for time-domain simulations. *IET Generation, Transmission & Distribution*, 11(7):1809–1819, 2017. 27, 31, 32, 40

[90] Xiaodong Liang and Wilsun Xu. Modeling variable frequency drive and motor systems in power systems dynamic studies. In *IEEE Industry Applications Society Annual Meeting*, pages 1–11, 2013. 31

[91] D Panasetsky, A Osak, D Sidorov, and Li Yong. Simplified variable frequency induction-motor drive model for power system stability studies and control. *IFAC-PapersOnLine*, 49(27):451–454, 2016. 32, 40

[92] Yuan Liu and Vijay Vittal. Modeling of rectifier-controlled induction motor drive load in transient stability simulation tools. *IEEE Trans. Power Syst.*, 33(5):4719–4729, 2018. 32, 40

[93] Pouyan Pourbeik, Juan J Sanchez-Gasca, Jayapalan Senthil, James D Weber, Pouya Sajjad Zadehkhost, Yuriy Kazachkov, Spencer Tacke, Jun Wen, and Abraham

Ellis. Generic dynamic models for modeling wind power plants and other renewable technologies in large-scale power system studies. *IEEE Trans. Energy Convers.*, 32(3):1108–1116, 2016. 32

[94] Spencer Tacke. Wecc remtf workshop. `https://www.wecc.org/Reliability/Wkshp_WECC_REMTF_Workshop_2016.pdf`, March 2016. 33, 34, 40

[95] Pouyan Pourbeik, Weber James, Deepak Ramasubramanian, Juan Sanchez-Gasca, Jay Senthil, Pouya Zadkhast, Jens Boemer, Anish Gaikwad, Irina Green, Spencer Tacke, Roberto Favela, Song Wang, Songzhe Zhu, and Matthew Torgesen. An aggregate dynamic model for distributed energy resources for power system stability studies. *Cigre Science & Engineering,(14)*, pages 38–48, 2019. 33, 34, 40

[96] Daijiafan Mao. *Integration of Plug-in Electric Vehicles into Power Grid: Impact Analysis and Infrastructure Planning.* PhD dissertation, The Ohio State University, 2019. 35, 37

[97] Murat Yilmaz and Philip T Krein. Review of Battery Charger Topologies, Charging Power Levels, and Infrastructure for Plug-in Electric and Hybrid Vehicles. *IEEE Trans. Power Electron.*, 28(5):2151–2169, 2013. 35

[98] Hussain Shareef, Md Mainul Islam, and Azah Mohamed. A review of the stage-of-the-art charging technologies, placement methodologies, and impacts of electric vehicles. *Renewable and Sustainable Energy Reviews*, pages 403–420, 2016. 35

[99] SAE Hybrid Committee et al. SAE Charging Configurations and Ratings Terminology. *Society of Automotive Engineers*, 2011. 35

[100] Salman Habib, Muhammad Mansoor Khan, Farukh Abbas, Abdar Ali, Muhammad Talib Faiz, Farheen Ehsan, and Houjun Tang. Contemporary trends in power electronics converters for charging solutions of electric vehicles. *CSEE Journal of Power and Energy Systems*, 2020. 35

[101] Sebastian Rivera, Bin Wu, Samir Kouro, Venkata Yaramasu, and Jiacheng Wang. Electric vehicle charging station using a neutral point clamped converter with bipolar DC bus. *IEEE Trans. Ind. Electron.*, 62(4):1999–2009, 2014. 36, 37, 39

[102] Sebastian Rivera and Bin Wu. Electric vehicle charging station with an energy storage stage for split-DC bus voltage balancing. *IEEE Trans. Power Electron.*, 32(3):2376–2386, 2016. 36, 37, 39

[103] Jia Ying Yong, Vigna K Ramachandaramurthy, Kang Miao Tan, and N Mithulananthan. Bi-directional electric vehicle fast charging station with novel reactive power compensation for voltage regulation. *International Journal of Electrical Power & Energy Systems*, 64:300–310, 2015. 36, 37, 38, 39

[104] Bo Sun, Tomislav Dragičević, Francisco D Freijedo, Juan C Vasquez, and Josep M Guerrero. A control algorithm for electric vehicle fast charging stations equipped with flywheel energy storage systems. *IEEE Trans. Power Electron.*, 31(9):6674–6685, 2015. 36, 37, 39

[105] Mohsen Ahmadi, Nadarajah Mithulananthan, and Rahul Sharma. Dynamic load control at a bidirectional DC fast charging station for PEVs in weak AC grids. In *IEEE PES Asia-Pacific Power and Energy Engineering Conference*, pages 1–5, 2015. 36, 37, 39

[106] Daniel Aggeler, Francisco Canales, H Zelaya-De La Parra, Antonio Coccia, Nick Butcher, and Oscar Apeldoorn. Ultra-fast DC-charge infrastructures for ev-mobility and future smart grids. In *IEEE PES Innovative Smart Grid Technologies Conference Europe*, pages 1–8, 2010. 36, 39

[107] Salman Habib, Muhammad Kamran, and Umar Rashid. Impact analysis of vehicle-to-grid technology and charging strategies of electric vehicles on distribution networks–a review. *Journal of Power Sources*, 277:205–214, 2015. 38

[108] Metin Kesler, Mithat C Kisacikoglu, and Leon M Tolbert. Vehicle-to-grid reactive power operation using plug-in electric vehicle bidirectional offboard charger. *IEEE Trans. Ind. Electron.*, 61(12):6778–6784, 2014. 38

[109] Wooyoung Choi, Woongkul Lee, and Bulent Sarlioglu. Reactive power control of grid-connected inverter in vehicle-to-grid application for voltage regulation. In *IEEE Transportation Electrification Conference and Expo*, pages 1–7, 2016. 38

[110] Mithat C Kisacikoglu, Burak Ozpineci, and Leon M Tolbert. Reactive power operation analysis of a single-phase EV/PHEV bidirectional battery charger. In *IEEE International Conference on Power Electronics-ECCE Asia*, pages 585–592, 2011. 38

[111] Seyedmahdi Izadkhast, Pablo Garcia-Gonzalez, Pablo Frìas, Laura Ramìrez-Elizondo, and Pavol Bauer. An aggregate model of plug-in electric vehicles including distribution network characteristics for primary frequency control. *IEEE Trans. Power Syst.*, 31(4):2987–2998, 2015. 38, 39

[112] Rodrigo Garcia-Valle and João A Peças Lopes. *Electric vehicle integration into modern power networks*. Springer Science & Business Media, 2012. 38, 39

[113] GD Marques. A simple and accurate system simulation of three-phase diode rectifiers. In *IEEE Industrial Electronics Society Conference*, volume 1, pages 416–421, 1998. 44

[114] Xiaojie Shi, Zhiqiang Wang, Yiwei Ma, Lijun Hang, Leon M Tolbert, and Fred Wang. Modeling and control of an LCL filter based three-phase active rectifier in grid emulator. In *IEEE Applied Power Electronics Conference and Exposition*, pages 992–998, 2013. 48

[115] Jessica D Boles, Yiwei Ma, Wenchao Cao, Leon M Tolbert, and Fred Wang. Battery energy storage emulation in a converter-based power system emulator. In *IEEE Applied Power Electronics Conference and Exposition*, pages 2355–2362, 2017. 51

[116] Paul C Krause, Oleg Wasynczuk, Scott D Sudhoff, and Steven Pekarek. *Analysis of electric machinery and drive systems*, volume 2. Wiley Online Library, 2002. 52, 55, 58, 61, 62, 64, 65, 66, 70

[117] U.S. department of energy. Adjustable speed drive part - load efficiency. `https://www.energy.gov/sites/prod/files/2014/04/f15/motor_tip_sheet11.pdf`, Nov 2012. 77

[118] U.S. department of energy. Determining electric motor load and eficiency. `https://www.energy.gov/sites/prod/files/2014/04/f15/10097517.pdf`, April 2014. 77

[119] Saskia. How to normalize the rmse. `https://www.marinedatascience.co/blog/2019/01/07/normalizing-the-rmse/`, January 2019. 90

[120] Martin Brown. Siemens standard drives application handbook. `https://cache.industry.siemens.com/dl/files/430/1160430/att_36835/v1/applications_e.pdf`, December 1997. 102

[121] Valery Vodovozov, Levon Gevorkov, and Zoja Raud. Circulation centrifugal pump with variable speed drives and minimal electricity consumption. In *IEEE International Conference on Compatibility, Power Electronics and Power Engineering*, pages 334–339, 2017. 102

[122] Angel Molina-García, Irene Munoz-Benavente, Anca D Hansen, and Emilio Gómez-Lázaro. Demand-side contribution to primary frequency control with wind farm auxiliary control. *IEEE Trans. Power Syst.*, 29(5):2391–2399, 2014. 122

[123] Angel Molina-Garcia, François Bouffard, and Daniel S Kirschen. Decentralized demand-side contribution to primary frequency control. *IEEE Trans. Power Syst.*, 26(1):411–419, 2010. 122

[124] Yu-Qing Bao and Yang Li. FPGA-based design of grid friendly appliance controller. *IEEE Trans. Smart Grid*, 5(2):924–931, 2014. 122

[125] S Ali Pourmousavi and M Hashem Nehrir. Real-time central demand response for primary frequency regulation in microgrids. *IEEE Trans. Smart Grid*, 3(4):1988–1996, 2012. 122

[126] Le-Ren Chang-Chien, Luu Ngoc An, Ta-Wei Lin, and Wei-Jen Lee. Incorporating demand response with spinning reserve to realize an adaptive frequency restoration plan for system contingencies. *IEEE Trans. Smart Grid*, 3(3):1145–1153, 2012. 122

[127] Benjamin Biegel, Lars Henrik Hansen, Palle Andersen, and Jakob Stoustrup. Primary control by ON/OFF demand-side devices. *IEEE Trans. Smart Grid*, 4(4):2061–2071, 2013. 122

[128] Yu-Qing Bao, Yang Li, Ying-Yi Hong, and Beibei Wang. Design of a hybrid hierarchical demand response control scheme for the frequency control. *IET Generation, Transmission & Distribution*, 9(15):2303–2310, 2015. 122, 123

[129] Haoran Zhao, Qiuwei Wu, Shaojun Huang, Hengxu Zhang, Yutian Liu, and Yusheng Xue. Hierarchical control of thermostatically controlled loads for primary frequency support. *IEEE Trans. Smart Grid*, 9(4):2986–2998, 2016. 122

[130] Hongxun Hui, Yi Ding, Yonghua Song, and Saifur Rahman. Modeling and control of flexible loads for frequency regulation services considering compensation of communication latency and detection error. *Applied Energy*, 250:161–174, 2019. 125

[131] WECC Significant Electrification Task Force. WECC significant electrification task force update. `https://www.wecc.org/Administrative/Melloni%20-%20Significnat%20Electrification.pdf`, Oct 2019. 133

[132] Clarence M Shepherd. Design of primary and secondary cells: II. an equation describing battery discharge. *Journal of the Electrochemical Society*, 112(7):657–664, 1965. 153

[133] Matthew Rylander, W Mack Grady, Ari Arapostathis, and Edward J Powers. Power electronic transient load model for use in stability studies of electric power grids. *IEEE Trans. Power Syst.*, 25(2):914–921, 2009. 164

[134] Jian Sun. Impedance-based stability criterion for grid-connected inverters. *IEEE Trans. Power Electron.*, 26(11):3075–3078, 2011. 164

[135] Mohsen Ahmadi and N Mithulananthan. Dynamic voltage stability of distribution grids with fast charging stations for EV units. In *International Conference on Smart Grid and Clean Energy Technologies*, pages 130–136, 2018. 164

[136] Bernardo Silva, Carlos Leal Moreira, Helder Leite, and JA Peças Lopes. Control strategies for ac fault ride through in multiterminal HVDC grids. *IEEE Trans. Power Del.*, 29(1):395–405, 2014. 164

[137] Soledad Bernal-Perez, Salvador Ano-Villalba, Ramon Blasco-Gimenez, and Johel Rodriguez-D'Derlee. Efficiency and fault ride-through performance of a diode-rectifier- and VSC-inverter-based HVDC link for offshore wind farms. *IEEE Trans. Ind. Electron.*, 60(6):2401–2409, 2012. 164

[138] G Ramtharan, Atputharajah Arulampalam, Janaka Bandara Ekanayake, FM Hughes, and Nick Jenkins. Fault ride through of fully rated converter wind turbines with AC and DC transmission systems. *IET Renewable Power Generation*, 3(4):426–438, 2009. 164

[139] Y Yu, Z Xu, and T An. Fault ride-through strategy for fully rated converter wind turbines connected to the grid via MMC-HVDC transmission. In *IET International Conference on AC and DC Power Transmission*, pages 1–5, 2016. 164

[140] Wenye Sun, Raymundo Enrique Torres-Olguin, and Olimpo Anaya-Lara. Investigation on fault-ride through methods for VSC-HVDC connected offshore wind farms. *Energy Procedia*, 94:29–36, 2016. 164

[141] Soumya Kundu and Ian A Hiskens. Overvoltages due to synchronous tripping of plug-in electric-vehicle chargers following voltage dips. *IEEE Trans. Power Del.*, 29(3):1147–1156, 2014. 165

[142] Power quality requirements for plug-in electric vehicle chargers, 2019. 165, 166, 167, 168

[143] Fred Friend. Cold load pickup issues. In *Annual Conference for Protective Relay Engineers*, pages 176–187, 2009. 167

[144] Roni Irnawan, FF da Silva, Claus Leth Bak, and TC Bregnhoj. Evaluation of half-bridge modular multilevel converter model for VSC-HVDC transient stability studies. In *IET International Conference on AC and DC Power Transmission*, pages 1–6, 2017. 167

[145] Ngoc-Tuan Trinh, Marcus Zeller, Klaus Wuerflinger, and Istvan Erlich. Generic model of MMC-VSC-HVDC for interaction study with AC power system. *IEEE Trans. Power Syst.*, 31(1):27–34, 2015. 167

[146] Julian Freytes, Lampros Papangelis, Hani Saad, Pierre Rault, Thierry Van Cutsem, and Xavier Guillaud. On the modeling of MMC for use in large scale dynamic simulations. In *Power Systems Computation Conference*, pages 1–7, 2016. 167

[147] Simon P Teeuwsen. Simplified dynamic model of a voltage-sourced converter with modular multilevel converter design. In *IEEE/PES Power Systems Conference and Exposition*, pages 1–6, 2009. 167

[148] Kou Longze, Zhu Lin, and Li Fangyuan. Electromechanical modelling of modular multilevel converter based HVDC system and its application. In *IEEE Conference on Energy Internet and Energy System Integration*, pages 1–6, 2017. 167

[149] Sheng Liu, Zheng Xu, Wen Hua, Geng Tang, and Yinglin Xue. Electromechanical transient modeling of modular multilevel converter based multi-terminal HVDC systems. *IEEE Trans. Power Syst.*, 29(1):72–83, 2013. 167

[150] Shuyao Wang, Xiaoying Zhao, Feng Xue, Wei Li, Huimin Peng, Di Shi, Siqi Wang, and Zhiwei Wang. Electromechanical transient modeling of modular multilevel converter based HVDC network. In *IEEE Sustainable Power and Energy Conference*, pages 1845–1850, 2019. 169

Appendices

A VSD Model Parameters Employed in the Detailed Model Developed in Simulink

The VSD load model with open/closed loop control schemes is developed in Simulink to verify the accuracy of the proposed simplified VSD load model. The critical parameters of the developed VSD load model are summarized from Table 1 to Table 5.

Parameters of the IM in the developed VSD load model are listed in Table 1.

Table 1: VSD load model parameters developed in Simulink: IM parameters.

Parameters	Value	Parameters	Value
$V_{IM,base}$	375.6 V	$P_{IM,base}$	37.3 kVA
T_{base}	197.9 Nm	$\omega_{r,base}$	377 rad/s
H_{IM}	0.79 s	Pole pair	2
R_s	0.015 p.u.	R_r	0.051 p.u.
L_{ls}	0.053 p.u.	L_{lr}	0.053 p.u.
L_m	2.31 p.u.		

Parameters of the active front-end rectifier in the developed VSD load model are listed in Table 1. The base value of the rectifier ac and dc sides are represented by $V_{ac,base}$ $V_{dc,base}$, $K_{p,dc}$ and $K_{i,dc}$ represent the PI controller parameters of constant V_{dc} control loop.

Table 2: VSD load model parameters developed in Simulink: active front-end rectifier.

Parameters	Value	Parameters	Value
$V_{ac,base}$	480 V	P_{base}	40 kVA
$V_{dc,base}$	800 V	C_{dc}	0.005 F
$K_{p,dc}$	109.08	$K_{i,dc}$	64165.66

Parameters of the VSD load adopting closed loop speed controllers are listed in Table 3 to Table 5, which represents the controller parameters of FOC, DTC and constant slip current control. $K_{p,T}$ and $K_{i,T}$ represent the PI controller parameters of generating $T_{e,ref}$ via the ω_r negative feedback control, $K_{p,I}$ and $K_{p,I}$ represent the PI controller parameters of stator current control loop, $K_{p,vq}$, $K_{i,vq}$, $K_{p,vd}$ and $K_{i,vd}$ represent the PI controller parameters of stator voltage control loop.

Table 3: VSD load model parameters developed in Simulink: FOC.

Parameters	Value	Parameters	Value
$K_{p,T}$	13	$K_{i,T}$	26
$K_{p,I}$	1.1	$K_{i,I}$	28.3
$\lambda_{r,ref}$	0.96 Wb		

Table 4: VSD load model parameters developed in Simulink: DTC.

Parameters	Value	Parameters	Value
$K_{p,T}$	13	$K_{i,T}$	26
$K_{p,vq}$	1.5	$K_{i,vq}$	100
$K_{p,vd}$	4000	$K_{i,vd}$	250
$\lambda_{s,ref}$	0.96 Wb		

Table 5: VSD load model parameters developed in Simulink: constant slip current control.

Parameters	Value	Parameters	Value
$K_{p,T}$	13	$K_{i,T}$	26
$K_{p,I}$	1.10	$K_{i,I}$	28.3

B VSD Load Model Parameters for Equivalent Droop Control Simulation

As mentioned in Section 4.2.3, there are 18 VSD simplified models employed in the simulation test to represents the aggregated performance of the VSD load groups. The parameters of the 18 VSD load units are listed below in Table 6

Table 6: 18 VSD load unit model parameters which are selected for representing the multiple VSD load aggregated performance.

VSD No.	H (s)	K_p	K_i	VSD No.	H (s)	K_p	K_i
1	1	20.04	3.51	10	1	199.97	349.99
2	1	20.05	3.51	11	1	199.97	349.99
3	1	20.05	3.51	12	1	199.97	349.99
4	1.5	30.02	5.25	13	1.5	299.96	524.95
5	1.5	30.03	5.255	14	1.5	299.96	524.95
6	1.5	30.03	5.255	15	1.5	299.96	524.95
7	2	40.02	7.004	16	2	399.94	699.97
8	2	40.02	7.004	17	2	399.94	699.97
9	2	40.02	7.004	18	2	399.94	699.97

C Electrical Model and Controller Parameters of the Studied Fast EV Charging Unit

Parameters of the EV charger load model developed in both TSAT® and PSCAD/EMTDC® are summarized in Table 7. $V_{dc,base}$, $V_{ac,base}$, and $P_{ac,base}$ represents the EV charger load dc side voltage base, the ac power network voltage base, and the ac power network power base; $K_{p,dc}$ and $K_{i,dc}$ represent the PI controller parameters for the constant V_{dc} control, $T_{dc,LPF}$ represents the low pass filter for the measured V_{dc}; $K_{p,Q}$ and $K_{i,Q}$ represent the PI controller parametesr for the constant Q_{EV} control, $T_{Q,LPF}$ represents the low pass filter for the Q_{EV}, $K_{p,I}$ and $K_{i,I}$ represent the PI controller parameters for the vector controller inner current loop.

Table 7: Critical parameters for the EV charging unit model.

Parameters	Value	Parameters	Value
$V_{dc,base}$	420 kV	$V_{ac,base}$	230 kV
$P_{ac,base}$	100 MVA	$K_{p,dc}$	0.035
$K_{i,dc}$	1.99	$T_{dc,LPF}$	0.01
$K_{p,Q}$	0.1	$K_{i,Q}$	0.1
$T_{Q,LPF}$	0.0038	$K_{p,I}$	300.53
$K_{i,I}$	0.0038	$K_{p,I}$	$1.77 \cdot 10^5$

Vita

Ms. Shuyao Wang was born in Shenyang, Liaoning Province, China in Oct, 1990. She received her Bachelor of Science and Master of Science degree from North China Electric Power University in Beijing, China in 2013 and 2016, respectively. She started her Ph.D. study in 2016 at the Center for Ultra-wide-area Resilient Electric Energy Transmission Networks (CURENT), the University of Tennessee, Knoxville. Her research interests include power electronics interfaced device modeling and control, HVDC transmission systems, renewable generation resources, etc. During this period, Shuyao Wang has also had two intern experiences: she worked as a power system engineer intern during May 2019 - Aug. 2019 at Global Energy Interconnection Research Institute North America (GEIRINA), and worked as intern engineer during Jan. 2021 - May 2021 at Tesla.